THESIS APPROVAL

GRADUATE SCHOOL, KASETSART UNIVERSITY

Doctor of Philosophy (Chemistry)

DEGREE

Chemistry	Chemistry
FIELD	**DEPARTMENT**

TITLE: Metal-decorated Carbon Nanotubes for Applications in Sensing and Catalysis: A Theoretical and Experimental Study

NAME: Miss Panvika Pannopard

THIS THESIS HAS BEEN ACCEPTED BY

______________________________ **THESIS ADVISOR**

(ProfessorJumrasLimtrakul, Ph.D.)

______________________________ **THESIS CO-ADVISOR**

(Mr. PipatKhongpracha, Ph.D.)

______________________________ **THESIS CO-ADVISOR**

(Miss ChompunuchWarakulwit, Ph.D.)

______________________________ **DEPARTMENT HEAD**

(AssociateProfessorWaraponParasuk, Dr.rer.nat.)

APPROVED BY THE GRADUATE SCHOOL ON ______________________________

______________________________ **DEAN**

(Associate Professor GunjanaTheeragool, D.Agr.)

THESIS

METAL-DECORATED CARBON NANOTUBES FOR APPLICATIONS IN SENSING AND CATALYSIS: A THEORETICAL AND EXPERIMENTAL STUDY

PANVIKA PANNOPARD

A Thesis Submitted in Partial Fulfillment of
the Requirements for the Degree of
Doctor of Philosophy (Chemistry)
Graduate School, Kasetsart University
2014

Panvika Pannopard 2014: Metal-decorated Carbon Nanotubes for Applications in Sensing and Catalysis: A Theoretical and Experimental Study. Doctor of Philosophy (Chemistry), Major Field: Chemistry, Department of Chemistry. Thesis Advisor: Professor Jumras Limtrakul, Ph.D. 180 pages.

The fabrication of metal nanoparticles decorated carbon nanotubes (MNPs-CNTs) is of current interest for the development of nanomaterial based catalysts and electronic devices. Here, the Density Functional Theory approach was employed to investigate the sensing and catalytic performances of MNPs-CNTs. The calculations show that Pt-doped CNT enhances, to a very large degree, the adsorptions and charge transfers of NO_2 and NH_3 toxic gas molecules and both processes cause changes in the electronic structure and charge distribution with greater and are more far-reaching than those of unmodified and defected CNTs. In the case of N_2O greenhouse gas decomposition, without metal doping, the reaction on the bare CNT proceeds via a high energy barrier (54.3 kcal mol^{-1}) which in the presence of active metals is reduced to 3.6, 8.0 and 10.2 kcal mol^{-1} for V-, Ti- and Sc-doped CNTs, respectively. Thus, MNPs can overcome the limitations of intrinsic CNTs. For experimental work, the novel-designed catalytic platform for the fuel cell system was constructed whereby the Nafion layer and PtNPs were formed inside the pores of the CNT-Anodic Aluminium Oxide composite. The PtNPs are successfully deposited with chemical reduction and loading of the small size alkane-thiolated PtNPs. The thin layer of Nafion could also be coated properly to PtNPs size along the tube. Furthermore, the facile electrostatic deposition of the size-controlled AuNPs onto the negatively charged AAO-templated CNTs is demonstrated as a new strategy to produce the structure-controllable AuNPs/CNTs usefully for nanoapplications. By increasing the mole ratios of polyvinylpyrrolidone and dimethylaminopyridine (PVP:DMAP) stabilizers, the average diameters of AuNPs are progressively decreased. In addition, CNTs facilitate the Au depositions without tedious pretreatment on CNT surfaces.

________________________ ________________________ ___ / ___ / ____

Student's signature | Thesis Advisor's signature

ACKNOWLEDGEMENTS

This dissertation would not have been possible without my advisor, Prof. Dr. Jumras Limtrakul, who always gave me excellent guidance, continuous support and all that I needed for doing research in the graduate program. A special thank you goes to my co-advisors, Dr. Pipat Khongpracha and Dr. Chompunuch Warakulwit, for their big help to develop my skill in computational chemistry and experiment and also for their insightful advices as well as patient corrections of my writing. For the time that I stayed in Japan, I would like to express my deepest gratitude to my Japanese supervisors, Prof. Dr. Takashi Kyotani and Asst. Prof. Dr. Yasuto Hoshikawa from Tohoku University and also Prof. Dr. Tatsuya Tsukuda, Asst. Prof. Dr. Hironori Tsunoyama and Dr. Risako Tsunoyama from Hokkaido University, for their kind training, challenging ideas and encouragement to accomplish my work. The JENESYS programme under the JSPS Exchange Program is also acknowledged.

During the course of this work at Kasetsart University, I was supported mainly by the Royal Golden Jubilee Ph.D. program (3.C.KU/50/A.1) from the Thailand Research Fund and Kasetsart University. Additionally, support by grants from the National Science and Technology Development Agency (NANOTEC Center for the Design of Nanoscale Materials for Green Nanotechnology and NSTDA Chair Professor), the Kasetsart University Research and Development Institute (KURDI) as well as under the Commission on Higher Education, Ministry of Education ("National Research University of Thailand" and "Postgraduate Education and Research Programs in Petroleum and Petrochemicals and Advanced Materials"). The support for CPU time on the Laboratory for Computational and Applied Chemistry (LCAC) and Tera cluster of the Thai National Grid is also acknowledged.

Last, but not least, I thank my family for giving life to me in the first place, for educating me, for their encouragement to pursue my interests and for believing in me.

Panvika Pannopard

July, 2014

TABLE OF CONTENTS

	Page
TABLE OF CONTENTS	i
LIST OF TABLES	ii
LIST OF FIGURES	iii
LIST OF ABBREVIATIONS	xii
INTRODUCTION	1
OBJECTIVES	20
LITERATURE REVIEW	21
MATERIALS AND METHODS	39
RESULTS AND DISCUSSION	67
CONCLUSION	135
LITERATURE CITED	139
APPENDIX	176
CURRICULUM VITAE	180

LIST OF TABLES

Table **Page**

Table		Page
1	The amounts of PVP and DMAP used in each sample of positively charged AuNPs and also the corresponding calculated mole ratios	66
2	Binding energies E_b between Pt and SWCNT and SWCNTVac and binding energies of NO_2 and NH_3 to the four types of SWCNTs. The structures are shown in Figures 35 and 37, respectively. The energies are given in kcal/mol	69
3	Partial molecular and atomic charges $q(e)$ and values of the HOMO-LUMO gap E_g(eV) of all studied complexes. Partial charge transfers and energy gap changes are indicated by the prefix delta (Δ). Refer to text for the definitions of the quantities	75
4	Partial molecular and atomic charge transfers, Δq(e) of all complexes for co-adsorption states (Δq_{ads}), transition states (Δq_{ts}) and final states (Δq_{prod}). The partial charges of the initial metal-doped (5,5)SWCNTs (without N_2O) are tabulated in Table 5	86
5	Partial molecular and atomic charges, q(e) of studied metal-doped (5,5)SWCNTs catalysts	86
6	Charge density differences of metal atoms in the metal-doped (5,5)SWCNTs and their TS for each molecular orbitals	90
7	Anodic and cathodic reactions in the electrolytic polishing of Al plate	93
8	Anodic and cathodic reactions of the anodization of the Al plate in an acid electrolyte. The selective dissolution of AAO layer with acid and the selective removal of Al with $CuCl_2$ are also elaborated	96
9	Zeta (ζ) potentials of CNTs, Au-(P) and Au-(P1024:D1) at pH ~7	121
10	Zeta (ζ) potentials of the synthesized AuNPs, Au-(D) to Au-(P512:D1), at pH ~7-8	125

LIST OF FIGURES

Figure		Page
1	Schematic illustration of the structure of a single-wall carbon nanotube (SWCNT) (a) and a multi-wall carbon nanotube (MWCNT) (b)	1
2	Schematic illustration of the methods for CNT synthesis arc discharge (a), laser vaporization (b) and chemical vapor deposition (c)	3
3	Schematic illustration of the chiral, armchair and zigzag SWCNTs defined by chiral vector and chiral angle	4
4	Schematic illustration introducing the relevant processes for selected fuel cells, accompanied by their corresponding applications	10
5	Schematic illustration of a typical PEMFC single cell and the chemical reactions proceeding at its electrodes (anode and cathode)	11
6	Schematic illustration of the three-phase boundary interfacial area formed at the catalyst layer that is required for the occurrence of the reactions for fuel cells	13
7	Schematic illustration showing an anodic aluminium oxide (AAO) structure prepared via an electrochemical anodization of aluminium (Al)	15
8	Schematic illustration showing the assembly of Nafion/PtNPs/CNT-AAO film and Nafion membrane. The triple phase reaction zone (Nafion/PtNPs/CNTs) constructed on the inner walls of the AAO pores also demonstrated	16
9	Schematic illustration showing the stabilization of AuNPs using DMAP capping agent	18
10	Schematic illustration of the Nafion structure in which x and y are repeat units of the hydrophobic backbone and z represents a repeat unit of side chain with a sulfonic acid group termination	29

LIST OF FIGURES (Continued)

Figure		Page
11	Initial geometries of pristine SWCNT (a), vacancy SWCNT (b), Pt-doped SWCNT (c) and Pt-deposited SWCNT (d). The inset is shown a side view under corresponding picture of (d)	41
12	Top and side views of initial configurations of the gas molecules oriented in different sites	42
13	Initial geometries of undoped (5,5)SWCNT (a), Sc-doped (5,5)SWCNT (b), Ti- doped (5,5)SWCNT (c) and V-doped (5,5)SWCNT (d)	44
14	Schematic illustration of the summarized procedures for fabrication of Nafion/PtNPs/CNT-AAO//Nafion membrane composite	46
15	Schematic illustration of the synthesis of open-ended AAO template with 90 nm pore diameter and 60 μm pore length with two-step anodization	47
16	Schematic illustration and photos of experimental set up for electropolishing of Al plate	48
17	Schematic illustration and photos of the experimental set up for anodization of Al plate	50
18	Photos of the experimental set up for the Al removal from the AAO-Al plate and for the opening pore bottoms of the synthesized AAO template	51
19	Schematic illustration and photo of the reactor set up for chemical vapor deposition	52
20	Temperature profile for chemical vapor deposition	53
21	Summarized procedures of two different synthesis routes of the direct deposition of PtNPs onto the inner walls of CNT-AAO film	54
22	Summarized procedures of two-phase synthesis of alkanethiolated PtNPs	56

LIST OF FIGURES (Continued)

Figure		Page
23	Summarized procedures of PtNPs loading into the pores of CNT-AAO film	56
24	TGA spectra of octadecanethiol ($C_{18}H_{37}SH$) and octadecanethiolated PtNPs. The heating rate is 5°C/min and the carrier gas is N_2	57
25	Photo of the experimental set up for dipping the CNT-AAO film into the Nafion solution	58
26	Summarized procedures of the introduction Nafion solution into the pores of CNT-AAO film by dropping method under the humidity control chamber	59
27	Summarized procedure of the hot pressing Nafion membrane to Nafion/PtNPs/CNT-AAO film	60
28	Schematic illustration of the synthesis of AAO template with 35 nm pore diameter and 20 μm pore length deposited on Al plate	61
29	Schematic illustration of the CNT synthesis by the template method	62
30	Photo of CNT-AAO-Al plates which will be treated in the oxygen plasma reactor	63
31	Photos of CNT-AAO-Al plate (a), liberated CNTs from AAO-Al plate (b) and Al plate (c) after AAO dissolution, dried CNTs (d) and CNTs dispersion (e)	64
32	Summarized procedures of the water-based synthesis of AuNPs stabilized with PVP and/or DMAP stabilizers	65
33	Optimized geometries of pristine SWCNT (a), vacancy SWCNT (b), Pt-doped SWCNT (c) and Pt-deposited SWCNT (d). Side views are shown under corresponding pictures. The yellow marks indicate the active site studied for the SWCNTs (a–d). Atom–atom distances (Å) around the active centers are also depicted	67

LIST OF FIGURES (Continued)

Figure		Page
34	All optimized geometries (Å) and binding energies (kcal/mol) obtained after optimizing the structures of SWCNT:NO_2 (a), $SWCNT_{Vac}$:NO_2 (b), $SWCNT_{Vac}$/Pt:NO_2 (c) and SWCNT/Pt:NO_2 (d) complexes	70
35	Front and side views of the most favorable binding geometries of NO_2 on each support type accompanied with their binding distances. Pt-C and some C-C distances (Å) are also given	71
36	All optimized geometries (Å) and binding energies (kcal/mol) obtained after optimizing the structures of SWCNT:NH_3 (a), $SWCNT_{Vac}$:NH_3 (b), $SWCNT_{Vac}$/Pt:NH_3 (c) and SWCNT/Pt:NH_3 (d) complexes	72
37	Front and side views of the most favorable binding geometries of NH_3 on each support type accompanied with their binding distances. Pt-C and some C-C distances (Å) are also given	73
38	Plots of the differential electron densities of all studied support-gas complexes. The 3D - surfaces are plotted at isovalues of ±0.009 $e/Å^3$. A red color denotes loss of density whereas blue denotes gain of electron density	76
39	Density of states (DOSs) for the studied supports (a-d) and their NO_2 complexes (e-h). Partial density of states (PDOSs) of all support-gas complexes (i-l) and orbital partial density of states (OPDOSs) of $SWCNT_{Vac}$/Pt:NO_2 and SWCNT/Pt:NO_2 (m and n) are also plotted for comparison. The Fermi levels (defined as the HOMO energies) are calibrated to locate at zero eV	77
40	Frontier molecular orbitals of the complexes with NO_2: HOMOs (a-d) and LUMOs (e-h)	79

LIST OF FIGURES (Continued)

Figure		Page
41	Density of states (DOS) for all studied supports (a-d) and their NH_3 complexes (e-h). Partial density of states (PDOS) of all support-gas complexes (i-l) are also plotted for comparison (blue lines: support; red lines: contributions from NH_3). The Fermi levels (defined as HOMO energies) are calibrated to locate at zero eV	80
42	Frontier molecular orbitals of all studied support-NH_3 complexes, HOMOs (a-d) and LUMOs (e-h)	81
43	Optimized geometries with bond lengths (Å) of undoped (5,5)SWCNT (a), Sc-doped (5,5)SWCNT (b), Ti- doped (5,5)SWCNT (c) and V-doped (5,5)SWCNT (d)	83
44	Adsorption complexes (Ads Cpx), transition state structures (TS) and products (Prod) of undoped (5,5)SWCNT:N_2O (a-c), Sc-doped (5,5)SWCNT:N_2O (d-f), Ti-doped (5,5)SWCNT:N_2O (g-i) and V-doped (5,5)SWCNT:N_2O (j-l) systems accompanied by some selected bond lengths (Å) and angles (degrees)	84
45	Energy profiles for the N_2O decomposition on undoped (dark solid line), Sc-doped (green dash dot line), Ti-doped (red dot line) and V-doped (orange dash line) (5,5)SWCNTs. The numbers in parentheses at transition and final states are activation energies, $E_a = E_{ts} - E_{ads}$, and reaction energies, $E_r = E_{prod}\text{-}E_{ads}$, respectively	85
46	Lowest unoccupied molecular orbitals (LUMOs) of undoped (5,5)SWCNT (a), Sc- doped (5,5)SWCNT (b), Ti- doped (5,5)SWCNT (c) and V-doped (5,5)SWCNT (d)	88
47	Overlapping molecular orbitals of the reactants: HOMO of N_2O (a) with LUMO of Ti-doped (5,5)SWCNT and LUMO of V-doped (5,5)SWCNT (b)	88

LIST OF FIGURES (Continued)

Figure		Page
48	Optimized geometry with bond lengths (Å) (a) and angel (degree), highest occupied molecular orbital (HOMO) (b) and lowest unoccupied molecular orbital (LUMO) (c) of isolated N_2O molecule	89
49	Photo of the Al plate after electropolishing. The small area at upper right corner is untreated surface	92
50	Current density vs. voltage for copper electropolishing in phosphoric acid	94
51	Schematic illustration of typical formation insulating layer on the anode surface	95
52	Schematic illustration of the pore formation by electrochemical anodization, formation of barrier oxide (a), formation of pits by local field fluctuations (b), initial pore formation by field-enhanced or/and temperature-enhanced dissolution (c) and steady-state pore growth (d).	98
53	Photo of the AAO film supported on Al plates (AAO/Al plate)	98
54	Photos of the synthesized AAO film with 1x1 cm^2	99
55	SEM images of pore side (a,b), barrier side before (c,d) and after (e,f) etching and side view of AAO film	100
56	The photo of CNT-AAO film prepared under a carbon deposition using the AAO as template (a), the scanning electron microscopic (SEM) photographs at pore side (b) and barrier side (c) and the transmission electron microscopic (TEM) photographs (d-h) with different positions and magnifications of the CNTs after AAO removal	101

LIST OF FIGURES (Continued)

Figure **Page**

57 SEM photographs of top views on pore side surface (a and c), barrier side surface (b and d) and cross-sectional views (e and f) of the PtNPs/CNT-AAO film prepared without washing excess metal precursor on the film surface before reduction 104

58 TEM photographs of the PtNPs/CNTs liberated from AAO template that were prepared without washing excess metal precursor on the AAO film surface before reduction, at both ends of CNT bundle (a and b) and at the middle of CNTs (c and d) 105

59 SEM photographs of top views on pore side surface (a and c), barrier side surface (b and d) and cross-sectional views (e and f) of the PtNPs/CNT-AAO film prepared with washing excess metal precursor on the film surface before reduction 106

60 TEM photographs of the PtNPs/CNTs liberated from AAO template that were prepared with washing excess metal precursor on the AAO film surface before reduction, at both ends of CNT bundle (a and b) and at the middle of CNTs (c and d) 107

61 TEM photographs of pre-synthesized PtNPs loaded CNTs prepared by the ultrasonic assisted dipping method (a and c) followed by heat treatment (b and d) 108

62 SEM photographs of top views on the pore side surface (a and c), barrier side surface (b and d) of the octadecanethiolated PtNPs/CNT-AAO film and TEM photographs at both sides of pore mouth of octadecanethiolated PtNPs/CNTs after heat treatment 109

LIST OF FIGURES (Continued)

Figure **Page**

63 Size distributions accompanied with the corresponding average sizes of PtNPs deposited inside the CNT-AAO film prepared by direct deposition with washing (a) and without washing (b) excess metal precursor on the film surface before reduction and by pre-synthesis the PtNPs before loading (c) 110

64 Proposed feature of the well-constructed three-phase boundary forming inside the pores of CNT-AAO film 111

65 TEM photographs of Nafion coated on the inner walls of CNTs by dipping (a-b) and dropping (c-d) methods whereby drying in ambient condition and also dropping method whereby drying in humidity control system (e-f) 113

66 SEM photographs of the top views on pore side surfaces, barrier side surfaces and cross-sectional views of Nafion/PtNPs/CNT-AAO film whereby the PtNPs are prepared by non-washing (a, b and c, respectively) and washing (d, e and f, respectively) the excess metal precursor on the surfaces of CNT-AAO film before reduction and also the PtNPs are pre-synthesized before loading into the pores of CNTs are then subjected to heat treatment prior to coating with the Nafion solution (g, h and i, respectively) 116

67 TEM photographs of Nafion/PtNPs loaded CNTs in which PtNPs are prepared by non-washing (a) and washing (b) the excess metal precursor on the surfaces of CNT-AAO film before reduction. For the last figure (c), PtNPs are pre-synthesized before loading into the pores of CNTs and subjected to the heat treatment prior to coating with Nafion solution 118

68 Membrane electrode assembly (MEA) of 5x5 cm^2 Nafion membrane and 1x1 cm^2 Nafion/PtNPs/CNT-AAO film 119

LIST OF FIGURES (Continued)

Figure **Page**

Figure		Page
69	TEM photographs of AAO-templated CNTs at different magnification	121
70	A photograph of colloidal AuNPs solutions synthesized by varying PVP:DMAP mole ratios according to Table 1, starting from Au-(D) (rightmost side) to Au-(P512:D1) (leftmost side)	122
71	UV–Vis absorption spectra of (a) all synthesized AuNPs samples and (b) AuNPs/CNTs composites synthesized by varying PVP:DMAP mole ratios, Au-(D) to Au-(P512:D1). The UV–Vis absorption spectrum of bare CNTs is also compared in panel (b). Moreover, the dashed line that vertically passes through both panels is the position of absorption wavelength at 520 nm	124
72	TEM images of all prepared AuNPs/CNTs composites, Au-(D)/CNTs to Au-(P512:D1)/CNTs	127
73	TEM images at higher magnification of all prepared AuNPs/CNTs composites, Au-(D)/CNTs to Au-(P512:D1)/CNTs	128
74	Zeta (ζ) potentials distributions of the synthesized AuNPs, Au-(D) to Au-(P512:D1)	129
75	Zeta (ζ) potentials distributions of CNTs (a), Au-(P) (b) and Au-(P1024:D1) (c)	129
76	TEM images of all Au-(P)/CNTs (a) and Au-(P1024:D1)/CNTs composites (b)	130
77	Highly-magnified TEM images of all prepared AuNPs/CNTs composites, Au-(D)/CNTs to Au-(P512:D1)/CNTs	131
78	Size distribution histograms of AuNPs in all prepared AuNPs/CNTs composites, Au-(D)/CNTs to Au-(P512:D1)/CNTs	132

LIST OF ABBREVIATIONS

AAO	=	anodic aluminium oxide
AC	=	activated carbon
ACL	=	anode catalyst layer
AFC	=	alkaline fuel cells
AuNPs	=	gold nanoparticles
BEA	=	beta zeolite
BP	=	bipolar plates
CNT	=	carbon nanotube
CB	=	carbon black
CCL	=	cathode catalyst layer
CVD	=	chemical vapor deposition
D	=	diamond powder
DFT	=	density functional theory
DMAP	=	4-(N,N-dimethylamino)pyridine
DNA	=	deoxyribonucleic acid
DND	=	double-numerical basis set + d-DNP basis except that no polarization functions
DNP	=	double numerical plus polarization function
DOS	=	density of state
ECSA	=	electrochemically active surface area
EDL	=	electric double layer
FAU	=	faujasite zeolite
FER	=	ferrierite zeolite
GDL	=	gas diffusion layer
GE	=	general electric
GGA	=	generalized gradient approximation
GWP	=	global warming potential
HOMO	=	highest occupied molecular orbital
HOR	=	hydrogen oxidation reaction
IR	=	infrared

LIST OF ABBREVIATIONS (Continued)

LUMO	=	lowest unoccupied molecular orbital
MCFC	=	molten carbonate fuel cells
MEA	=	membrane electrode assembly
MWCNT	=	multi-walled carbon nanotube
MWCO	=	molecular weight cutoff
NASA	=	national aeronautics and space administration
ORR	=	oxygen reduction reaction
PAA	=	poly(acrylic acid
PAFC	=	phosphoric acid fuel cells
PANI	=	polyaniline
PBE	=	Perdew-Burke-Ernzerhof functional
PDDA	=	poly(diallyldimethylammonium)chloride
PDOS	=	partial density of state
PEI	=	polyethyleneamine
PEMFC	=	proton exchange membrane fuel cells
PF	=	pitch fiber
PMBA	=	polymethacryloyl β-alanine
PSS	=	polystyrene sulfonate
PTFE	=	polytetrafluoroethylene
PtNPs	=	platinum nanoparticles
PVP	=	poly(N-vinyl-2-pyrrolidone)
PW91	=	Perdew-Wang 91 functional
SDS	=	sodium dodecyl sulfate
SEM	=	scanning electron microscopy
SOFC	=	solid oxide fuel cells
SPR	=	surface plasmon resonance
STP	=	standard temperature and pressure
SWCNT	=	single-walled carbon nanotube
TEM	=	transmission electron microscopy
TGA	=	thermogravimetric analysis

LIST OF ABBREVIATIONS (Continued)

THF	=	tetrahydrofuran
TOABr	=	tetraoctylammonium bromide
TS	=	transition state
UV-Vis	=	ultraviolet isible
VACNT	=	vertically aligned carbon nanotube
ZSM-5	=	zeolite socony mobil
cm	=	centimeter
cm^2	=	square centimeter
cm^3	=	cubic centimeter
cm^3/min	=	cubic centimeter per minute
e	=	electron
E_{ads}	=	adsorption energy
E_b	=	binding energy
E_{prod}	=	energy of product
E_T	=	total energy
E_{ts}	=	energy of transition state
E_g	=	energy gap
eV	=	electron volt
g	=	gram
h	=	hour
kcal	=	kilocalories per mole
kDa	=	kilodalton
kg/cm^2	=	kilograms per square centimeter
M	=	Molar
mg	=	milligram
mg/cm^2	=	milligrams per square centimeter
min	=	minute
ml	=	milliliter
mm	=	millimeter
m^2	=	square meter

LIST OF ABBREVIATIONS (Continued)

mV	=	millivolt
nm	=	nanometer
q	=	charge
sec	=	second
vol %	=	volume percent
wt%	=	weight percent
°C	=	degree of Celsius
μl	=	microliter
μm	=	micrometer

METAL-DECORATED CARBON NANOTUBES FOR APPLICATIONS IN SENSING AND CATALYSIS: A THEORETICAL AND EXPERIMENTAL STUDY

INTRODUCTION

Carbon allotropes with sp^2 hybridized graphitic structure can exist in a variety of forms. In addition to the well-known graphene and graphite, the sp^2 carbon atoms are also found in the fullerene related family with a soccer-ball-like molecular shape. The first such discovered structure was the C_{60} molecule by Kroto *et al.* in 1985 and it has been designated as "Buckminsterfullerene" (Kroto *et al.*, 1985). Subsequently, although the fullerenes have been intensively investigated, it was not until 1991, that Iijima (Iijima, 1991) first observed the tubular carbon structures obtained from the modified C_{60} synthesis (direct current arc discharge evaporation method). They were named as "carbon nanotubes" (CNTs) due to their nanoscale diameters (4-30 nm). The synthesized tubes comprise coaxial of several graphitic cylindrical sheets, ranging in number from 2 to about 50. Two years later, in 1993, CNTs with a single-layer graphene sheet were produced (Iijima and Ichihashi, 1993). Since that time, CNTs are classified into two major kinds by their wall numbers, i.e., single-walled carbon nanotubes (SWCNTs) and multi-walled carbon nanotubes (MWCNTs) as depicted in Figure 1.

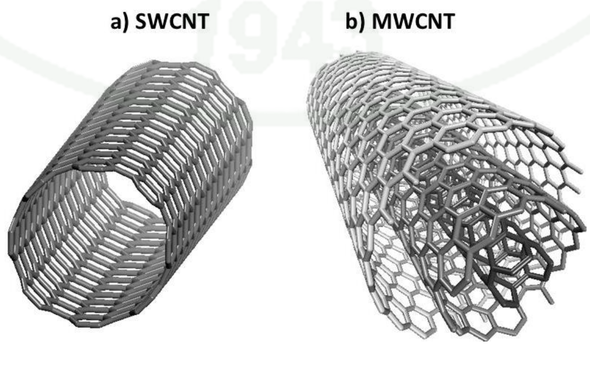

Figure 1 Schematic illustration of the structure of a single-wall carbon nanotube (SWCNT) (a) and a multi-wall carbon nanotube (MWCNT) (b).

Both MWCNTs and SWCNTs have been produced mainly by three techniques which are: arc discharge (Bethune *et al.*, 1993; Iijima, 1991; Iijima and Ichihashi, 1993; Journet *et al.*, 1997), laser ablation (Guo *et al.*, 1995; Thess *et al.*, 1996), and catalytic chemical vapor deposition (Cheng *et al.*, 1998; Dai *et al.*, 1996; Endo *et al.*, 1995; Hafner *et al.*, 1998; Hernadi *et al.*, 1996; José-Yacamán *et al.*, 1993; Kong *et al.*, 1998). Arc discharge and laser vaporization methods are based on the evaporation of graphite by direct current arcing and laser irradiation, respectively (Figures 2a and 2b). Both methods are the principal methods for obtaining high crystallinity and few defects in CNTs. However, these methods suffer from some drawbacks that include low production yield, high cost equipment, non-continuous processes and difficulty in fabricating nanotube-device. Contrary to the arc discharge and laser ablation, chemical vapor deposition (CVD) is a simple and economic method for production of CNTs. By this method, a hydrocarbon vapor is passed through a catalyst material at sufficiently high temperature to decompose the hydrocarbon, then forming as CNTs on such catalyst surfaces (Figure 2c). This synthesis method provides the use of a variety of hydrocarbons and various substrates and allows the growth of CNTs in different forms, such as powder, film and patterned substrate with entangled or aligned structures. Thus, CVD is today's most popular technique for the CNT synthesis.

Nowadays, experimental and theoretical studies have been carried out on CNTs due to their extraordinary mechanical, chemical and electrical properties (Dai 2002; Hamada *et al.*, 1992; Kang *et al.*, 2006; Popov 2004; Saito *et al.*, 1992; Tasis *et al.*, 2006). CNTs are strong and flexible materials that can be shaped by bending or stretching without structural damage. These properties originated from the strong covalent bonding between the carbon atoms and the seamless cylindrical hexagonal network. Moreover, CNTs are one of the most promising candidates as catalyst supporting materials because of their large surface area that is available for reaction and high thermal conductivity which reduces the temperature gradient during the reaction. Such steady state temperature can prevent the catalyst deactivation from the side reactions occurring at the hot spots in the catalyst bed.

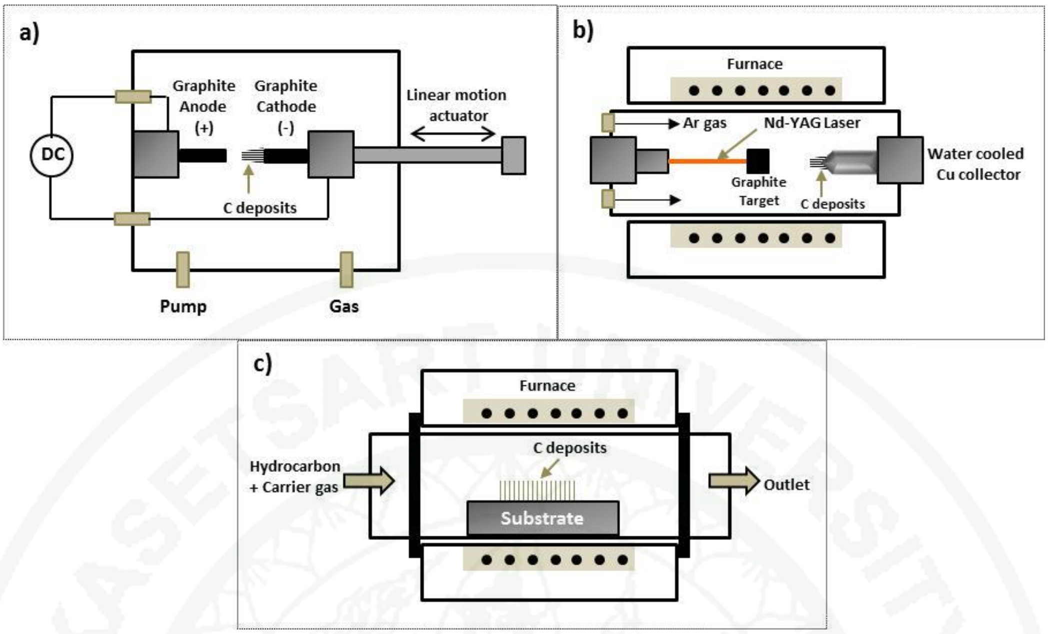

Figure 2 Schematic illustration of the methods for CNT synthesis (a) arc discharge, (b) laser vaporization and (c) chemical vapor deposition.

Furthermore, CNTs are furthermore known to be reactive for the reaction that serves to saturate the carbon atoms because the local strain from the pyramidalization and the π- orbital misalignment between adjacent pairs of conjugated carbon atoms are relieved (Niyogi *et al.*, 2002). As for the electrical property, the exotic characteristics revealed from calculations on the electronic properties of individual SWCNTs (Saito *et al.*, 1992) is that SWCNT is possibly metallic or semiconducting nanowire depending on its chirality. Such parameter is determined by the chiral vector ($\mathbf{C_h}$) defined in Equation 1 and along with Figure 3 where $\mathbf{a_1}$ and $\mathbf{a_2}$ are the graphene lattice vectors and n and m are integers.

$$\mathbf{C_h} = n\mathbf{a_1} + m\mathbf{a_2} \qquad (1)$$

The rolled up area of SWCNT is determined by $\mathbf{C_h}$ accompanied with the translation vector **T** which is along the tube axis and orthogonal to $\mathbf{C_h}$. An additional parameter to indicate the type of SWCNT is the chiral angle defined as the angle between $\mathbf{C_h}$ and $\mathbf{a_1}$. From the above definition, SWCNTs are then classified into three different types: armchair, zigzag and chiral SWCNTs. Armchair SWCNTs are constructed if n equals to m and the chiral angle is 30°. Whereas, when either n or m is zero and the chiral angle is 0°, the zigzag SWCNTs are formed. All other (n.m) chiral vectors and chiral angles (intermediate between 0° and 30°) correspond to the chiral SWCNTs. These (n,m) indices determine whether a SWCNT will be metallic or semiconducting according to the relationship in Equations 2 and 3 which were proved experimentally in 1998 (Odom *et al.*, 1998; Wildöer *et al.*, 1998).

.

$$\text{Metallic:} \quad \frac{(2m+n)}{3} \quad = \quad \text{interger} \tag{2}$$

$$\text{Semiconducting:} \quad \frac{(2m+n)}{3} \quad \neq \quad \text{interger} \tag{3}$$

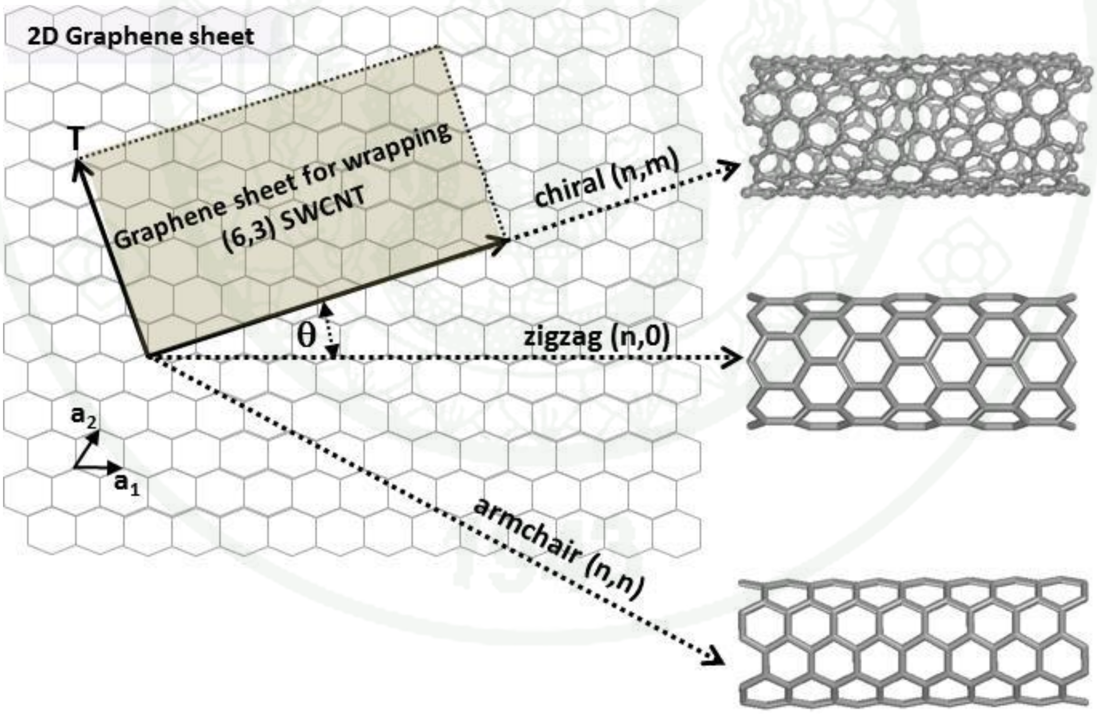

Figure 3 Schematic illustration of the chiral, armchair and zigzag SWCNTs defined by chiral vector and chiral angle.

According to the outstanding properties mentioned above, numerous frontier applications have been explored including ultra-strength composites, nanocatalysts, miniature electronic devices (sensor, field emission displays, field effect transistors, etc.) (Balasubramanian and Burghard 2005; Baughman *et al.*, 2002). However, due to the perfect hexagonal sp^2 bonding network, CNTs are still chemically inert to form strong chemical bonds with most molecules. For this reason, in order to extend the utilization of CNTs in diversified applications, it is necessary to generate a suitable active site on CNT surfaces. One of the most potential strategies to function CNTs is the decoration of CNT sidewalls with transition metal nanoparticles. CNTs decorated with metal nanoparticles have been found to show several improvements over the bare CNTs, such as the emitter and sensor properties and also catalytic efficiency (Cho *et al.*, 2008; Penza *et al.*, 2007; Rakhi *et al.*, 2008; Star *et al.*, 2006; Vairavapandian *et al.*, 2008).

For application in sensors, CNTs have been used as a highly sensitive material for sensing toxic or explosive gases (Kong *et al.*, 2000). One of the effective miniature sensor devices was fabricated as a single-chip platform composing of multiple sensor arrays that are made of conducting channels of SWCNTs decorated with some transition metals (Lu *et al.*, 2004; Mubeen *et al.*, 2007; Penza *et al.*, 2007; Penza *et al.*, 2008). The metal component functions as recognition layers and exhibits a specific selectivity toward the detection. In the meantime, since the sensor devices based on metal-decorated CNTs have been reported extensively, various approaches have been developed for decorating metals on CNTs (Lu *et al.*, 2004; Mubeen *et al.*, 2007; Penza *et al.*, 2007, 2008; Vairavapandian *et al.*, 2008). Among the metals used for coating CNTs, platinum (Pt) and gold (Au) have proved to be two of the most efficient metals that provide the hybrid materials, which exhibit good sensing sensitivity. One of the applications in which these materials present excellent sensitivity is the sensing of ammonia (NH_3) and nitrogen dioxide (NO_2), which are of the important industrial toxic and air pollutant gases. Compared to the bare CNTs, the Pt and Au-decorated tubes give better sensitivity by more than two times of magnitude for both gases (Penza *et al.*, 2007).

Nevertheless, by using a simple decoration method in which the metal particles are prepared directly on the unmodified surface of CNTs, low content and large size metal particles are typically obtained. This is because of both the inactive nature of the stable C-C network of the pristine tubes that leads to weak interaction to the metal species and the strong cohesive force between the metal atoms. As the particles are large, the active particle surface for contacting the examined gas is then small. As a result, the sensing performance of the devices constructed from the hybrid materials of metal nanoparticles and the pristine tubes is not as good as one would expect.

Recently, it was found that the loading of Pt in the case of defective CNTs is higher than that in the case of perfect CNTs (Kim *et al.*, 2007). This increased loading improves the sensing performance of the device. In that article, the results in part of the density functional calculations indicate that the Pt atom can strongly bind to the vacancy site of CNT. The Pt atom is stabilized by simply saturating the dangling bonds of the adjacent carbon atoms in the vacancy forming a hexagon. Regarding above mentioned results, SWCNTs, which are simple and practical models for theoretical study, with a vacancy defect (designated as $SWCNT_{Vac}$) are promising as materials for supporting metal catalysts. This is because the stability and reactivity of the sensor would be improved by the well-formed structures and enlarged active surfaces of the catalytic metals supported on the defective tubes. Moreover, the doping fashion probably facilitates the synergetic working of CNTs and metals greater than the common surface binding because such a strong bonding from saturation would help to increase the sensor sensitivity. Pt itself is well-known for its adsorption capabilities of small molecules (Grabow *et al.*, 2008; Orita and Inada, 2005; Wang and Balbuena, 2004; Zhou *et al.*, 2007). In this study, the sensing performance of $SWCNT_{Vac}$/Pt, which is a fascinating material to be applied for sensor application, was examined in the first part. Its catalytic behaviors were compared with that of the pristine SWCNTs, the vacancy defected SWCNT ($SWCNT_{Vac}$) and the Pt-deposited on perfect SWCNT (SWCNT/Pt) in order to make a systematical evaluation. NH_3 and NO_2 were chosen as the probing molecules. This is because they contribute as main environmental pollutants and toxicants and they are also good representative models for electron donor and electron acceptor substances, respectively.

Among the examined hazardous substances, greenhouse gases like nitrous oxide (N_2O) are a great challenge. Even though N_2O is a non-CO_2 greenhouse gas, it is known as a true climate killer. It is the strongest greenhouse gas causing the stratospheric ozone destruction as recognized in the Kyoto Protocol (Jenkin. and Clemitshaw, 2000; Kasimir-Klemedtsson *et al.*, 1997). It has not only almost 300 times more global warming potential (GWP) than CO_2 but also an extremely long atmospheric lifetime of about 120 years (Khalil 2000; Ravishankara *et al.*, 2009; Trogler 1999). Therefore, the finding of efficient emission control processes for N_2O abatement is considered to be a seriously urgent issue for the environment (Kapteijn *et al.*, 1996). Many strategies for N_2O abatement have been proposed including the selective catalytic reduction (SCR) and direct catalytic decomposition (Abu-Zied *et al.*, 2008). The most important elementary step of these processes is the dissociation of the N_2O molecule into the N_2 and O-adsorbed species.

Metal-exchanged zeolites have been widely used to catalyze N_2O conversion due to their excellent catalytic activity (Abu-Zied *et al.*, 2008; Pantu *et al.*, 2008). Nevertheless, the performance of the zeolites is often hindered under realistic conditions such as in feed gas streams containing oxygen (O_2), water (H_2O), sulfur dioxide (SO_2) and so on. This is because of their inherently poor hydrothermal stability as well as their sensitivity to the sulfur poisoning (Kapteijn *et al.*, 1996; Zhu *et al.*, 1999). Beside zeolites, many carbonaceous materials with absorbed metals such as the Ni, V or Cu particles-supported carbon substrates also present high catalytic activity for the N_2O conversion (Carabineiro *et al.*, 2000, 2005, 2008; Ma *et al.*, 2000; Zhu *et al.*, 1999). Such good catalytic activity is somewhat governed by the good dispersion of metals on the carbon surface. Among carbon materials, carbon nanotubes (CNTs) are expected to be a superb catalyst supporting material for metals due to several reasons as follows: (i) CNTs possess a large surface area for decorating the metals, (ii) the well-ordered structure of CNTs can aid the dispersion of the metals, thus maximizing the active surface for the reaction, and also can prevent the diffusion of reactants and products back into the bulk, (iii) CNTs interact specifically with the metals, thus providing a unique synergistic effect on the reaction, (iv) CNTs exhibit high surface chemical stability, thereby significantly reducing unwanted side reactions, and (v) CNTs, owing to good thermal conductivity, reduce the temperature gradient during the reaction (Kyotani *et al.*, 1996).

The results from a recent theoretical study of the N_2O decomposition over CNTs in the absence of other additional catalysts shows that both perfect and defected tubes can also themselves also behave as catalysts by driving the electron transfer to dissociate the N_2O molecule. However, the reaction passes over a high activation barrier of about 40-48 kcal mol^{-1} via this process (Namuangruk *et al.*, 2007). Therefore, the decoration of active metal catalysts on the tube sidewall is expected to provide a well-suited catalyst platform for the reaction since the intrinsically inert reactivity of the tube can be improved whereby the deposited metals are able to promote the electron transfers between the tubes and the attacked molecules (Pannopard *et al.*, 2009). From a theoretical study regarding the reactions of N_2O with Sc, Ti and V producing metal oxides and N_2 molecules, it was found that the reactions proceed via very low energy barriers, below 2 kcal mol^{-1}, and are exothermic (Delabie *et al.*, 2001; Ritter and Weisshaar, 1990; Stirling, 1998, 2002). This finding hereby motivates us to investigate the properties of CNT modified with Sc, Ti and V for N_2O decomposition experimentally. Therefore, another aim of this study is to provide guidance for developing an efficient alternative catalyst for N_2O decomposition and other related reactions.

Going along with such an investigation, the synthesis of CNTs and their functionalization with the metal nanoparticles were experimentally studied here in order to attain an efficient strategy to fabricate hybrid materials being suitable for fuel cell and other important applications. Fuel cells have received much attention in recent years as important power devices since they are able to satisfy the requirements for future clean technologies. While the fossil fuels, which now meet most of the world’s energy demand, in spite of the fact that petroleum reserves are finite and will be depleted eventually. Moreover, the burning of fossil fuels has adverse effects for the environment due to carbon dioxide emission, which is the crucial contribution to global warming, climate change and rising sea level. Accordingly, there has been a growing interest in the use of sustainable and low emission alternative fuels. Fuel cells promise to deliver power efficiently by combining a fuel (e.g., hydrogen, methanol, etc.) and an oxidant (air or pure oxygen) in an electrochemical device that directly converts chemical energy to electrical energy with very low or even zero emission of harmful pollutant gases (Boudghene and Traversa, 2002; Kirubakaran *et al.*, 2009; Kordesch and Simader, 1995; Perry and Fuller, 2002; Ticianelli *et al.*, 1988.

Every fuel cell consists of two electrodes, the anode and the cathode, separated by an electrolyte. Several types of such cells are being developed; their classification is generally based on the electrolyte material used. This includes alkaline fuel cells (AFC), proton exchange membrane fuel cells (PEMFC), phosphoric acid fuel cells (PAFC), molten carbonate fuel cells (MCFC), and solid oxide fuel cells (SOFC), as detailed in Figure 4, sorted by operating temperatures (Boudghene and Traversa, 2002; Kirubakaran *et al.*, 2009; Kordesch and Simader, 1995; Perry and Fuller, 2002). Among these, polymer electrolyte membrane fuel cells (PEMFC) are the most widely used ones since they are best-suited for transportation, stationary and mobile applications. High energy conversion efficiency, rapid start-up and shut down (low-operating temperature, below 100°C), a favorable power-to-weight ratio (lightweight and compact) and robustness (flexible solid electrolyte does not leak or crack) (Costamagna and Srinivasan, 2001; Peighambardoust *et al.*, 2010; Wang *et al.*, 2011; Wee, 2007) are further advantages of these systems. The components of a PEMFC along with the electrochemical reactions and pathways are shown schematically in Figure 5 (Cindrella *et al.*, 2009; Haile, 2003; Li and Sabir, 2005; Litster and McLean, 2004).

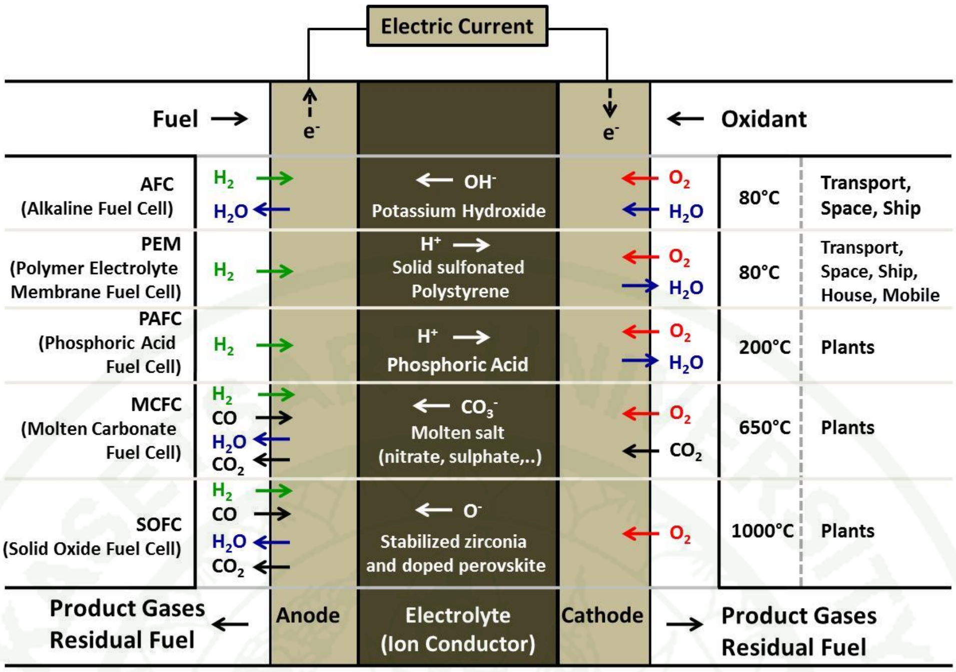

Figure 4 Schematic illustration introducing the relevant processes for selected fuel cells, accompanied by their corresponding applications.

In common cases of PEMFC, hydrogen fuel is fed into the cell at the anode side and oxygen gas is introduced at the cathode side. The bipolar plates (BP in Figure 5) have four crucial functions: (i) to supply the fuel and oxidant to the proper location in the cell, (ii) to remove the reaction products, (iii) to collect the produced current, and (iv) to provide the mechanical support for the cell in the stack. The gas diffusion layer (GDL) allows a direct and uniform transport of the reactant gas to the catalyst layer. It also allows water to be drained out from the catalyst layer and conducts electrons in the cell with a low contact resistance. Activated by a catalyst, hydrogen molecules split into protons and electrons. Because of the insulating nature of the electrolyte, only the protons pass through it whereas the electrons are driven to the current collectors, thus producing a current that can be utilized in an external circuit before returning to the cathode side for recombination with incoming protons and oxygen in the presence of a catalyst to form water, thereby completing the circuit.

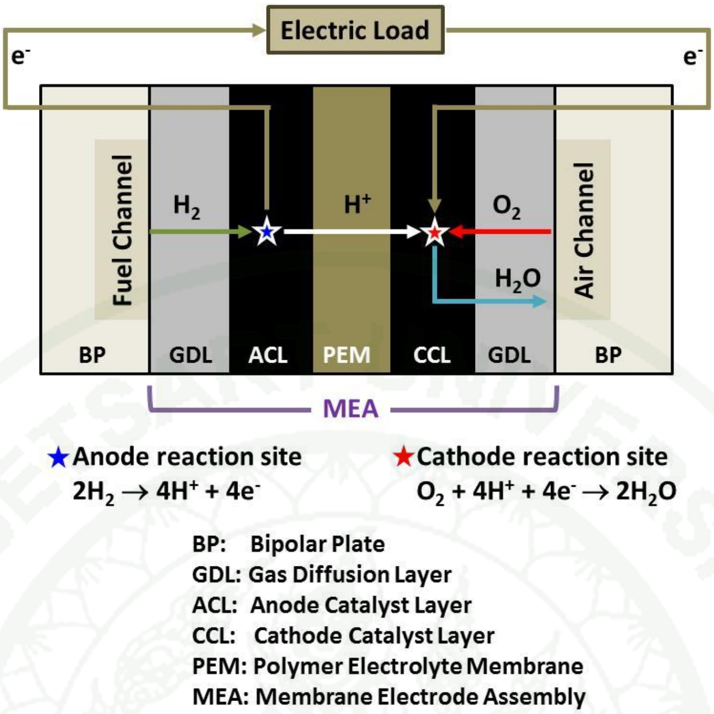

Figure 5 Schematic illustration of a typical PEMFC single cell and the chemical reactions proceeding at its electrodes (anode and cathode).

The central core of PEMFC is a membrane electrode assembly (MEA), which consists of: (i) a solid polymer electrolyte membrane, (ii) two dispersed catalyst layers and/or not, (iii) two gas diffusion layers (Litster and McLean, 2004; Mehta and Cooper, 2003; Peighambardoust *et al.*, 2010; Wilson and Goffesfeld, 1992). The development of catalyst layers to be incorporated into the MEA is a crucial area of research concerning PEMFC. Because of the oxidation-reduction or redox reactions on the electrodes are the surface processes so a supporting material with large surface area is required for supporting the nano-sized electrocatalyst particles in order to obtain a well-performed electrode. Up until the present, many carbon-supported Pt catalysts have been commonly used for this purpose because of their attractive features for the electrochemical applications Antolini, 2009; Chan *et al.*, 2004; Costamagna and Srinivasan, 2001; Lee *et al.*, 2006; Sharma and Pollet, 2012; Ticianelli *et al.*, 1988; Wee *et al.*, 2007; Yu and Ye, 2007a, 2007b; Zhang *et al.*, 2010a) (Ref 26). The Balandin volcano plots show that Pt has the highest activity among the metal catalysts toward both the hydrogen oxidation reaction (HOR) and the oxygen reduction reaction (ORR) occurred at the anode and cathode, respectively (Holton and Stevenson, 2013; Jaksic *et al.*, 1998; Nørskov *et al.*, 2004). Pertaining to the carbon supports, they are not only low-cost materials serving the way for commercialization but also exhibit good electrical conductivity and acceptable chemical stability that make it suitable for use in fuel cells (Antolini, 2009; Dicks, 2006; Lee *et al.*, 2006a, 2006b; Sharma and Pollet, 2012).

In general, carbon blacks (CBs) with a high degree of graphitic character such as Vulcan XC-72R, Black Pearls 2000, Ketjen Black, etc., have been conventionally utilized for PEMFC to disperse Pt nanoparticles (PtNPs) (Antolini, 2009; Bayrakçeken *et al.*, 2008; Chan *et al.*, 2004; Le Gratiet *et al.*, 1996; Umeda *et al.*, 2003; Zhou *et al.*, 2003). However, the CBs often make poor Pt utilization via two ways. Firstly, PtNPs are often trapped in the micropores (with size of <2 nm), which are the main pores of CB, and the PtNPs are in turn not involved in the electrochemical reactions because the appropriate three-phase reaction zone (gas–electrolyte–electrode) could not be constructed (Gasteiger *et al.*, 2005; Li *et al.*, 2003; Park *et al.*, 2002; Thompson *et al.*, 2001; Uchida *et al.*, 1996). Usually, in order to obtain a well-catalyzed reaction, an appropriate three-phase reaction zone where the catalyst contacted with the interfacial region between the polymer electrolyte and the electron conducting center must be constructed (see Figure 6). This contact zone is the highly essential reactive site where both proton and electron transfer occur. In addition, the bare regions over the catalyst sites have to be preserved in order to facilitate the fast access of the reactant gases to undergo the reactions. In the case of CBs, the micelle diameter of electrolyte polymer, at least 4 nm, is larger than the carbon micropores in which most PtNPs reside. Thereby, the electrolyte substance would be hindered to construct the three-phase active site. In the second way, CB can itself undergo the electrochemical oxidation during the long-term operation of the cell, thereafter resulting in the detachment of PtNPs from the support and aggregation into larger-size clusters. As a result of that, the catalytic surface area is reduced (Gasteiger *et al.*, 2005; Thompson *et al.*, 2001; Zhai *et al.*, 2007). Moreover, the random porous structure of CB typically prevents the supplying of the fuel and oxidizing gases to the catalytic sites, and also, retards water to be drained out from its pores.

Hence, a new class material with an optimum structure is required to overcome the aforementioned disadvantages. To replace traditional carbon powders, CNTs have been suggested to be used (Carmo *et al.*, 2005; Gong *et al.*, 2009; Hatanaka *et al.*, 2006; Li *et al.*, 2005; Liu *et al.*, 2002, 2008; Maiyalagan *et al.*, 2005; Matsumoto *et al.*, 2004a, 2004b; Nagle and Rohan, 2008; Tang *et al.*, 2010; Wang *et al.*, 2004; Zhang *et al.*, 2010a, 2010b).

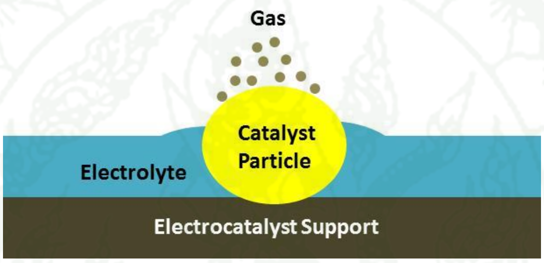

Figure 6 Schematic illustration of the three-phase boundary interfacial area formed at the catalyst layer that is required for the occurrence of the reactions for fuel cells.

They are expected to be superior to the conventional carbon black in supporting the PtNPs for fuel cell application because of the following configurations: (i) CNTs possess high surface to volume ratio and have no micropores in which the PtNPs are possibly trapped inside, (ii) the ordered tubular structure of CNTs facilitates the smooth mass transportation of molecules into the structure, (iii) the high graphiticity of CNTs assists the electrical conductivity as well as provides high resistivity for acid and oxidative etchings, (iv) CNTs, owing to p-electrons, interact specifically to the Pt, owing to d-electrons, thus enhancing the catalytic activity of the PtNPs (Antolini, 2009; Dicks, 2006; Gamez *et al.*, 1996; Kinoshita, 1990; Li *et al.*, 2003; Matsumoto *et al.*, 2004b; Ralph and Hogarth, 2002; Tauster *et al.*, 1981).

Although both as-received and purified CNTs have been used for PEFC as supports for Pt electrocatalysts, they do not exhibit good behaviors for fuel cells since typically their structures are not aligned and thus, obstructing good gas, water and electron transports. In addition, by the drop casting or pellet pressing of MEA assembly, PtNPs are buried deep within the electrode layer. For this reason, the utilization of alternative vertically aligned CNTs is considered to be promising for fuel cells as their pore structure is regular and straight, and thus, providing the uniform diffusion paths for gas and water molecules in the cells (Gong *et al.*, 2009; Hatanaka *et al.*, 2006; Liu *et al.*, 2008; Xiong *et al.*, 2010; Zhang *et al.*, 2010b). Moreover, since the electrical conductivity of CNTs along the tube axis is higher than that across the direction, the aligned tube arrays could deliver better cell performance compared to the tangled ones.

Anyhow, in the real applications during the pressing process for MEA preparation, such aligned free-standing tubes can be pushed out from the arrays. These misaligned tubes impair the molecular diffusion in the cell and lower the available surface area (Hatanaka *et al.*, 2006). To overcome this problem, we suggested the use of the vertically aligned carbon nanotubes (VACNTs) embedded in the channels of other patterned material such as the anodic aluminium oxide (AAO) template (Kyotani *et al.*, 1995, 1996; Maiyalagan *et al.*, 2005; Nagle and Rohan, 2008; Rajesh *et al.*, 2002; Ye *et al.*, 2008). The CNT-AAO hybrid material can be simply prepared via chemical vapor deposition (CVD) method of a hydrocarbon source in the presence of AAO at about 600-900°C.

AAO templates have not only been used for producing the arrays of VACNTs but also exploited for synthesis of other nanomaterials with well-ordered and controllable porous structure such as titanium oxide (TiO_2), polyaniline (PANI) and gold nanotubes (Brumlik and Martin, 1991; Xiong *et al.*, 2004; Ye *et al.*, 2008). The typical nanostructure of AAO can be described as hexagonally ordered array of parallel cylindrical nanochannels perpendicular to the Al substrates (Figure 7). The fabrication of AAO is usually based on the self-ordering processes of nanopores via the electrochemical anodization of aluminium in an aqueous electrolyte. By regulating the anodization conditions, the pore geometries, i.e., interpore distance, pore diameter and pore length, can be precisely tuned. The AAO template-confined carbonization has been known as the process for the production of CNTs with a uniform and tunable pore size distribution.

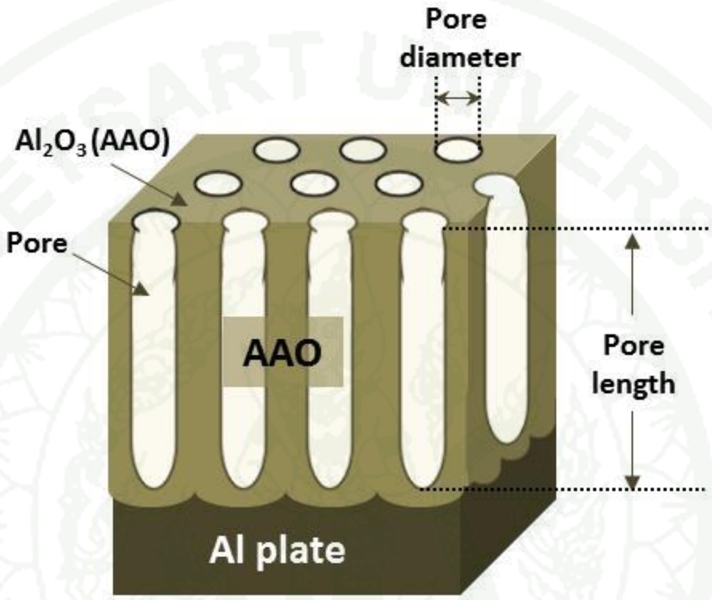

Figure 7 Schematic illustration showing an anodic aluminium oxide (AAO) structure prepared via an electrochemical anodization of aluminium (Al).

We expected that a stable 3D electrode of VACNTs produced in the presence of an AAO template will keep the tubes as arrays during the MEA manipulations since the rigid AAO film is likely to withstand the pressing force and thus preserves the alignment of the tubes. Upon this proposed strategy, the formation of bundled VACNTs (because of the van der Waals interactions between nearby tubes), that would cause a significant loss of active surface and flow channels, can be avoided as well. Encouraged by this, the VACNTs synthesized by CVD technique were taken advantage of here for the MEA fabrication by employing the AAO film as a robust support to keep the standing arrays intact and also as a structural template to tailor the carbon nanostructure with desired pore length and diameter. Then, a properly featured triple phase reaction zone was constructed on the inner walls of the CNT-AAO pores (see Figure 8).

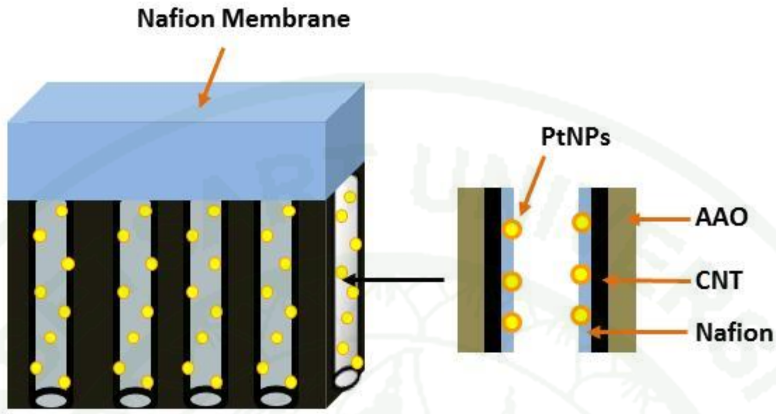

Figure 8 Schematic illustration showing the assembly of Nafion/PtNPs/CNT-AAO film and Nafion membrane. The triple phase reaction zone (Nafion/PtNPs/CNTs) constructed on the inner walls of the AAO pores is also demonstrated.

This interfacial structure comprises a proton conducting layer (Nafion), electron conducting layers (CNTs) and layers of adsorbed reactant (platinum nanoparticles, PtNPs). The well-constructed composites of Nafion/PtNPs/CNT-AAO and Nafion membrane were attempted to be fabricated in order to achieve a membrane electrode assembly (MEA) suitable for PEMFC.

In addition to the hybrid PtNP/CNT materials, the hybrid materials of gold nanoparticles (AuNPs) and CNTs (AuNP/CNT) have also been used as nanocomponents for sensor or catalytic applications due to their outstanding properties (Alexeyeva and Tammeveski, 2008; Cai *et al.*, 2007a; Dong *et al.*, 2008; Lim *et al.*, 2004; Lin *et al.*, 2009; Xu *et al.*, 2008). Up until now, there have been three main approaches to prepare AuNP/CNT among which covalent, non-covalent and direct depositions have been mentioned (Zhang and Olin, 2011). In the direct attachment approach, AuNPs are formed on the sidewalls of CNTs without extra-functionalized molecules (Kim *et al.*, 2003; Satishkumar *et al.*, 1996; Warakulwit *et* *al.*, 2008; Zhang *et al.*, 2000). Even though the direct formation provides high purity composites, there are some critical limitations, e.g. the requirement of sophisticated equipment, the ineffective size control of the AuNPs and the instability of the particle adsorption. The covalent binding method is thus getting more attractive for improving the stability of the attachment of the particles on the tube surface (Azamian *et al.*, 2002; Gobbo *et al.*, 2013; Liu *et al.*, 1998). Nevertheless, some important drawbacks of the covalent attachment involving the multistep and complex reactions still need to be addressed. Because of this, the non-covalent deposition has been developed in numerous ways (Carrillo *et al.*, 2003; Jiang *et al.*, 2003; Jiao *et al.*, 2012; Wang *et al.*, 2006), particularly the electrostatic self-assembly. This is, firstly, a technique whereby CNTs and AuNPs can be tailored to be negatively or positively charged. Secondly, the electrostatic binding is strong enough to withstand hydrodynamic and ultrasonic forces during auxiliary processes in the experiments. Finally, the presence of ionic or polar functional groups on the hydrophobic CNT surface make them more hydrophilic and well-dispersed in aqueous solutions, thus promoting the attachment of the counter-charged AuNPs.

Using these means, the wrapping of CNTs with ionic polymers, followed by the assembly with oppositely charged particles, has been very widely employed (Carrillo *et al.*, 2003; Jiang *et al.*, 2003; Kim and Sigmund, 2004). Nevertheless, it should be noted that the covering CNTs with polymer layers may hinder the electron transfer between the component species and also between the composite and other molecules. Because of this, naked CNTs are more preferable.

In this sense, it is fortunate that it was found that the negatively charged CNs can be obtained in the case of the CNTs prepared by using the AAO template after the removal process of the oxide from the tubes spontaneously without any tedious post-treatment (Orikasa *et al.*, 2006, 2008). The resulting outer surface charges are mainly caused by the oxygen functional groups formed during the removal process with alkaline solutions. Such oxygen-containing functional groups also induce an electric double layer (EDL) around each CNT, which consequently enhances the water dispersibility of the tubes. Such a simple process yielding the water-dispersible tubes with their inherent characteristics and without using any harsh and complicated modifications is truly promising. Apart from the simplicity of the process, its ability to yield the tubes with well-ordered structure and uniform length and diameter is of our interest. This is because such characteristics are suitable for various applications including sensors and catalysis. On account of this, the unmodified but negatively charged CNTs obtained after the removal of AAO are suitable to act as a platform for the loading of positively charged AuNPs via electrostatic self-assembling.

4-(N,N-dimethylamino)pyridine, or DMAP, was utilized here as a non-ionic capping ligand that is non-covalently bound to the AuNP surfaces through the endocyclic nitrogen (see Figure 9). The positive charges, which can bind to the negatively charged surface of CNTs, are polarized at the DMAP/water interfaces by exocyclic amine group of DMAP. DMAP-protected AuNPs (Au-DMAP) are of current interest arisen from good water-dispersible and versatile precursor for many substrates (Gittins *et al.*, 2002; Yu *et al.*, 2003; Zhang *et al.*, 2007).

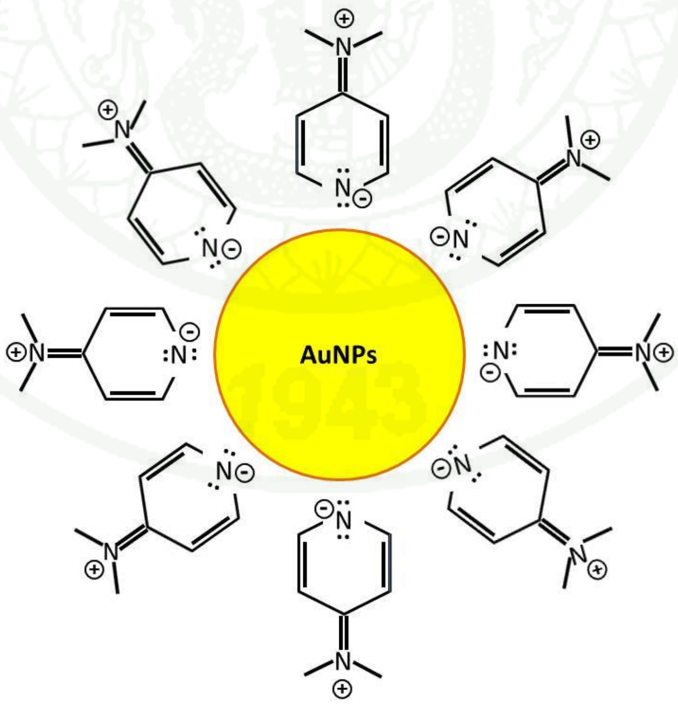

Figure 9 Schematic illustration showing the stabilization of AuNPs using the DMAP capping agent.

A general preparation method of the Au-DMAP relies on the spontaneous phase transfer of AuNPs from toluene to water phases that is a result of the ligand exchange of tetraoctylammonium bromide (TOABr) with DMAP (Gittins and Caruso, 2001). Anyhow, it is hard to find the reports about one-step and one-phase synthesis of Au-DMAP, and especially in non-toxic aqueous solutions (Danger *et al.*, 2012; Raj *et al.*, 2011). Moreover, the control over of the particle size of Au-DMAP, which influences their optical, electrical and catalytic properties, has not been studied systematically until recently. For this reason, in this work, we aim to discover a new method to satisfy such requirements.

To the best of our knowledge, poly(N-vinyl-2-pyrrolidone) or PVP is one of the most effective capping agents for fabricating the water-soluble AuNPs. This is because PVP provides an effective steric stabilization to the particles, and thus, preventing them from aggregation. Therefore, typically the resulted AuNPs are of small size, around 1-2 nm, and their size distribution is mono-disperse (Tsunoyama *et al.*, 2004, 2005, 2006, 2008, 2011). In addition, the stable colloidal solution of the stabilized particles can be obtained without the use of any additional hazardous chemicals. Accordingly, PVP was chosen as the co-stabilizer with DMAP because the sizes of AuNPs obtained by using only DMAP as a single stabilizer and using both DMAP and PVP as stabilizers are expected to be varied. The core size of the particles is proposed to be controlled by varying the amount and ratio of DMAP and PVP. This synthetic protocol is expected to open up a novel feature of CNTs (with AuNPs) for the applications ranging from industrial catalysis to nanoelectronics.

OBJECTIVES

1. To evaluate the sensing properties of Pt-doped SWCNT ($SWCNT_{Vac}$/Pt) comparing with those of pristine SWCNTs (SWCNTs), vacancy defected SWCNTs ($SWCNT_{Vac}$) and Pt-deposited SWCNT (SWCNT/Pt) for NO_2 and NH_3 detections by means of DFT calculations.

2. To investigate the catalytic activities of transition metals (Sc, Ti, V) decorated SWCNTs and pristine SWCNTs for N_2O removal by means of DFT calculations.

3. To fabricate a novel design electrode for PEMFC application by constructing the triple boundary interfacial structure including a proton conducting layer (Nafion), electron conducting layer (CNTs) and a reactant adsorbed layer (platinum nanoparticles, PtNPs), on the inner walls of AAO pores and to prepare the composite of Nafion/PtNPs/CNT-AAO electrode and Nafion membrane as well.

4. To fine-tune the sizes of positively charged AuNPs by adjusting the amount of PVP and DMAP stabilizers and then synthesize the AuNPs/CNTs nanocomposite by the facile electrostatic deposition of those size-controlled AuNPs onto the AAO-templated CNTs.

LITERATURE REVIEW

Well-performing chemical sensors based on CNTs have attracted a great interest for detecting pollutants and toxic gases. The semiconducting SWCNTs were found to exhibit a great potential in the gas sensing applications for the first time by Kong *et al.* (Kong *et al.*, 2000). The single SWCNT was used as a transistor channel between two gold electrodes (source and drain) and the experiments were carried out to monitor the resistance of the SWCNT upon the flows of NO_2 or NH_3 gases. Such nano-scale assembly exhibited high sensitivity and fast response, even at ambient temperature.

The sensing performance of SWCNTs has been found to relate with the charge transfer between it and the analyzed gas. Many former computational studies indicated that both NO_2 and NH_3 molecules were physisorbed on the tube surfaces, causing only a small charge transfer and low conductance responses (Chang *et al.*, 2001; Lu *et al.*, 2005; Santucci *et al.*, 2003). In contrast to the results obtained from the experimental works, which were found that the tubes provided high sensing response for the probing molecules. Therefore, several assumptions were given to elucidate these findings. The indirect mechanism was regularly proposed for NO_2 and NH_3 systems (Valentini *et al.*, 2004). For instance, because of the low diffusion barrier of NO_2 on tube surfaces, the chemical reaction of NO_2 occurred easily, thus producing NO_3 species, which have strong binding energy and long life on the tube surfaces. While in the case of NH_3, the strong interaction between NH_3 molecules and the pre-adsorbed oxygen species on SWCNT were assumed to be the possible mechanisms. However, those complicated phenomena generally excluded the rational design of improved sensors.

On account of that, there have been many attempts to tailor the selectivity and sensitivity of CNTs for the sensing application. The generation of new active sites on their surface is the premier strategy to surmount the drawback of the intrinsically inert CNT structure. The introduction of structural defects on the sidewalls of CNTs, especially ones associated with vacancies, has been proven to be able to enhance the sensitivity of the tubes for small probing molecules like NO_2 and NH_3 (Andzelm *et al.*, 2006; Mercuri *et al.*, 2005). In addition, the decoration of SWCNT network arrays with some transition metals (Pd, Pt, Rh, and Au) allowed the fabrication of the single-chip device (Star *et al.*, 2006). This could enlarge the diversity of identified molecular species including H_2, CH_4, CO, and H_2S. It was also shown that, the embedding of foreign atoms on CNTs makes them possible to examine a variety of gases as well. By altering the dopants, B-, N- and Al doped CNTs had proven to be highly sensitive to NH_3, NO_2, CO, H_2O and HCOH (Bai and Zhou, 2007; Peng and Cho, 2003; Wang *et al.*, 2006, 2007). The metal-decorated CNTs were likewise found to be promising as the active and selective sensing materials. Compared to the bare CNTs, the Pt- and Au-functionalized MWCNTs were found to be more sensitive for NH_3 and NO_2 detections by more than two times of sensitivity defined in terms of percentage relative resistance change (Penza *et al.*, 2007).

From the aforementioned above, the metal-decorated CNTs are promising to be served as the active and selective sensor elements. Typically, the efficiency of sensory platform strongly depends on the amount of active sites located on its surface. When the metal nanoparticles are considered to response the sensing process such as in the case of the CNT/metal hybrid materials, small-sized metal particles such as nanoparticles or nanoclusters with a narrow size distribution and a good dispersibility on the supporting surface, providing high active surface area, are required in order to deliver a good sensing performance.

The direct surface adsorption of metal clusters on as-synthesized CNTs has been considered to be non-tedious techniques for sensor fabrication (Krishna Kumar and Ramaprabhu, 2006; Mubeen *et al.*, 2007; Penza *et al.*, 2007; Star *et al.*, 2006). The electrochemical deposition and the sputtering methods were employed by Star *et al.* and Penza *et al.*, respectively to directly deposit metals on the sidewalls of CNTs (Penza *et al.*, 2007; Star *et al.*, 2006). Nevertheless, the former method produced the aggregate metal clusters (~200 nm) whereas, in the latter case, the smaller particles were obtained but with a broad size distribution. The large and non-uniform size of the metal clusters on the CNT sidewalls produced by these techniques may lead to an unfavorably small specific surface. Interestingly, recent experiments suggest that defective CNTs were capable of increasing more than triple the Pt loading content from 10% on pristine CNTs to 32% on defected CNTs (Kim *et al.*, 2007). The density functional calculations were performed to understand this occurrence. It was found that Pt atom is preferable to adsorb onto the vacancy site of the tube with the largest binding energy of 143 kcal/mol by forming a hexagon, resembling conventional doping. For enhancing the stability and reactivity of the sensing device, the vacancy defected SWCNTs ($SWCNT_{Vac}$) are thereby promising for using as metal support.

As for the catalytic metal, Pt is one of the metals that are commonly used for catalysis and sensor. It has adsorption capability of small probing molecules such as O_2, CO, H_2, NH_3 and NO_2 (Grabow *et al.*, 2008; Orita and Inada, 2005; Penza *et al.*, 2007; Wang and Balbuena, 2004; Zhou *et al.*, 2007). Hence, the Pt-doped SWCNTs (SWCNTVac/Pt) are fascinating to be applied as the sensing platform in this study. The performances of corresponding structures are also compared including pristine SWCNTs, vacancy defected SWCNT ($SWCNT_{Vac}$) and Pt-deposited on perfect SWCNT (SWCNT/Pt). Ammonia (NH_3) and nitrogen dioxide (NO_2) have been chosen because of their importance as pollutants and industrial toxicants and also because they are good models for electron donors and electron acceptors, respectively.

Not only the detection technology for toxic or pollutant gases has been continuously developed, but also the elimination of them has also been extensively studied. Particularly, the removing and reducing of the greenhouse gases such as CO_2, N_2O, and CH_4 that contribute to the global warming crisis by destructing the ozone layer in the stratosphere has been considered as an issue for environments with the major priority. Among of the greenhouse gases, although CO_2 is a major source resulting on the greenhouse effect, the eliminations of CH_4 and N_2O are somewhat more attractive to be considered. This is because their Global Warming Potential (GWP) values, which is a relative measures of the ability of each greenhouse gas to trap heat in the atmosphere relative to carbon dioxide (CO_2) over a specified time horizon, are much higher than that of CO_2; CH_4 has a 25 times higher impact on climatic warming than CO_2, and N_2O has 300 times more impact than CO_2, (Kasimir-Klemedtsson *et al.*, 1997). Because of the great GWP value of N_2O, the elimination of N_2O is of our focus.

N_2O is emitted from both natural (vegetation and the oceans) and anthropogenic (human-made) sources. Naturally, N_2O is emitted from the soil and ocean. Many human activities such as agriculture, fossil fuel combustion, and industrial processes such as the productions of adipic acid and nylon add up the amount of N_2O in the atmosphere.

Up until the present time, many routes for the reduction of emitted N_2O have been proposed. Two major solutions are suggested, including (i) the indirect catalytic decomposition by selective catalytic reduction of N_2O or utilization of N_2O to produce value added products and (ii) the direct catalytic decomposition of N_2O into N_2 and its corresponding oxide complex. As an example for the first case, NH_3, CO, and various hydrocarbons such as CH_4, C_2H_4, C_2H_6, C_3H_6 and C_3H_8 were employed as effective reducing gases for removing the surface oxygen and in turn regenerating the active sites (Angelidis andTzitzios, 2003; Boissel *et al.*, 2006; Chaki *et al.*, 2005; Coq *et al.*, 2000; Debbagh *et al.*, 2007; Hirano *et al.*, 2007; Jurczyk and Drago, 1998; Kögel *et al.*, 1999; Nobukawa *et al.*, 2007; Ruiz-Martínez *et al.*, 2005; Sugawara *et al.*, 2007; Yoshida *et al.*, 2004). There were numerous research groups taking advantage of N_2O as the oxidant in one-step oxidation of benzene to phenol which is of potential interest for the chemical industry (Iwamoto *et al.*, 1983; Jia *et al.*, 2004; Panov *et al.*, 1998; Pillai, K. S. *et al.*, 2004; Pirutko, L. V. *et al.*, 2002). Compared to the first method, the direct catalytic decomposition method has also attracted much attention because it is a relatively simple method and there are no extra costs from the external supply of reducing gases (Abu-Zied *et al.*, 2008; Ohnishi *et al.*, 2007; Pantu *et al.*, 2008; Sun *et al.*, 2006; Wącław *et al.*, 2004).

The inevitable elementary step of all mentioned N_2O decomposition processes is the dissociation N_2O into N_2 and O-adsorbed species. The catalytic metals adsorbed on various types of supports have shown to have potential to catalyze this reaction, particularly the metal-exchanged zeolites exhibit very high catalytic activity for the reaction. Abu-Zied *et al.* investigated the N_2O decomposition over several transition metal exchanged ZSM-5 zeolites. Among of the studied catalysts, they found that Co-, Cu- and Fe-ZSM-5 catalysts exhibit high activities (Abu-Zied *et al.*, 2008). Many zeolites with the Fe content such as Fe-FER, Fe-ZSM-5, Fe-BEA, and Fe-FAU were also studied both theoretically and experimentally (Pantu *et al.*, 2008). The activity trend given by the experiments is Fe-FER > Fe-BEA > Fe-ZSM-5 >> Fe-FAU. The results indicate that apart from the Fe species, the nanostructured pore networks of zeolites play themselves an important role on the catalytic activity of N_2O decomposition. Although some zeolite materials exhibit very high activity for the reaction, the zeolite structure could be intrinsically destructed through the chemical removal of alumina or aluminates by the water vapor presented in the system at high temperature in which the reaction takes place. This poor hydrothermal stability may limit the practical applications of zeolites for the N_2O decomposition (Kapteijn *et al.*, 1996).

Alternatively, the N_2O decomposition has been carried out over various carbon-supported catalysts (Carabineiro *et al.*, 2000, 2005, 2008; Ma *et al.*, 2000; Zhu *et al.*, 1999). Carabineiro *et al.* indicated that vanadium (V) impregnated activated carbon (AC) could catalyze the N_2O conversion at the temperature lower than that of the unmodified AC since the V performed as an active oxygen acceptor, which facilitated the N_2O adsorption (Carabineiro *et al.*, 2000). Moreover, Zhu *et al.* studied the activities of Nickel (Ni) supported activated carbon (AC) with and without acid treatments on the N_2O reduction (Zhu *et al.*, 1999). They found that the acid treated AC could aid the dispersion of Ni catalyst and preserved the uniform dispersion during reaction stage resulted in the improving catalytic activity. Similar aspects were obtained from the research work of Ma and coworkers (Ma *et al.*, 2000) whereby the Copper (Cu) supported on different allotropic forms of carbon materials including activated carbon (AC), pitch fiber (PF) and diamond powder (D) were comparativly studied as catalysts for N_2O decomposition. Among all catalysts tested, the Cu/D showed the highest activity. This was because the Cu metals on D substrates appeared to give good wetting and spreading action on the support surfaces. From this finding, it could be deduce that the activity of the metal-supported carbon catalyst for the N_2O decomposition was most directly related to the dispersion of active metals. However, the amorphous carbon particles contain many dangling bonds and deep pores leading to form highly dense aggregate particles and causing an unfavorably low specific surface area.

Because of such problems, CNTs are thereby very attractive to be used as support material for catalysts, especially metal catalysts. This is not only because of their high specific surface area but also their unique characteristics and properties such as well-ordered structure, good conductivity and high thermal and chemical resistances. Apart from behaving as catalyst supporting materials, some theoretical investigations of the N_2O decomposition on perfected and defected SWCNTs indicated that CNTs can themselves act as a catalyst for the reaction because of their electron donor property. However, their catalytic activity is not high. They provided relatively high activation energies in the range of 40-48 kcal/mol (Namuangruk *et al.*, 2007). Furthermore, although in the case of chloride anion encapsulated into the perfect and defect SWNTs for extremely enhancing the electron transfer from the tube to the N_2O molecule, the smallest activation barrier of these systems (32 kcal/mol) was rather high. To enhance the catalytic activity of CNTs, the metal decoration is thus considered again to create an active center in electron transfer towards the approaching N_2O molecule.

As to the metal selection, the theoretical study of N_2O dissociation on transition metal atom by Stirling *et al.* revealed that the activation energies of the oxygen abstraction reactions of N_2O by Sc, Ti, and V were very low, all by less than 5 kcal/mol, (Stirling, 1998, 2002). These values are in agreement with that obtained from the experimental studies (Futerko and Fontijn, 1991; Ritter and Weisshaar, 1990). In accordance with the calculations from Delabie *et al.*, the reactions of Sc, Ti, and V with N_2O producing metal oxide and N_2 proceeded almost without energy barriers and are quite exothermic (Delabie *et al.*, 2001). For this reason, the Sc, Ti, and V- decorated CNTs are, as expected, suitable catalysts for N_2O decomposition and this study is the first attempt to evaluate the capability of newly modified CNTs with transition metals (Sc, Ti, V) for N_2O removal in the theoretical aspects.

From the above literatures in both topics, it could be proposed that the metal-CNTs hybrid material is probably able to provide a strong potential in other fields of applications also. Apart from the computational study, this research is also extended to the experimental fabrications of CNTs and their functionalization with particular metal nanoparticles in order to achieve the novel composite nano-structure feasibly applied in fuel cell and other important applications.

Petroleum shortage is increasingly becoming a serious issue since fossil fuels will be depleted in near future. While the continued use of fossil fuels will inevitably generate CO_2 greenhouse gas which strongly impacts on the environment. Consequently, the development of other methods using sustainable energy resources such as wind, solar and hydropower are energetically pursued to satisfy the need for the establishment of renewable energy systems that are independent of petroleum fuel along with the increasing environmental concern. Unfortunately, these resources can only be harvested in some areas, which experience the adequate sunlight, moving of wind and water, respectively. Then, the use of these renewable energy sources is somehow limited.

An alternatively promising possibility is to exploit the energy from the fuel cells because a particular environment is not necessary in the fuel cell system. Fuel cell is an electrochemical device that generates electricity via a chemical reaction of fuel and an oxidant in the presence of a catalyst and then produces heat, water and trace gaseous pollutants as its byproducts. As compared with the traditional combustion engine, the fuel cell is more effective because there is no need for an intermediate mechanical energy conversion which in turn reduces the efficiency and also does not produce CO, HC, or NO_x. The fuel cell is widely accepted as the power source of the future since it generates electricity with high efficiency and very low pollution (Boudghene and Traversa, 2002; Kirubakaran *et al.*, 2009; Kordesch and

Simader, 1995; Perry and Fuller, 2002; Ticianelli *et al.*, 1988; Wang *et al.*, 2011; Wee, 2007).

The first fuel cell was invented in 1839 by Sir William Grove and his device was named a gas battery (Bacon, 1969; Boudghene and Traversa, 2002; Perry and Fuller, 2002; Srinivasan *et al.*, 1990). It consisted of two platinum electrodes placed in the test tubes containing hydrogen and oxygen gases separately. One end of each platinum electrode was immersed in a bath of sulphuric acid. The current could be generated by the electrons flowing between the electrodes. Due to the problems of inconsistency in cell performance from the corrosion of electrodes, Grove’s fuel cell was not practical. In the late 1950s, Francis Bacon's research team successfully produced a more workable fuel cell for NASA's Apollo moon missions and Skylab programs. For this fuel cell, the alkaline electrolyte (molten KOH) and porous sintered nickel electrode were used instead of sulphuric acid and the bulk platinum electrode, respectively. By this modification, the contact area between the electrodes, the gases and the electrolyte was much higher than that obtained in the Grove’s cell, thus increasing the power density of the fuel cell. Even so, it was only after an efficient newly design of a polymer electrolyte membrane (PEM) fuel cell was made in the early 1960s by General Electric (GE) for the Gemini and Apollo space mission.

After over 150 years of research, fuel cells can be divided into five primary types according to the nature of the electrolyte material. These include alkaline fuel cell (AFC), phosphoric acid fuel cell (PAFC), solid oxide fuel cell (SOFC), molten carbonate fuel cell (MCFC) and proton exchange membrane fuel cell (PEMFC) (Boudghene and Traversa, 2002; Kirubakaran *et al.*, 2009; Kordesch and Simader, 1995; Perry and Fuller, 2002). Among them, the PEMFC is the most widely used due to its fast startup time, favorable power-to-weight ratio and long lifetime (Costamagna and Srinivasan, 2001; Peighambardoust *et al.*, 2010; Wang *et al.*, 2011; Wee, 2007).

Two major performance improvements had been made in PEMFC technology since the application in NASAs Gemini space flights in the 1960s. One extreme development was when the polystyrene sulfonic acid membrane (the electrolyte used in the GE PEMFC) was replaced by the Du Pont's perfluorosulfonic acid membrane namely Nafion, which is more stable memebrane, in 1970s (Costamagna and Srinivasan, 2001; Grot, 1985; Perry and Fuller, 2002). The chemical structure of Nafion consists of a polytetrafluoroethylene (PTFE) backbone with perfluorinated-vinyl-polyether side chains containing terminal sulfonic acid groups to exchange the protons (Figure 10). Based on the molecular structure, Nafion does not suffer from rapid degradation as happens in the case of a polystyrene sulfonic acid membrane. This is because the C-F bonds of Nafion are stronger than C-H bonds of polystyrene sulfonic acid. Thus, the life time of such Nafion-based PEMFC was prolonged at by least four orders of magnitude.

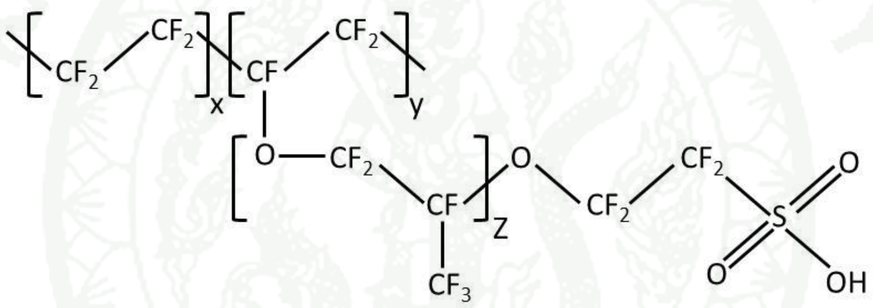

Figure 10 Schematic illustration of the Nafion chemical structure in which x and y are repeat units of the hydrophobic backbone and z represents a repeat unit of the side chain with a sulfonic acid group termination.

The second important development of PEMFC was the dramatic reduction of catalyst loadings which was accomplished by Los Alamos National Laboratory in the 1980s and 1990s (Raistrick, 1989; Ticianelli *et al.*, 1988; Wilson and Goffesfeld, 1992). The platinum loading was 10-fold reduced from about 4 mg cm^{-2} used in the Gemini space flights to less than 0.4 mg cm^{-2}, while the performance was also increased. This achievement was made able by employing the newly designed electrocatalyst of Pt dispersed on high surface area carbon particles (e.g., carbon blacks, Vulcan XC72R) instead of pure Pt black as used in the Gemini fuel cells. This was able to considerably reduce the Pt usage along with increasing the triple-phase boundary or reaction zone of the electrode by impregnation of the proton conductor (e.g., Nafion) into the catalyst layer. Subsequently, carbon blacks (CBs) are generally employed as support for Pt dispersion in fuel cells due to not only their large surface area and good electro-conductivity but also their low cost and high availability.

Numerous researches have been conducted to investigate the effect of the CB structure on the metal dispersions and on the activities of those metal-supported electrocatalysts (Antolini *et al.*, 2002; Fraga *et al.*, 2002; McBreen *et al.*, 1981; Rao *et al.*, 2005; Stevens and Dahn, 2005; Takasu *et al.*, 2003; Uchida *et al.*, 1995; Watanabe *et al.*, 1988, 1989). By the observations on the different types of CB, Uchida *et al.* found that, the particle size of Pt decreased with increasing the surface area of CB (Uchida *et al.*, 1995). The influence of the CB characteristic on the fuel cell performance (when the Pt-CB hybrid material was used) was further studied by Watanabe *et al.* (Cai *et al.*, 2007b; Gruver, 1978; Watanabe *et al.*, 1988). They observed that acetylene black-supported Pt catalyst presented a better activity than the Pt-supported oil-furnace black despite the fact that the former has larger size of Pt particles. The explanation of this phenomenon goes to the CB pore structures. Acetylene black possess the higher amount of pores with a diameter of 3–8 nm, which are beneficial for the fuel diffusion, than for oil-furnace black supports.

Heretofore, there have been several studies examining the stability of carbon support from the particle sintering and releasing from the carbon support which impacts on the loss of the platinum surface area (Gruver, 1978; Stonehart, 1984; Uchida *et al.*, 1995; Wang *et al.*, 2007; Watanabe *et al.*, 1988). Uchida *et al.* (Uchida *et al.*, 1995) obtained the results that the carbon support dissolution in sulfuric acid solution at 60°C of CBs with the larger surface area (e.g., furnace blacks) was more than that of CBs with a smaller surface area (e.g., acetylene blacks). Moreover, the CBs with less support corrosion resistance brought the higher amount of the Pt loss and larger Pt particle size. These results corresponded well with that reported by Wang *et al.* (Wang *et al.*, 2007). Accordingly, although many kinds of CBs have been widely used as a catalyst support, it still suffers from the mentioned problems which limit the activity of the catalyst.

The emergence of novel carbon support materials, such as graphite nanofibers (GNFs) (Bessel*et al.*, 2001; Steigerwalt *et al.*, 2001), carbon nanotubes (CNTs) (Carmo *et al.*, 2005; Kim *et al.*, 2004; Liu *et al.*, 2002; Matsumoto *et al.*, 2004b; Rajesh *et al.*, 2002; Wang *et al.*, 2004; Xing, 2004), carbon nanohorns (Joo *et al.*, 2001; Yoshitake *et al.*, 2002) and carbon nanocoils (Chai *et al.*, 2004; Hyeon *et al.*, 2003; Park *et al.*, 2004) opens up new ways to improve the electrochemical activity and stability of the fuel cell catalyst. Especially for CNTs, they are believed to be superior to CBs because of their high surface area, good crystallinity and well-ordered tubular structure with low or absence of micropores (Liu *et al.*, 2002; Maiyalagan *et al.*, 2005; Zhang *et al.*, 2000). There are a significant number of papers demonstrating the higher catalytic activity of Pt supported CNTs than that of the same catalysts deposited on CBs. Maiyalagan *et al.* (Maiyalagan *et al.*, 2005) reported that the catalyst of Pt supported on nitrogen containing CNT (Pt/N-CNT) presented a ten-fold increase in the catalytic activity for oxygen reduction compared to the Pt-supported commercial Vulcan. It was suggested that this was due to that the Pt/N-CNT made the higher Pt dispersion and stronger interaction between the support and the Pt particles.

The testing carried out under the PEMFC simulating conditions by Wang *et al.* indicated that the MWCNTs could be more durable than VulcanXC-72 with less surface oxide formation and 30% lower corrosion current (Wang *et al.*, 2006). Likewise, Girishkumar and co-workers also showed the improved stability of Pt particles by CNTs in which Pt/CBs lost 50% whereas Pt/CNT lost only 16% of its electrochemically active surface area (ECSA) after performing the repeated potential cycling over a period of 36 h (Kongkanand *et al.*, 2006).

The fabrication of the CNT-based MEA commonly involves the deposition of CNTs powder with metal particles and then pressing those composite materials on the membrane. By this assembly process, the disadvantage in catalyst performance could be obtained since the alignments of CNTs are unable to be manipulated and some Pt particles are wasted by being buried deep within the electrode layer. Alternatively, free-standing vertically aligned CNTs (VACNT) electrodes have been intensively studied due to their regular pore structures. As compared with the flat graphite electrode, Tang *et al.* achieved a four-fold improvement in electrocatalytic current by using a VACNT network because of the higher catalytic utilization (Chan *et al.*, 2004; Tang *et al.*, 2004). Zhang *et al.* also demonstrated the sandwich structured MEA of the Pt-decorated free-standing CNTs on a Nafion membrane (VACNTs/Nafion membrane/VACNTs) (Zhang *et al.*, 2010b). It was found that the PEMFC performance of this developed single cell was two times higher than that of the cell with the conventional Pt/CB electrodes. The advantages of VACNTs over random-distributed CNTs likely originated from the continuous and direct diffusion path due to the vertical orientations of CNTs. A similar experiment was also carried out by Hatanaka *et al.* (Hatanaka *et al.*, 2006) whereby the cell voltage at high electrical loading of the single cell composed of the Pt-coated well-aligned CNTs and Nafion membrane was remarkably higher than that composed of the Pt-carbon black. Nevertheless, under the hot pressing process of MEA fabrication, the layer of the VACNT was compressed to over 75% of the original thickness. As a result, the VACNTs were obviously pressed downward, becoming misaligned arrays. This feature might impair the diffusion channels and also lower the available surface area. One interesting method for the preparation of VACNTs that can preserve the array of VACNTs during the hot pressing process is the chemical vapor deposition (CVD) to form VACNTs in tubular porous template of anodic aluminium oxide (AAO).

This technique was firstly presented by Kyotani *et al.* (Kyotani, 1995, 1996, 2006). Briefly, an AAO film was introduced in a temperature-controllable reactor. The chemical vapor deposition of propene at 800 °C was performed. The homogeneous carbon coating on the inner wall of the nanoporous template was obtained. The resultants of isolated CNTs were obtained just after removing AAO template with HF solution. Many other researchers have utilized the CVD-combined template technique for producing CNTs because that allows one to prepare the CNTs with controllable and uniform diameter and length without any use of a metal catalyst (Che *et al.*, 1998a, 1998b; Jin Seung *et al.*, 2001; Li *et al.*, 1999). Rajesh *et al.* applied this synthesis method to prepare VACNTs for PEMFC applications (Rajesh *et al.*, 2002). The catalytic nanoparticles were loaded into the nanochannels of VACNTs before the dissolution of AAO. The nanoparticles exhibited a good dispersion inside the pores of tubes, thus resulting in an improved electrocatalytic performance for methanol oxidation compared to the metal-decorated Vulcan XC72R. Similar results were also found by Maiyalagan *et al.* (Maiyalagan *et al.*, 2005). They also showed that Pt catalysts were highly dispersed on the inner walls of nitrogen containing CNTs, which were prepared by the template method. The obtained composite material provides better catalytic performance than the commercial Pt/Vulcan (E-TEK) electrode.

Notwithstanding this, up until the present time, there has been no research work to take advantage of the AAO template as the protecting film for VACNTs from the pressing force during MEA fabrication. In this study, VACNTs synthesized by the CVD technique are selected to be utilized for fabrication of MEA by employing AAO film as a template. The AAO template is expected to keep the standing of the tube arrays intact, to prevent the tube bundling closed by the van der Waals interactions between CNT surfaces and also to tailor the carbon nanostructure in uniform pore length and diameter.

Furthermore, owing to the synergistic actions of constituents, the hybrid of different nanoscaled materials is thereby a prevailing strategy to create the novel functional properties that often drive the emergence of new frontier applications. Among various nanocomponents, other than PtNPs/CNTs, gold nanoparticles (AuNPs) and carbon nanotubes (CNTs) are also commonly used building blocks due to their outstanding properties and versatile syntheses. On account of that, the development of AuNPs/CNTs composites is concerned primarily with the wide area of uses such as optical, chemical and biological sensing, electronic and catalytic applications. Lim *et al.* demonstrated that Au–CNT based genosensor exhibited as a reliable device to differentiate between the complementary and mismatched DNA hybridizations (Lim *et al.*, 2004). The capability of this heterostructure originated from the complementary roles of AuNPs and CNTs by which the AuNPs served as the anchoring sites for the thiolated biomolecules via the well-known gold–sulfur linkage. Meanwhile, CNTs performed as not only as a support but also as a fast electron-transfer center. In addition to the ability for the immobilization of probe molecules in

DNA and protein sensors (Dong *et al.*, 2008; Guo *et al.*, 2010; Lim *et al.*, 2004; Lin *et al.*, 2009; Ma *et al.*, 2008; Qin *et al.*, 2010), AuNPs can be the active sites to catalyze some important electrochemical reactions. The exploitation the cooperative works of the AuNPs catalyst and the CNT support, which perform excellently for electron transfer and metal dispersion, are favorable in a glucose sensor, toxic chemical sensors of mercury (II), arsenic (III) and hydrogen peroxide and fuel cell applications (Alexeyeva and Tammeveski, 2008; Cai *et al.*, 2007b; Kim *et al.*, 2009; Li *et al.*, 2009; Li *et al.*, 2012; Shi *et al.*, 2009; Xiao *et al.*, 2008; Xu *et al.*, 2008; Zhu *et al.*, 2009).

The fabrication of AuNPs/CNTs can be performed via several practical routes, thus allowing selection of the most proper preparation method to accomplish the desired property. Generally, based on the binding mode between AuNPs and CNTs, the decorations AuNPs onto the surfaces of CNTs are classified into three ways including covalent, non-covalent and direct depositions (Georgakilas *et al.*, 2007; Singh *et al.*, 2010; Zhang and Olin, 2011).

For the direct deposition, AuNPs are attracted onto the sidewalls of CNTs without linking molecules by employing thermal and electron-beam evaporations, normal and microwave-assisted chemical reductions, chemical vapor deposition and electrodeposition (Bittencourt *et al.*, 2006; Choi*et al.*, 2002; Dong *et al.*, 2006; Gingery and Bühlmann, 2008; Kim *et al.*, 2003; Quinn *et al.*, 2005; Raghuveer *et al.*, 2006; Satishkumar *et al.*, 1996; Tello *et al.*, 2008; Warakulwit *et al.*, 2008; Xu *et al.*, 2008; Xue *et al.*, 2001; Zhang *et al.*, 2009; Zhang and Wang, 2007; Zhang *et al.*, 2000). Although the direct formation provides high purity composite of AuNPs/CNTs, some limitations of this method are still found e.g., the requirement of specific equipment such as vacuum system, the difficulty in regulating the sizes of AuNPs originated from the different local variations on the tube surface and the high aggregation tendency together with somewhat losing of AuNPs due to the unstable adsorption.

For the most applications of AuNP/CNTs, the robust hybrid nanostructure is required in order to prolong the capability of the fabricated device. The covalent binding is developed to surmount the stability of AuNPs/CNTs composite (Azamian *et al.*, 2002; Choi *et al.*, 2011; Coleman *et al.*, 2003; Gobbo *et al.*, 2013; Hatanaka *et al.*, 2006; Hu *et al.*, 2005; Ismaili *et al.*, 2011; Liu *et al.*, 1998; Peng and Wong, 2009; Zhang *et al.*, 2008). For instance, Azamian *et al.*, Hu *et al.* and Shi *et al.* carried out the functionalization of oxidized CNTs with the thiol compounds which then bond to the AuNPs via the thiolate groups (Azamian *et al.*, 2002; Hu *et al.*, 2005; Shi *et al.*, 2006). Likewise the research work of Choi *et al.*, thiolate-Au bonds could be formed on the 4-mercaptobenzoyl functionalized MWCNTs, which were prepared by the direct Friedel-Crafts acylation reaction of MWCNTs and 4-mercaptobenzoic acid (Choi *et al.*, 2011). Moreover, the diazirine-modified AuNPs covalently attached onto the MWCNTs by using a photoinitiated carbene addition approach were also synthesized by Ismaili *et al.* (Ismaili *et al.*, 2011). Some researchers attempted to attain better control over the size and shape of AuNPs by pre-synthesizing them with well-established procedures prior to anchoring with functionalized MWCNTs. Of course, the drawbacks of the covalent attachment are taken into consideration including the dealing with the multistep chemical reactions and also the aggressive pretreatments on CNT surfaces that mostly damage the CNT structures and diminish their superior electrical and mechanical properties.

Accordingly, there have been increasingly developed non-covalent deposition so as to preserve the excellent intrinsic properties of CNTs by utilizing hydrophobic, electrostatic, van der Waals and also π-π stacking interactions to link the unmodified or treated CNTs with functionalized AuNPs (Carrillo *et al.*, 2003; Correa-Duarte *et al.*, 2004, 2005; Dudin *et al.*, 2010; Ellis *et al.*, 2003; Herrero *et al.*, 2010; Jiang *et al.*, 2003; Jiang and Gao, 2003; Jiao *et al.*, 2012; Kim and Sigmund, 2004; Kim *et al.*, 2010; Kumar *et al.*, 2009; Li *et al.*, 2010; Ou and Huang, 2006; Rabbani *et al.*, 2009; Rance *et al.*, 2010; Wang *et al.*, 2006, 2007; Yu *et al.*, 2011). Among those techniques, the electrostatic self-assembly has been widely used. Up until present, the wrapping of CNTs with ionic polymer followed by the assembling with the oppositely charged AuNPs has been exploited extensively. Jiang *et al.* tuned the surface charges of CNTs via electrostatic interaction between carboxyl groups of the oxidized nanotubes and the cationic chains of the poly(diallyldimethylammonium)chloride (PDDA). The negatively charged AuNPs were subsequently anchored to the positively charged CNTs through the electrostatic interaction (Jiang *et al.*, 2003).

Based on this schematic experiment, several types of cationic and anionic polyelectrolytes could effectively modify the CNT surfaces such as polyethyleneamine (PEI), polymethacryloyl β-alanine (PMBA), polystyrene sulfonate (PSS) and poly(acrylic acid) (PAA) (Carrillo *et al.*, 2003; Correa-Duarte *et al.*, 2004, 2005; Jiang and Gao, 2003; Kim and Sigmund, 2004; Kim *et al.*, 2010; Kumar *et al.*, 2009; Rabbani *et al.*, 2009; Yu *et al.*, 2011). In a similar manner, the charge of colloidal AuNPs could also be adjusted depending on their dispersion agent. For example, trisodium citrate, polyvinylpyrrolidone (PVP) and sodium dodecyl sulfate (SDS) were employed to introduce the negative charges on the AuNP surfaces whereas positive charges could be induced by 4-dimethylaminopyridine (DMAP) stabilizer (Kim and Sigmund, 2004; Kim *et al.*, 2010; Kumar *et al.*, 2009; Rabbani *et al.*, 2009; Yu *et al.*, 2011).

However, covering of CNTs with a polymer layer may block the electron transport pathway of the nanotubes, thereby diminishing the conductivity of the composite. In order to avoid such a problem, using of the naked CNTs should be the better strategy. Regarding to the previous work, Orikasa *et al.* successfully prepared the water-dispersible CNTs via the template-enhanced CVD method (using AAO as the template) without any further post-treatments (Orikasa *et al.*, 2006, 2008). The intrinsic hydrophilicity of the obtained CNTs were derived by the oxygen-containing functional groups formed during the template removal process with alkaline solution. These surface oxygen groups enabled the CNTs to be of negative charge. Those unmodified CNTs are thus suitable to be taken advantage of here as a negatively charged platform for loading AuNPs by means of electrostatic self-assembling. Following such an experimental scheme, the positively charged AuNPs need to be synthesized.

The 4-(N,N-dimethylamino)pyridine or DMAP is used hereof as a non-ionic capping ligand which can polarize the positive charges on AuNPs surfaces. DMAP-protected AuNPs (AuNPs-DMAP) are of current interest because of their good stability in water media and exhibit as an excellent responsive precursor for various kinds of substrates such as biomolecules, polyelectrolyte materials, polymer-wrapped CNTs, which are applicable in biolabelling, photonic crystals, sensors and catalysis (Biver *et al.*, 2012; Cho and Caruso, 2005; Gittins *et al.*, 2002; Liang *et al.*, 2003; Liang *et al.*, 2002; Rabbani *et al.*, 2009; Raj *et al.*, 2011; Yu *et al.*, 2003; Yu *et al.*, 2009; Zhang *et al.*, 2007).

A general preparation of AuNPs-DMAP bases on the method of Gittins *et al.* (Gittins and Caruso, 2001). In this method, the AuNPs were firstly synthesized in the toluene phase by using tetraoctylammonium bromide (TOABr) as a phase transfer agent for assisting the metal salt move toward the organic solvent. After that the as-prepared AuNPs were spontaneously phase transferred into water under mixing with DMAP aqueous solution. Although this synthesis was quite simple, not time consuming and reproducible of AuNPs with uniform size (around 5-6 nm), it was carried out in the toxic organic solvent. To avoid harmful substances, water-based synthesis is preferable. However, there have been only few experiments so far on the one-step and one-phase synthesis of AuNPs-DMAP in an aqueous solvent. Amal Raj *et al.* synthesized the AuNPs-DMAP in an aqueous medium by adding the DMAP after the metal salt reduction process (Raj *et al.*, 2011). The obtained particles were spherical-like in shape with a broad size distribution from 7-18 nm. Danger *et al.* attempted to tune the shape of AuNPs-DMAP in an aqueous system by varying the pre-reduction time of the Au^{III} ion with DMAP before the complete reduction by the addition of $NaBH_4$ (Danger *et al.*, 2012). The nanoparticle with various shapes including spheres with non-uniform size (3-4 nm), rods (~40 nm), and long-armed branched nanopods (~100 nm) could be produced. Beside both articles, there is still a lack of study as to systematically regulating the particle size of AuNPs-DMAP synthesized in an aqueous system.

Apart from DMAP, poly(N-vinyl-2-pyrrolidone) or PVP is one of the most common capping agent to produce the water-soluble AuNPs. Almost all syntheses of AuNPs-PVP proceed with using neither very hazardous chemicals nor strong conditions. Tsunoyama *et al.* prepared the AuNPs-PVP by the reduction of $HAuCl_4$ with $NaBH_4$ in the presence of PVP via the conventional batch method and homogeneous microfluidic mixing (Tsunoyama *et al.*, 2004, 2005, 2006, 2008, 2011). The sizes of AuNPs-PVP were uniform with an average diameter of less than 2 nm. The formation of the small AuNPs could be ascribed to the suppression of Au nuclei growth by the high stabilizing ability of the polymer backbone of PVP and very low temperature of the reaction medium.

Hence, PVP is, therefore, promising to be exploited as a co-stabilizer with DMAP for receiving AuNPs with more sizes and narrower size distribution than of AuNPs prepared by using DMAP alone. The aim of this work is to synthesize positively charged AuNPs with various core sizes governed by the used amounts of DMAP and PVP stabilizers. The production of AuNPs-CNTs composites via electrostatic self-assembly of the positively charged AuNPs with different sizes and the negatively charged CNTs derived from template method are thereafter investigated.

MATERIALS AND METHODS

1. Materials

All materials and chemicals for the fabrication of Nafion/PtNPs/CNT-AAO and CNTs/AuNPs composites were used as received without further purification.

For the fabrication of Nafion/PtNPs/CNT-AAO composite, the required materials and chemicals include aluminium (Al) and nickel (Ni) plates (with a purity of 99.99%) with a thickness of 0.5 mm, perchloric acid ($HClO_4$), oxalic acid ($(COOH)_2$), phosphoric acid (H_3PO_4), nitric acid (HNO_3), chromic acid (CrO_3), hexachloroplatinic acid (H_2PtCl_6), sodium borohydride ($NaBH_4$), octadecanethiol ($C_{18}H_{37}SH$), Nafion solution, polyvinyl chloride (PVC) resin, ethanol (C_2H_5OH), tetrahydrofuran (THF, C_4H_8O), toluene (C_8H_{10}), acetone (C_3H_6O), deionized water, nitrogen (N_2) gas and acetylene (C_2H_2) gas. The Nafion 117 membrane was employed for assembling with Nafion/PtNPs/CNT-AAO film. In the case of the synthesis of CNTs/AuNPs composite, the used materials and chemicals include aluminium (Al) and nickel (Ni) plates (with a purity of 99.99%) with a thickness of 0.5 mm, perchloric acid ($HClO_4$), sulfuric acid (H_2SO_4), sodium hydroxide (NaOH), sodium chloride (NaCl), sodium borohydride ($NaBH_4$), gold (III) chloride trihydrate ($HAuCl_4$. $3H_2O$), polyvinylpyrrolidone (PVP K10, MW 10000, $(C_6H_9NO)_n$), 4-(dimethylamino)pyridine (DMAP, $(CH_3)_2NC_5H_4N$)), deionized water, nitrogen (N_2) and acetylene (C_2H_2) gases.

2. Equipment and Instruments

To fabricate the Nafion/PtNPs/CNT-AAO composite, the important items of equipment employed for AAO and CNT syntheses with anodization and chemical vapor deposition (CVD) approaches, respectively were power supply (KIKUSUI PWR1600L), temperature-controlled water bath (Yamato Thermo-Mate BF400), homemade acrylic plastic cell and CVD reactor (built in-house). The hot hydraulic compression press system (PHI) was used to attach the Nafion membrane to the synthesized Nafion/PtNPs/CNT-AAO film. The structural characterizations were carried out with a transmission electron microscope, TEM (JEOL, JEM-2010) and a field emission-scanning electron microscope, FE-SEM (Hitachi S-4800). The thermogravimetric analyzer (TG; Shimadzu, TGA-51H) was used to observe the decomposition temperature of octadecanethiol. Regarding the CNTs/AuNPs composite, all necessary items for AAO and CNT syntheses were similar to those for the fabrication of the Nafion/PtNPs/CNT-AAO. The additional devices used in CNTs synthesis were a plasma reactor (Yamato Scientific, PR-301) and filter membranes (Whatman, Anodisc, pore diameter 0.02 μm). The common stirrer, centrifugal filter unit (MWCO 10000) and microcentrifuge tubes were also necessary equipment for AuNPs preparation. The structural characterizations were carried out with a transmission electron microscope, TEM (JEOL, JEM-2100). Ultraviolet and visible (UV–vis) spectroscopy was operated on a UV-670 spectrophotometer (JASCO Analytical Instruments). Zeta potential was measured with a Zetasizer Nano ZS90 (Malvern Instruments).

3. Methods

3.1 Methodology for the evaluation of sensing properties of Pt-doped SWCNTs ($SWCNT_{Vac}$/Pt), pristine SWCNTs (SWCNTs), vacancy defected SWCNTs ($SWCNT_{Vac}$) and Pt-deposited SWCNT (SWCNT/Pt) for NO_2 and NH_3 detections

Fully optimized geometries and the properties of all systems were derived by means of density functional calculations in the spin-unrestricted generalized gradient approximation with double-numerical polarized (DNP) basis sets by using the DMol^3 code (Delley, 1990, 2000). The calculations were performed with the PW91 (Gülseren *et al.*, 2002) density functional which can efficiently be applied to large periodic systems because dispersion energy contributions are not included. This method has been used on a numerous number of comparable systems in good agreement with experimental information. DFT semicore pseudopotentials (Blase *et al.*, 1994) were employed to represent the interactions between core and valence electrons. The real-space orbital cutoff was set to 4.0 Å, the force threshold for optimizations was 0.01

eV and the Brilloiouin zone k-point sampling was performed in a 1 x 1 x 2 Monkhorst–Pack mesh (Monkhorst and Pack, 1976). These values of the parameters correspond to a medium quality calculation which provides computational feasibility for such large systems with high accuracy. Periodic-boundary conditions were applied with a tetragonal unit cell of 20 x 20 x 12.78 $Å^3$. This was large enough to virtually avoid interactions with images in neighboring cells. An (8,0)SWCNT with 96 carbon atoms was selected as a model of an unmodified SWCNT. The chosen chirality principally exhibits a semiconducting electronic property, a prerequisite feature for the sensor circuit. The calculated a HOMO–LUMO energy gap of (8,0)SWCNT is 0.63 eV, which agrees well with previous DFT studies (Durgun *et al.*, 2003; Gülseren *et al.*, 2002). Based on this SWCNT, the models for the Pt-deposited, and Pt-doped, and SWCNTs with vacancy defects were derived. They are shown and explained in Figure 11.

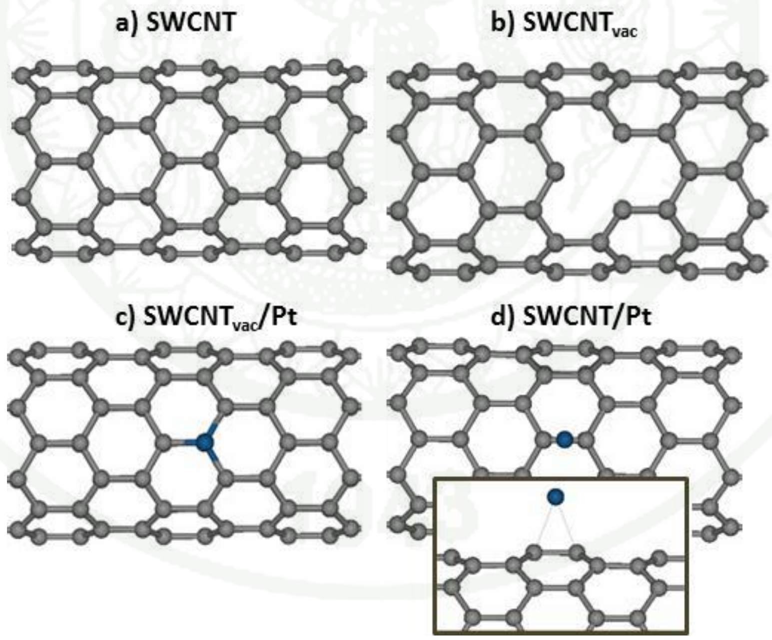

Figure 11 Initial geometries of pristine SWCNT (a), vacancy SWCNT (b), Pt-doped SWCNT (c) and Pt-deposited SWCNT (d). The inset is shown a side view under corresponding picture of (d).

The different sites of the gas molecules adsorbed above the hexagonal carbon ring of the CNT were investigated. NO_2 was oriented parallel or perpendicular to the SWCNT surface. For the latter one, three orientations with N pointing to the SWCNT were determined, with a single O atom or both O atoms pointing to the SWCNT. Likewise, NH_3 was placed above a carbon atom, between two carbons and above the center of a hexagonal ring. For each case, one H atom or all three H atoms were oriented towards the CNT surface. The N–H bonds were parallel to the hexagonal carbon framework or rotated away by 60°. Detailed pictures of the initial structures are available in Figure 12.

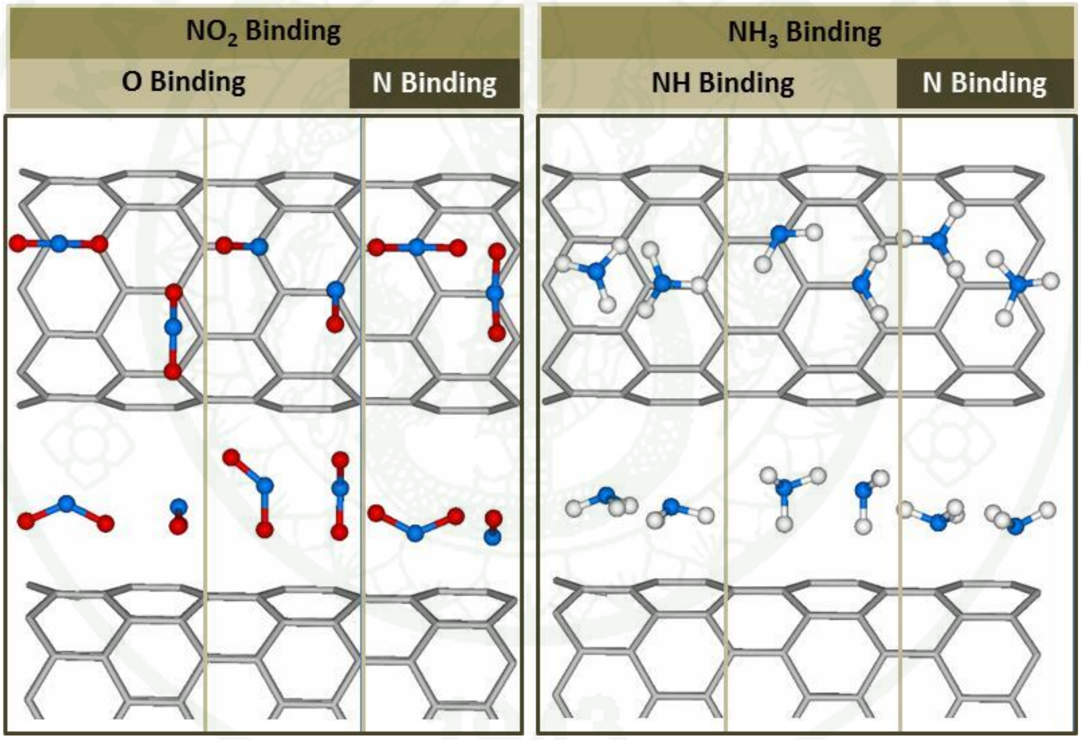

Figure 12 Top and side views of initial configurations of the gas molecules oriented in different sites.

The binding energies (E_b) between the gas molecules and the SWCNT were calculated according to Equation 4 where E_T (support:gas) is the total energy of a gas molecule adsorbed on the active site of support and E_T (support) and E_T (gas) are the total energies of the support and the gas molecule, respectively. All E_T values refer to quantum chemical energies at optimized geometries.

$$E_b = E_T \text{ (support : gas) - } E_T \text{ (support)- } E_T \text{ (gas)} \quad (4)$$

The electronic structures of the energetically most favorable complexes were analyzed in order to estimate the sensing susceptibility with respect to the property as follows. The partial and net charge transfers were obtained from a Mulliken population analysis. The partial and total density of states (PDOSs and DOSs) were calculated and the frontier molecular orbitals were analyzed. Electron density difference maps of optimized structures were calculated with a plane-wave basis set and ultrasoft pseudopotentials (Chen and Kawazoe, 2006) as implemented in the CASTEP program (Zhang *et al.*, 2006).

3.2 Methodology for the investigation of the catalytic activities of newly modified SWCNTs with transition metals (Sc, Ti, V) and the unmodified SWCNTs for N_2O removal

Recent experiments and calculations indicate that in defective CNTs both loading content and size distribution of the metal are improved over perfect ones. The metal atoms prefer to adsorb on a vacancy site with high stability, a process that resembles conventional doping (Kim *et al.*, 2007; Pannopard *et al.*, 2009). The Sc-, Ti- and V-doped and undoped armchair (5,5)SWCNTs were employed as catalysts for studying N_2O decomposition. SWCNTs were modeled by applying periodic boundary conditions to simulate infinite tubes. A tetragonal unit cell of 20 x 20 x 12.30 Å^3 was used. This was large enough to virtually avoid interactions between images in neighboring cells. A (5,5)SWCNT with 100 carbon atoms was chosen as the model of an undoped SWCNT and (5,5)SWCNTs with 99 carbon atoms and one Sc-, Ti- or V atom at vacancy sites were used as models for the doped ones. The structures are shown in Figure 13.

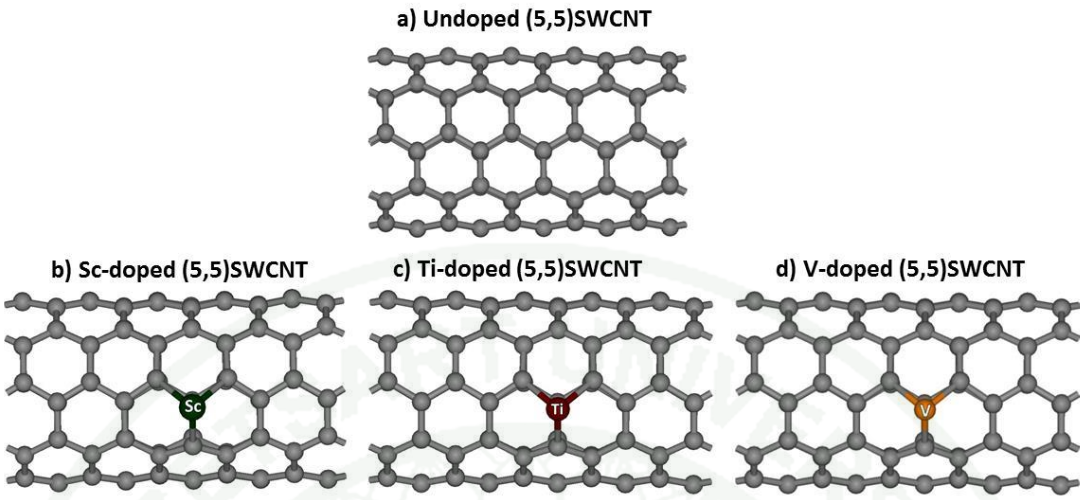

Figure 13 Initial geometries of undoped (5,5)SWCNT (a), Sc-doped (5,5)SWCNT (b), Ti- doped (5,5)SWCNT and (c) and V-doped (5,5)SWCNT (d).

Fully optimized geometries and the properties of the systems were derived by means of density functional calculations in the spin-unrestricted generalized gradient approximation. The DMol^3 code (Delley, 1990, 2000) with a double-numerical basis set with polarization functions (DND) was used for all calculations. These calculations were performed with the PW91 (Perdew and Wang, 1992) density functional which can efficiently be applied to large periodic systems. The interactions between core and valence electrons were represented by DFT semicore pseudopotentials (Delley, 2002). The real-space orbital cutoff was set to 5.0 Å and the force threshold for optimizations was 0.01 eV. Since these calculations were not very time-consuming, a 1 x 1 x 2 Monkhorst–Pack mesh (Monkhorst and Pack, 1976) was kept for the Brillouin zone k-point sampling.

The energies of adsorption (E_{ads}) of the transition state (E_{ts}) and of the final state (E_{prod}) were calculated as differences between the energies of adsorption complexes, transition state structures and products, respectively, and the total energies of E_T(bare (5,5)SWCNT) or E_T(metal-doped (5,5)SWCNT) plus E_T(N_2O). The E_T values refer to total energies at optimized geometries. The partial molecular and atomic charge transfers were obtained from a Mulliken population analysis. For transition state optimization, the two main approaches to locate transition states are the search for a first order saddle point from a single initial structure and the synchronous transit method which finds the transition state by seeking the maximum energy structure along the interpolated reaction pathway between the given reactant and product structures.

An initial transition state structure could be simply predicted by performing a potential energy scan and, therefore, used the first method by the following procedure: The first step consists of guessing a reasonable transition state geometry. In the concerted mechanism of N_2O decomposition, a prediction of the transition structure could be done by systematically adjusting the lengths of bonds being formed (M-O) and broken (N-O). A potential energy scan was performed with respect to these coordinates with all others fully optimized. The structure with maximal energy on the potential energy scan surface then served as the guess for the transition state search. The second step was the transition state optimization where this structure was further optimized by relaxing all geometrical parameters. The last step was verifying the transition state. For this, a vibrational analysis was performed since a true transition state must have exactly one imaginary eigenvalue whose vibrational mode corresponds to the reaction coordinate.

3.3 Method for the fabrication of well-constructed Nafion/PtNPs/CNT-AAO and its membrane electrode assembly (MEA)

The preparation of Nafion/PtNPs/CNT-AAO and the MEA fabrication of this composite with a nafion membrane involve several procedures (see Figure 14) which are explained step by step as following:

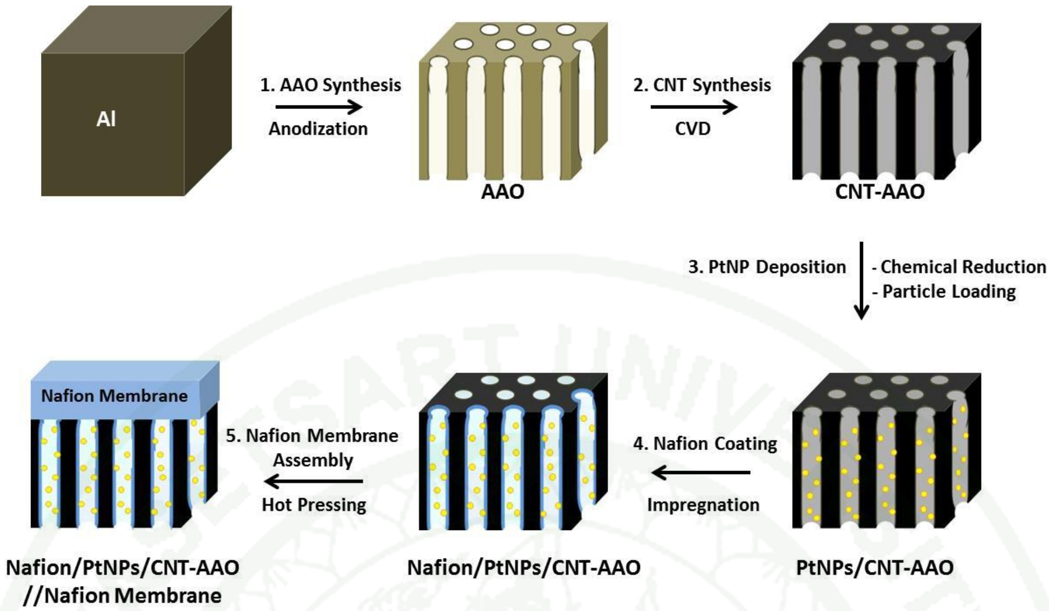

Figure 14 Schematic illustration of the summarized procedures for fabrication of Nafion/PtNPs/CNT-AAO//Nafion membrane composite.

3.3.1 The fabrication of Anodic Aluminium Oxide (AAO) template

There are six major steps to produce AAO film which comprise of (i) electropolishing, (ii) first step anodization, (iii) selective dissolution of AAO, (iv) second step anodization, (v) selective removal of Al and (vi) opening the pore bottoms. All of them are summarized in Figure 15.

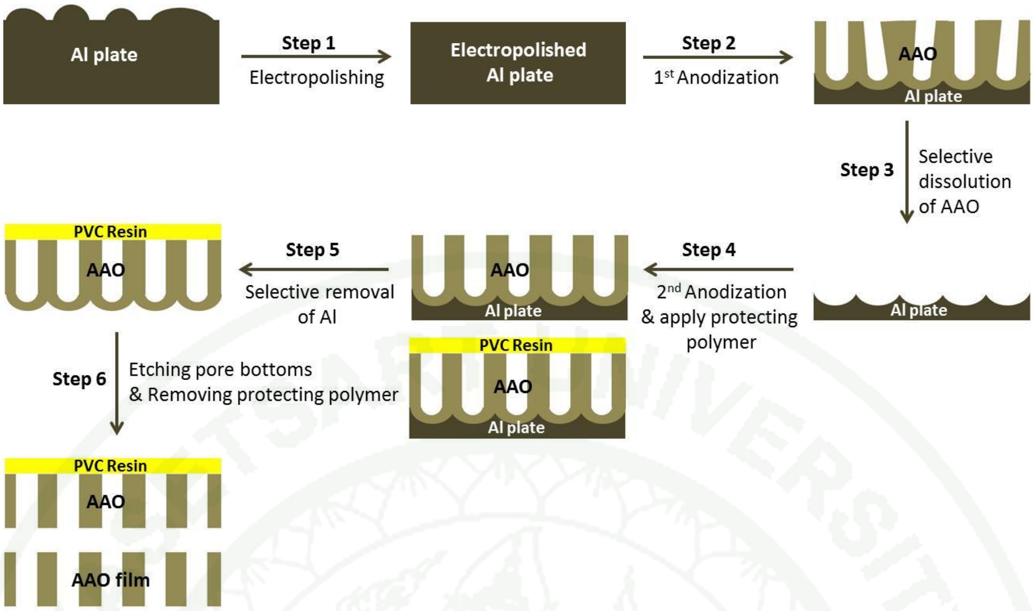

Figure 15 Schematic illustration of the synthesis of open-ended AAO template with 90 nm pore diameter and 60 μm pore length with two-step anodization.

The electropolishing process is an electrochemical surface treatment technique to reduce surface roughness which is a prerequisite for the formation of self-ordered porous alumina (step 1 in Figure 15). The experimental set up is depicted in Figure 16. Prior to electropolishing, as received aluminium (Al) plate with a size of 5 cm x 5 cm x 0.5 mm was degreased with acetone in an ultrasonic bath and washed with deionized water. Then, the cleaned Al plate was covered with plastic tape on one side. This Al plate served as an anode whereas Ni plate, the same size as the Al plate acted as a cathode. Both electrodes were immersed into the electrolyte solution (10 wt% $HClO_4$ in ethanol). The electropolishing was performed at 5^{o}C, 20 V for 10 min and after that the oxidized surface on the naked side of the Al plate was rapidly washed with acetone to remove the corroded matter.

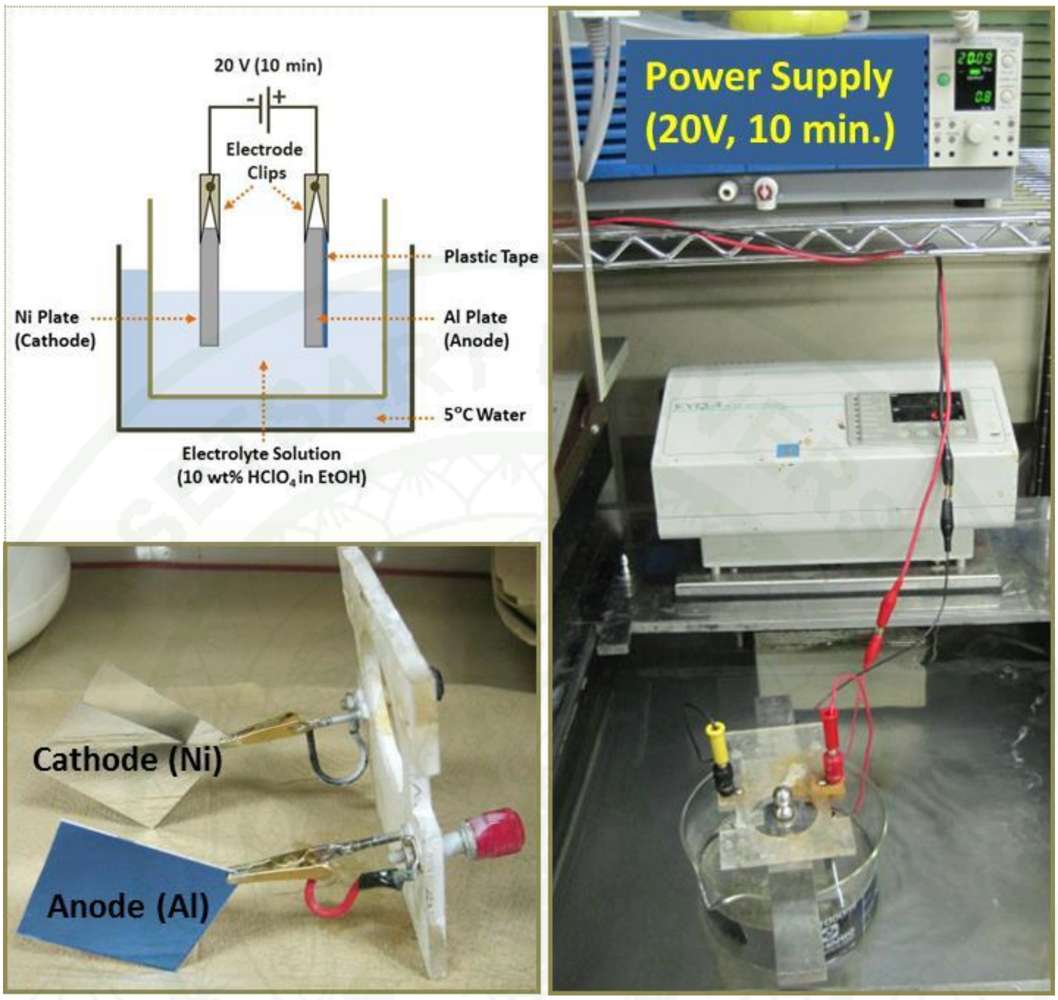

Figure 16 Schematic illustration and photos of the experimental set up for electropolishing of the Al plate.

The porous type AAO film with 90 nm pore diameter and 20 μm pore length was employed as the platform for building up the triple phase boundary inside AAO pores. These porous parameters were selected rationally in which the pore space left after embedding the ionomer and metal particles would even be large enough to facilitate the gas and water flows whereas the transportation path distance was based on the thickness of electrode used in the previous studies. The formation of this AAO film on the Al plate was carried out via anodization, which is an electrochemical process to create an oxide layer on a surface of metal substrate. In a typical anodizing process of aluminium (Al), an Al foil or plate is connected to the anode of a dc power supply and any unreactive conducting plate in the electrolyte is connected to the cathode. The nature of the aluminium oxide produced on the Al surface depends particularly on the electrolyte used. Flat nonporous aluminium oxide film, commonly called a barrier type alumina film, can be formed in a neutral electrolyte, e.g., ammonium borate and ammonium tetraborate in ethylene glycol whereas the anodization of Al in an acid electrolyte leads to the formation of a porous type alumina film. In the case of porous alumina membrane synthesis, the anodizing parameters can directly govern the features of the pore structure whereby the pore diameter and pore length are proportional to the applied voltage and time, respectively. However, the maximum voltage before the oxide layer breakdown is restricted by the conductivity and pH value of the electrolyte which intrinsically depend on the electrolyte concentration, composition and temperature. Sulfuric acid, oxalic acid and phosphoric acid are typically used for anodization of Al in low (5-40 V), medium (30-120 V) and high (80-200 V) potential ranges, respectively. Those three specific conditions can correspondingly produce the porous alumina with pore size about 50, 100 and 500 nm.

In this study, the highly ordered porous structure of AAO was therefore fabricated in oxalic acid solution so as to obtain the AAO membrane with a pore diameter about 90 nm and the synthesis was also based upon the approach of the two-step anodization first demonstrated by Masuda and Fukuda (Masuda, H. and K. Fukuda, 1995). Briefly, a first anodized porous layer was removed to pre-texture on an Al substrate, which facilitates the formation of long-range order nanopores in a subsequent anodization step. The second stage of this AAO synthesis involves the first step anodization, the selective dissolution of AAO and the second step anodization on the electropolished Al plate. More details on this experiment are explained as follows. Firstly, the non-oxidized side of the electropolished Al plate and one side of another cleaned but unpolished Al plate were insulated with plastic tape. Both prepared plates were assembled with an acrylic plastic cell by turning the bare surface inside as shown in Figure 17. Then oxalic acid solution (1.8 wt % in water) was filled into the cell until exceeding the exposed circle area (4.5 cm in diameter) of the Al plates. The electropolished Al plate was connected to the positive (anode) and the unelectropolished Al plate was connected to the negative (cathode) terminals of the power supply. The first anodization was performed at a constant voltage of 80V for 2000 sec at 10°C. The bath temperature was kept lower than room temperature to relieve the local heat causing fast dissolution and the electrical breakdown of the formed oxide. During the course of anodization, the oxide film took place on the anode via the electrochemical reaction. Generally, pores are randomly created on the surface as depicted in Figure 15 after step 2. These irregular alumina pore arrays were then chemically etched away by using the mixed solution of 1.8 wt% H_2CrO_4 and 6 wt% H_3PO_4 at 60 °C for 1 h in order to leave only patterns that were replicas of the former hexagonal pore array. This strategy allowed the preparation of pores with a high regularity by a subsequent second anodization under the same conditions as the first anodization. The received AAO-Al plate from the last anodization was washed with deionized water and dried at 60 °C.

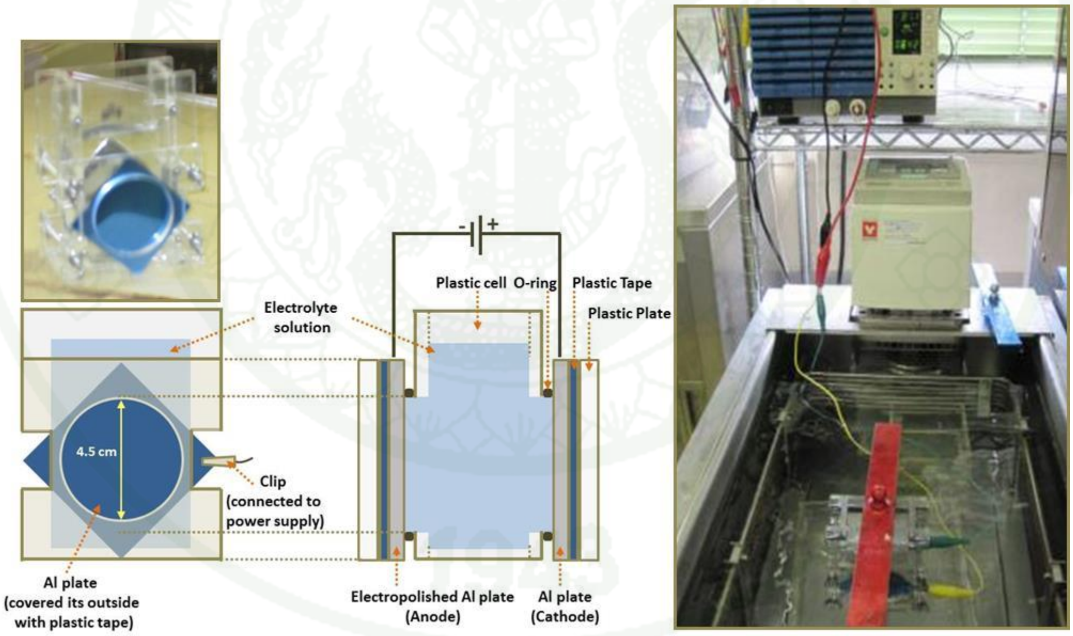

Figure 17 Schematic illustration and photos of the experimental set up for anodization of the Al plate.

After anodization, the Al substrate of AAO-Al plate was selectively removed in 10 wt% $CuCl_2$ solution (Figure 18a). Before the Al removal process, the pore mouth of the AAO deposited on Al plate was protected by coating the PVC suspension resin and drying under air for over 12 h to avoid the pore corrosion from the etching solution used in the next step. In addition, PVC coated AAO-Al plate was cut into the small pieces of 1x1 cm^2 which was also the general size of the catalyst layer in single cell testing. After these preparations, the pore bottoms were opened by chemical etching in 1 M H_3PO_4 solution at 30°C for 90 min (Figure 18b) and thereafter the PVC protecting layer was dissolved with THF solvent to recover the pore mouths.

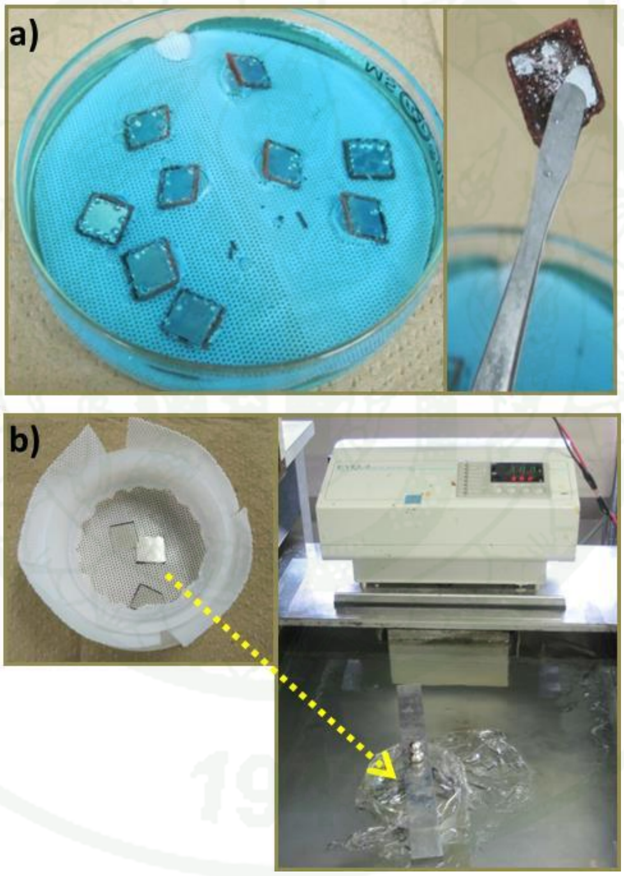

Figure 18 Photos of the experimental set up for the Al removal from the AAO-Al plate and for the opening of the pore bottoms of the synthesized AAO template.

3.3.2 Synthesis of CNT deposited AAO film (CNT-AAO)

The combination of CVD and template synthesis methods was utilized to fabricate the CNT-AAO. These processes involve the dissociation of hydrocarbon molecules to be the reactive species under high temperature. In the presence of the AAO template, the pyrolytic carbons are deposited onto the template surface resulted in the formation of a tubular structure corresponding to the template used. The equipment for CNT synthesis is demonstrated in Figure 16 and the details of the synthesis are also described below.

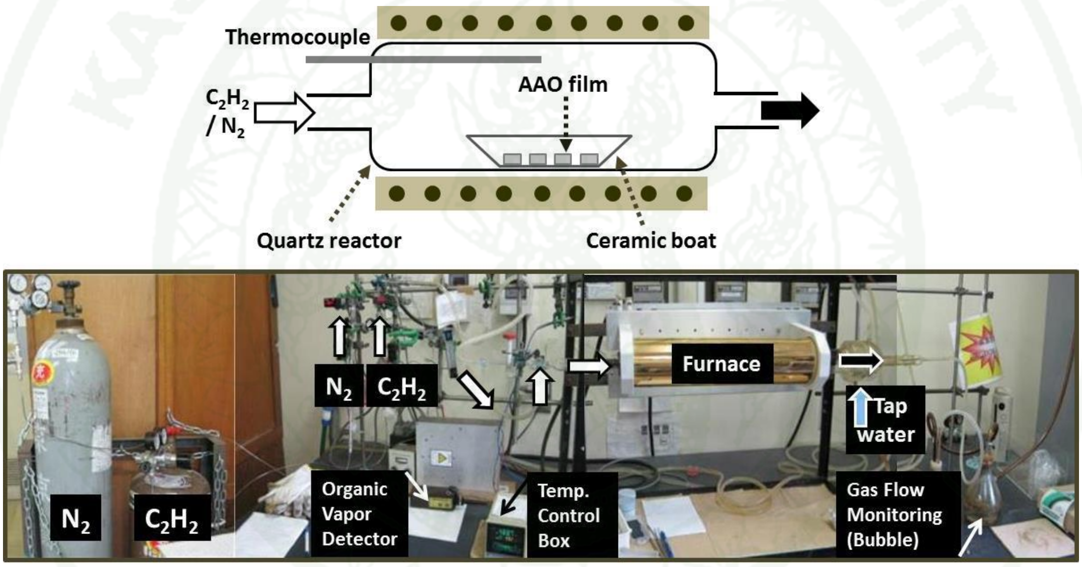

Figure 19 Schematic illustration and photo of the reactor set up for chemical vapor deposition.

The as received 1x1 cm^2 AAO templates were placed in a horizontal quartz reactor. The overall temperature program is displayed in Figure 20. For the first step, the reactor was heated to 600°C at a rate of 10°C/min under N_2 atmosphere. Then C_2H_2 gas (20 vol % in N_2) was flowed through the reactor at a total flow rate of 500 cm^3 (STP) min^{-1} for 2 h. After deposition time, the temperature of the reactor was retained constantly at 600°C under the flow of N_2 for 1 h to compete the decomposition of the remaining hydrocarbon gas in the system. At the final stage the reactor was gradually cooled down to room temperature under normal conditions.

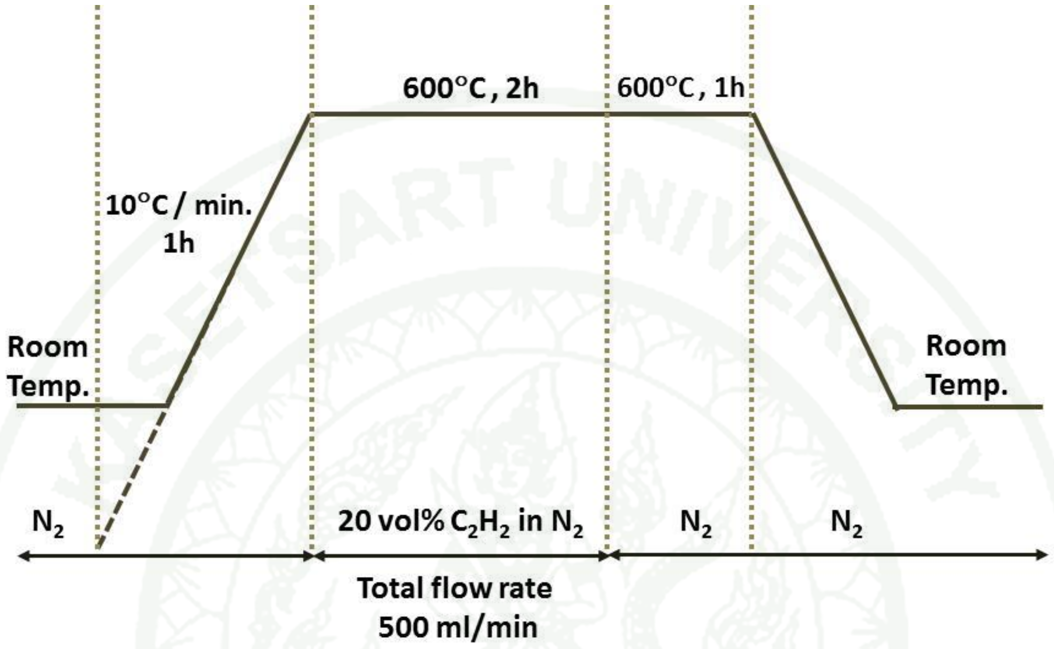

Figure 20 Temperature profile for chemical vapor deposition.

3.3.3 Decoration of the inner walls of CNT-AAO with platinum nanoparticles (PtNPs/CNT-AAO)

The method for decorating PtNPs onto the inner walls of CNT-AAO was mainly divided into two routes, which were direct deposition and loading the pre-synthesized PtNPs. For the former one, the chemical reduction reaction between the Pt precursor and the reducing agent took place inside the pores of CNT-AAO whereas for the latter case, the PtNPs were synthesized prior to their introduction into the nanochannels. Both procedures are described in the following.

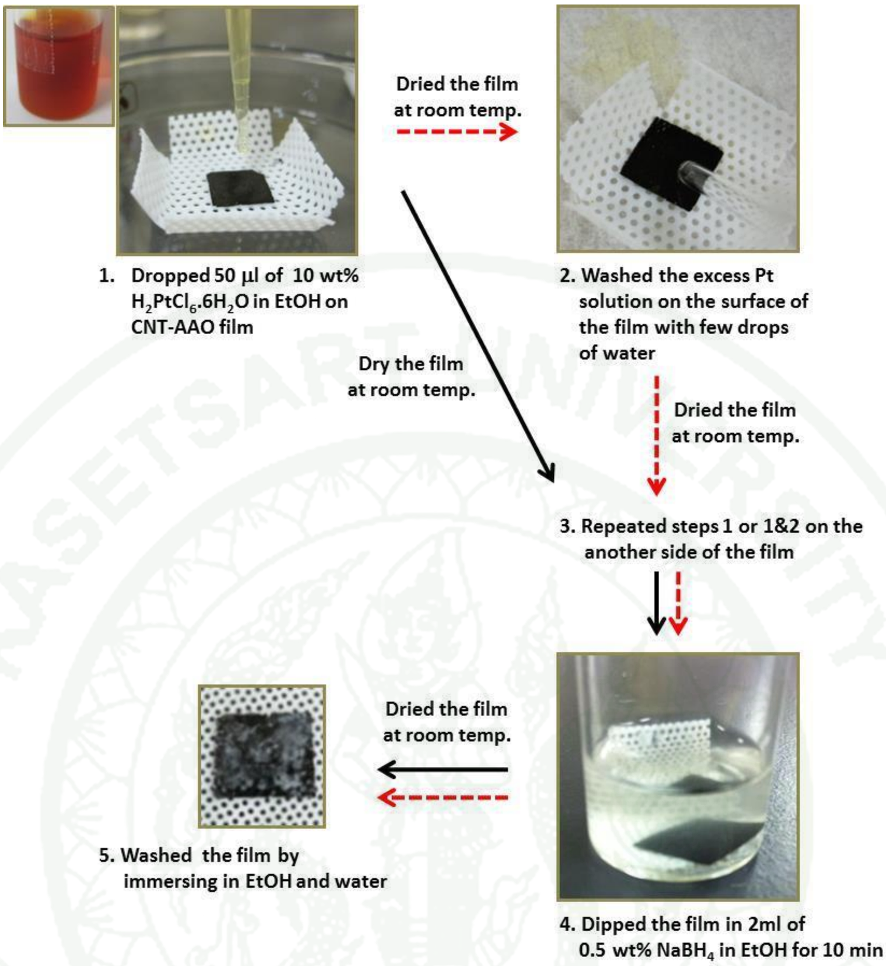

Figure 21 Summarized procedures of two different synthesis routes of the direct deposition of PtNPs onto the inner walls of CNT-AAO film.

The direct deposition PtNPs onto the inner walls of CNT-AAO are displayed in Figure 21. Along the black solid line, the 50 µl of solution containing 10 wt% of H_2PtCl_6 in ethanol was dropped on the 1x1 cm^2 CNT-AAO followed by leaving the film to dry for 30 min at ambient temperature. The same dropping was repeated on the other side of the film. Then, the reduction reaction took place by dipping the dried film into 2 ml of 0.5 wt% of $NaBH_4$ in ethanol for 10 min and left to dry at room temperature for 30 min. The product residue which appears as a white solid on the film surface was washed by soaking in ethanol and water.

However, the alternative route is proposed to avoid the aggregations of PtNPs on the pore mouths of CNT-AAO. The above explained method was modified with a surface washing technique but follows the additional steps on the red dash line pathway of Figure 21. The extra process was rinsing the surface of the dried CNT-AAO film after introducing H_2PtCl_6 solution with few drops of water. Then the washed-CNT-AAO film was dried for 30 min at room temperature before immersing it in $NaBH_4$ solution in order to prevent the side reactions between the remains water and $NaBH_4$.

Another techniques was loading with pre-synthesized PtNPs. PtNPs were synthesized based on previous methods with minor modification (Yang *et al.*, 2003) as explained in Figure 22. Firstly, 10 ml of 2 mM H_2PtCl_6 solution was mixed with 100 mg of 1-octadecanethiol dissolved in 10 ml of toluene. After vigorous stirring in ice bath for 30 min, 0.2 ml of 0.11 M $NaBH_4$ fresh solution was added quickly to the water-toluene mixture and stirring continued for 15 min. After that, the organic phase was separated from the two-phase solution and then the toluene solvent was evaporated to collect the solid sample. These obtained alkanethiolated PtNPs still contained an excess amount of octadecanethiol which was reduced by washing several times with warm ethanol. Finally, the product was kept as a dried solid in a refrigerator.

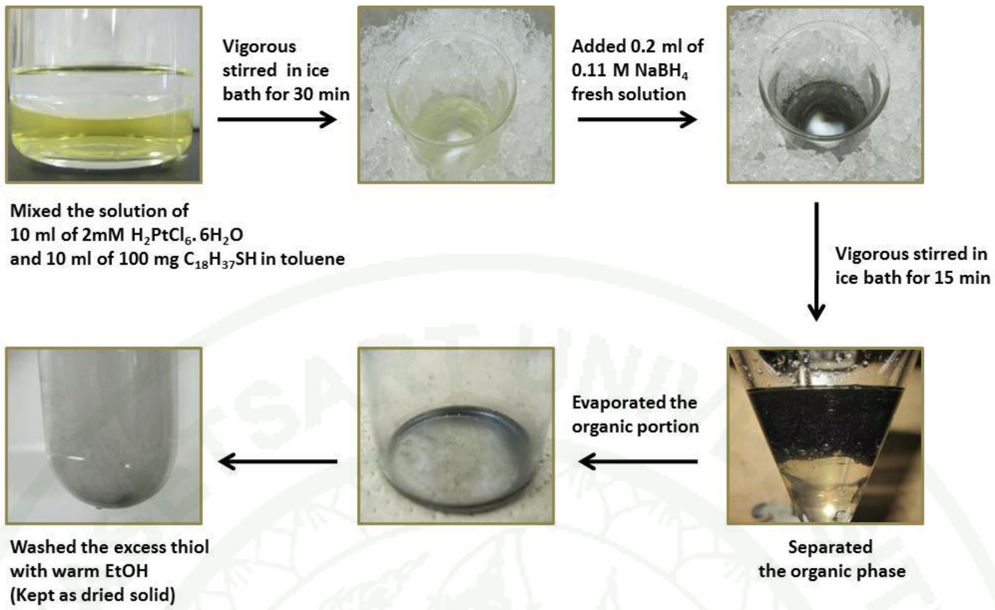

Figure 22 Summarized procedures of two-phase synthesis of alkanethiolated PtNPs.

The next step after obtaining the alkanethiolated PtNPs was loading such metal particles into the pores of CNT-AAO. The technique for propelling metal particles into the nano-channel of CNT-AAO was done with a simple ultrasonication (Figure 23). The 1x1 cm^2 CNT-AAO film was immersed into 0.5 ml of 16 mg/ml PtNPs solution in toluene and was ultrasonicated for 30 min. The films from both processes were thereafter washed by dipping quickly into toluene solvent and then the films were dried at room temperature.

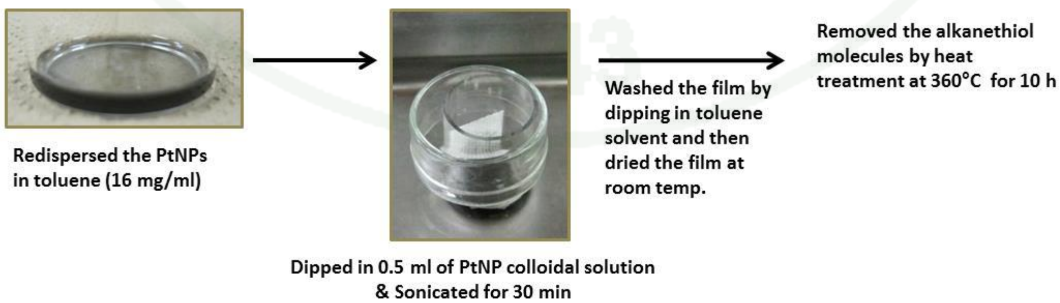

Figure 23 Summarized procedures of PtNPs loading into the pores of CNT-AAO film.

Prior to utilizing the alkanethiolated metal cluster as a catalyst, the exposure of the active surface by heat treatment to remove the surrounding ligand is a prerequisite. The decomposition temperature was selected based on the result of thermogravimetric analysis (TGA) of alkanethiolated PtNPs. The TGA spectra of octadecanethiol ($C_{18}H_{37}SH$) and octadecanethiolated PtNPs are shown in Figure 24. It determines that the stabilizer was completely decomposed at a temperature above 350°C. However, the temperature and time of the heat treatment should be carefully controlled because both parameters make strong impacts on size, crystallinity and stability of PtNPs. The literature report is also helpful to choose the appropriate condition. From (Liu *et al.*, 2004), they stated that the colloidal particles on carbon black followed by thermal treatment (in an inert gas at 360°C for 10h) to remove the alkanethiol layer did not bring about significant morphological changes and also enhanced crystallinity of Pt/C. Thus, in this experiment, the heat treatment on CNT-AAO/PtNPs film at 360°C for a period of time of 10 h was also chosen to observe the effect of thermal treatment on the size and shape of PtNPs deposited on the inner walls of CNT-AAO.

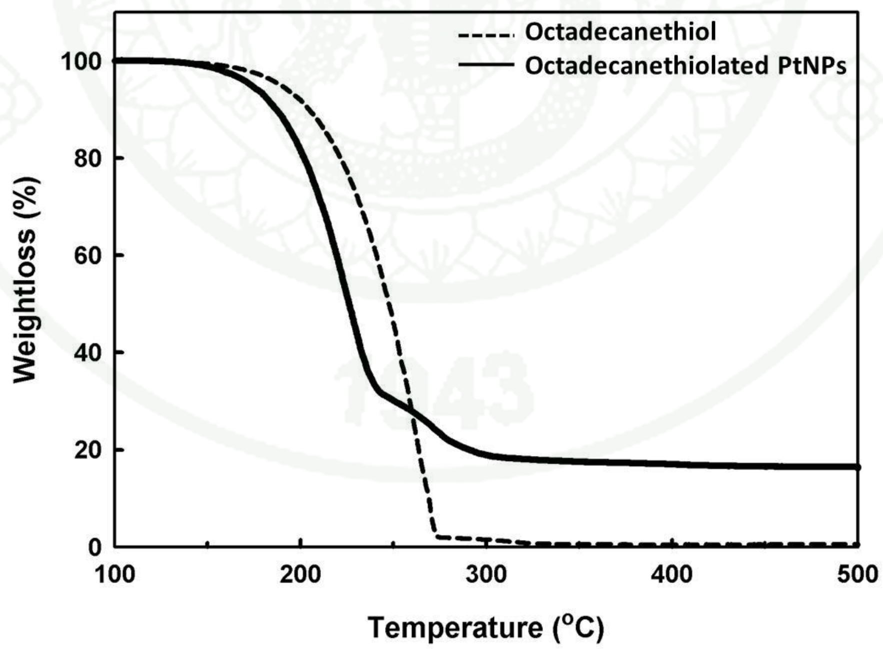

Figure 24 TGA spectra of octadecanethiol ($C_{18}H_{37}SH$) and octadecanethiolated PtNPs. The heating rate is 5°C/min and the carrier gas is N_2.

3.3.4 Optimization of the thickness of the Nafion layer coated on the inner walls of CNT-AAO film

The last layer for constructing the triple phase morphology is the proton conducting phase normally using Nafion. There were three techniques employed for constructing the Nafion layer inside the pores of CNT-AAO film.

The first method for building up the Nafion layer was simply soaking the CNT-AAO film into the 2 ml of 0.5 wt% Nafion solution diluted with 1-propanol for 30 min and then the film was dried under ambient condition (Figure 25).

Figure 25 Photo of the experimental set up for dipping the CNT-AAO film into the Nafion solution.

The second approach differs from the former one by dropping 30 μl of 0.5 wt% Nafion in 1-propanol onto the CNT-AAO film and drying the film under ambient condition. Finally, the dropping technique was still employed but with some modifications whereby much more diluted Nafion solution was dropped onto the CNT-AAO film under atmospheric humidity control. For the experimental procedure, the closed chamber containing the CNT-AAO film and the vessel of 5 ml of 1-proponal were incubated at 30 °C for 1 h (Figure 26). Thereafter, 10 μl of 0.05 wt% Nafion in 1-propanol was dropped on the CNT-AAO film and left to partially dry for about 15 min. The Nafion dropping was repeated until the total volume of used solution reached to 300 μl.

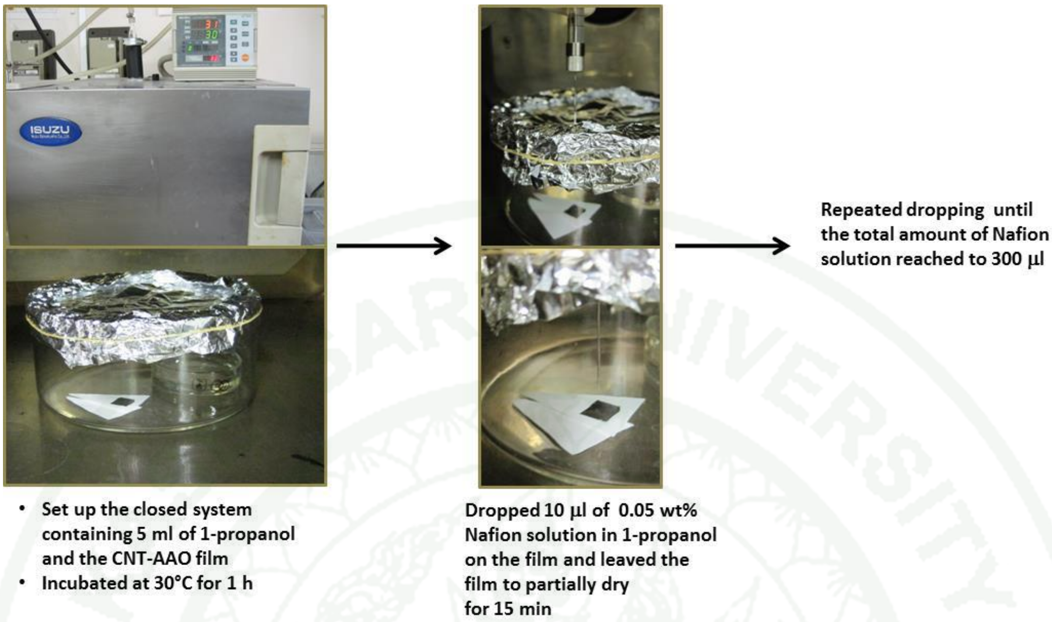

Figure 26 Summarized procedures of the introduction of Nafion solution into the pores of CNT-AAO film by the dropping method under the humidity control chamber.

3.3.5 Fabrication of the composite material of Nafion/PtNPs/CNT-AAO film and its assembly with a Nafion membrane (Membrane Electrode Assembly, MEA)

The three phase boundary was constructed on the inner walls of CNT-AAO film in which the PtNPs were firstly deposited and followed by the Nafion coating. The methods selected for both PtNPs deposition and Nafion coating will be shown and the reasons explained in the discussion part for choosing those.

For the last step, MEA was fabricated by hot-pressing the Nafion/PtNPs/CNT-AAO electrodes to the Nafion membrane as demonstrated in Figure 27. The Nafion membrane was swollen in 1-propanol and was expanded on a 5x5 cm^2 plastic plate. The synthesized Nafion/PtNPs/CNT-AAO film was then placed onto the prepared Nafion-plastic substrate and was covered with another bare plastic plate before taking the whole sandwich assembly to be processed with a hot hydraulic pressure of 300 kg/cm^2 at 140 °C for 10 min. The resulting Nafion/PtNPs/CNT-AAO film//Nafion membrane (MEA) was softy peeled off in water to avoid the film cracking.

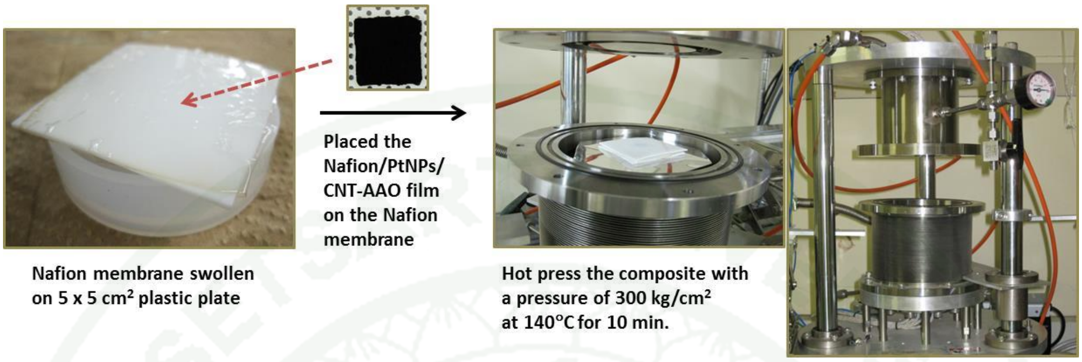

Figure 27 Summarized procedure of the hot pressingof the Nafion membrane to the Nafion/PtNPs/CNT-AAO film.

3.4 Method for fine-tuning the sizes of positively charged AuNPs by adjusting the amount of PVP and DMAP stabilizers and synthesizing the AuNPs/CNTs nanocomposite by the facile electrostatic deposition of the size-controlled AuNPs onto the AAO-templated CNTs.

3.4.1 Synthesis of Anodic aluminium oxide template (AAO)

Only three major steps were performed to prepare porous type AAO film with 35 nm in pore diameter and 20 μm in pore length comprising the electropolishing, the anodization and the pore widening processes as summarized in Figure 28.

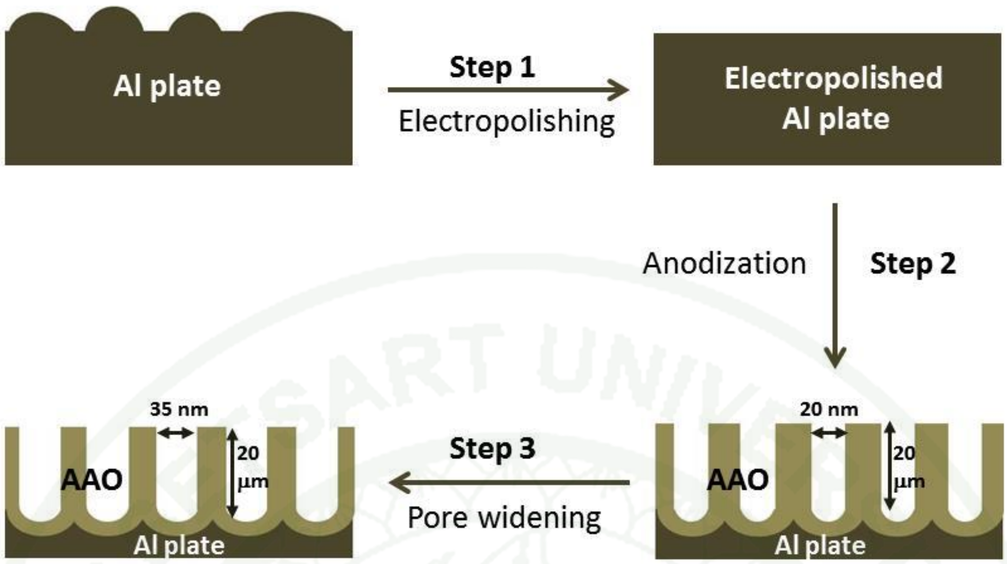

Figure 28 Schematic illustration of the synthesis of the AAO template with 35 nm pore diameter and 20 μm pore length deposited on the Al plate.

Every step of the electropolishing was totally the same as the one mentioned earlier in the Section 3.3.1. As for the anodization, the experimental setup was again based on that demonstrated in Section 3.3.1. However, the anodization was carried out with different conditions. The porous structure was firstly tuned to 20 nm in diameter and 20 μm in length by performing the anodic oxidization with a constant voltage of 20V for 1413 sec in 20 wt% H_2SO_4 at 5^{o}C. Due to this study mainly focusing on the decoration of AuNPs on the outer walls of CNTs, either open-ended or close-ended CNTs would provide the same performance of decoration. For ease of the CNTs preparation, the as prepared AAO film was thus not detached from the Al plate so as to skip some tasks of Al removal and to avoid working on the thin brittle AAO film. By means of that, the test-tube like CNTs were produced.

In the final step, the AAO/Al plate was chemically etched with 20 wt% H_2SO_4 for 1h at 25^{o}C in order to widen the AAO pore size from 20 nm to 35 nm because the CNTs with a diameter of 20 nm are probably not sizable for decorating some large AuNPs (~18 nm) which was synthesized solely with DMAP. Meanwhile, the AAO derived CNTs of more than 35 nm in size could also not be highly-dispersed in water.

3.4.2 Synthesis of CNTs by using the prepared AAO film on the Al plate as template

The CVD technique on the AAO/Al plate was also employed to produce CNTs used in this experiment. The CVD conditions were still the same as those described in Section 3.3.2. There were two sequential steps involved after the CVD synthesis in order to get the isolate dispersed CNTs that are depicted in Figure 26 and described below.

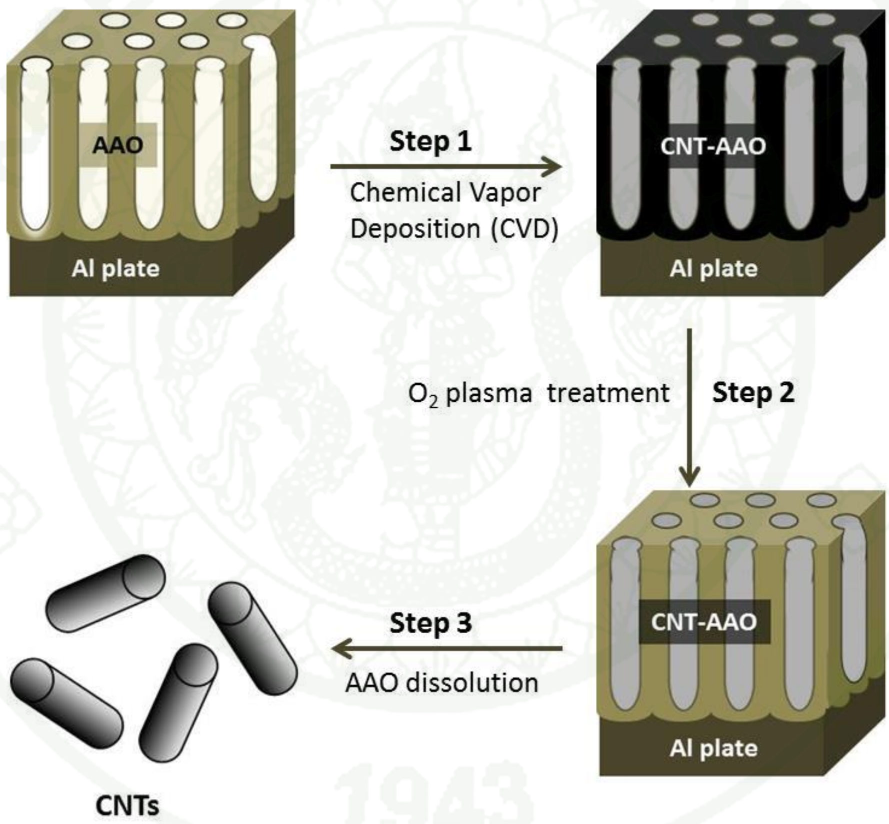

Figure 29 Schematic illustration of the CNT synthesis by the template method.

The pyrolytic carbon deposition took place not only on the inner wall of the AAO nanochannels but also on the external surface of the AAO film. The latter caused the connecting CNT to form into a bundle and subsequently resulted in poor dispersion in the aqueous solution. To remove only the carbon layer deposited on the outer surface of the AAO film (step 2 in Figure 29), the CNTs/AAO/Al plate was exposed to oxygen plasma conducted by using a plasma reactor at 100 watts power under an O_2 flow of 30 cm^3/min for 50 sec (Figure 30).

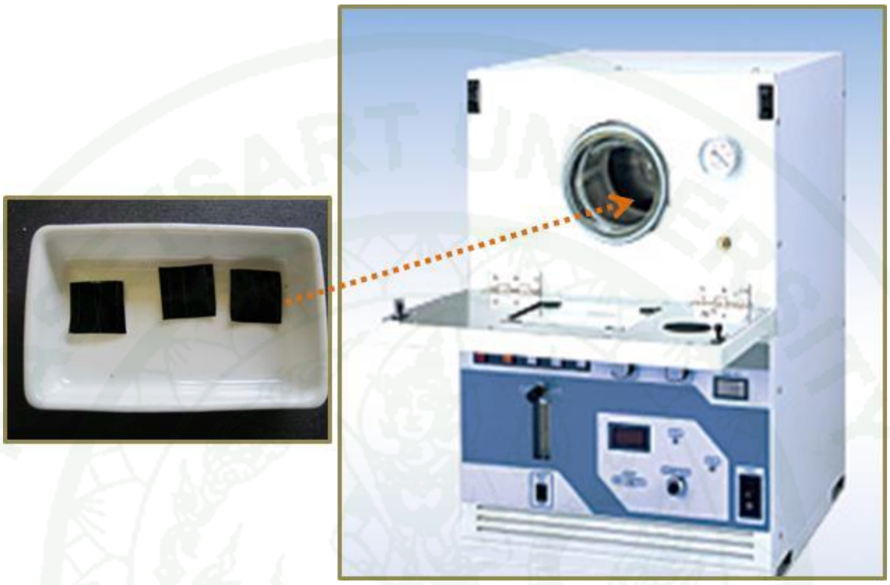

Figure 30 Photo of CNT-AAO-Al plates which will be treated in the oxygen plasma reactor.

The CNTs were liberated by immersing the O_2 plasma treated CNTs/AAO/Al plate in 3 M NaOH aqueous solution to dissolve the AAO film (step 3 in Figure 29 and Figure 31). After whole tubes detached from the substrate (Figure 31b), the Al substrate was taken out of the solution to prevent the ongoing reaction between Al and NaOH (Figure 31c). The dispersed CNTs were washed to remove the Al ions that were also produced during the template etching. The cleaning process comprised of centrifugation, decantation, and rewashing with 0.1 M NaOH aqueous solution with several cycles. To neutralize the alkaline suspension, the CNTs were salted out with 1.8 wt % NaCl solution in a similar manner of washing. Finally, the Al ion-free CNTs were filtered by using a membrane filter, washed with deionized water and dried overnight at 60°C under a vacuum system (Figure 31d). The stock suspension of CNTs was prepared for the next metal deposition process by adding 1 mg of dried

CNTs into 50 ml of deionized water and then sonication until well dispersed (Figure 31e).

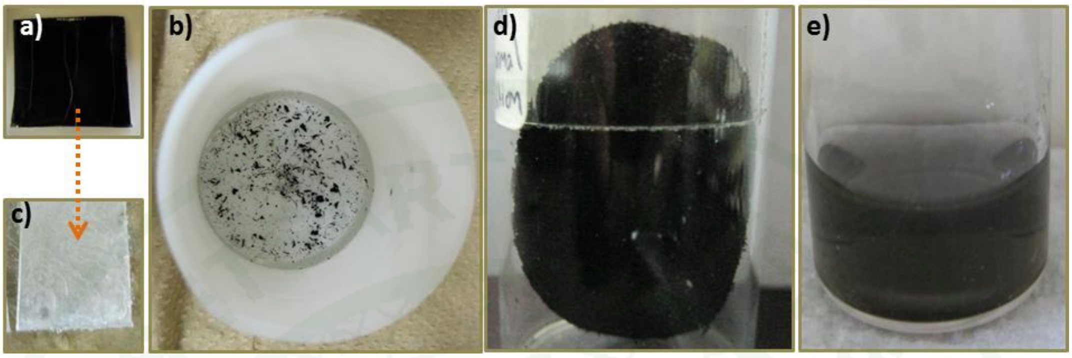

Figure 31 Photos of CNT-AAO-Al plate (a), liberated CNTs from AAO-Al plate (b) and Al plate (c) after AAO dissolution, dried CNTs (d) and CNTs dispersion (e).

3.4.3 Synthesis of AuNPs

The synthesis of the positively charged AuNPs was based on the method of Tsunoyama *et al.* (Tsunoyama *et al.*, 2006, 2007) as depicted in (Figure 32). An aqueous solution of $HAuCl_4$ (1 mM, 50 ml) was mixed with two different stabilizers i.e., PVP (K-10, 10 kDa) and DMAP. Twenty mole ratios of PVP:DMAP were investigated as listed in Table 1. At the beginning of the AuNPs preparations, 5 mmol each of PVP and DMAP (entry 10 in Table 1) was used and the trial mole ratios of PVP:DMAP were then varied in two ways by decreasing amounts of PVP or DMAP. From the entries 1 to 9, half the amount of DMAP was decreased twofold from that of entry 10 (PVP:DMAP=1) until the PVP:DMAP mole ratio reached to 512:1 while the amount of PVP was kept constant. On the other hand, all samples of entries 11 to 19 were prepared in the same manner but by varying the amounts of PVP instead. Moreover, AuNPs without PVP (entries 20) was also prepared for referencing the pre-controlled size of AuNPs. Then, the mixture of gold salt precursor and stabilizers was stirred for 30 min in an ice bath. Thereafter, an aqueous solution of $NaBH_4$ (0.1 M, 5 ml) was quickly added into the metal salt-stabilizer solution under vigorous stirring and further stirred for 1 h. For the washing process, the obtained suspension was centrifuged with centrifugal filter unit (MWCO 10000) to remove the ion impurities such as Na^+ and Cl^- ions and also the some of the excess PVP and DMAP. Finally, the concentrated washed product was diluted to 20 ml with deionized water and kept as stock AuNPs solution.

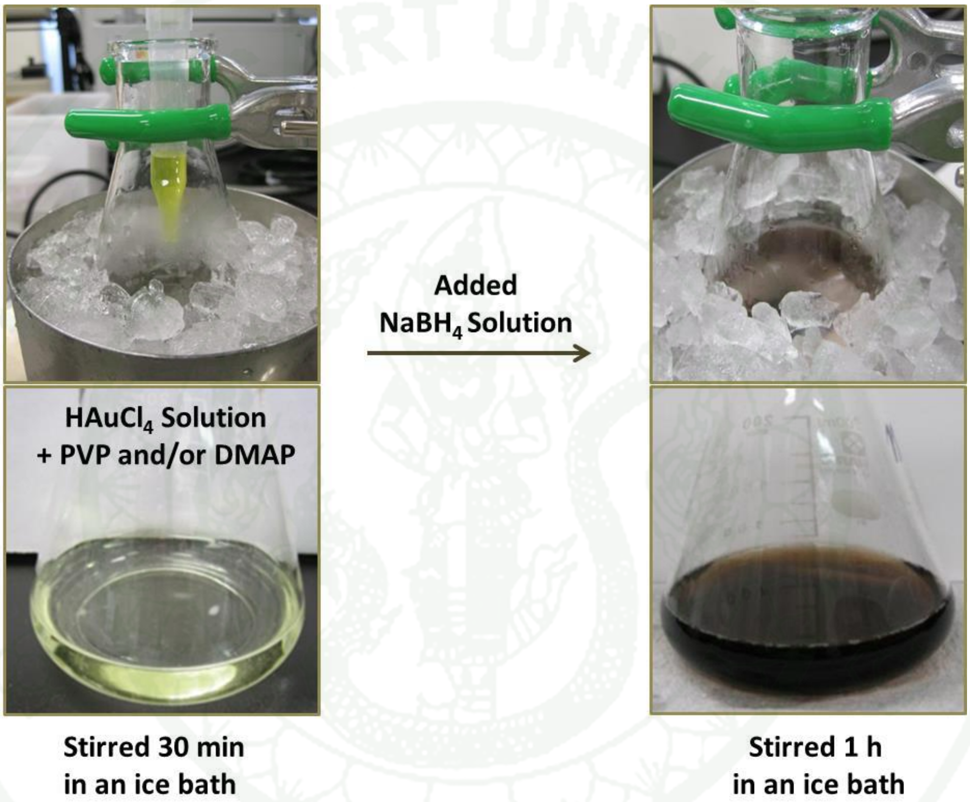

Figure 32 Summarized procedures of the water-based synthesis of AuNPs stabilized with PVP and/or DMAP stabilizers.

3.4.4 Deposition of AuNPs on CNTs

In the first step, 2 ml of the colloidal AuNPs stock solution was added into 2 ml of prepared CNTs suspension under vigorous stirring for 30 min. After common mixing, the inherent negatively charged CNTs were self-assembled with the positively charged AuNPs. The resultant of AuNPs/CNTs was obtained by centrifugation and washed with water several times. Finally, the wet sediment was resuspended in 2 ml of deionized water for characterizations. All samples of AuNPs/CNTs were prepared with the same procedure.

Table 1 The amounts of PVP and DMAP used in each sample of positively charged AuNPs and also the corresponding calculated mole ratios.

Entry	Sample	Amount of stabilizer (g)		Mole ratio of
		PVP	**DMAP**	**PVP[a]:DMAP[b]**
1	Au-(P512:D1)	0.555	0.001	512:1
2	Au-(P256:D1)	0.555	0.002	256:1
3	Au-(P128:D1)	0.555	0.005	128:1
4	Au-(P64:D1)	0.555	0.010	64:1
5	Au-(P32:D1)	0.555	0.019	32:1
6	Au-(P16:D1)	0.555	0.038	16:1
7	Au-(P8:D1)	0.555	0.076	8:1
8	Au-(P4:D1)	0.555	0.153	4:1
9	Au-(P2:D1)	0.555	0.306	2:1
10	Au-(P1:D1)	0.555	0.611	1:1
11	Au-(P1:D2)	0.278	0.611	1:2
12	Au-(P1:D4)	0.139	0.611	1:4
13	Au-(P1:D8)	0.069	0.611	1:8
14	Au-(P1:D16)	0.035	0.611	1:16
15	Au-(P1:D32)	0.017	0.611	1:32
16	Au-(P1:D64)	0.009	0.611	1:64
17	Au-(P1:D128)	0.004	0.611	1:128
18	Au-(P1:D256)	0.002	0.611	1:256
19	Au-(P1:D512)	0.001	0.611	1:512
20	Au-(D)	0.000	0.611	-

[a] molecular weight of PVP is 111.1 g/mol per monomer

[b] molecular weight of DMAP is 122.17 g/mol

RESULTS AND DISCUSSION

1. The evaluation of sensing properties of Pt-doped SWCNTs ($SWCNT_{Vac}$/Pt) with pristine SWCNTs (SWCNTs), vacancy defected SWCNTs ($SWCNT_{Vac}$) and Pt-deposited SWCNT (SWCNT/Pt) for NO_2 and NH_3 detections.

1.1 Energetics and optimized geometries

The optimized geometries of pristine, defective, Pt-doped and Pt-deposited SWCNTs serving as the sensing platforms are firstly considered (Figure 33).

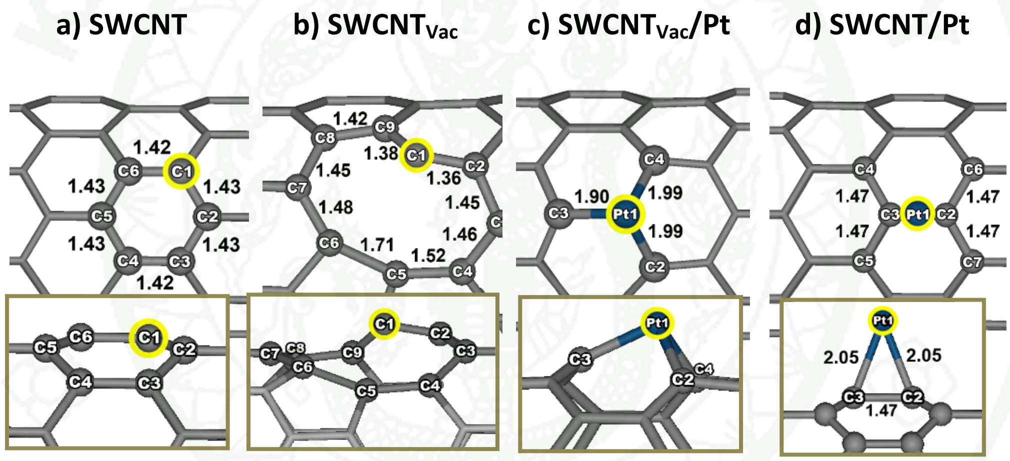

Figure 33 Optimized geometries of pristine SWCNT (a), vacancy SWCNT (b), Pt-doped SWCNT (c) and Pt-deposited SWCNT (d). Side views are shown under corresponding pictures. The yellow marks indicate the active site studied for the SWCNTs (a–d). Atom–atom distances (Å) around the active centers are also depicted.

Figure 33a shows the common SWCNT with a typical C–C bond length of about 1.42 Å and a nanotube diameter of 6.38 Å closely matching that of previous studies (Gülseren *et al.*, 2002). In Figure 33b, the single vacancy defected SWCNT is shown. It results from the 12-membered ring created by removing one carbon atom from the graphene sheet and the subsequent reconstruction to a 5-membered ring and a 9-

membered ring. It holds one unsaturated carbon (C1), slightly sticking out from the tube surface. The rearrangement deforms the structure to obtain an elliptical cross section with major and minor diameters of 6.56 Å and 6.17 Å, respectively. Doping of the large Pt atom to the vacancy (Figure 33c) causes a deformation of the nearby hexagonal rings in the doping region. The Pt–C distance is 1.9 Å and Pt protrudes outside of the SWCNT surface. Even though in this structure the SWCNT is apparently distorted (elliptic diameters: 6.49 Å and 6.28 Å), the Pt atom is bound with 163.62 kcal/mol (Table 2). This value is similar to the one reported by Kim *et al.* (Kim *et al.*, 2007). This stabilization can be ascribed to the saturation of the dangling C bonds and the formation of stable hexagonal rings. Consequently, the binding energy in Pt-deposited SWCNT is smaller (53.39 kcal/mol). Figure 33d shows the energetically most favorable conformation with Pt residing above the C2–C3 bond (Chen and Kawazoe, 2006; Durgun *et al.*, 2003) with a Pt–C distance of 2.05 Å. The geometry of the tube is changed due to strong Pt–CNT interaction causing nonidentical diameters with 6.48 Å and 6.29 Å of the longest and the shortest ones, respectively. In a long-lived sensor, the attachment of Pt to the SWCNT must be stable enough to withstand temperature and environmental effects. Although this is difficult to quantify, also the Pt-deposited SWCNT should still be a stable enough device.

1.1.1 NO_2 Adsorptions

All SWCNT:NO_2 configurations obtained after optimizing the structures shown in Figure 12 are given in Figure 34. From these results, the most stable optimized geometries, their geometrical parameters and the binding energies of NO_2 adsorption on each support are summarized as well in Figure 35 and Table 2. Nevertheless, there are some experimental and computational studies revealing that the nitro derivative on fullerenes can be found (Chiang*et al.*, 1996; Slanina *et al.*, 1999). Though due to the chemically inert CNT system, the functionalization of NO_2 on the CNT sidewall should be more difficult than that of a fullerene surface.

Table 2 Binding energies E_b between Pt and SWCNT and SWCNTVac and binding energies of NO_2 and NH_3 to the four types of SWCNTs. The structures are shown in Figures 35 and 37, respectively. The energies are given in kcal/mol.

Sensing Support	***E*_b(SWCNT/Pt)**	
$SWCNT_{Vac}/Pt$	163.62	
SWCNT/Pt	53.39	
	E_b(Support:NO_2)	**E_b(Support:NH_3)**
SWCNT	1.96	1.33
$SWCNT_{Vac}$	55.90	2.76
$SWCNT_{Vac}/Pt$	50.91	30.52
SWCNT/Pt	34.92	40.96

One can see that the NO_2 molecule is merely physisorbed on the pristine SWCNT with the lowest absorption energy (1.96 kcal/mol) and a distance of 3.11 Å between N and C. The monomer geometries of the SWCNT and the NO_2 molecules are undisturbed. In $SWCNT_{Vac}$, the unsaturated carbon atom (C1) binds to the nitrogen atom of NO_2 ($r_{C–N}$ = 1.46 Å) with an interaction energy of 55.90 kcal/mol. The binding can be attributed to the undercoordinated carbon atoms near the vacancy. C1 is the most negatively charged carbon and attracts the partially positively charged N atom of NO_2. Excess electrons are located in the antibonding orbitals of the NO_2 molecule causing a change of the N–O distance from 1.21 Å to 1.24 Å, The stability of the $SWCNT_{Vac}/Pt:NO_2$ complex (50.91 kcal/mol) is similar to that of $SWCNT_{Vac}$. Pt bonds to both oxygens of NO_2 causing an elongation of the N–O bond to 1.28 Å. The interaction between NO_2 and the Pt atom in SWCNT/Pt:NO_2 is similar to the one described above. In the SWCNT/Pt:NO_2 model, the SWCNT–Pt distances increased from 2.05 Å to 2.11 Å after NO_2 binding, indicating that the strong binding of NO_2 (34.92 kcal/mol) comes at the expense of a destabilization of the Pt–SWCNT stability.

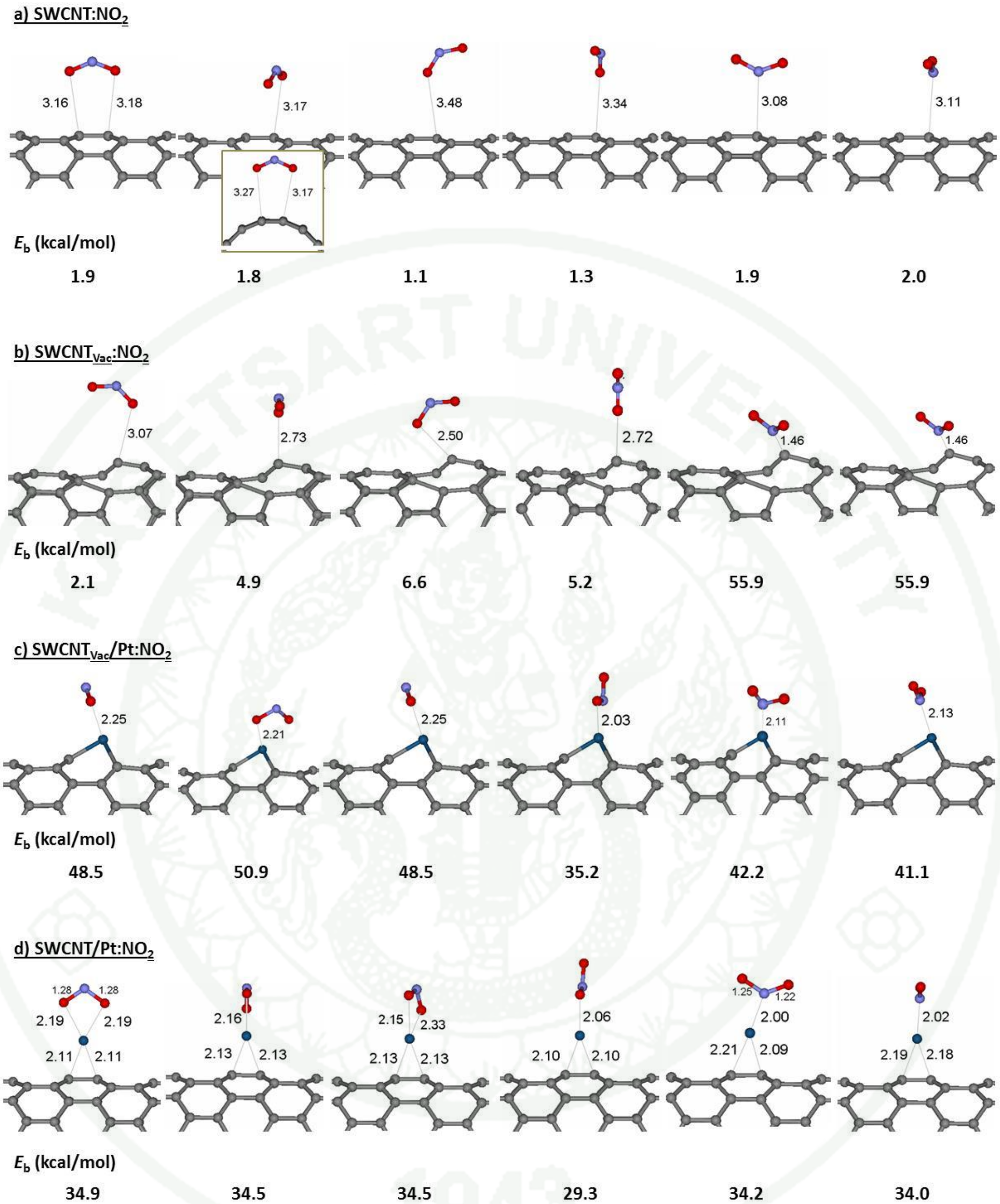

Figure 34 All optimized geometries (Å) and binding energies (kcal/mol) obtained after optimizing the structures of SWCNT:NO_2 (a), $SWCNT_{Vac}$:NO_2 (b), $SWCNT_{Vac}$/Pt:NO_2 (c) and SWCNT/Pt:NO_2 (d) complexes.

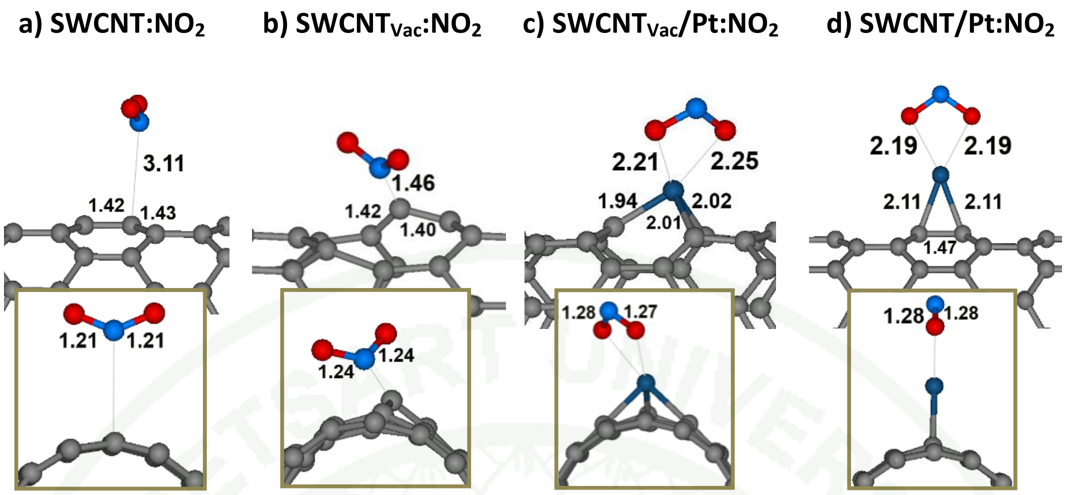

Figure 35 Front and side views of the most favorable binding geometries of NO_2 on each support type accompanied with their binding distances. Pt-C and some C-C distances (Å) are also given.

1.1.2 NH_3 Adsorptions

All SWCNT:NH_3 adsorption complexes obtained after optimizing the structures shown in Figure 12 are given in Figure 36. The most stable optimized geometries of NH_3 adsorbed on each support are depicted in Figure 37, together with the relevant distances. Their binding energies are tabulated in Table 2.

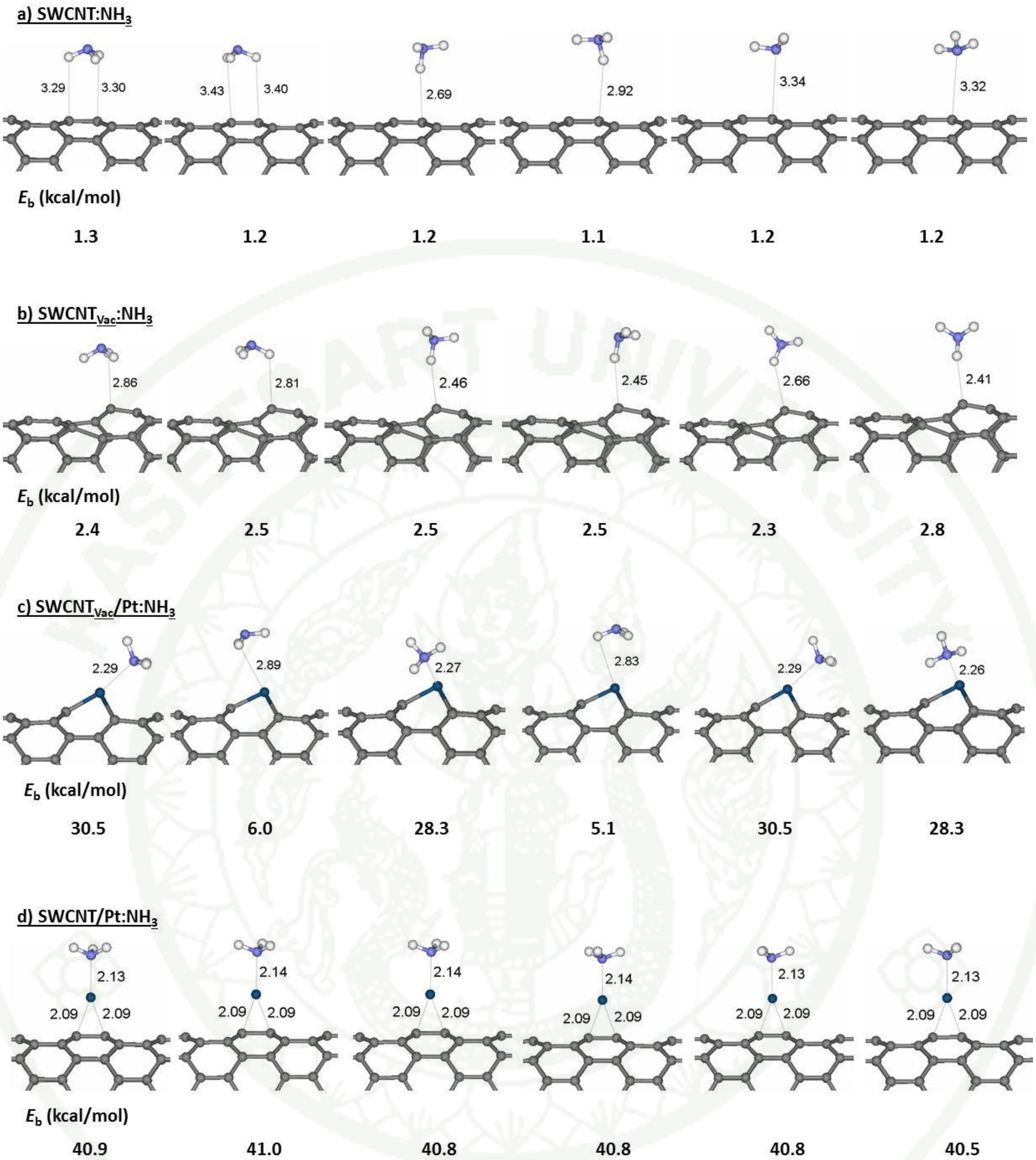

Figure 36 All optimized geometries (Å) and binding energies (kcal/mol) obtained after optimizing the structures of $SWCNT:NH_3$ (a), $SWCNT_{Vac}:NH_3$ (b), $SWCNT_{Vac}/Pt:NH_3$ (c) and $SWCNT/Pt:NH_3$ (d) complexes.

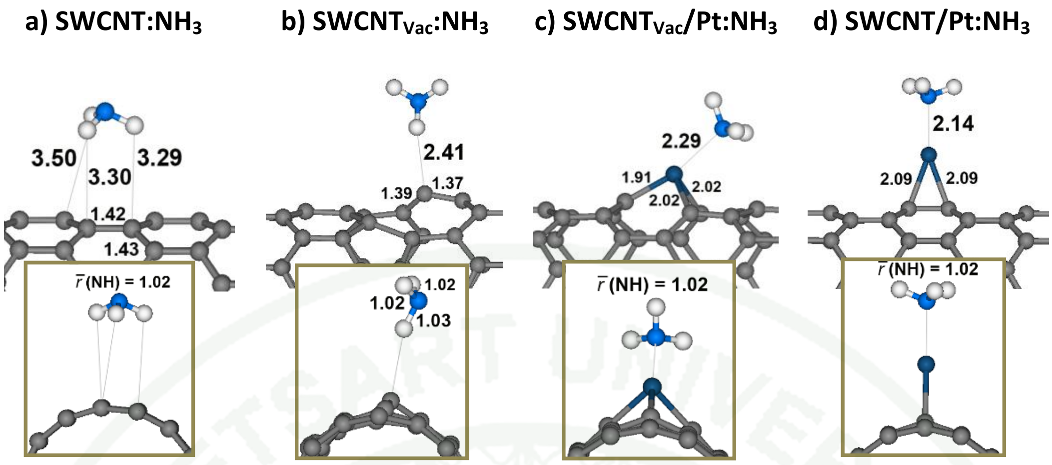

Figure 37 Front and side views of the most favorable binding geometries of NH_3 on each support type accompanied with their binding distances. Pt-C and some C-C distances (Å) are also given.

In agreement with previous studies (Bai and Zhou, 2007; Lu *et al.*, 2005) () in the preferred orientation, the hydrogen atoms of NH_3 point towards the SWCNT (Figure 37a). NH_3 is noncovalently bound with only 1.33 kcal/mol and a C–H distance of about 3.3 Å. In contrast to NO_2, the interaction in $SWCNT_{Vac}$:NH_3 is only slightly stronger (2.76 kcal/mol) because in both cases a hydrogen bonded interaction is the only possibility. Here, the more negatively charged C1 acts as the electron donor and a C···H–N hydrogen bond can be formed (Figure 37b). These weak interactions mean that materials consisting of both SWCNT and $SWCNT_{Vac}$ are inappropriate sensing platforms for NH_3 detection. In $SWCNT_{Vac}$/Pt:NH_3 and SWCNT/Pt:NH_3, NH_3 is strongly bound. In $SWCNT_{Vac}$/Pt:NH_3 and SWCNT/Pt:NH_3, ammonia is bound by 30.52 and 40.96 kcal/mol. The Pt–N distances are 2.29 and 2.14 Å, respectively. The strong binding of NH_3 to Pt via its nitrogen atom has a larger influence on the active region than the one caused by its weak H-bonded interaction with $SWCNT_{Vac}$, as can be seen from the redistribution of electron density (Figure 38). As expected, the SWCNT–Pt distances increase somewhat from 2.05 Å to 2.09 Å after the NH_3 complexation. The N–H distances of all adsorbed NH_3 molecules are unaffected by the complexation and stay at 1.02 Å. The affinity of SWCNT/Pt to NH_3

already approaches the binding energy of the attached Pt to the SWCNT, which is a disadvantage since it might in practice lead to its destruction.

1.2 Electronic properties of the platform and sensitivity to NO_2 and NH_3

The effects of gas adsorption on the electronic properties of the SWCNTs were investigated by computing the charge transfers (q_{Gas}) between the gas molecule and support and the HOMO–LUMO energy gap modulations (ΔEg). The results are summarized in Table 3. In addition, electron density difference maps HOMO and LUMO orbitals and electronic densities of states (DOSs) have been derived. They are depicted in Figures 38 - 42.

1.2.1 NO_2 Detection

Since NO_2 is an electron-withdrawing molecule with an unusually large electron affinity between two and three eV, electrons are transferred from supports to it (Table 3). For $SWCNT_{Vac}$:NO_2, $SWCNT_{Vac}$/Pt:NO_2 and SWCNT/Pt:NO_2 these shifts amount to -0.27, -0.38 and -0.35 *e*, respectively. The values for SWCNT/Pt:NO_2 and $SWCNT_{Vac}$/Pt:NO_2 are similar, but a more detailed analysis shows some differences. The positive value of Δq_{SWCNT} in $SWCNT_{Vac}$/Pt:NO_2 (0.32 *e*) is larger than the one in SWCNT/Pt:NO_2 (0.22 *e*). Three-dimensional plots of the differential electron density can give detailed information of the rearrangement of the complex formation. Figure 38 shows isosurfaces of certain density changes.

Table 3 Partial molecular and atomic charges $q(e)$ and values of the HOMO-LUMO gap E_g(eV) of all studied complexes. Partial charge transfers and energy gap changes are indicated by the prefix delta (Δ). Refer to text for the definitions of the quantities.

System	$\boldsymbol{E_g}$	$\boldsymbol{q_{SWCNT}}$	$\boldsymbol{q_{Pt}}$	$\boldsymbol{q_{Gas}}$	[a]$\boldsymbol{\Delta E_g}$	[b]$\boldsymbol{\Delta q_{SWCNT}}$	[c]$\boldsymbol{\Delta q_{Pt}}$
SWCNT	0.63	0.00					
$SWCNT_{Vac}$	0.26	0.00					
$SWCNT_{Vac}$/Pt	0.39	0.12	-0.12				
SWCNT/Pt	0.58	0.05	-0.05				
SWCNT:NO_2	0.31	0.05		-0.05	-0.32	0.05	
$SWCNT_{Vac}$:NO_2	0.12	0.27		-0.27	-0.14	0.27	
$SWCNT_{Vac}$/Pt:NO_2	0.14	0.44	-0.06	-0.38	-0.25	0.32	0.06
SWCNT/Pt:NO_2	0.17	0.27	0.08	-0.35	-0.41	0.22	0.13
SWCNT:NH_3	0.63	-0.01		0.01	0.00	-0.01	
$SWCNT_{Vac}$:NH_3	0.28	0.01		-0.01	0.02	0.01	
$SWCNT_{Vac}$/Pt:NH_3	0.29	-0.09	-0.18	0.27	-0.10	-0.21	-0.06
SWCNT/Pt:NH_3	0.62	-0.06	-0.22	0.28	0.04	-0.11	-0.17

[a]ΔE_g = E_g(support:gas) - E_g(bare support)

[b]Δq_{SWCNT} = q_{SWCNT}(support:gas) - q_{SWCNT}(bare support)

[c]Δq_{Pt} = q_{Pt}(support:gas) - q_{Pt}(bare support)

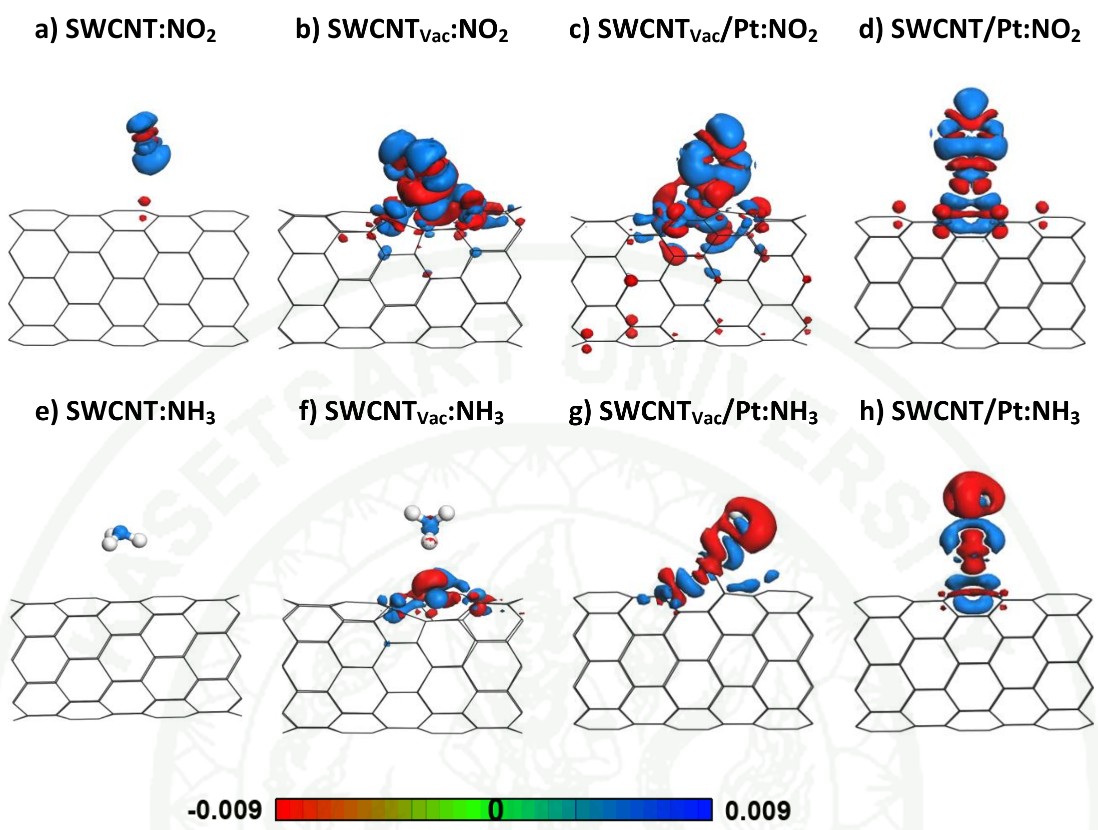

Figure 38 Plots of the differential electron densities of all studied support-gas complexes. The 3D - surfaces are plotted at isovalues of ±0.009 *e*/Å^3. A red color denotes loss of density whereas blue denotes gain of electron density.

It can be seen that NO_2 adsorption (Figures 38a-d) on $SWCNT_{Vac}$/Pt causes a depletion of electron density (Figure 38c) throughout, which is expected to change the electric properties of the nanotube dramatically. In contrast, electron relocation in SWCNT/Pt:NO_2 occurs only locally at the Pt-NO_2 moiety. The change of the energy gap (ΔE_g) during the adsorption process is also related to the sensitivity of a sensor for particular analyte. In Table 3, a negative sign of ΔE_g refers to a reduction of the energy gap in the complex compared to the bare support. It was found that the energy gaps of all systems decrease after NO_2 adsorption by -0.32, -0.14, -0.25 and -0.41 eV for SWCNT:NO_2, $SWCNT_{Vac}$:NO_2, $SWCNT_{Vac}$/Pt:NO_2 and SWCNT/Pt:NO_2, respectively. This agrees well with experimental reports that the conductivity of

CNTs, defected-CNTs and Pt doped-CNTs increase when exposed to NO_2 (Kong *et al.*, 2000; Penza *et al.*, 2007; Santucci *et al.*, 2003). Electron density transfer to NO_2 generates holes in the support. The enhanced conductivities are directly related to the abundance of hole carriers, so these pristine and modified SWCNTs behave as p-type semiconductors as well and are also susceptible to become metallic after stimulated by NO_2, especially in the $SWCNT_{Vac}:NO_2$, $SWCNT_{Vac}/Pt:NO_2$ and $SWCNT/Pt:NO_2$ systems. One can further see that the ΔE_g values are proportional to the amount of charge transfer, except for ΔE_g of SWCNT where NO_2 is very weakly bound. To clarify this further, the DOSs and PDOSs are analyzed (Figure 39).

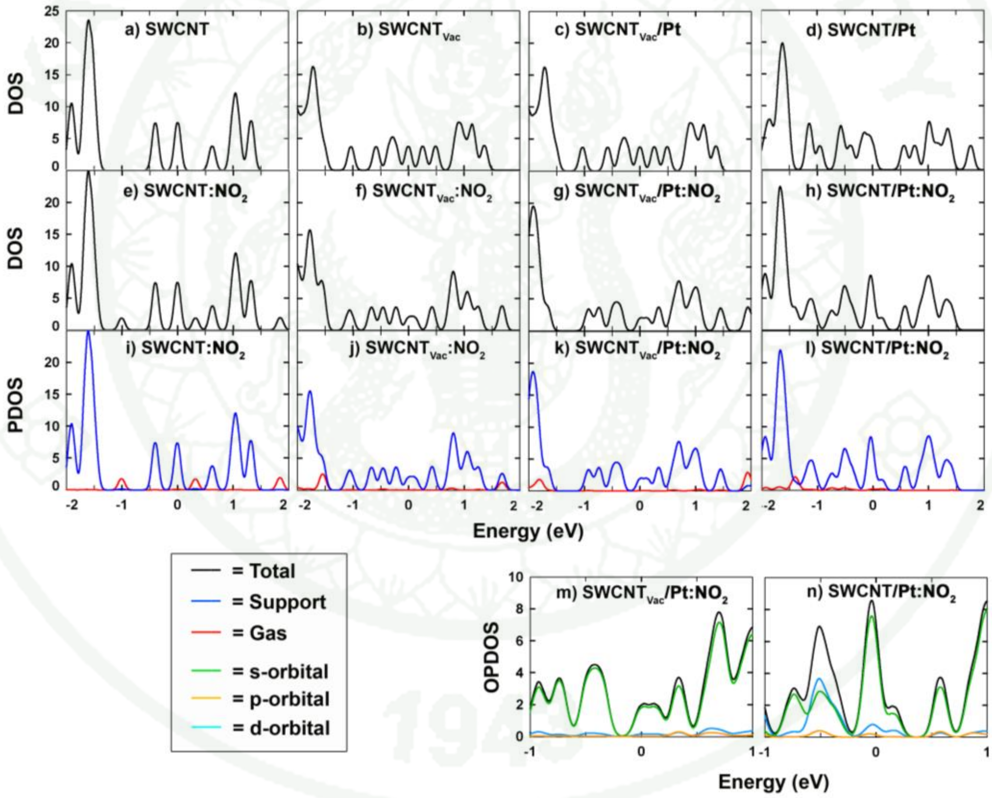

Figure 39 Density of states (DOSs) for the studied supports (a-d) and their NO_2 complexes (e-h). Partial density of states (PDOSs) of all support-gas complexes (i-l) and orbital partial density of states (OPDOSs) of $SWCNT_{Vac}/Pt:NO_2$ and $SWCNT/Pt:NO_2$ (m and n) are also plotted for comparison. The Fermi levels (defined as the HOMO energies) are calibrated to locate at zero eV.

Comparing the DOS diagrams of SWCNT:NO_2 and SWCNT (Figures 39e and 39a, respectively), one sees the appearance of an acceptor state in the middle of the HOMO-LUMO gap of the SWCNT, when NO_2 is bound (Zhang *et al.*, 2006). When this state receives electrons from the valence band of the SWCNT the resistance of the system should decrease. Since this state is contributed from the NO_2 radical, as is indicated by the PDOSs and LUMO scheme of SWCNT:NO_2 (Figures 39i and 39e, respectively), it is plausible that the measured energy gaps vary with the number of NO_2 molecules. SWCNT/Pt exhibits the highest change ΔE_g of its energy gap when NO_2 is bound to it (Table 3). However, that does not much affect the electronic structure of the SWCNT, as can be seen by the charge and electron density differences in Table 3 (Δq_{SWCNT} = 0.22 e) and Figure 38d, respectively. Moreover, the HOMO and LUMO orbitals (Figures 37d and 37h, respectively), to which ΔE_g is related, have prominent contributions only in the area close to Pt and NO_2 and mostly involve the d-orbitals of Pt. Also the partial density of states distribution (Figure 39n) shows the density near the Fermi level in SWCNT/Pt:NO_2 originating from these d-orbitals. The HOMO and LUMO of $SWCNT_{Vac}$/Pt:NO_2, (Figures 40c and 40g, respectively) contain AO contributions from Pt and from the p-orbitals of the NO_2 oxygen atoms as well as from the nanotube mixed into the molecular orbitals of the whole system, whereas in SWCN/Pt:NO_2, solely the first two and not the nanotube contribute to the frontier orbitals. Accordingly, despite the larger value of ΔE_g, in SWCNT/Pt:NO_2, its localized response to NO_2 binding makes it less suitable as a sensor.

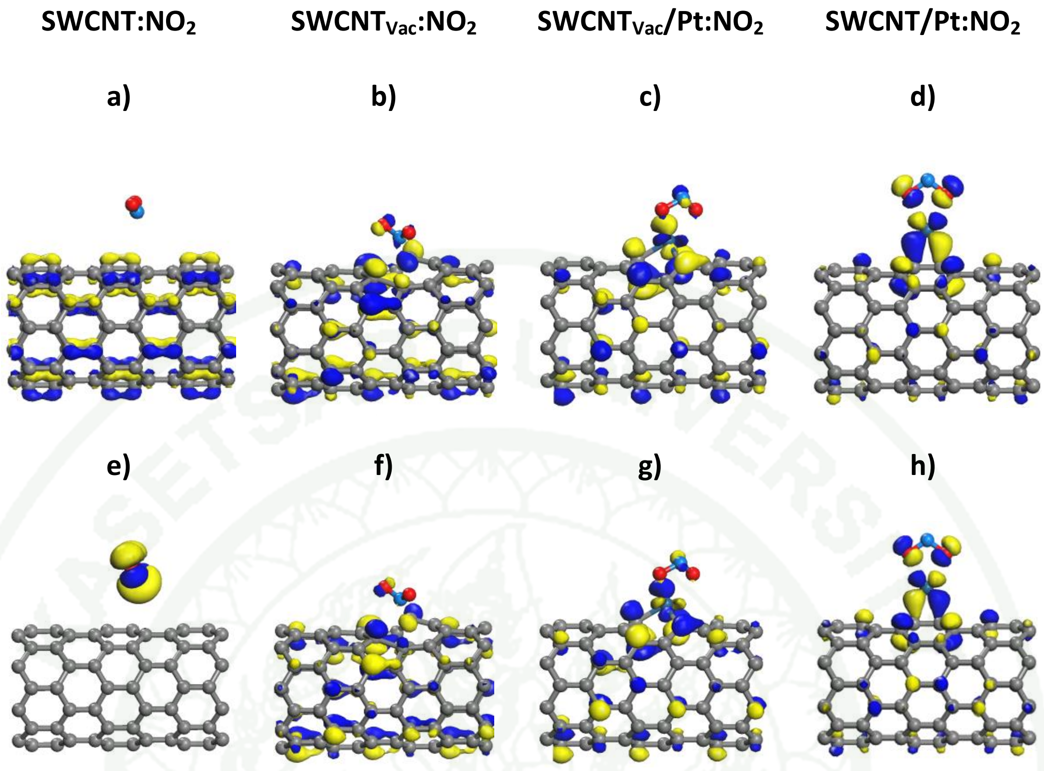

Figure 40 Frontier molecular orbitals of the complexes with NO_2: HOMOs (a-d) and LUMOs (e-h).

1.2.2 NH_3 Detection

In this section the sensitivity of the three supports to NH_3 detecting is discussed. The lone pair electrons at the N atom of NH_3 can readily be donated to the molecule interacting with it. Consequently, the charge of adsorbed NH_3 is positive by 0.01, 0.27 and 0.28 *e* in SWCNT:NH_3, $SWCNT_{Vac}$/Pt:NH_3 and SWCNT/Pt:NH_3, respectively, except for $SWCNT_{Vac}$:NH_3 (-0.01 *e*) where C$\cdots$H-N resembles a hydrogen bond and H-N behaves as the electron acceptor. The complexes with weak adsorption via the H atom, i.e., SWCNT:NH_3 and $SWCNT_{Vac}$:NH_3, also exhibit insignificant charge transfers of only 0.01 and -0.01 *e*, respectively. Together with the unnoticeable electron density difference, the energy gap is also unchanged. This is associated with the bare SWCNT character of the PDOSs near the Fermi level (Figures 41i and 41j) and is also visible in the HOMO-LUMO pictures of both complexes (Figures 42a, 42b, 42e and 42f). This infers that SWCNT and $SWCNT_{Vac}$ have very low sensibility to NH_3 gas.

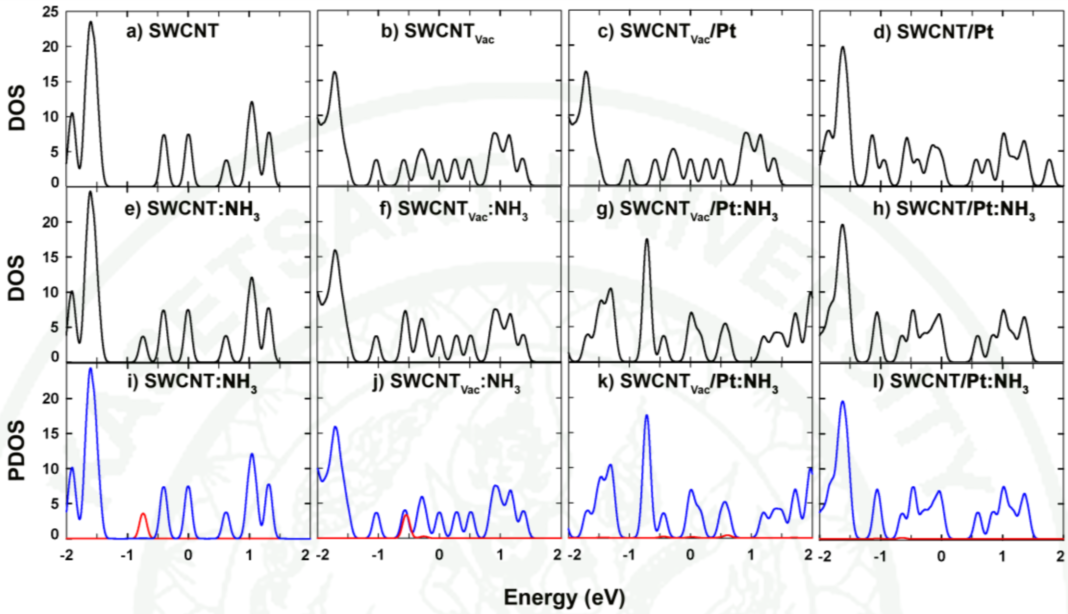

Figure 41 Density of states (DOS) for all studied supports (a-d) and their NH_3 complexes (e-h). Partial density of states (PDOS) of all support-gas complexes (i-l) are also plotted for comparison (blue lines: support; red lines: contributions from NH_3). The Fermi levels (defined as HOMO energies) are calibrated to locate at zero eV.

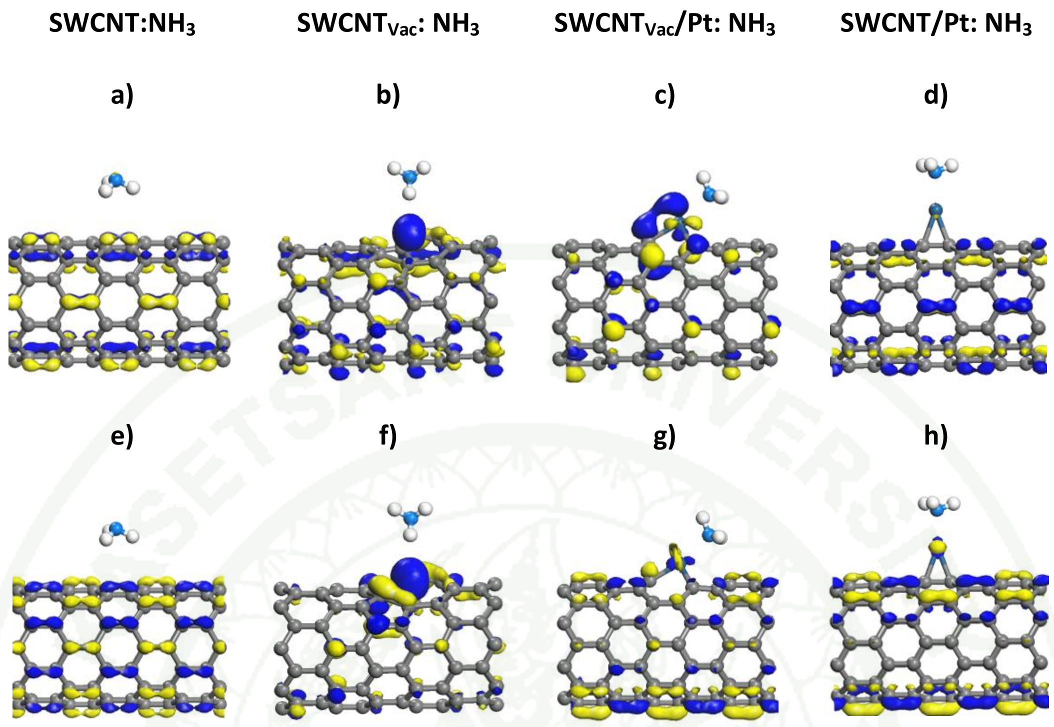

Figure 42 Frontier molecular orbitals of all studied support-NH_3 complexes, HOMOs (a-d) and LUMOs (e-h).

Extraordinarily large charge transfers are found in $SWCNT_{Vac}$/Pt:NH_3 and SWCNT/Pt:NH_3 with values of 0.27 and 0.28 *e*, respectively. Amounts and directions of NH_3 charge transfer of both complexes are quite similar and also their electron density difference maps are similar as shown in Figures 38g and 38h, respectively. The better efficiency is derived from the existence of the Pt active site and N-contacted mode which enhance the outflow of nitrogen lone pair electron density.

Generally, giving up electrons from NH_3 to a p-type semiconductor support reduces the hole carrier density and thus decreases the conductivity of the system, correlated with the widening of its HOMO-LUMO gap (Kong *et al.*, 2000). Even though the flow of NH_3 electrons into $SWCNT_{Vac}$/Pt:NH_3 and SWCNT/Pt:NH_3 have the same direction, which indicates that they become less conductive, the signs of their ΔE_g values which represent how the conductivity changes are opposite. The energy gap of SWCNT/Pt:NH_3 is slightly widened (0.04 eV) whereas that of the

$SWCNT_{Vac}/Pt:NH_3$ is significantly narrowed (-0.10 eV). These phenomena should principally interrelate to the electron redistribution in the support, especially of the SWCNT since the PDOSs near the Fermi level (Figures 41k and 41l) and HOMO-LUMO features of both complexes (Figures 42c, 42d, 42g and 42h) are merely contributed from it. Both Δq_{SWCNT} values of $SWCNT_{Vac}/Pt:NH_3$ and $SWCNT/Pt:NH_3$ are negative (-0.21 *e* and -0.11 *e*, respectively) due to the accumulation of electrons in the SWCNTs. Remarkably, the $SWCNT_{Vac}/Pt:NH_3$ tube can receive twice the electron density than $SWCNT/Pt:NH_3$ does. This can change its electrical characteristic from p-type to n-type, which explains the observed increase in the conductivity after NH_3 adsorption. The reason for the poorer electron transfer to SWCNT in $SWCNT/Pt:NH_3$ is the weaker interaction between SWCNT and Pt in the latter, which is further diminished by the adsorbed gas. The electron density acquired from NH_3 hardly moves to SWCNT as is shown by the accumulation of electron density on the Pt atom (Δq_{Pt}, -0.17 *e*) after interacting with NH_3. Up until this point, $SWCNT_{Vac}/Pt$ adequately satisfies the basic sensitivity requirements and induces more electronic change in terms of both the energy gap and partial charge transfer to the SWCNT than to the SWCNT/Pt.

2. The investigation of catalytic activities of newly modified SWCNTs with transition metals (Sc, Ti, V) and the unmodified SWCNTs for N_2O removal

The geometries after optimizing the structures of Figure 13 are shown in Figure 43 and these serve as catalysts for N_2O decomposition. A concerted reaction mechanism was studied in which the oxygen atom of N_2O is transferred to the active site on the catalyst in a single step, consequently releasing a N_2 molecule and producing an oxide species on the catalyst surfaces. Such a reaction pathway is generally proposed for oxygen abstraction from N_2O with Sc, Ti and V transition metals (Stirling, 1998). The reaction mechanisms and the summarized energy profiles of undoped and metal doped-catalysts are illustrated in Figures 44 and 45, respectively. Partial and net charge transfers are tabulated in Table 4.

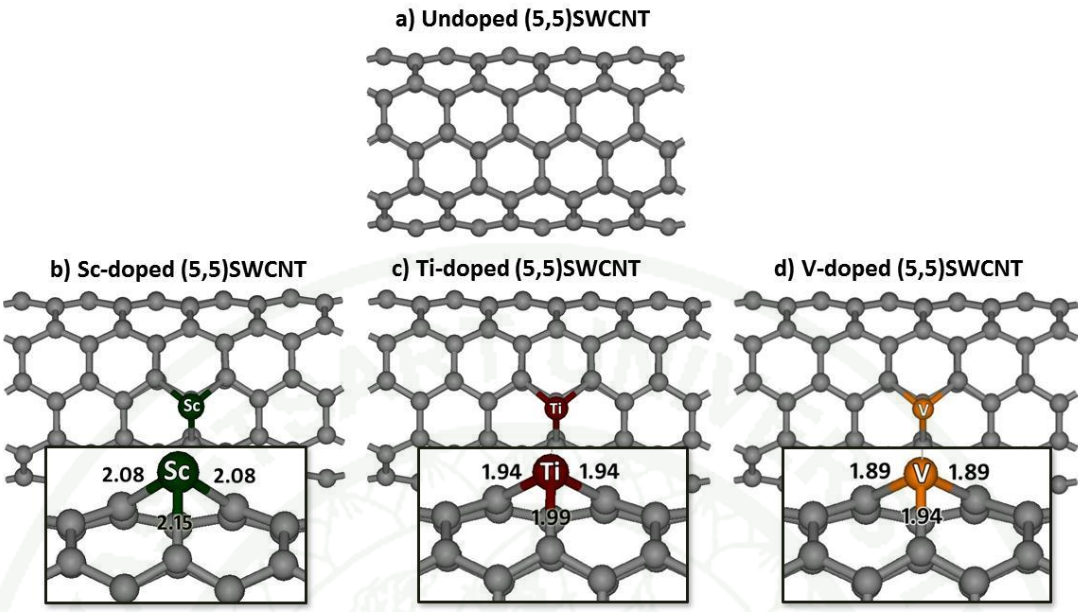

Figure 43 Optimized geometries with bond lengths (Å) of undoped (5,5)SWCNT (a), Sc-doped (5,5)SWCNT (b), Ti- doped (5,5)SWCNT (c) and V-doped (5,5)SWCNT (d).

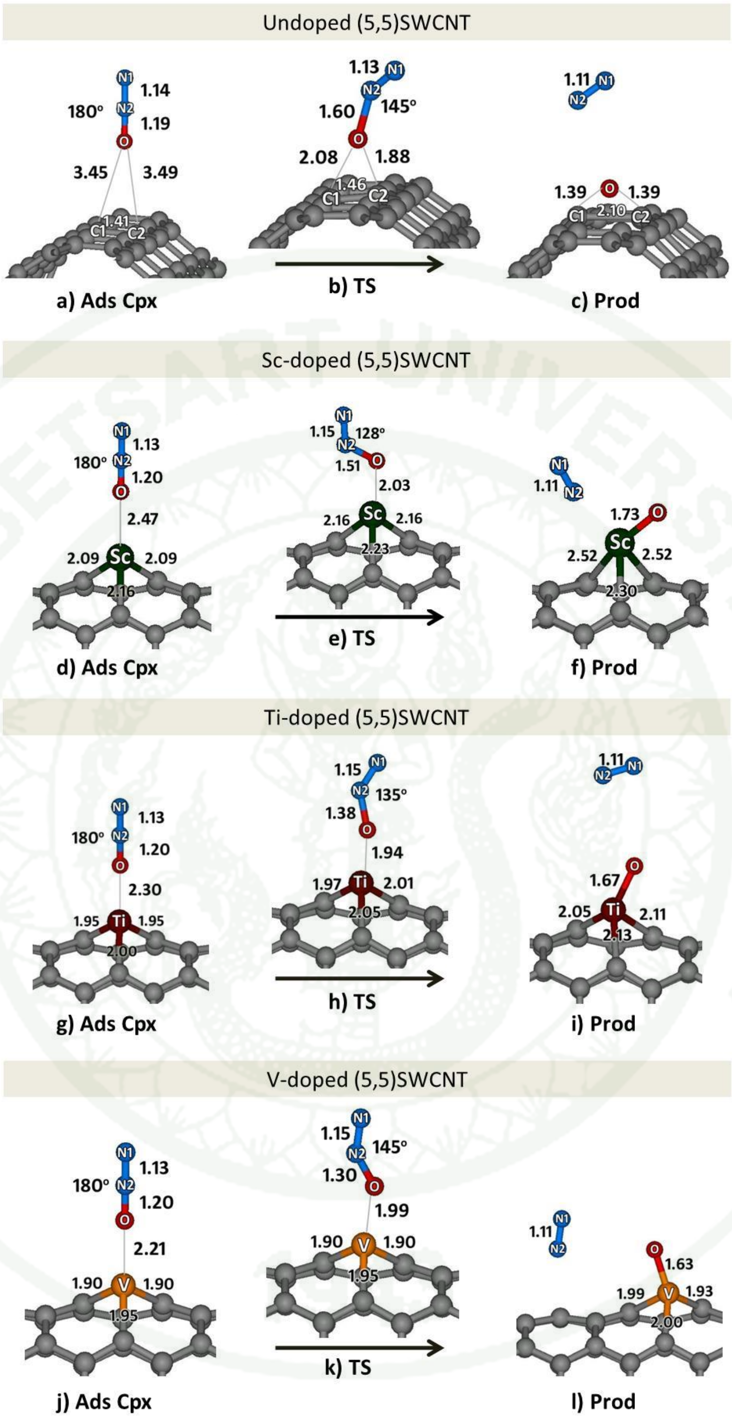

Figure 44 Adsorption complexes (Ads Cpx), transition state structures (TS) and products (Prod) of undoped (5,5)SWCNT:N_2O (a-c), Sc-doped (5,5)SWCNT:N_2O (d-f), Ti-doped (5,5)SWCNT:N_2O (g-i) and V-doped (5,5)SWCNT:N_2O (j-l) systems accompanied by some selected bond lengths (Å) and angles (degrees).

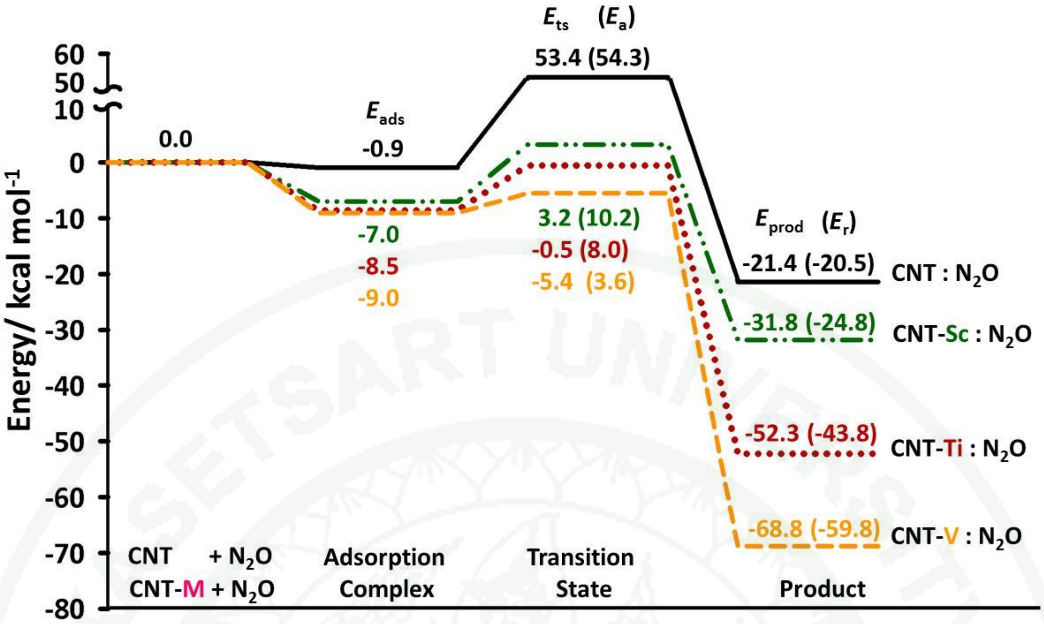

Figure 45 Energy profiles for the N_2O decomposition on undoped (dark solid line), Sc-doped (green dash dot line), Ti-doped (red dot line) and V-doped (orange dash line) (5,5)SWCNTs. The numbers in parentheses at transition and final states are activation energies, $E_a = E_{ts} - E_{ads}$, and reaction energies, $E_r = E_{prod}$-E_{ads}, respectively.

Table 4 Partial molecular and atomic charge transfers, Δq(e) of all complexes for co-adsorption states (Δq_{ads}), transition states (Δq_{ts}) and final states (Δq_{prod}). The partial charges of the initial metal-doped (5,5)SWCNTs (without N_2O) are tabulated in Table 5.

System	**Δq_{ads} [a]**			**Δq_{ts} [b]**			**Δq_{prod} [c]**		
	CNT	**Metal**	**N_2O**	**CNT**	**Metal**	**N_2O**	**CNT**	**Metal**	**N_2O**
CNT:N_2O	-0.006	-	0.006	0.233	-	-0.233	0.224	-	-0.224
CNT-Sc:N_2O	-0.042	0.006	0.036	0.343	0.223	-0.566	0.032	0.009	-0.041
CNT-Ti:N_2O	-0.051	0.000	0.051	0.235	0.161	-0.396	0.090	0.018	-0.108
CNT-V:N_2O	-0.044	-0.009	0.053	0.180	0.057	-0.237	0.115	0.191	-0.306

[a] $\Delta q_{ads}(X) = q(X)$ in adsorption complex – $q(X)$ in isolated molecule

[b] $\Delta q_{ts}(X) = q(X)$ in transition state – $q(X)$ in adsorption complex

[c] $\Delta q_{pro}(X) = q(X)$ in product – $q(X)$ in transition state

Table 5 Partial molecular and atomic charges, q(e) of studied metal-doped (5,5)SWCNTs catalysts.

System	***q*(SWCNT)**	***q*(Metal)**
(5,5)SWCNT-Sc	-0.600	0.600
(5,5)SWCNT-Ti	-0.386	0.386
(5,5)SWCNT-V	-0.151	0.151

2.1 Adsorption Complexes

In the first step, the adsorption complexes are analyzed. For the bare (5,5)SWCNT system (Figure 44a), the C1-C2 pair site was chosen as the active position to absorb N_2O since it has been shown to be more reactive than the C2-C3 site (Bettinger, H. F., 2006; Lu *et al.*, 2002, 2003). The adsorption energy is very low, about 1 kcal mol^{-1} (Figure 45), in accordance with a long C···O distance of about 3.5 Å. The doped SWCNTs take over some electron density from the metals. The amount of charge transfer is 0.60*e* for Sc which also has the smallest ionization energy of the three elements, 0.39*e* for Ti and 0.15*e* for V. Their adsorption complexes are also much more exothermic (7.0, 8.5 and 9.0 kcal mol^{-1}; c.f. Figure 45). The metal···O distances are 2.47, 2.30 and 2.21 Å, respectively (Figures 44d, 44g and 44j). In the adsorption complexes, N_2O is still retained as a linear molecule (c.f. Figure S1A) with its N-O bond slightly lengthened by 0.01 Å and the N-N bond shortened by the same amount. The charge redistribution in the complexes is related to the binding strengths mentioned above. The electron transfer Δq_{ads} caused can be defined by the adsorption process as the partial charge difference of the atom or molecule with respect to the isolated systems. Positive values of $\Delta q_{ads}(N_2O)$ infer an electron transfer to the catalyst. $\Delta q_{ads}(N_2O)$ for the undoped (5,5)SWCNTs is +0.006*e*, while for Sc-, Ti- and V-doped (5,5)SWCNTs values of +0.036*e*, +0.051*e* and +0.053*e*, respectively, are found (Table 4). The order of these values correlates with the binding strengths mentioned above. The electron density in the metal doped (5,5)SWCNTs is mostly distributed towards the SWCNT segments which serve as electron collecting regions as can be seen by the corresponding negative values of Δq_{ads}(SWCNT). In the bare SWCNT there is almost no charge transfer. The lowest unoccupied molecular orbitals (LUMOs) on the active sites of the metal doped (5,5)SWCNTs (Figures 46b, 46c and 46d) can specifically interact with the incoming molecules, which is not the case in the undoped (5,5)SWCNTs (Figure 46a). Moreover, the d-orbitals in those MOs possess large polarizabilities and can promote electron transfers. An analysis of the LUMOs of the metal doped (5,5)SWCNTs shows the characteristics of their binding capabilities with N_2O. The d-orbital contributions are more prominent in the LUMOs of Ti- and V-doped (5,5)SWCNTs (Figures 46c and 46d) than in the ones of the Sc-doped (5,5)SWCNT (Figure. 46b). From Figure 47 one sees that Ti and V have the best spatial extent for overlapping with the HOMO orbital of N_2O (Figure 48).

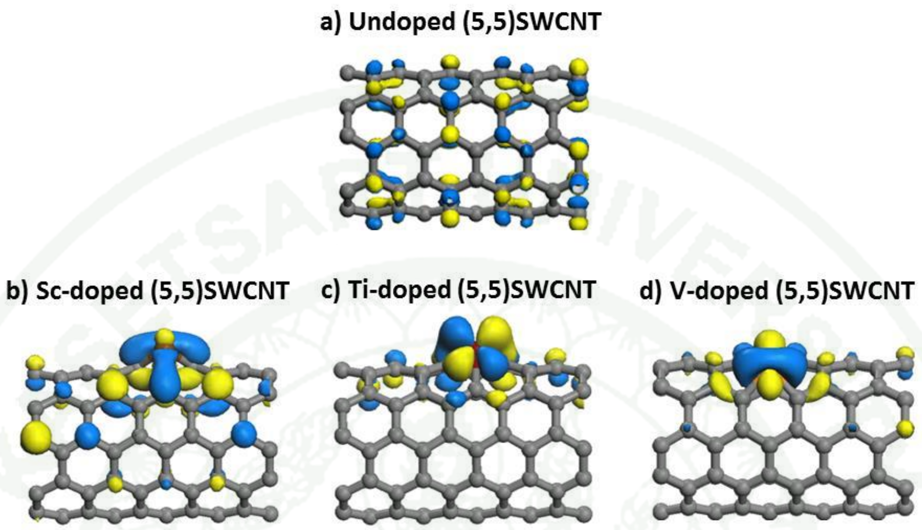

Figure 46 Lowest unoccupied molecular orbitals (LUMOs) of undoped (5,5)SWCNT (a), Sc- doped (5,5)SWCNT (b), Ti- doped (5,5)SWCNT (c) and V-doped (5,5)SWCNT (d).

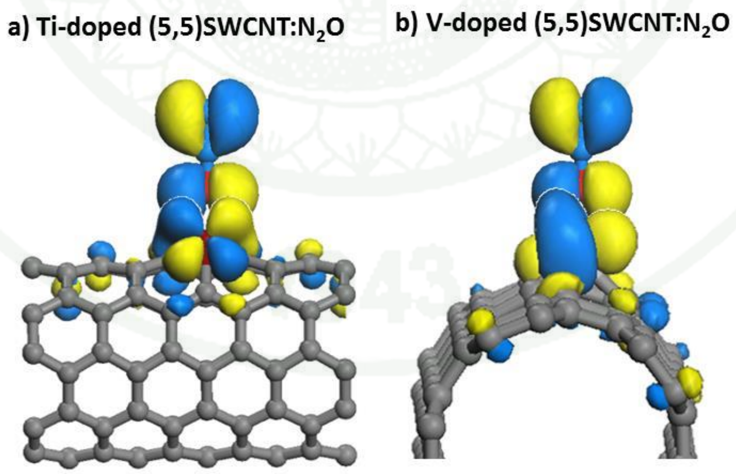

Figure 47 Overlapping molecular orbitals of the reactants: HOMO of N_2O (a) with LUMO of Ti-doped (5,5)SWCNT and LUMO of V-doped (5,5)SWCNT (b).

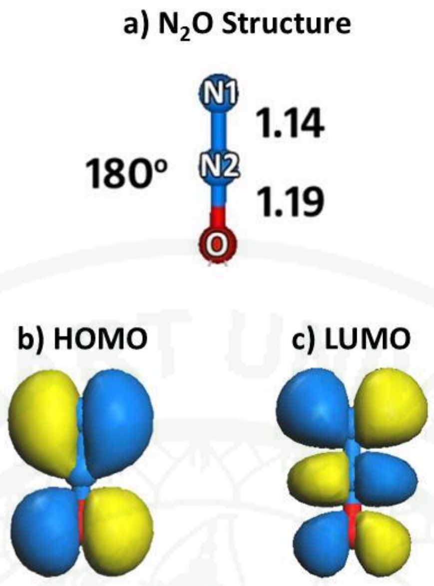

Figure 48 Optimized geometry with bond lengths (Å) (a) and angle (degree), highest occupied molecular orbital (HOMO) (b) and lowest unoccupied molecular orbital (LUMO) (c) of isolated N_2O molecule.

2.2 Transition state structures

In the next step, the transition structures (TS) are analyzed connecting the adsorption complex with the product. In undoped (5,5)SWCNT, the TS lies 54.3 kcal mol^{-1} above the reactants but this value is reduced to 10.2, 8.0 and 3.6 kcal mol^{-1} for Sc-, Ti- and V-doped (5,5)SWCNTs, respectively (Figure 45). Similar to the co-adsorption state, the energetic order in the TS from lower to higher barriers is V- < Ti- < Sc-doped < undoped (5,5)SWCNTs. The TS geometries show that the oxygen atom of N_2O approaches the active sites with the N-O bond dissociation taking place concurrently. In the TS the C···O and M···O distances decrease to 2.00, 2.03, 1.94 and 1.99 Å and the N-O bond lengths increase from 1.2 Å to 1.60, 1.51, 1.38 and 1.30 Å for undoped-, Sc-, Ti- and V-doped (5,5)SWCNTs, respectively (Figures 44b, 44e, 44h and 44k). The NNO angles are tilted from linearity to around 140 degrees. The weakening of the N-O bond arises from electron transfer from the catalyst to the LUMO of N_2O (Figure 48c) which has a π-character with a node plane perpendicular to the N-O bond.

This can be seen from the negative values of $\Delta q_{TS}(N_2O)$ which are -0.233*e* for undoped CNT and -0.566*e*, -0.396*e* and -0.237*e* for Sc-, Ti- and V-doped (5,5)SWCNT, respectively (Table 4). The metal center and the SWCNT both contribute to this transfer of electron density, the SWCNT losing about half of its negative charge. Both the 4s and 4d orbitals of the metal atoms donate charge density to the antibonding π^* orbital of N_2O. For Sc this density transfer amounts to about 0.15*e* from 4s and 4d each (Table 6). The amount of electron transfer is similar for Ti whereas in the case of V, almost only the 4d orbital contributes. As a net result the metal atoms become even more positively charged.

The structure of the V-doped (5,5)SWCNT/N_2O TS bears the most resemblance to its adsorption complex and also N_2O in this transition state is least deformed (Figure 44k). This is a manifestation of Hammond's postulate which states the structural similarity between reactant and transition state structures for exothermic reactions. It is worth mentioning that for Sc- and Ti- doped (5,5)SWCNTs, the transition state energies are higher than or similar to the adsorption energies. However, that does not mean that the adsorption is followed by desorption. Rather, N_2O will be adsorbed and the associated energy will in any case dissipate rather rapidly. The energy delivered by the former exothermic dissociation processes can assist the adsorption state to move on to the transition state, largely independent of the adsorption energy.

Table 6 Charge density differences of metal atoms in the metal-doped (5,5)SWCNTs and their TS for each molecular orbital.

Metal	**Molecular Orbital**		
	4s	**4p**	**4d**
Sc	0.127	-0.077	0.179
Ti	0.106	-0.086	0.140
V	0.039	-0.113	0.123

2.3 Products

In the products, the metal atoms of the doped carbon nanotubes are bound to the oxygen atoms from N_2O molecules with metal···O distances of 1.73, 1.67 and 1.63 Å for - Sc-, Ti- and V-doped (5,5)SWCNTs, respectively (Figures 44f, 44i and 44l). For the undoped SWCNT, the C-O distance is 1.39 Å. The N-O bonds of the N_2O molecules are completely dissociated with N_2 molecules being formed. The charge rearrangement in this step is similar to the one discussed above for the formation of the TS with the additional density on the O atoms comparing both the metals and the SWCNT which, at that stage, is nearly neutral. The decomposition of N_2O into the oxide and N_2 can be compared with the corresponding gas-phase reaction. After some debate it is now established that N_2O has a negative electron affinity, i.e., it forms no stable anion (Bettinger, H. F., 2006; Lu *et al.*, 2002, 2003). The attachment of an electron breaks the N-O bond which is just the extreme case of our situation when electron density is supplied via the metal atoms.

Overall, the reactions are exothermic, due to the very stable oxide products. Again, the order of the relative stability of the products, VO- > TiO- > ScO-doped (5,5)SWCNTs > O-(5,5)SWCNT (Figure 45), is the same as the order of the transition state barrier heights and is again consistent with Hammond's postulate in the sense that a lower activation barrier causes the reaction to become more exothermic. From the charge analysis (Table 4), it can be seen that the product oxygens obtain negative partial charges. They and their bonds are stabilized by electrons from SWCNTs. Thus, the driving force behind the N_2O binding in the transition states is finally the formation of these stable oxide complexes. For a working system, the catalyst must finally be recovered. This can happen by the combination of two oxygen atoms to form O_2 which can desorb at elevated temperatures or by the subsequent reaction of one oxygen atom with another N_2O molecule into N_2 and O_2. An undesirable reaction would of course be the reaction of the oxygen with a carbon atom of the SWCNT. Obviously, models with higher dopant and adsorbate coverages would be needed for the understanding of a real catalytic system. Conversely, a single dopant allows the evaluation of the intrinsic activity of the studied metal without consideration of the morphology, crystal plane or surface coverage effects. Therefore, an investigation of these basic systems is a prerequisite before moving on to higher coverages.

3. The fabrications of well-constructed Nafion/PtNPs/CNT-AAO and its membrane electrode assembly (MEA)

3.1 The fabrication of Anodic Aluminium Oxide (AAO) template

From the electropolishing treatment, only the Al on the bare side (uncovered with plastic tape) was oxidized. As compared with the non-oxidized area at the upper right corner of the plate which was not immersed in the solution, the electropolished Al plate looks obviously brighter (Figure 49) indicating the appearance of a smooth surface. It resulted from the elimination of surface roughness about 100 – 200 microns from the anode surface according to equations summarized in Table 7.

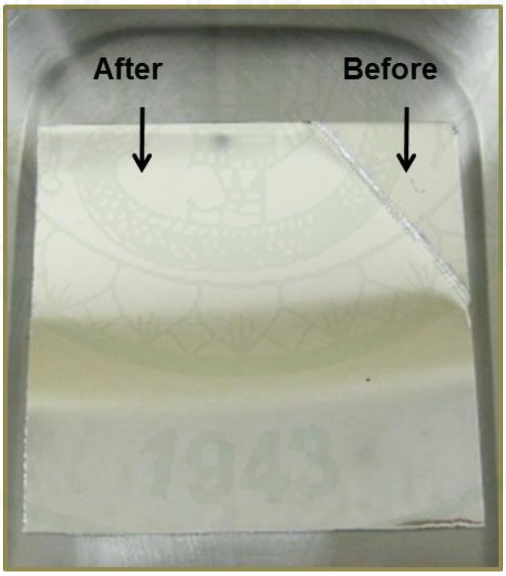

Figure 49 Photo of the Al plate after electropolishing. The small area at upper right corner is an untreated surface.

Table 7 Anodic and cathodic reactions in the electrolytic polishing of the Al plate.

Anodic Reactions	**Cathodic Reactions**
1. Transfer of metal ions into the solution $Al \rightarrow Al^{3+} + 3e^-$	1. Hydrogen evolution $2H_2O + 2e^- \rightarrow H_2 + 2OH^-$
2. Formation of oxide layers $2Al + 6OH^- \rightarrow Al_2O_3 + 3H_2O + 6e^-$	2. Oxygen reduction $O_2 + 2H_2O + 4e^- \rightarrow 4OH^-$
3. Oxide Dissolution $6H^+ + Al_2O_3 \rightarrow 2Al^{3+} + 3H_2O$	
4. Evolution of oxygen $4OH^- \rightarrow O_2 + 2H_2O + 4e^-$	

The above anodic reactions are related to the I-V characteristics of the electropolishing of copper in phosphoric acid firstly observed by Jacquet (Jacquet, 1935). He found that, during the applied voltage increasing, it was possible to obtain pitting, polishing and gas evolution as shown in Figure 50. Up to the voltage value at V_A, the surface showed some signs of pitting (anodic reaction 1). A drop in current density was found after V_A , but remained constant over the horizontal range (V_B – V_C) in which the anodic reactions 2 and 3 or the polishing occurred. The best result was obtained near point V_C because, at point V_C, the bubbles of gaseous oxygen appeared on the anode (anodic reaction 4) could be trapped on the surface and thus generated some defects.

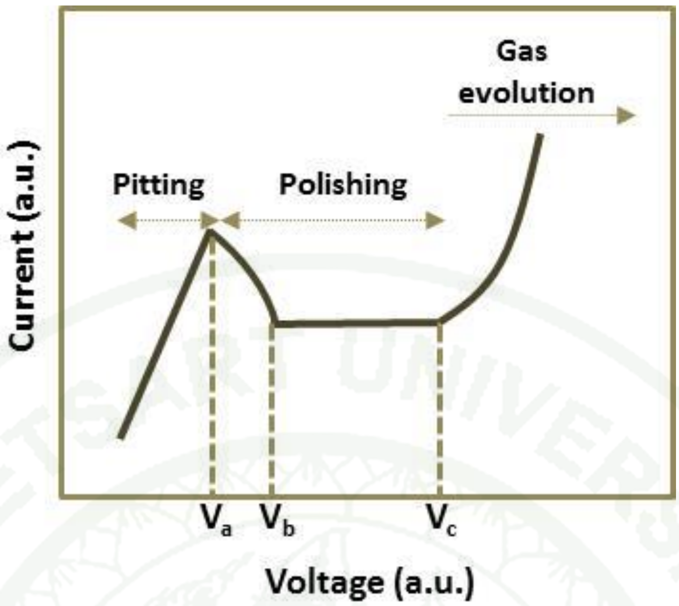

Figure 50 Current density vs. voltage for copper electropolishing in phosphoric acid.

Source: Jacquet (1935)

Generally, when a current passes across the electrolyte, the anodic film has higher viscosity and higher electrical resistivity than the bulk of the electrolyte. The thickness of the insulating layer on a rough surface (Figure 51) differs from site to site by being greater in valleys (α) than on protrusion (β). On account of that, the current density on protrusion is higher than in well. Consequently, β apex dissolves more rapidly than the α cavity, and results in surface-leveling. Electropolishing is beneficial for the formation of self-ordered porous alumina by leading to the perfect arrangement of pores especially at the beginning of pore formation. The porous alumina membranes prepared without electropolishing will not provide any ordered pore domains.

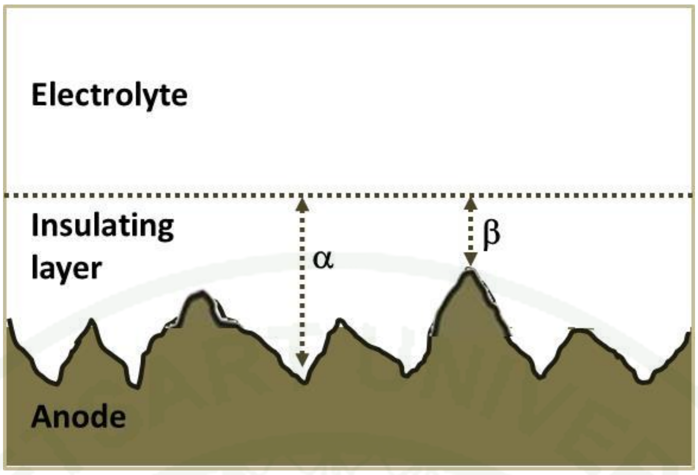

Figure 51 Schematic illustration of typical formation insulating layer on the anode surface.

Source: Hoar and Mott (1959)

For the AAO synthesis, a two-step anodization process is normally used to fabricate the high-ordered arrangements of nanopores. From Figure 15, although the initial anodization creates the pores on Al surfaces with irregular arrangement, highly ordered pore arrays are formed at the metal/oxide interface. After selectively removing the oxide layer, the patterns which are replicas of the pore arrays are revealed as indented landscape covering the surface of the Al substrate. This allows the preparation of pores with high order, straight and parallel by a subsequent second anodization under the same conditions as the first one. The reactions occurring in anodic oxidation and also oxide dissolution are summarized in Table 8.

Table 8 Anodic and cathodic reactions of the anodization of the Al plate in an acid electrolyte. The selective dissolution of the AAO layer with acid and the selective removal of Al with $CuCl_2$ are also elaborated.

Anodization	
Cathode	**Anode**
$\mathbf{6H^+ + 6e^- \rightarrow 3H_2}$	$\mathbf{2Al + 3H_2O \rightarrow Al_2O_3 + 6H^+ + 6e^-}$
	1. Al dissolution: $2Al \rightarrow 2Al^{3+} + 6e^-$
	2. Oxide Formation
	Metal/Oxide boundary: $2Al^{3+} + 3O^{2-} \rightarrow Al_2O_3$ or $2Al^{3+} + 3OH^- \rightarrow Al_2O_3 + 3H^+$
	3. Oxide Dissolution
	Oxide/Electrolyte boundary: $Al_2O_3 + 6H^+ \rightarrow 2Al^{3+} + 3H_2O$
Selective dissolution of AAO layer	
$Al_2O_3 + 6H^+ \rightarrow 2Al^{3+} + 3H_2O$	
Selective removal of Al	
$2Al + 3CuCl_2 \rightarrow 2AlCl_3 + 3Cu$	

When external voltage is applied, hydrogen ions from the acid electrolyte are reduced at the cathode to develop hydrogen gas at the same time as the oxidation of Al into Al_2O_3 at the anode. The widely accepted pore formation mechanism of the AAO membrane in an acid is based on two continuous processes which are the oxide growth at the metal/oxide interface and the oxide dissolution at the oxide/electrolyte interface (Adelkhani *et al.*, 2009; Jessensky *et al.*, 1998; Landolt, 1987; Li *et al.*, 1998; Ono *et al.*, 2004; Parkhutik and Shershulsky, 1992).

The porous oxide growth involves several stages as schematically presented in Figure 52. In the initial stage (stage i), the compact barrier oxide layer starts to grow covering the entire surface of the Al substrate via the elementary processes 1 and 2. Under the electric field, aluminium at the metal/oxide interface will be oxidized into Al^{3+} cations and some of them interact with the oxide anions, O^{2-} or OH^{-}, which are electric field-enhanced, migrate from the electrolyte/oxide interface to form Al_2O_3 at the metal/oxide interface. However, some of Al^{3+} cations move across the oxide layer by an applied electric field and are ejected into the electrolyte. Another mechanism for losing Al^{3+} cations proposed that, when the Al_2O_3 contacts with the acid solution, it is dissolved into the electrolyte together with the water formation from the as segregated oxide ions (elementary process 3). When Al^{3+} cations are drifted from the oxide surface, cation vacancies or voids emerged and propagated as pits leading to the locally focused electric field (stage ii). Consequently, electric-field-assisted dissolution of the formed oxide layer occurs and then pores are firstly developed on these pits (stage iii). The pit sites have a relatively thinner oxide layer therefore enhancing the oxide growth rate. At this stage, there are competitive reactions between oxide formation at the metal/oxide interface and oxide dissolution at the oxide/electrolyte interface. Finally, the pore growth process approaches a steady state and a uniform porous structure is formed (stage iv). The pore size, the distance between pores and pore wall length of the AAO membrane are principally determined by the acid electrolyte, its concentration, the anodic voltage and time and bath temperature. The outcome of the AAO film deposited on the Al plate after the 2^{nd} anodic oxidation is shown in Figure 53. The white circle, 4.5 cm in diameter, is the region of Al plate that is exposed to the electrolyte, in turn, homogeneously and uniformly transformed to the porous type aluminium oxide under this anodizing condition.

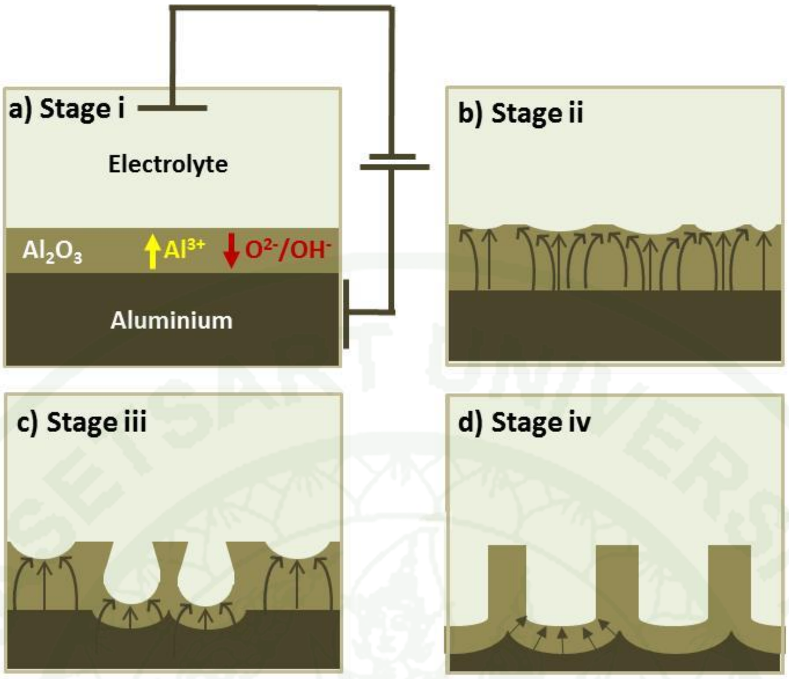

Figure 52 Schematic illustration of the pore formation by electrochemical anodization, formation of barrier oxide (a), formation of pits by local field fluctuations (b), initial pore formation by field-enhanced or/and temperature-enhanced dissolution (c) and steady-state pore growth (d).

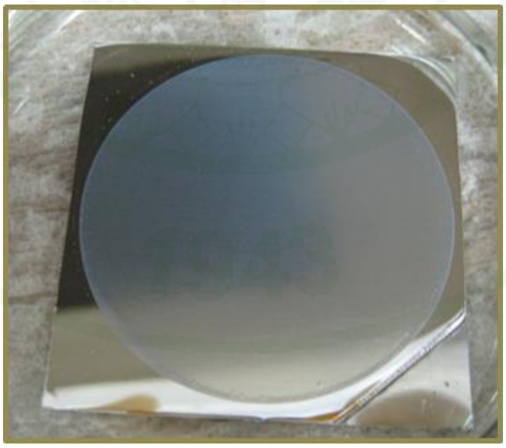

Figure 53 Photo of the AAO film supported on Al plates (AAO/Al plate).

After removing the Al substrate and opening the pore bottom by the reactions shown in Table 8, the pale yellow thin film of solely AAO are obtained (Figure 54). Even though the synthesized AAO films are fragile because of their low thickness and brittle nature, most of them are not broken and preserve their original size of the cut AAO/Al plate (1x1 cm^2). It should be noted that keeping the AAO film deposited on the Al plate together with the PVC coating before cutting and the removal of the Al substrate offer great benefits for supporting the weak AAO film during the subsequent experiments.

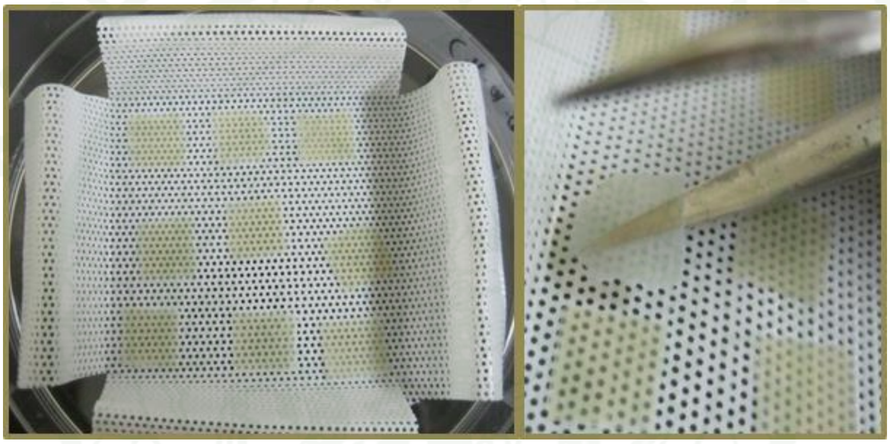

Figure 54 Photos of the synthesized AAO film with 1x1 cm^2.

The scanning electron images of the resultant AAO film are displayed in Figure 55. Although the commencement of the growing pores at the upper or pore side surface (Figures 55a -b) are randomly distributed, the ordered densely packed hexagonal structures can be observed at the bottom or barrier side of the film (Figures 55c-d). This almost perfectly ordered structure is accompanied by the uniform depth of neighboring pores leading to the smooth lower surface. By chemical etching in the solution of phosphoric acid, the pore bottoms are all opened as well as homogeneously widened (Figures 55e and 55f). However, the density of the pore arrays at the pore side is found to be typically higher than at the barrier side of the AAO film, indicating that some of the pores stop growing either shortly after their nucleation or during the self –organization process.

The pore size measured at the pore mount, pore bottom and pore wall are quite similar, approximately 90 nm (Figures 55b, 55f and 55h). In addition, the obtained AAO film has the even thickness which is estimated to be 20 μm (Figure 55g). Upon this employed anodic oxidation condition including the type and concentration of acid used, the anodization voltage, time and temperature, the tubular pores of synthesized AAO film are tuned to be uniform in both pore size of 90 nm and length of 20 μm.

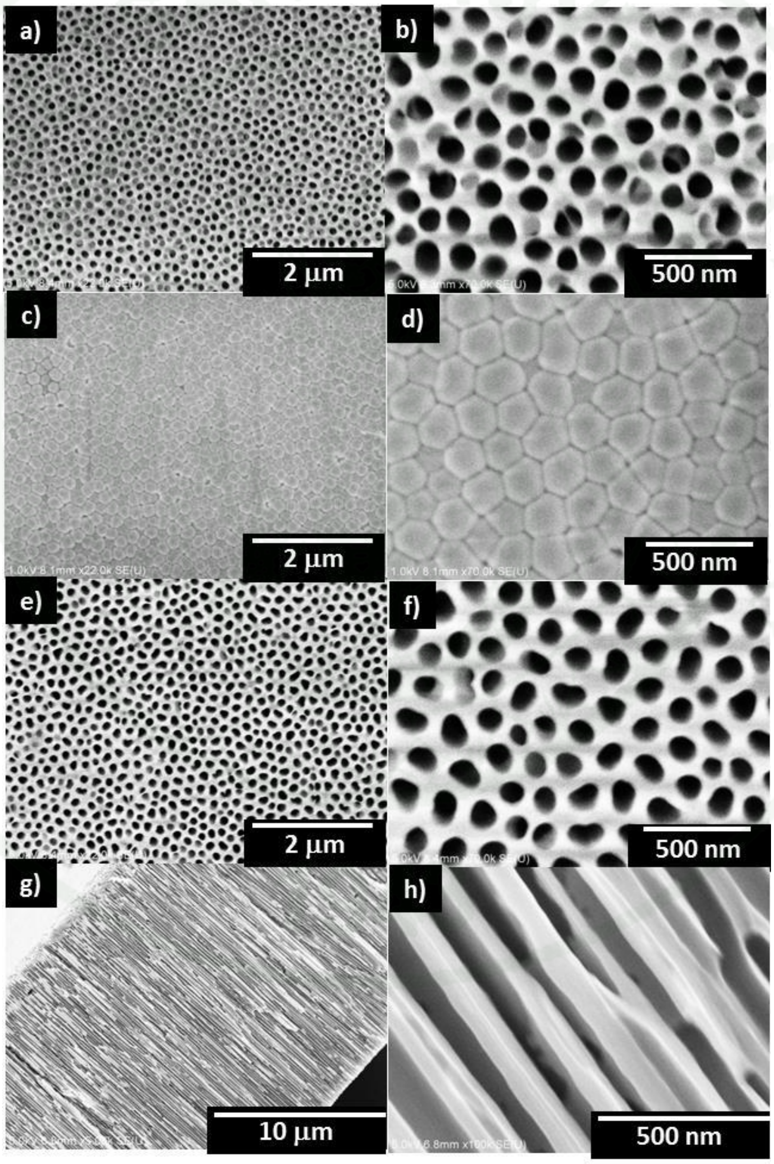

Figure 55 SEM images of pore side (a,b), barrier side before (c,d) and after (e,f) etching and side view of AAO film.

3.2 Synthesis of CNT deposited AAO film (CNT-AAO)

Figure 56a presents the CNTs deposited AAO template (CNT-AAO) in which the color of AAO film is turned from light yellow to black because of the successful carbon coating. Owing to the low-temperature CVD process at 600°C (lower than the first phase change temperature of Al_2O_3 at 850°C), such AAO templates still remain flat without severely bending such that they are a well-suited substrate for assembling the flat Nafion membrane by the hot pressing method.

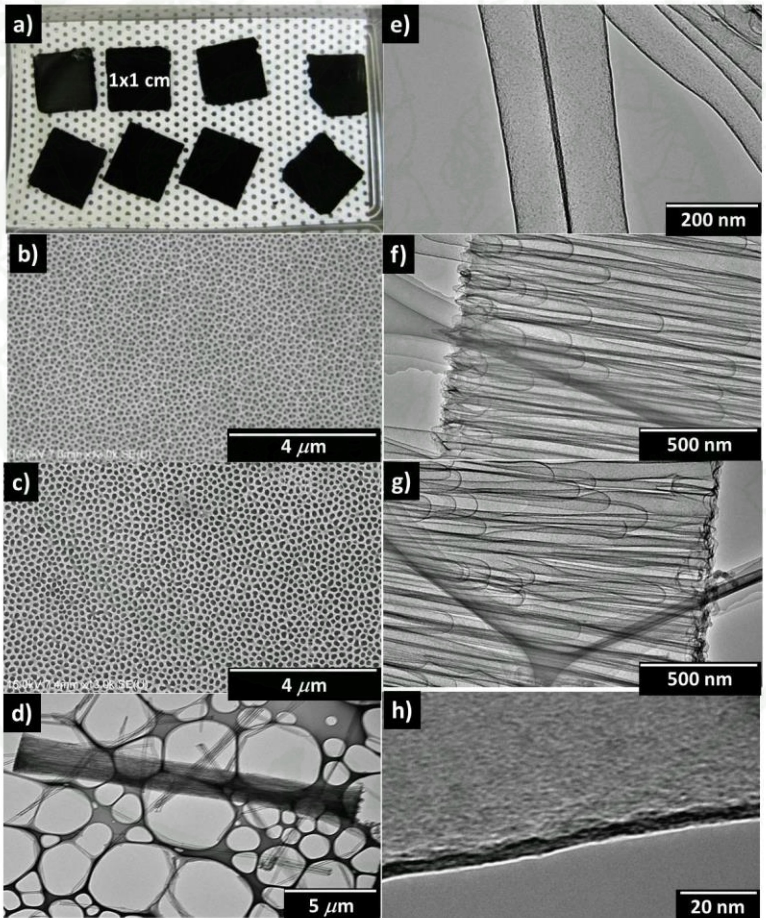

Figure 56 The photo of the CNT-AAO film prepared under a carbon deposition using the AAO as template (a), the scanning electron microscopic (SEM) photographs at pore side (b) and barrier side (c) and the transmission electron microscopic (TEM) photographs (d-h) with different positions and magnifications of the CNTs after AAO removal.

More importantly, this operating CVD temperature is lower than the self-decomposition temperature of acetylene in the vapor phase i.e., about 650°C, hence there is no other form of carbon precipitating and blocking on the pore mouths of both sides of the CNT-AAO film (Figures 56b-c). From the TEM images of CNTs after AAO dissolution (Figures 56d-f), they all evidence that the carbon deposition from the pyrolysis acetylene precursor under these employed experimental conditions creates CNTs within the pores of the membrane. It has been known that aluminium oxide itself exhibits as a Lewis acid catalyst strong enough to catalyze the acetylene decomposition without the need of other metals. On account of that, not only the metal-free CNTs can be obtained but also there is no tedious step and cost of adding a metal catalyst.

At low magnification in Figure 56d, many of the tubes are bundled by carbon deposition taken place on the external surface of the AAO film. These bundles are helpful to measure the length of CNTs which is averaged to be 20 μm and exactly the same as the thickness of the corresponding template film. But some of the CNTs are separated from the cluster during the washing step as can be observed in the other pictures. From the observations in Figures 56e-g, it can determine that these CNTs are hollow with open ends.

Some tubes branch out into several tubes near the end that is imitated from the similar branchlike pore structure of the synthesized AAO template. The magnified TEM images (Figures 56e and 56h) confirm the tubular shape formation with an outer diameter of 90 nm, again corresponds to the pore size of the used AAO film. The wall thickness of the resultant CNTs is homogeneous all along the tube and roughly estimated to be 5 nm. That is due to the uniform catalytic property of the internal alumina walls resulting in the simultaneous carbon deposition on the entire inner surface of pores with no coatings at any particular site or location. The above outcomes elucidate that the CNTs with uniform diameter, length and thickness can be prepared inside the pores of AAO film by this employed method. Such morphologies are probably beneficial for facilitating the flows of reactants and products during the operation of the fuel cell device.

3.3 Decoration of the inner walls of CNT-AAO with platinum nanoparticles (PtNPs/CNT-AAO)

The PtNPs deposited onto the innerwall of CNT-AAO were prepared by the direct reduction of the Pt salt solution by the commonly used reducing agent, $NaBH_4$, according to the reaction shown below:

$$H_2PtCl_6 + 6NaBH_4 + 18H_2O \rightarrow Pt + 6B(OH)_3 + 6NaCl + 22H_2 \quad (5)$$

The surface appearances on both sides of the PtNPs/CNT-AAO film prepared without washing off the excess metal precursor on the film surface are depicted in Figures 57a-d. It is easy to observe that almost all pore mounts of the film are clogged by the large-sized (ca. 100 nm) and dense PtNPs. These aggregated clusters are taken placed not only on the outer surfaces of the film but are also extended into the inner walls close to pore mouths as evidenced in Figures 57e and 55a-b. However, the PtNPs with a smaller average size, ca. 5.2 nm (evaluated from size distribution in Figure 63a), are decorated on the inner walls along the whole tube adjacent to the pore mouths at both sides (Figures 58c-d). Consider the cause of the big metal cluster formation, it perhaps originated from the high reactivity of $NaBH_4$ which is able to react quickly with the Pt precursor accumulated on the surfaces prior to moving into the pore channels. These aggregations seem to be an adverse aspect since the gas and water transports in the fuel cell device might be blocked by these congested clusters. Consequently, the involved chemical reactions cannot proceed and eventually the electricity will no longer be produced.

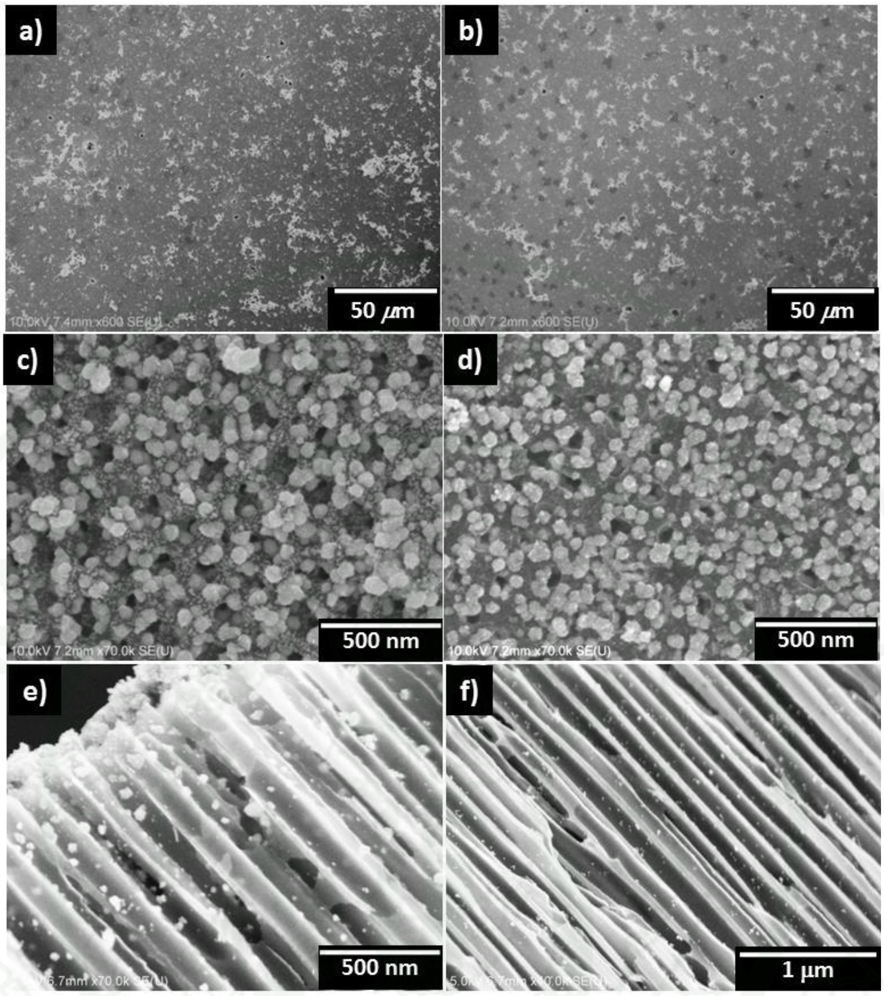

Figure 57 SEM photographs of top views on the pore side surface (a and c), barrier side surface (b and d) and cross-sectional views (e and f) of the PtNPs/CNT-AAO film prepared without washing excess metal precursor on the film surface before reduction.

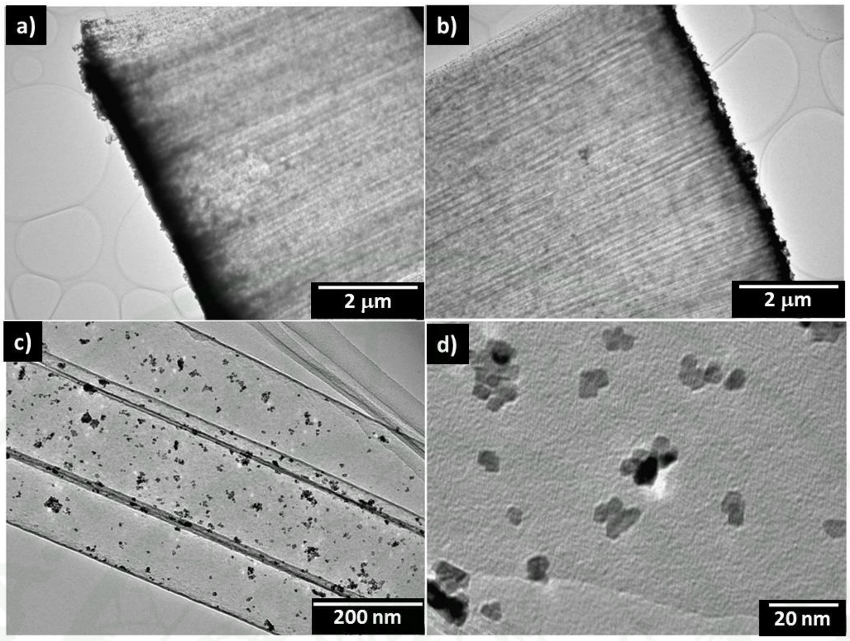

Figure 58 TEM photographs of the PtNPs/CNTs liberated from the AAO template that were prepared without washing the excess metal precursor on the AAO film surface before reduction, at both ends of the CNT bundle (a and b) and at the middle of CNTs (c and d).

The alternative strategy in avoiding aggregations of PtNPs at the pore mouths is suggested by washing the excess Pt precursor on the film surface before interacting with the $NaBH_4$ solution as demonstrated in Figure 21 along the inserted red dotted line route. Water was utilized as the cleaning solvent because of its intrinsic hydrophilic property which is capable of completely dissolving Pt ions on the surface but hardly penetrates into the hydrophobic carbon channels. Thus the dropped water will not elute the Pt ions impregnated into the internal carbon surfaces. The greatly improved results from the minor modified process are presented in Figures 59-60. The bulky agglomerated PtNPs are no longer generated on the both the side surfaces (Figures 59a-d) and also the inner pore mouths (Figures 59e and 60a-b). The film surface washing can give positive effects on not only flow gateways but also the particle size of PtNPs. The particle size of PtNPs prepared with this developed method is estimated to be 3.2 ± 0.4 nm (Figure 63b) which is of smaller size and narrower distribution compared to that of PtNPs prepared by the earlier method ie., 5.2 ±0.8 nm. The reduced and more uniform PtNP size would result from the more homogeneous and lower concentration of Pt precursor deposited on the surface and also into the pores. There are no abundant Pt ions on the film surfaces diffusing into the pore for enhancing the growth of particles as in the unwashed system. Even though the Pt ions on the surface of the film are reduced by washing, the density of PtNPs inside the pores remains high as shown in Figures 59f and 60c-d. From the overall results, it can be stated that the surface washing method could overcome the drawback of pore mouth blocking and is beneficial for synthesizing the uniform and small size PtNPs deposited inside the pores of CNTs.

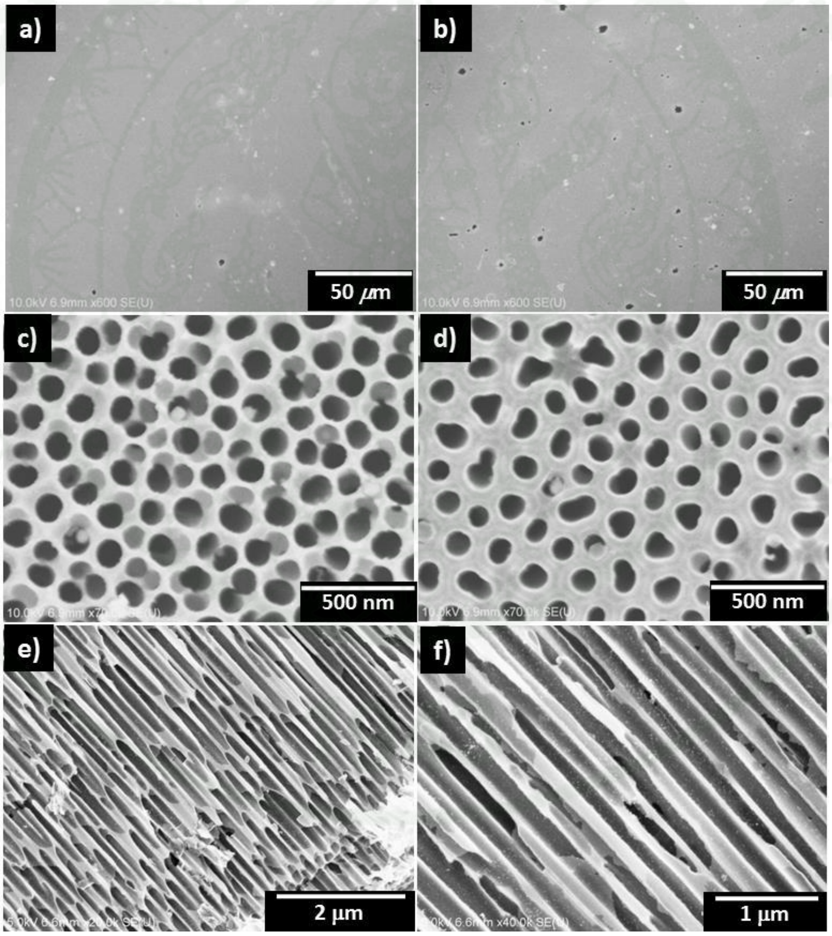

Figure 59 SEM photographs of top views on the pore side surface (a and c), barrier side surface (b and d) and cross-sectional views (e and f) of the PtNPs/CNT-AAO film prepared with washing the excess metal precursor on the film surface before reduction.

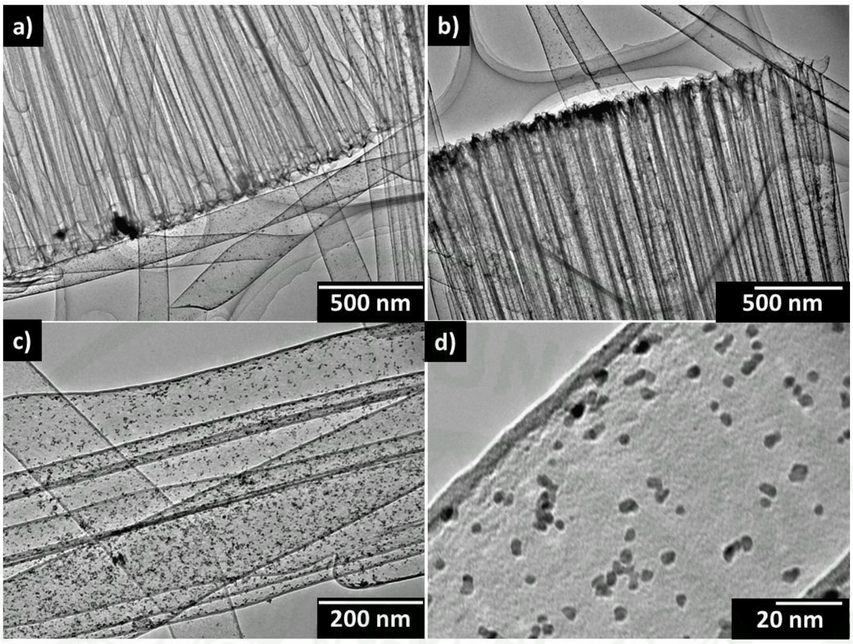

Figure 60 TEM photographs of the PtNPs/CNTs liberated from AAO template that were prepared by washing the excess metal precursor on the AAO film surface before reduction, at both ends of the CNT bundle (a and b) and at the middle of CNTs (c and d).

The last method of PtNPs deposition is loading with pre-synthesized PtNPs. The aim of this approach is to enlarge the surface area of the metal catalyst by producing the PtNPs with small and uniform size governed by the role of alkanethiol stabilizer. The reaction of PtNP synthesis still relies on the direct reduction route with $NaBH_4$ as outlined in the previous section, except in the presence of the alkanethiol capping agent dissolved in toluene solvent. Owing to that, the reduction reaction of the Pt precursor salt takes place in a two-phase mixture of water and organic solvent and the forming PtNPs could be directly transferred to the organic phase for thiolation without using any phase-transfer agent. The alkanethiolated PtNPs would offer the strong benefit of introducing themselves into the CNTs nanochannels because of the non-polar interaction between their hydrocarbon chains and the hydrophobic CNT surfaces and also the low surface tension of organic solvent used for dispersion. Furthermore, the alkanethiol molecule is decomposed at low temperature, in the range of 200°C to 300°C, which presumably affects less the agglomeration of particles during the ligand removal process by heat treatment. The results of octadecanethiolated PtNPs filled CNTs under the ultrasonication before heat treatment are shown in Figures 61a and 61c. It is clearly seen that almost every CNT contains plenty of PtNPs inside. Despite the dense deposition on the inner wall of CNTs, the PtNPs remain well-dispersed with only a few interparticle aggregations that might be ascribed to the influences of ultrasonic power and also nonpolar compatibility of CNT support on hindering the interdigitation between alkyl chains surrounded on the individual Pt cluster.

The employed condition of heat treatment, at 360°C for 10 h, has no significant impact on that homogeneous dispersion (Figures 61b and 61d). The size of pre-synthesized PtNPs after removal of the protecting ligand is averaged to be 1.3 ± 0.3 nm (Figure 63c), which is prominently smaller and somewhat more uniform than those of PtNPs synthesized without using a stabilizing agent. As a matter of course, the PtNPs with small size and high dispersion are possible to provide the promising catalytic performance because of their large surface area.

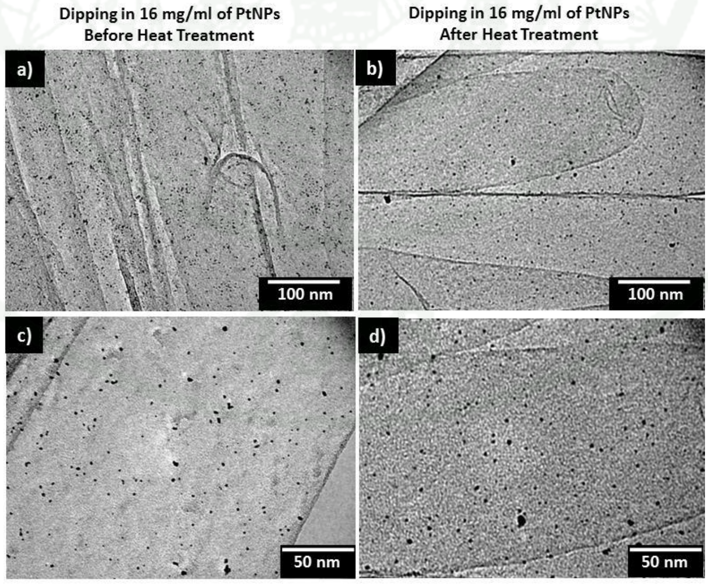

Figure 61 TEM photographs of pre-synthesized PtNPs loaded CNTs prepared by the ultrasonic assisted dipping method (a and c) followed by heat treatment (b and d).

Additionally, there are interesting results from SEM and also TEM observations (Figure 62) on and inside the pre-synthesized PtNPs/CNT-AAO film after heat treatment, respectively whereby almost pore mounts of CNTs are not blocked by the pre-synthesized PtNPs. Therefore, although the carbon surfaces on the external film are also compatible with the hydrocarbon backbone of alkanethiol, the pre-synthesized PtNPs are eluted effectively by washing with toluene. Even so, there are agglomerated Pt clusters to some extent found in the Figures 62e-f, however, only in the branch like tubes which might not limit the flows along the electrode. This can be suggested that not only the small and uniform size of catalyst particles but also the well-suited feature for facilitating the water and gas transports during the fuel cell operation can be achieved by means of loading the pre-synthesized PtNPs into the nanochannels of CNT-AAO film.

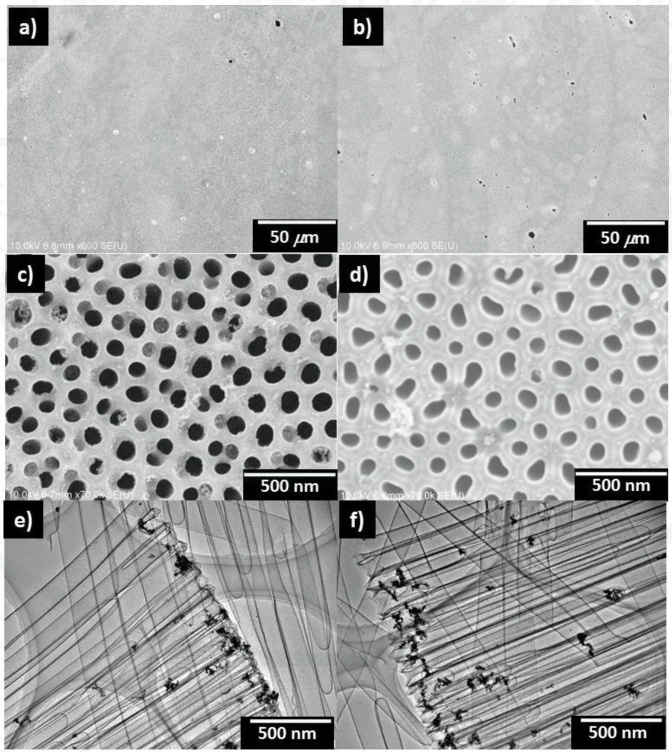

Figure 62 SEM photographs of top views on the pore side surface (a and c), barrier side surface (b and d) of the octadecanethiolated PtNPs/CNT-AAO film and TEM photographs at both sides of the pore mouth of octadecanethiolated PtNPs/CNTs after heat treatment.

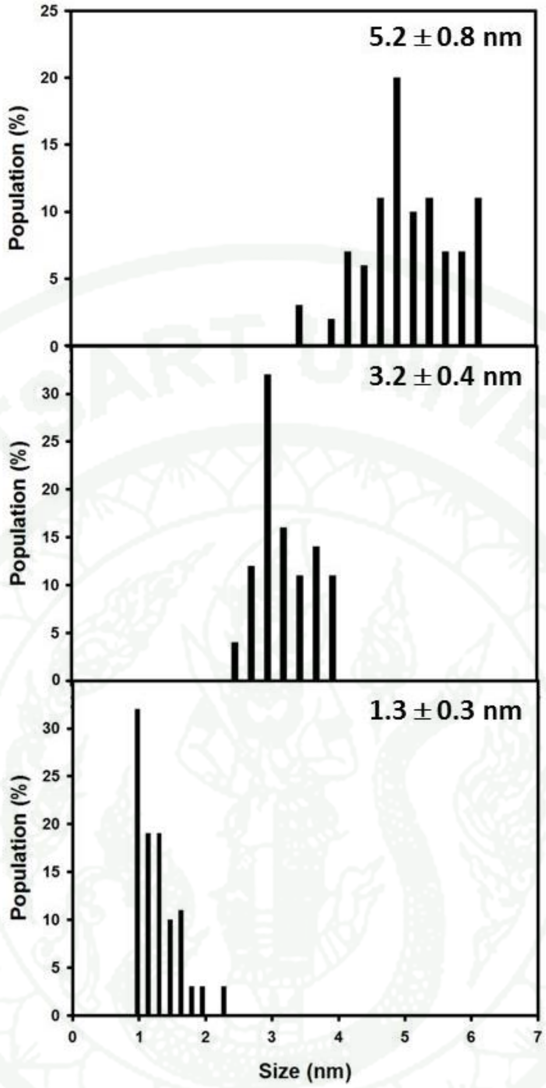

Figure 63 Size distributions accompanied with the corresponding average sizes of PtNPs deposited inside the CNT-AAO film prepared by direct deposition with washing (a) and without washing (b) excess metal precursor on the film surface before reduction and by pre-synthesis the PtNPs before loading (c).

3.4 Optimization of the thickness of the Nafion layer coated on the inner walls of CNT-AAO film.

In an ideal case of three phase boundary, the Nafion layer should not cover the metal particle where served as an active site for the electrochemical reaction or as an accessible area of fuel gases that is demonstrated in Figure 64. Thus, one of the important aims in this research is the optimization of the Nafion layer thickness properly with the deposited PtNPs size.

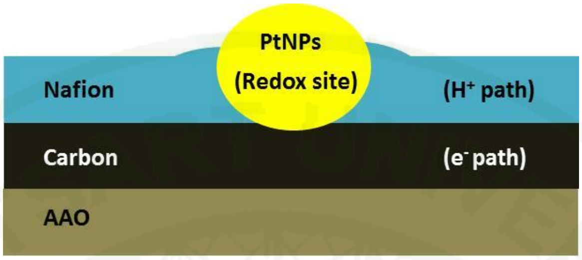

Figure 64 Proposed feature of the well-constructed three-phase boundary forming inside the pores of CNT-AAO film.

The first discussion on Nafion coating on the inner pore-wall of CNT-AAO film goes to the results from dipping the film in 0.5 wt% Nafion solution (dilution with 1-propanol) and drying under ambient condition as shown in Figures 62a-b. It is obvious that the electrolyte layers could be established and appear as the non-smooth coatings next to the carbon cavity along the tube. The Nafion layers are almost fully filled in the tube cavity so that they might cover the PtNP surfaces completely and would result in the difficult access of reactant gases towards the Pt catalyst sites. Hence to avoid such problem, the Nafion layer has to be thinner.

In order to decrease the thickness of the Nafion layer, the amount of Nafion substance should be carefully controlled. The values of the inner-wall surface area of CNTs and the metal particle size are both needed to estimate the amount of Nafion matter appropriate for forming a triple phase interfacial structure. Based on the equation for the cylindrical surface area i.e., $2\pi rh$, one CNT with 90 nm diameter, 20 μm in length and 5 nm in wall thickness is of 5.024×10^{-12} m^2 surface area. When multiplied with the pore number of 1x1 cm^2 CNT-AAO plate (2.6×10^9), the total pore surface area is approximated to be 13.0624×10^{-3} m^2. As mentioned before, that the Nafion thickness should be a bit less than the particle size of the deposited PtNPs and in the preliminary testing, PtNP size of 5 nm is selected to optimize the thickness of the Nafion layer. As multiplied, such total pore surface area with the target thickness of Nafion layer, the volume of the Nafion layer is about 65.312 x 10^{-9} cm^3 and the required weight of Nafion substance calculated with its density (2 mg/ml) will be 0.13 mg. At the concentration of 0.5 wt% of Nafion solution, in order to coat 0.13 mg of Nafion on the inner pore-wall of 1x1 cm^2 CNT-AAO film, 30 μl are thereby used (density of 1- propanol is 0.896 g/ml).

The obtained weight of Nafion after dropping with 30 μl of 0.5 wt% Nafion in 1-propanol is closer to that of calculation, which is about 0.1308 mg/1cm^2 CNT-AAO film. Therefore, the amount of Nafion coating is effectively controllable by dropping approach. Figures 65c-d present the outcomes prepared by the dropping and drying method in a normal system. The observed coating layers are quite thinner than those prepared by the previous dipping method. Nevertheless, the average thickness is still in the range of 30-40 nm, which is much more than the size of PtNPs (2-5 nm). Such that there are possible factors other than the rational quantity of applied Nafion matter that influence the forming aspect of the Nafion layer. As for the initial assumption, the higher thickness of the Nafion layer than the expected value may come from the rapid evaporation of the solvent in air hence, the Nafion matter is dried before going along the tube.

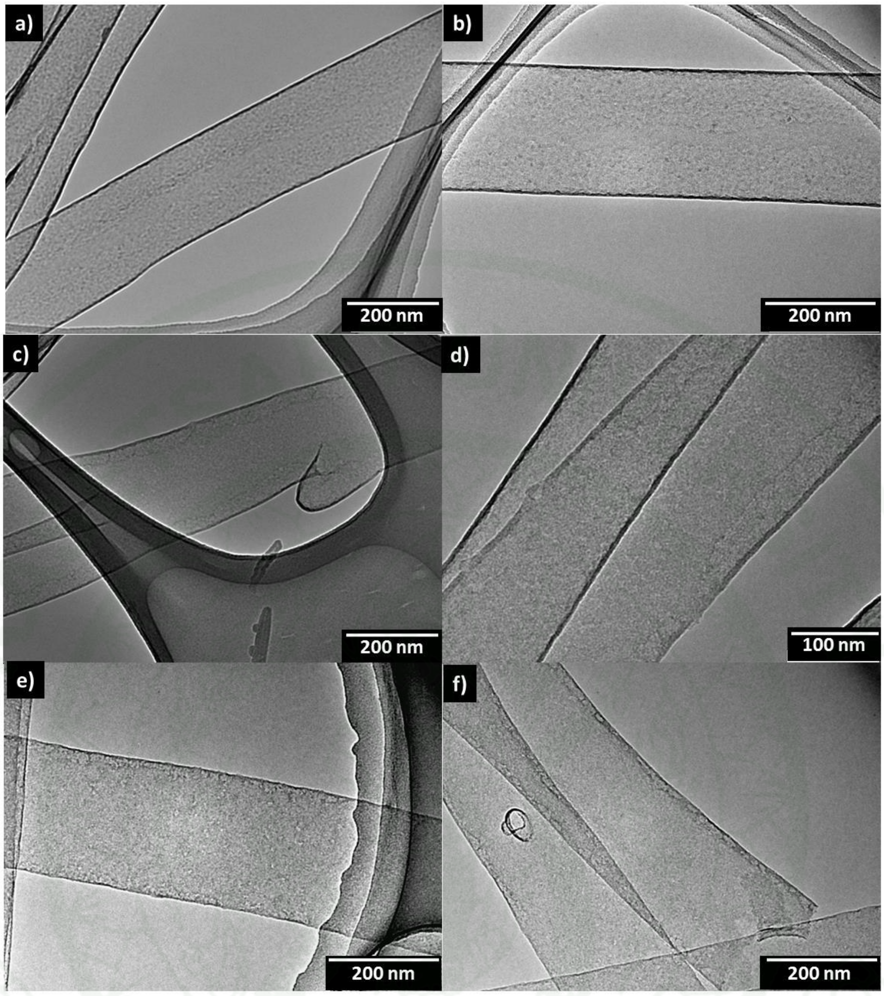

Figure 65 TEM photographs of Nafion coated on the inner walls of CNTs by dipping (a-b) and dropping (c-d) methods whereby drying in ambient condition and also dropping method whereby drying in a humidity controlled system (e-f).

As a matter of course, many physical parameters have a significant effect on the film appearance, such as viscosity, evaporation rate and surface tension of applied solution. Regarding this system, the low viscosity of the penetrated solution would enable Nafion to spread throughout the tube smoothly. Particularly, as combined with the atmospheric humidity control, whereby drying the film under the vapor of the solvent with regulated temperature, allows the formation of a homogeneous Nafion layer. Because of that, the solvent evaporation is retarded by the accumulated gaseous solvent in the drying chamber and, in turn, the Nafion could move along the tube entirely before drying up. According to the above reasons, the 10 times lower Nafion concentration at 0.05 wt% in 1-propanol is employed to introduce it into the CNT-AAO pores accompanied with drying under the abundant solvent vapor. The measured weight of dried Nafion, 0.1031 mg/1cm^2 CNT-AAO film, is a bit lower than that of dried Nafion prepared by normal dropping. This might be caused by the loss of being-dried Nafion solution because of its low viscosity. However, the received value remains in accordance with the calculation. In considering the Nafion features shown in Figures 65e-f, their layers are very thin with about 10-15 nm in thickness.

Nonetheless, to get a thinner Nafion layer, the concentration or the amount of Nafion solution should be reduced. Nafion concentration lower than 0.05 wt% makes the loss of dropped solution because of it easily spreading out from the CNT-AAO platform. Even dropping with less volume to avoid that loss, the process will be impractical due to it taking very long periods of time. In the case of the amount of reduction, the twice-lower volume of 0.05 wt% Nafion solution (150 μl) is used instead of the predicted volume from calculation. It relatively becomes relatively harder to indicate the Nafion layer, possibly because of the transparency of the very thin and loose layer. The slightly dense layer can be, however, observed in some tubes but they are found in similar manners as those prepared by dropping with 300 μl of 0.05 wt% of Nafion solution. Even though the thickness of the Nafion layer is not perfectly suitable with the size of PtNPs, the modified drying technique combined using a reasonable amount of Nafion matter is considered to be the effective strategy for casting a Nafion thin layer with the thickness most closely matching the size of PtNPs.

3.5 Fabrication the composite material of Nafion/PtNPs/CNT-AAO film and its assembly with a Nafion membrane (Membrane Electrode Assembly, MEA)

This section involves the construction of three phase interfacial structures of Nafion/PtNPs/CNT-AAO film whereby the PtNPs are synthesized via three different technique including (i) non-washing, (ii) washing the excess metal precursor on the surfaces of CNT-AAO film before metal reduction and (iii) pre-synthesizing the PtNPs before loading into the pores of CNTs followed by heat treatment to remove protecting ligands. As discussed earlier, the different methods allow the production of different sizes of deposited PtNPs in which the average sizes of about 5, 3 and 1.5 nm are produced by the methods (i), (ii) and (iii), respectively. Each PtNPs/CNT-AAO sample thus requires a specific amount of Nafion which can be approximated in the same way as in the Nafion coating experiment. Based on such calculations, 300 μl, 175 μl and 90 μl of 0.05wt% Nafion solution or equal to 0.131 mg, 0.078 mg and 0.036 mg of Nafion substance are needed for those aforementioned systems (i), (ii) and (iii), respectively. Again, the amount of Nafion phase is still in line with its corresponding estimation whereby the nafion dried weights of systems (i), (ii) and (iii), are 0.121, 0.072 and 0.040 mg, respectively.

From the observations on pore side and barrier side surfaces of Nafion/PtNPs/CNT-AAO films (Figure 66), the appearances of two samples in which the PtNPs are prepared by the washing technique (Figures 66d-e) and are pre-synthesized before loading into the pores of CNTs (Figures 66g-h), quite resemble the corresponding films before Nafion coating. The pore mouths on both sides of such films are not covered or plugged by Nafion polymer, implying that the entering of Nafion solution into the CNT pores is facilitated because of the absence of large PtNPs accumulated at the pore mouths.

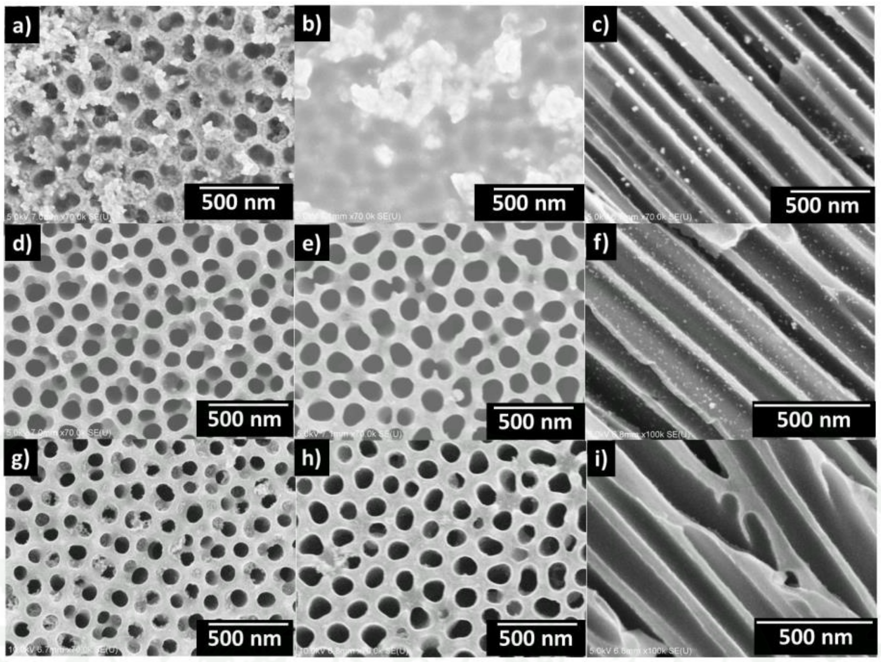

Figure 66 SEM photographs of the top views on pore side surfaces, barrier side surfaces and cross-sectional views of Nafion/PtNPs/CNT-AAO film whereby the PtNPs are prepared by non-washing (a, b and c, respectively) and washing (d, e and f, respectively) the excess metal precursor on the surfaces of CNT-AAO film before reduction and also the PtNPs are pre-synthesized before loading into the pores of CNTs are then subjected to heat treatment prior to coating with the Nafion solution (g, h and i, respectively).

Contrary to the non-washing sample, hinted by the low resolution of the image, there might be a thin insulating Nafion layer existing on the barrier side (Figure 66b) where the Nafion solution is dropped. Moreover, Nafion matter is also found to somewhat extent on the pore side of the CNT-AAO film (Figure 66a). This appearance on the film surface originated from the drying of some of the Nafion solution which could not penetrate into the tube cavities due to the flow hindrance caused by the large aggregated PtNPs at the pore mouths. This emphasizes that the congested PtNPs at the channel entrances would exhibit an adverse effect on the liquid and also gas transportations in the fuel cell. For the cross-sectional views of

Nafion/PtNPs/CNT-AAO film in Figures 66c, 66f and 66i, the size and dispersion of PtNPs deposited inside the pores are similar to those of the corresponding PtNPs/CNT-AAO samples. However, in the Nafion/pre-synthesized PtNPs/CNT-AAO, it is quite hard to determine these PtNPs because of the limitation of the SEM technique in detecting very small sized particles. Likewise, but by the intrinsic insulating property, the layer of Nafion is also identified as being difficult. Up to this point, it could be stated from these SEM images that the Nafion substance is plausibly coated as a thin layer without the formation itself in bulk shape such as a thin plate or rod inside the pores of CNTs.

TEM images in Figure 67 provide more and better details of the morphologies of PtNPs and Nafion decorated on the inner walls of tubes. The thin layers of Nafion can be observed along the tubes of all three samples. They are rough surfaces since the low concentrated solution of Nafion must pass through a great number of metal clusters which act as obstructions causing an unsmooth flow. Again, the morphological features of PtNPs are in accordance with those of SEM images and also of the corresponding PtNPs/CNT-AAO samples, implying that the PtNPs are well stabilized on the carbon surfaces and thereby are not agglomerated upon the diffusion of Nafion polymer.

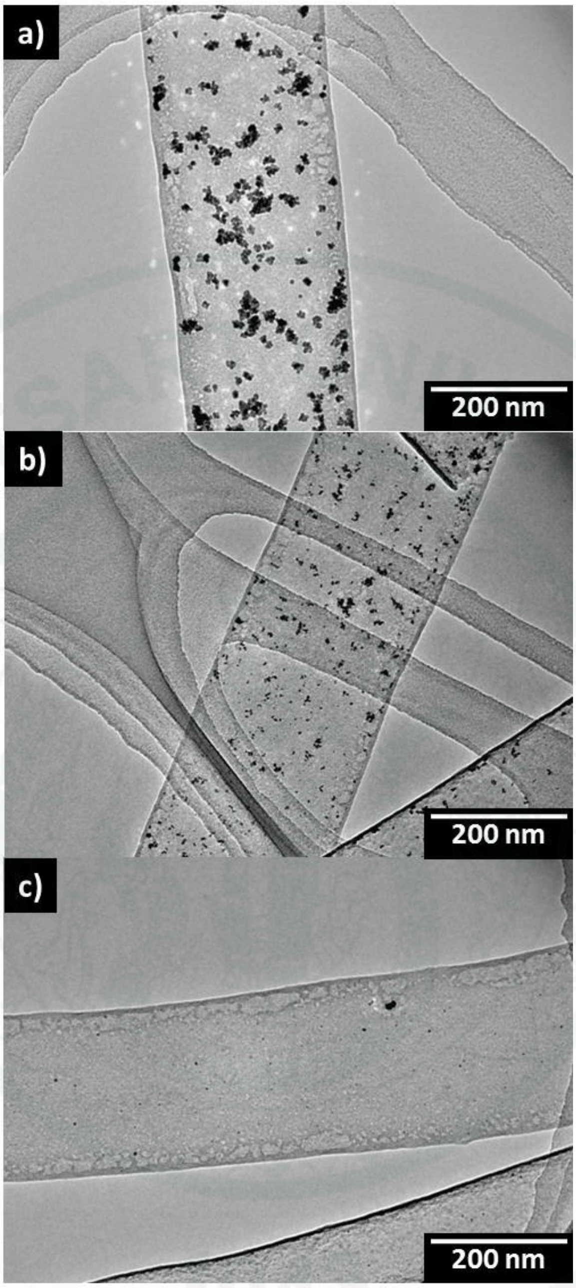

Figure 67 TEM photographs of Nafion/PtNPs loaded CNTs in which PtNPs are prepared by non-washing (a) and washing (b) the excess metal precursor on the surfaces of CNT-AAO film before reduction. For the last figure (c), PtNPs are pre-synthesized before loading into the pores of CNTs and subjected to the heat treatment prior to coating with Nafion solution.

All obtained Nafion/PtNPs/CNT-AAO films are taken for fabricating their MEA with Nafion membrane by the hot pressing approach. Whole parts of 1x1 cm^2 square film of Nafion/PtNPs/CNT-AAO are successfully attached on the Nafion membrane without cracking into small pieces as shown in Figure 68. Thus, the employed hot pressing condition in this study is quite appropriate to assemble Nafion film with even a brittle and thin CNT-AAO film. On the other hand, the CNT-AAO film is also one of versatile electrode platforms for fabricating MEA with the generally used hot pressing technique. The integrity of the hot pressed film could infer that the aligned pore structure of CNT-AAO film is still intact as the intended design for fuel cell application.

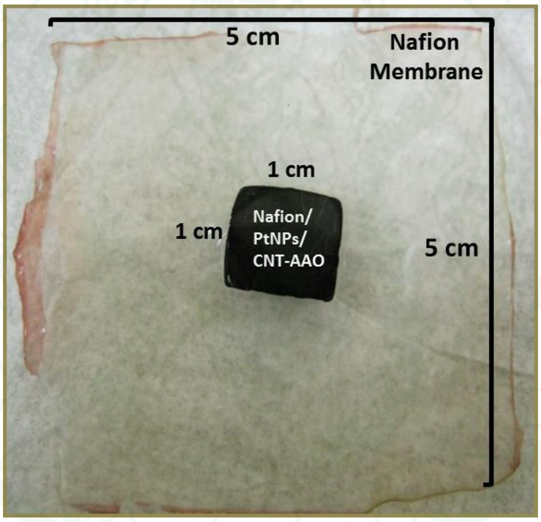

Figure 68 Membrane electrode assembly (MEA) of 5x5 cm^2 Nafion membrane and 1x1 cm^2 Nafion/PtNPs/CNT-AAO film.

4. Fine-tuning the sizes of positively charged AuNPs by adjusting the amount of PVP and DMAP stabilizers and synthesizing the AuNPs/CNTs nanocomposite by the facile electrostatic deposition of the size-controlled AuNPs onto the AAO-templated CNTs.

From the results of CNTs synthesis, the diameter and length of synthesized CNTs correspond to the pore size and the film thickness of the AAO template i.e., 35-55 nm and 20 μm, respectively (Figures 69a-c). Most observed CNTs are individual, that is one of the required features, for the absorption of AuNPs on the walls of CNTs to be facilitated. Nevertheless, few bundles of CNTs remain because of the incomplete removal of the carbon layer deposited on the AAO surface, but they help to make the measurement of the length of CNTs easier. Although the length of the initial liberated CNTs from the AAO template are quite uniform, the shorter CNTs could be found in the last step of the metal/CNTs preparation due to their being cut during the sonication applied for the washing and dispersion processes. In a high magnification TEM image (Figure 69d), under the used reaction parameters of CVD synthesis, the average wall thickness of CNTs is approximated to be 5 nm but the wall structure is of low crystallinity because the tube formation occurred at a low temperature. Consequently, the obtained CNTs contain many defects on their walls which in turn are reactive to interact with some incoming molecules. Especially for this case when the ill-crystalline sites were exposed to NaOH solution during the AAO dissolution step, the oxygen-containing functional groups could be readily formed on the outer surfaces of CNTs. Such polar oxygen species not only enhance the water dispersibility of CNTs by inducing an electric double layer (EDL) around each tube but are also the cause of the intense negative charges on CNTs surfaces evidenced by the substantial negative value of ζ-potential (-36.6 mV at pH ~7) as shown in Table 9.

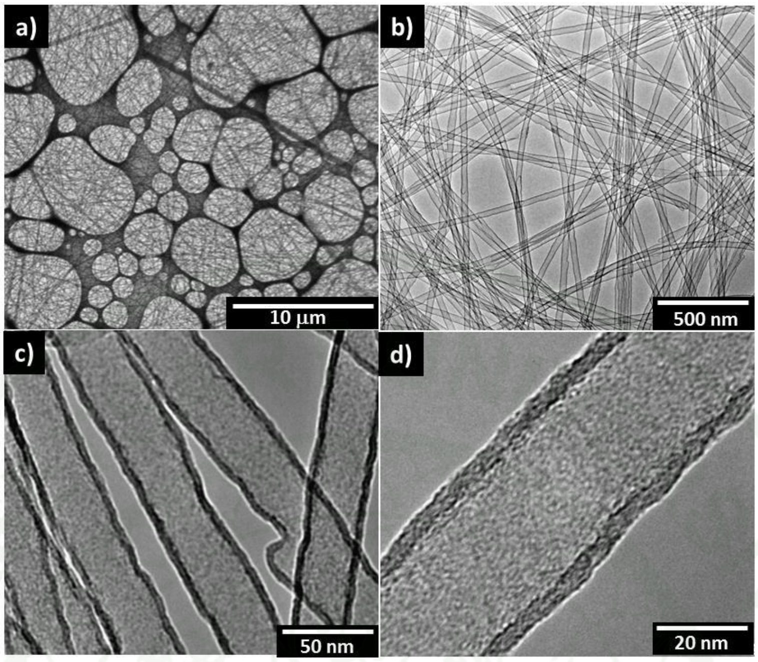

Figure 69 TEM photographs of AAO-templated CNTs at different magnification.

Table 9 Zeta (ζ) potentials of CNTs, Au-(P) and Au-(P1024:D1) at pH ~7.

Entry	Sample	Zeta Potential (mV)
1	CNTs	-36.6
2	Au-(P)	-31.2
3	Au-(P1024:D1)	-9.2

Accordingly, under the aims of this study, these bare CNTs without any post treatment are supposed to be the potential negatively charged support for depositions the positively charged AuNPs with the approach of electrostatic self-assembling. Besides tuning the surface charges over AuNPs, to establish the new method for size-controlled synthesis of such positively charged AuNPs is also the objective task. DMAP was utilized together with PVP to accomplish both goals in which the former could polarize positive the charge on the cluster surfaces of AuNPs whereas the latter is expected to limit the core size of AuNPs lower than that of ones synthesized with only a DMAP stabilizer. Therefore, the mixing ratio of PVP and DMAP is considered as a key parameter to produce AuNPs with various core sizes and, simultaneously, to engender the different degrees of positive surface charges of AuNPs due to the partially negative charges of oxygen-containing PVP molecules. The correlation between the size of AuNPs and their colloidal color is firstly discussed. Regarding to the surface plasmon resonance (SPR) phenomenon, the color of AuNPs solution depends on the size and shape of their particles. Such a unique property is normally used as a simple optical approach to roughly determine the relative size of AuNPs. Many experiments demonstrate that the colloidal AuNPs solutions exhibit systematical color changings from red to pink, violet and then blue if the sizes of AuNPs are bigger. Furthermore, very tiny AuNPs (~1-2 nm) present the brown color of the solution (Ghosh and Pal, 2007; Tsunoyama *et al.*, 2004, 2005, 2006;). As compared with our results in Figure 70, which is a photograph of all synthesized positively charged AuNPs solutions, there are also noticeable those aforementioned colors by developing from blue to violet, pink, red and brown when the mole ratios of PVP:DMAP are getting higher (rightmost to leftmost sides of Figure 70). These primary results follow with our precedent prediction in which the core size of AuNPs could be tuned by adjusting the PVP:DMAP ratios and the sizes of AuNPs become smaller as the PVP:DMAP ratios are increased due to the sterically hindering Au atom agglomerations of bulky PVP ligands.

Figure 70 A photograph of colloidal AuNPs solutions synthesized by varying PVP:DMAP mole ratios according to Table 1, starting from Au-(D) (rightmost side) to Au-(P512:D1) (leftmost side).

The SPR also contributes importantly to the UV−visible spectrum and generally, the SPR band of spherical Au nanostructure appears at around 520 nm (Ghosh and Pal, 2007). These characteristic peaks of all prepared AuNPs samples are normalized and shifted lower in respect to the increasing ratios of PVP:DMAP for ease of comparison of their curves as illustrated in Figure 71a. It is apparent that the Au-(D) shows the single SPR band with a strong and broad peak reaching into near-IR region, often because of the inhomogeneous size distribution of large and anisotropic AuNPs. However, the absorption bands of Au-(P1:D512) to Au-(P512:D1) are gradually less prominent, narrower and blue-shifted, perhaps arisen from the size reduction and more sphericity of particles which can be polarized by UV-Vis light homogeneously. Therefore, by raising the mole ratio of PVP:DMAP, the morphology of AuNPs are suggested to become not only smaller in size but also have a more isotropic structure. For the circumstances that AuNPs are functionalized onto the walls of CNTs (AuNPs/CNTs), SPR bands of all AuNPs/CNTs samples (Figure 71b) present similar fashions but slightly red-shifted as compared to corresponding the SPR bands of isolated AuNPs. The red-shift of SPR band of AuNPs in the composite is plausibly ascribed to the interparticle plasmon coupling from close adjacent particles and/or the interaction with the support. The above conjecture from the results implies that AuNPs are successfully immobilized on the bare CNTs.

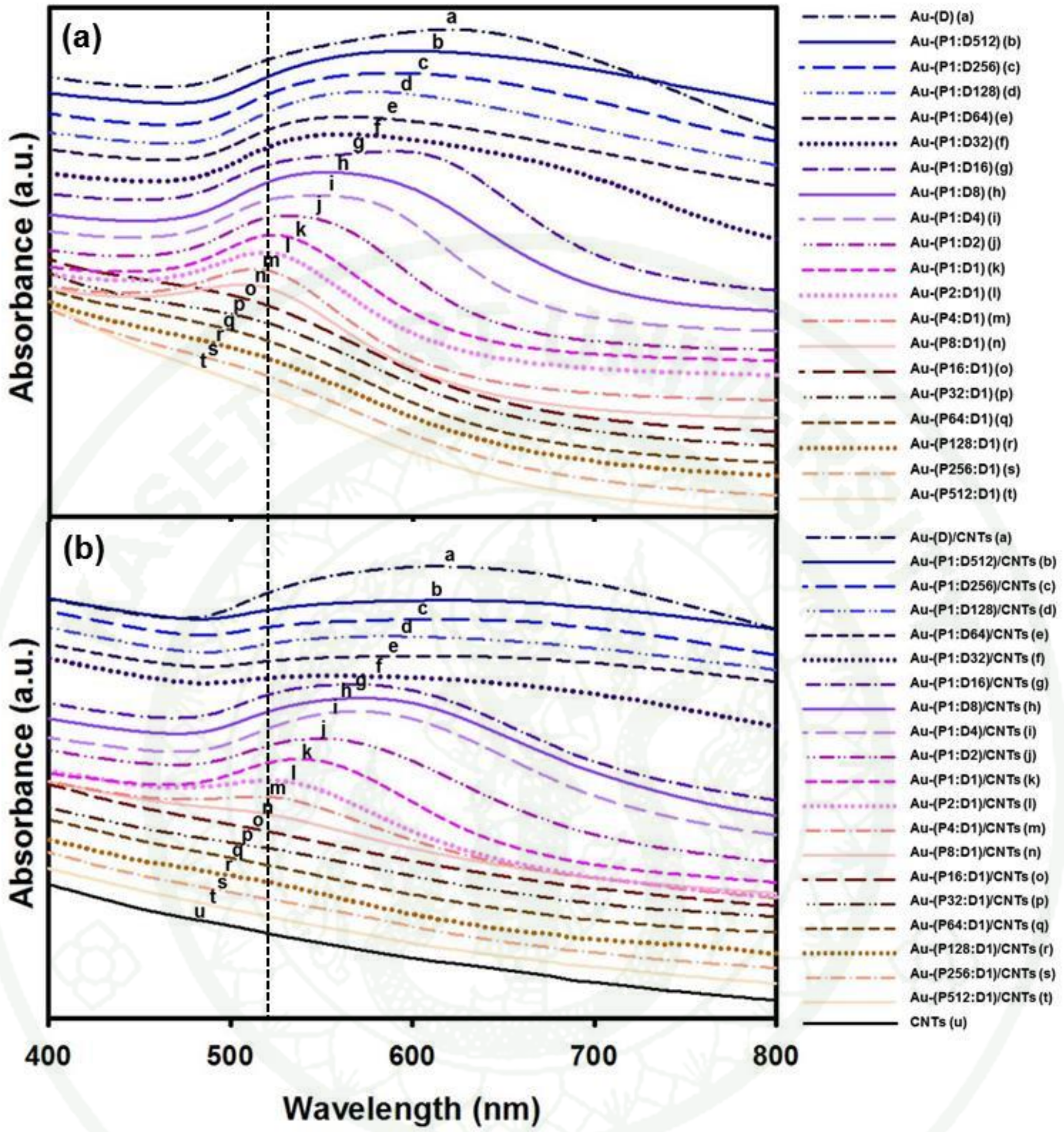

Figure 71 UV–Vis absorption spectra of (a) all synthesized AuNPs samples and (b) AuNPs/CNTs composites synthesized by varying PVP:DMAP mole ratios, Au-(D) to Au-(P512:D1). The UV–Vis absorption spectrum of bare CNTs is also compared in panel (b). Moreover, the dashed line that vertically passes through both panels is the position of absorption wavelength at 520 nm.

On the basis of electrostatic deposition, ζ potentials of interacting components are the crucial information to speculate whether the self-assembling is able to take place. Almost all ζ potentials of AuNPs samples (Table 10) are the positive values owing to positive charge density from the exocyclic nitrogen atom of DMAP. Especially for the sample without a nucleophilic PVP molecule, Au-(D), the ζ potential is maximized up to 19.6 eV but continuously reduced to 6.6 eV when the PVP:DMAP mole ratio is elevated equals to 1:4. Nevertheless, if the mole ratios of PVP:DMAP are over 1:4, there are only small fluctuations of ζ potential values from 4.0 to 6.0 eV. It is presumable that PVP has considerable influence to lessen the degree of positive surface charge on AuNPs. Particularly in the Au-(P512:D1) sample, the ζ potential abruptly changes to -2.3 eV. Up until this point, we can propose that all prepared AuNPs except Au-(P512:D1) will well self-assemble well towards the unmodified CNTs driven by the force of electrostatic attraction from the opposite charges between AuNPs and CNTs.

Table 10 Zeta (ζ) potentials of the synthesized AuNPs, Au-(D) to Au-(P512:D1), at pH ~7-8.

Entry	**Sample Code**	**ζ Potential (mV)**	**Entry**	**Sample Code**	**ζ Potential (mV)**
1	Au-(P512:D1)	-2.3	11	Au-(P1:D2)	5.5
2	Au-(P256:D1)	4.7	12	Au-(P1:D4)	6.6
3	Au-(P128:D1)	4.4	13	Au-(P1:D8)	10.3
4	Au-(P64:D1)	4.0	14	Au-(P1:D16)	9.9
5	Au-(P32:D1)	5.9	15	Au-(P1:D32)	12.4
6	Au-(P16:D1)	5.7	16	Au-(P1:D64)	14.8
7	Au-(P8:D1)	4.2	17	Au-(P1:D128)	15.4
8	Au-(P4:D1)	5.3	18	Au-(P1:D256)	17.2
9	Au-(P2:D1)	4.5	19	Au-(P1:D512)	19.3
10	Au-(P1:D1)	5.1	20	Au-(D)	19.6

According to the assumption, AuNPs are deposited densely and rather uniformly distributed along the outer walls of CNTs as shown in Figures 72 and 73 of low and high magnification TEM images of all studied AuNPs/CNTs samples. Moreover, the bindings between the AuNPs and the CNTs are robust enough to avoid the serious loss of particles even with repeated washing. Unexpectedly, Au-(P512:D1) particles are also attached on CNTs in spite of the fact that its colloidal solution has the negative ζ potential. In order to clarify further, the ζ potential distribution (Figure 74) of AuNPs colloids should be analyzed insightfully on the proportion of positively and negatively charged particles existing in the solution. It is found that, Au-(D) sample contains only positively charged particles, meanwhile the distribution peaks are gradually shifted to the lower ζ potential if increasing PVP:DMAP mole ratio. Particularly the Au-(P512:D1) sample, more than half of the distribution area is collected from negatively charged AuNPs that originates the negative value of ζ potential. Nonetheless, the remaining region of this distribution curve reveals that the positively charged AuNPs are still available for binding with CNTs. This thus elucidates why observing the depositions of AuNPs on CNTs in the Au-(P512:D1)/CNTs system. Moreover, AuNPs synthesized with the P1024:D1 mole ratio and with only PVP are also examined to emphasize the above explanations. Their values and distribution of ζ potential are demonstrated in Table 9 and Figure 75, respectively, indicate that almost all AuNPs of both samples are no longer positively charged. Hence, few AuNPs are capable of approaching CNTs as displayed in Figure 76. As far as we know from the literature, this is a new finding that CNTs obtained by the template method possess sufficient intense negative charge to assemble with positively charged AuNPs directly without any treatment on the surface of CNTs.

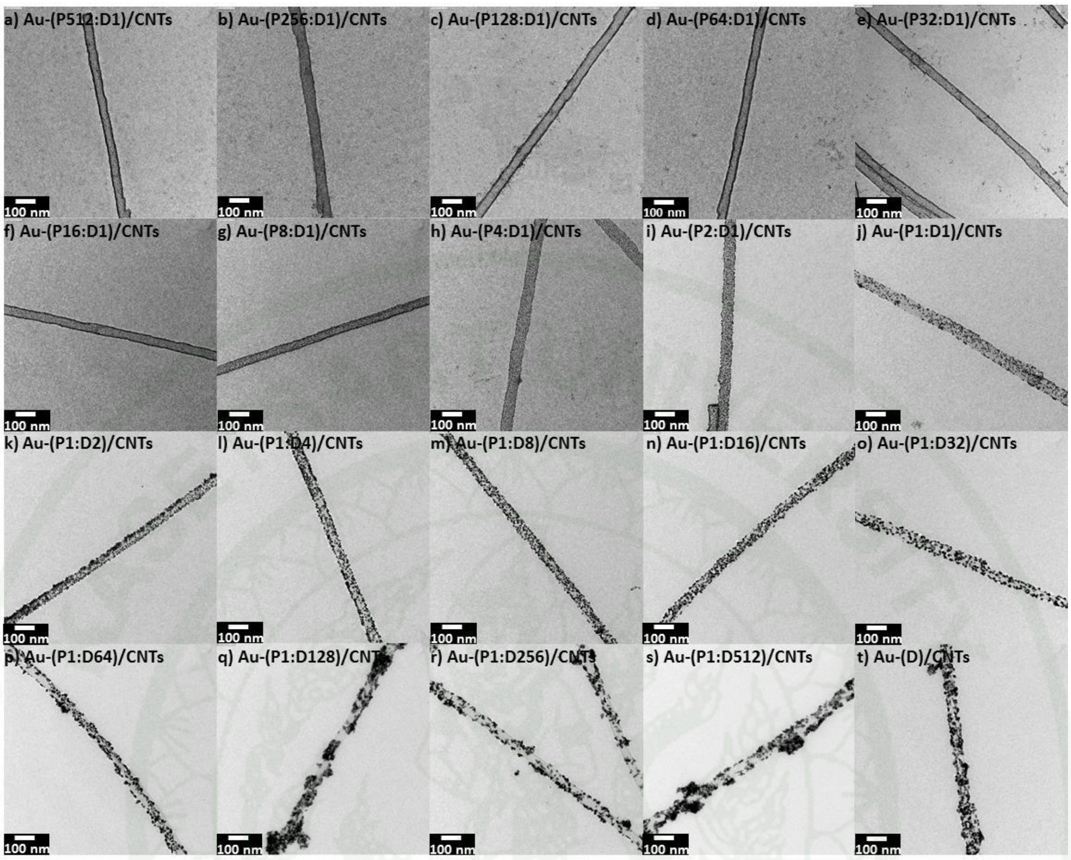

Figure 72 TEM images of all prepared AuNPs/CNTs composites, Au-(D)/CNTs to Au-(P512:D1)/CNTs.

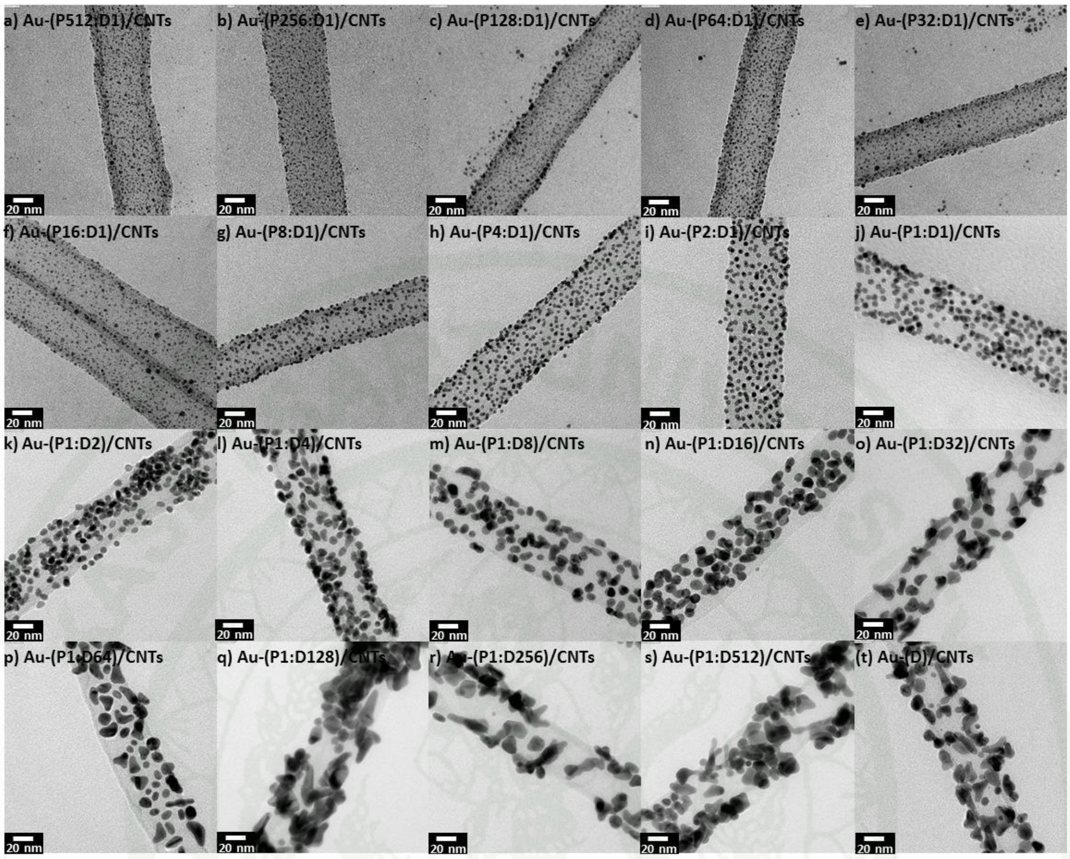

Figure 73 TEM images at higher magnification of all prepared AuNPs/CNTs composites, Au-(D)/CNTs to Au-(P512:D1)/CNTs.

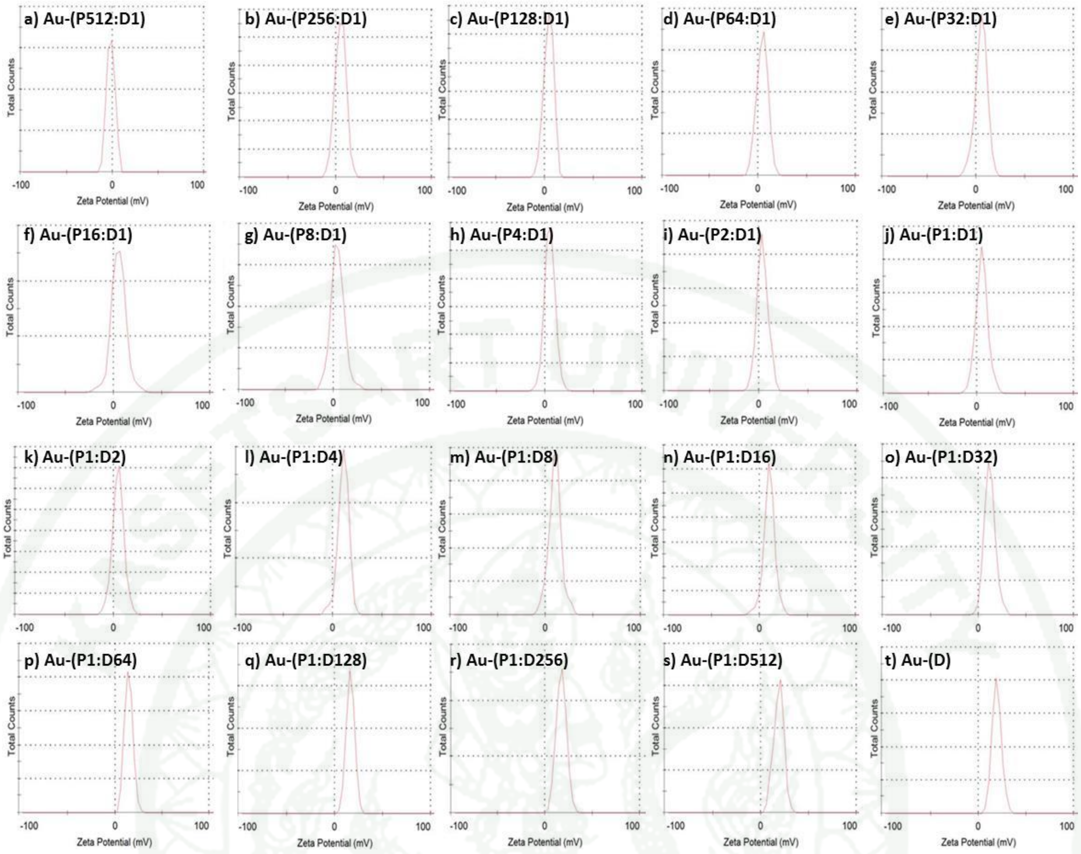

Figure 74 Zeta (ζ) potentials distributions of the synthesized AuNPs, Au-(D) to Au-(P512:D1).

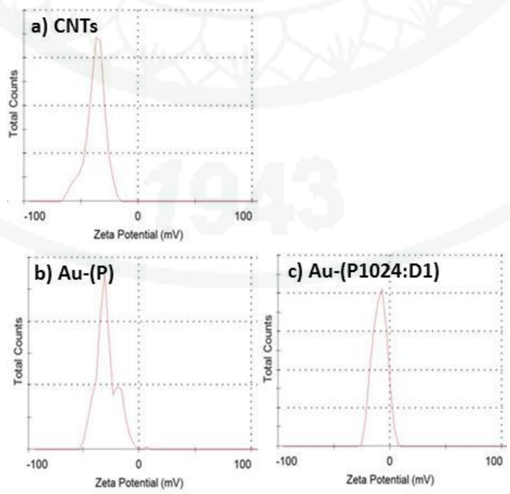

Figure 75 Zeta (ζ) potentials distributions of CNTs (a), Au-(P) (b) and Au-(P1024:D1) (c).

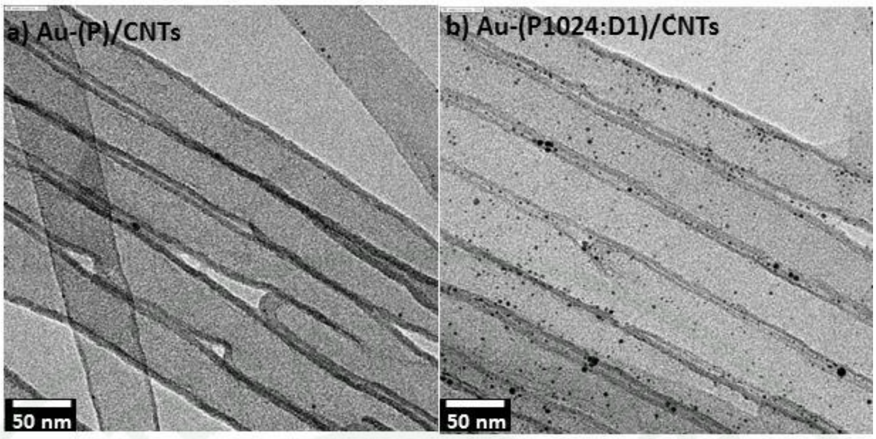

Figure 76 TEM images of all Au-(P)/CNTs (a) and Au-(P1024:D1)/CNTs composites (b).

Additionally, besides attaining the alternative procedure to optimize the molecular charges of AuNPs and CNTs suited for electrostatic self-assembling, we also get the great achievement within this method to produce such AuNPs/CNTs composites with several Au core sizes. In comparing the highly- magnified TEM images of all studied AuNPs/CNTs samples in Figure 77, it can be seen that the sizes of AuNPs decorated on the sidewalls of CNTs are quite different. For intensive evaluation pertaining to particle size, 250 AuNPs on CNTs are measured and summarized with the size distribution histograms accompanying the value of the average size in Figure 78.

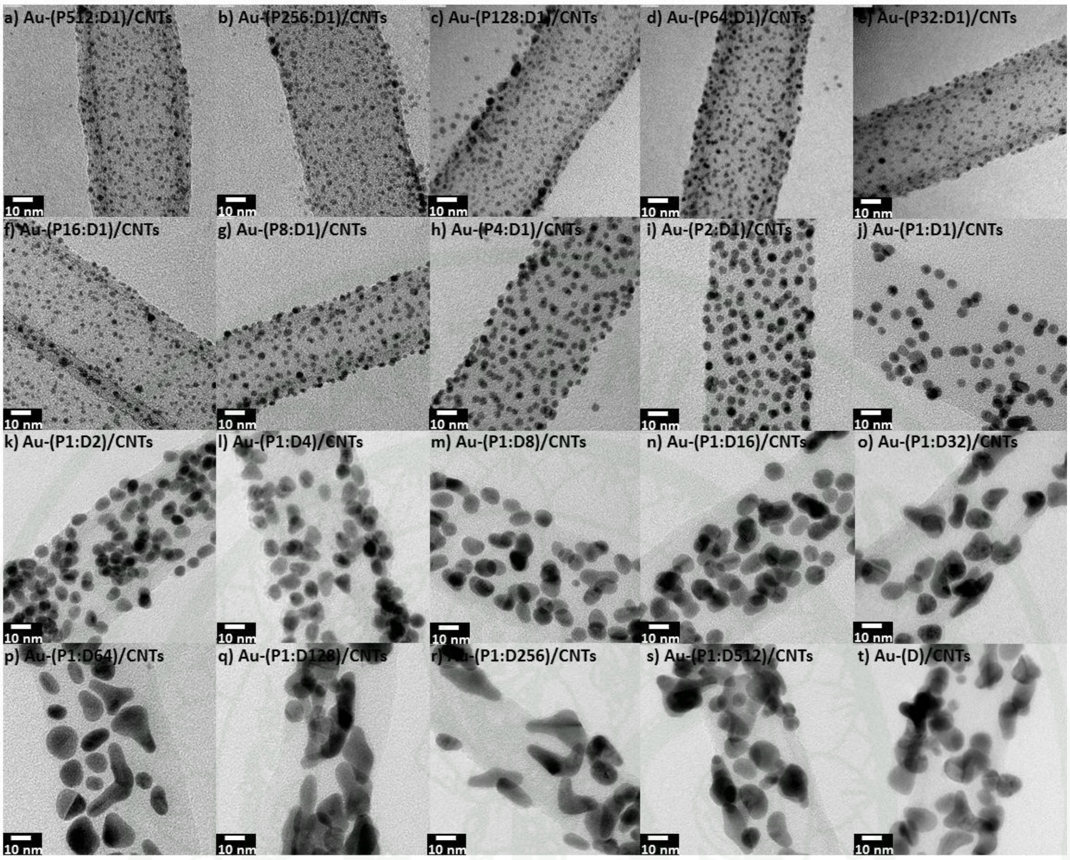

Figure 77 Highly-magnified TEM images of all prepared AuNPs/CNTs composites, Au-(D)/CNTs to Au-(P512:D1)/CNTs.

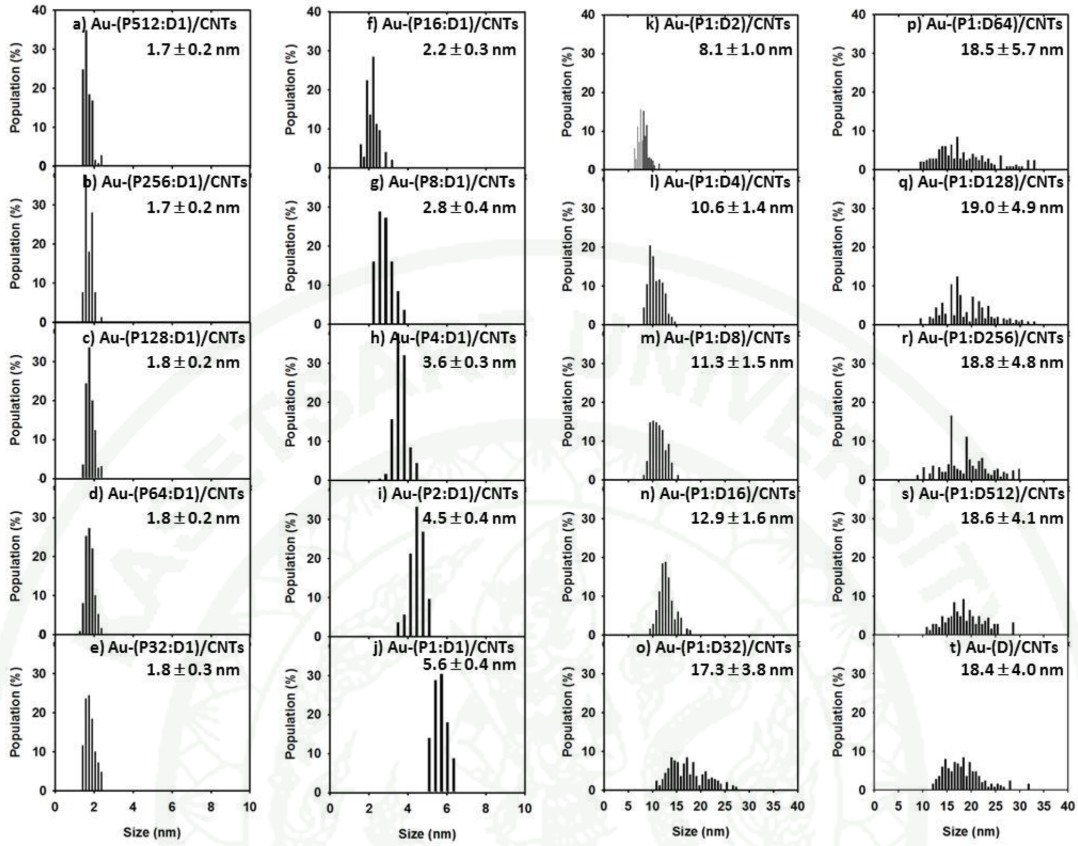

Figure 78 Size distribution histograms of AuNPs in all prepared AuNPs/CNTs composites, Au-(D)/CNTs to Au-(P512:D1)/CNTs.

Starting with the Au-(D)/CNTs sample (Figure 78t), due to the several anisotropic shapes of Au-(D), the size distribution of them is thereby polydisperse i.e., 10-30 nm together with the large average size of 18 nm. This outcome discloses that the DMAP molecule has low capability to prevent against the coalescence between reduced Au species during the chemical reduction process, possibly attributed to its less steric structure. One rational mechanism for anisotropic growth of DMAP stabilized AuNPs proposed by Danger *et al.* is the partial reduction of Au^{III} to Au^{I} species by Lewis base, DMAP (Danger *et al.*, 2012). After adding the strong reducing agent ($NaBH_4$), the pre-generated Au^{I}-DMAP complex is slowly transformed to Au^{0} monomer and then allows the thermodynamic adsorption of DMAP on Au(100) surface of the growing seed. This brings the overgrowth along the Au(111) direction and the creation of anisotropic AuNPs. Similar morphologies are also sustained in the

AuNPs/CNTs samples with increasing the mole ratios of PVP:DMAP until 1:32. It could be inferred that 1:32 is the minimum PVP:DMAP mole ratio in which PVP still has adequate competence to render the size of AuNPs.

Over this limitation level, the average diameters of AuNPs are significantly decreased with the estimated changing step about 2.3 nm i.e., from 17.3 nm of Au-(P1:D32)/CNTs to 12.9, 11.3, 10.6, 8.1, 5.6 nm of Au-(P1:D16)/CNTs, Au-(P1:D8)/CNTs, Au-(P1:D4)/CNTs, Au-(P1:D2)/CNTs and Au-(P1:D1)/CNTs, respectively (Figures 78j-o). In addition, by increasing PVP:DMAP mole ratios, those unsymmetrical particles are also transformed to be elliptical and eventually uniform spherical clusters. Accordingly, PVP plays more important role in the formations of small size and uniform spherical AuNPs. For the upper P1:D1 ratio, the mean sizes of AuNPs are also progressively decreased but with fewer changing steps about 0.7 nm i.e., from 5.6 nm of Au-(P1:D1)/CNTs to 4.5, 3.6, 2.8, 2.2 and 1.8 nm of Au-(P2:D1)/CNTs, Au-(P4:D1)/CNTs, Au-(P8:D1)/CNTs, Au-(P16:D1)/CNTs and Au-(P32:D1)/CNTs, respectively (Figures 78e-j).

By the keeping constant the amount of PVP but reducing that of DMAP instead, it ascertains that PVP is able to restrict the particle growth better than DMAP does. Unlike DMAP, PVP acts as only capping agent. Once Au^0 is initiated by $NaBH_4$, the PVP molecule can cover the nanocrystal nuclei quickly through the preferential coordination bonding with O atom. Attendance with the steric hindrance of the long polymer chain, PVP is certainly more powerful to impede the Au^0 aggregations and thus gives rise to the small and regular shaped AuNPs. It would be said that the success in tuning the sizes of AuNPs is owed to both thermodynamic and kinetic controls of DMAP and PVP, respectively. These results also prove that even though the varying of particle sizes lower than 5 nm is perceived as a difficult manipulation, our strategy by adjusting the PVP:DMAP mole ratios can certainly provide superior performance on fine-tuning the core sizes of AuNPs. However, the AuNPs of Au-(P32:D1)/CNTs to Au-(P512:D1)/CNTs (Figures 78a-e) are subtly different in core size, only 0.1 nm. This occurrence resembles that of the PVP:DMAP mole ratio lower than 1:32, but 32:1 is the maximum PVP:DMAP mole ratio that the

DMAP contributes for regulating the sizes of AuNPs. From the above results, the propensity of these size and shape alterations is consistent with the hints from the colors and UV-Visible spectra of AuNPs samples.

CONCLUSION

The sensing performances of Pt-SWCNT with defective and pristine SWCNTs for NO_2 and NH_3 are qualitatively studied by means of first principle calculations. Overall, in both Pt-deposited and Pt-doped SWCNTs, platinum increases the charge transfer and other calculated properties. For the adsorption of NO_2, the Pt-doped SWCNT shows slightly smaller binding energies and gap changes than the Pt-deposited SWCNT and the pristine SWCNT, respectively. Its electronic structure modulations are greater than that of the pristine SWCNT and its electron densities in the SWCNT unit are more disturbed than the ones of the Pt deposited SWCNT. The binding of Pt to the SWCNT in the doped case is much stronger than if it is deposited on the surface. For NH_3 adsorption, the Pt-doped SWCNT shows the largest electron transfers to the SWCNT. The Pt-doped SWCNT is further compared with the well-known reactive defected-SWCNT. Their abilities for capturing a NO_2 molecule are similar but for NH_3 the Pt-doped SWCNT is far better. The sensitivity of Pt-doped SWCNT is superior for both the detection of NO_2 and NH_3, because it exhibits larger energy gap changes and a larger charge transfer. These findings should be useful for the development of SWCNT-based nanosensor devices.

As for the decomposition of N_2O on stable composite catalysts consisting of Sc-, Ti- and V-doped (5,5)SWCNTs is investigated by periodic DFT calculations and compared with the same process on pristine (5,5)SWCNTs, the Sc-, Ti- and V-doped (5,5)SWCNTs behave like one would expect of potent catalysts for N_2O conversion. The barriers for the concerted activation of the metal-doped (5,5)SWCNTs are at least 5 times lower than the barrier for the undoped (5,5)SWCNT. Among the metal-doped (5,5)SWCNTs, the one doped with Vanadium is most active because it exhibits the strongest binding to N_2O and its reaction proceeds almost barrierless. The findings suggest that the ability of transition metal decorating nanotubes to deliver highly improved reaction kinetics for N_2O decomposition might also be worth investigating experimentally.

Apart from the theoretical investigation, the experimental fabrications of CNTs and their functionalization with commonly-used metal nanoparticles in applications are also studied.

The novel design electrode for fuel cell application is proposed by using AAO film as a well-aligned and uniform porous platform. Upon this model, the triple phase boundary reaction zone including proton conducting layer (Nafion), electron conducting layer (CNTs) and reactant adsorbed layer (platinum nanoparticles, PtNPs) are thus built on the inner walls of AAO pores. In order to satisfy the assumption of a high performance fuel cell catalyst, the electrode features and those three-phase interfacial structures are optimized properly to the requirements.

Firstly, the PtNPs can be stably and homogeneously decorated on the inner pore surfaces of CNT-AAO film. The catalyst particles are also able to be tuned in small and narrow distribution diameters of 3 and 1.5 nm by a common chemical reduction method and simply loading pre-synthesized alkanethiolated PtNPs, respectively. These sizes of PtNPs are known as an effective size range of electrocatalyst used in fuel cells. Moreover, owing to the trick of washing metal salt accumulated on the film before reduction, the pore entrances are no longer clogged by the large clusters of PtNPs that benefits the water and gas transports smoothly.

Secondly, the layer of Nafion electrolyte phase is successfully applied on pore walls of PtNPs/CNT-AAO film and thereby completing the three-phase reaction site. On the dropping method, the amount of Nafion substance is controllable in line with the calculated value relying on the size of PtNPs. Combining the developed slow drying technique under solvent vapor, the Nafion can be coated along the tube as thin layers ca. 10-15 nm. However, due to the non-smooth surface and low density of Nafion matter, the actual thickness is difficult to be identified. Nevertheless, it is found that this modified Nafion coating strategy creates the layer thickness which more closely matches to the size of PtNPs than those prepared by dipping and normal dropping methods.

The membrane electrode assembly (MEA) of Nafion/PtNPs/CNT-AAO electrode and Nafion membrane can be achieved as well without breakage by the commonly-used hot pressing approach. Therefore, the AAO film exhibits as not only the ordered porous scaffold for the catalyst layer but also as the robust supporter to preserve the aligned pore arrays intact. Up until this point, it could be suggested that the Nafion/PtNPs/CNT-AAO fabricated in this study is an alternative electrode architecture feasibly applied in PEMFC.

For the development of the new strategy to fine-tune the sizes of positively charged AuNPs by varying the used amount of PVP and DMAP stabilizers in which the mole ratios of PVP:DMAP were increased from 1:512 to 512:1. Each prepared AuNP sample was attracted by an electrostatic force to the outer walls of AAO-templated CNTs which were readily negatively charged during AAO dissolution. Under this one-step synthesis of AuNPs in an aqueous phase, the structures and charges of AuNPs are governed by both PVP and DMAP. The DMAP-protected AuNPs (Au-(D)) held the strong positive charge stemming from the exocyclic amine group but they possess the large size (~18 nm) and irregular shape. Meanwhile, the AuNPs become gradually smaller (until ~1.8 nm) and more spherical when the mole ratio of PVP:DMAP is getting higher starting from 1:32 to 32:1. Thus, it should be proposed that PVP performs the rendering morphologies of these positively charged AuNPs to be small and uniform particles. However, the positive charge values of AuNPs are consequently reduced as well due to the polar oxygen groups of PVP, and eventually leading to the electrostatic repulsion between AuNPs and CNTs if the mole ratio of PVP:DMAP exceeds 512:1.

All resultant positively charged AuNPs are densely and rather homogeneously deposited along the bare CNTs. Therefore, apart from good dispersibility in water, this is the first time that it is revealed that AAO-templated CNTs also exhibit the potential for decoration of positively charged AuNPs with a variety of sizes and amounts of surface charge. Moreover, the absence of modification over the CNTs surfaces makes this method much simpler and might lessen the hindrance of intermolecular electron transport in AuNPs/CNTs.

It is expected that these morphology-tunable AuNPs/CNTs composites would facilitate tailoring the structure dependent properties which are fundamental for the development of advanced nanodevices used in catalytic, electronic and optical applications. In addition, this approach is suggested to be a feasible model for preparing heterostructures of CNTs and other reactive metals.

LITERATURE CITED

Abu-Zied, B.M., W. Schwieger and A. Unger. 2008. Nitrous Oxide Decomposition over Transition Metal Exchanged ZSM-5 Zeolites Prepared by the Solid-State Ion-Exchange Method. **Appl. Catal. B: Environ.** 84 (1-2): 277-288.

Adelkhani, S. Nasoodi and A.H. Jafari. 2009. A Study of the Morphology and Optical Properties of Electropolished Aluminum in the VIS-IR Region. **Int. J. Electrochem. Sci.** 4 (2): 238-246.

Alexeyeva and Tammeveski. 2008. Electroreduction of Oxygen on Gold Nanoparticle/PDDA-MWCNT Nanocomposites in Acid Solution. **Anal. Chim. Acta** 618 (2): 140-146.

Andzelm, N. Govind and A. Maiti. 2006. Nanotube-Based Gas Sensors - Role of Structural Defects. **Chem. Phys. Lett.** 421 (1-3): 58-62.

Angelidis, T.N. and V. Tzitzios. 2003. Promotion of the Catalytic Activity of a Ag/Al_2O_3 Catalyst for the N_2O + CO Reaction by the Addition of Rh a Comparative Activity Tests and Kinetic Study. **Appl. Catal. B: Environ.** 41 (4): 357-370.

Antolini, E. 2009. Carbon Supports for Low-Temperature Fuel Cell Catalysts. **Appl. Catal. B: Environ.** 88 (1-2): 1-24.

Antolini, F. Cardellini, E. Giacometti and G. Squadrito. 2002. Study on the Formation of Pt/C Catalysts by Non-Oxidized Active Carbon Support and a Sulfur-Based Reducing Agent. **J. Mater. Sci.** 37 (1): 133-139.

Azamian, B.R., K.S. Coleman, J.J. Davis, N. Hanson and M.L.H. Green. 2002. Directly Observed Covalent Coupling of Quantum Dots to Single-Wall Carbon Nanotubes. **Chem. Commun.** (4): 366-367.

Bacon, F.T. 1969. Fuel Cells, Past, Present and Future. **Electrochim. Acta** 14 (7): 569-585.

Bai and Zhou. 2007. Computational Study of B- or N-Doped Single-Walled Carbon Nanotubes as NH_3 and NO_2 Sensors. **Carbon** 45 (10): 2105-2110.

Balasubramanian, K. and M. Burghard. 2005. Chemically Functionalized Carbon Nanotubes. **Small** 1 (2): 180-192.

Baughman, R.H., A.A. Zakhidov and W.A. De Heer. 2002. Carbon Nanotubes - the Route toward Applications. **Science** 297 (5582): 787-792.

Bayrakçeken, A. Smirnova, U. Kitkamthorn, M. Aindow, L. Türker, I. Eroğlu and C. Erkey. 2008. Pt-Based Electrocatalysts for Polymer Electrolyte Membrane Fuel Cells Prepared by Supercritical Deposition Technique. **J. Power Sources** 179 (2): 532-540.

Bessel, C.A., K. Laubernds, N.M. Rodriguez and R.T.K. Baker. 2001. Graphite Nanofibers as an Electrode for Fuel Cell Applications. **J. Phys. Chem. B** 105 (6): 1115-1118.

Bethune, D.S., C.H. Kiang, M.S. De Vries, G. Gorman, R. Savoy, J. Vazquez and R. Beyers. 1993. Cobalt-Catalysed Growth of Carbon Nanotubes with Single-Atomic-Layer Walls. **Nature** 363 (6430): 605-607.

Bettinger, H.F. 2006. Addition of Carbenes to the Sidewalk of Single-Walled Carbon Nanotubes. **Chem. Eur. J.** 12 (16): 4372-4379.

Bittencourt, A. Felten, B. Douhard, J. Ghijsen, R.L. Johnson, W. Drube and J.J. Pireaux. 2006. Photoemission Studies of Gold Clusters Thermally Evaporated on Multiwall Carbon Nanotubes. **Chem. Phys.** 328 (1-3): 385-391.

Biver, A. Corti, N. Eltugral, E. Lorenzini, M. Masini, A. Paolicchi, A. Pucci, G. Ruggeri, F. Secco and M. Venturini. 2012. Analysis of 4-Dimethylaminopyridine (Dmap)-Gold Nanoparticles Behaviour in Solution and of Their Interaction with Calf Thymus DNA and Living Cells. **J. Nanopart. Res.** 14 (2):

Blase, L.X. Benedict, E.L. Shirley and S.G. Louie. 1994. Hybridization Effects and Metallicity in Small Radius Carbon Nanotubes. **Phys. Rev. Lett.** 72 (12): 1878-1881.

Boissel, S. Tahir and C.A. Koh. 2006. Catalytic Decomposition of N_2O over Monolithic Supported Noble Metal-Transition Metal Oxides. **Appl. Catal. B: Environ.** 64 (3-4): 234-242.

Boudghene Stambouli, A. and E. Traversa. 2002. Fuel Cells, an Alternative to Standard Sources of Energy. **Renew.Sust.Energ.Rev.** 6 (3): 297-306.

Brumlik, C.J. and C.R. Martin. 1991. Template Synthesis of Metal Microtubules. **J. Am. Chem. Soc.** 113 (8): 3174-3175.

Cai, Y. Yu, Y. Lan, F.J. Dufort, G. Xiong, T. Paudel, Z. Ren, D.J. Wagner and T.C. Chiles. 2007a. Glucose Sensors Made of Novel Carbon Nanotube-Gold Nanoparticle Composites. **BioFactors** 30 (4): 271-277.

Cai, Y. Yu, Y. Lan, F.J. Dufora, G. Xiong, T. Paudel, Z. Ren, D.J. Wagner and T.C. Chiles. 2007b. Glucose Sensors Made of Novel Carbon Nanotube-Gold Nanoparticle Composites. **BioFactors** 30 271-277.

Carabineiro, S.A., F. Brás Fernandes, A.M. Ramos, J. Vital and I.F. Silva. 2000. Vanadium as a Catalyst for NO, N_2O and CO_2 Reaction with Activated Carbon. **Catal. Today** 57 (3-4): 305-312.

Carabineiro, S.A., F.B. Fernandes, J.S. Vital, A.M. Ramos and I.M. Fonseca. 2005. N_2O Conversion Using Manganese Binary Mixtures Supported on Activated Carbon. **Appl. Catal. B: Environ.** 59 (3-4): 181-186.

Carabineiro, S.A., F.B. Fernandes, R.J.C. Silva, J.S. Vital, A.M. Ramos and I.M. Fonseca. 2008. N_2O Reduction by Activated Carbon over Iron Bimetallic Catalysts. **Catal. Today** 133-135 (1-4): 441-447.

Carmo, V.A. Paganin, J.M. Rosolen and E.R. Gonzalez. 2005. Alternative Supports for the Preparation of Catalysts for Low-Temperature Fuel Cells: The Use of Carbon Nanotubes. **J. Power Sources** 142 (1-2): 169-176.

Carrillo, J.A. Swartz, J.M. Gamba, R.S. Kane, N. Chakrapani, B. Wei and P.M. Ajayan. 2003. Noncovalent Functionalization of Graphite and Carbon Nanotubes with Polymer Multilayers and Gold Nanoparticles. **Nano Lett.** 3 (10): 1437-1440.

Chai, G.S., S.B. Yoon, J.S. Yu, J.H. Choi and Y.E. Sung. 2004. Ordered Porous Carbons with Tunable Pore Sizes as Catalyst Supports in Direct Methanol Fuel Cell. **J. Phys. Chem. B** 108 (22): 7074-7079.

Chaki, M. Arai, T. Ebina and M. Shimokawabe. 2005. Catalytic Reduction of N_2O by Various Hydrocarbons over Fe-ZSM-5: Nature and Reactivity of Carbonaceous Deposits. **J. Mol. Catal. A: Chem.** 227 (1-2): 187-196.

Chan, K.Y., J. Ding, J. Ren, S. Cheng and K.Y. Tsang. 2004. Supported Mixed Metal Nanoparticles as Electrocatalysts in Low Temperature Fuel Cells. **J. Mater. Chem.** 14 (4): 505-516.

Chang, J.D. Lee, S.M. Lee and Y.H. Lee. 2001. Adsorption of NH_3 and NO_2 Molecules on Carbon Nanotubes. **Appl. Phys. Lett.** 79 (23): 3863-3865.

Che, B.B. Lakshmi, E.R. Fisher and C.R. Martin. 1998a. Carbon Nanotubule Membranes for Electrochemical Energy Storage and Production. **Nature** 393 (6683): 346-349.

Che, B.B. Lakshmi, C.R. Martin, E.R. Fisher and R.S. Ruoff. 1998b. Chemical Vapor Deposition Based Synthesis of Carbon Nanotubes and Nanofibers Using a Template Method. **Chem. Mater.** 10 (1): 260-267.

Chen and Kawazoe. 2006. Interaction between a Single Pt Atom and a Carbon Nanotube Studied by Density Functional Theory. **Phys. Rev. B: Condens. Matter Mater. Phys.** 73 (12):

Cheng, H.M., F. Li, X. Sun, S.D.M. Brown, M.A. Pimenta, A. Marucci, G. Dresselhaus and M.S. Dresselhaus. 1998. Bulk Morphology and Diameter Distribution of Single-Walled Carbon Nanotubes Synthesized by Catalytic Decomposition of Hydrocarbons. **Chem. Phys. Lett.** 289 (5-6): 602-610.

Chiang, L.Y., J.B. Bhonsle, L. Wang, S.F. Shu, T.M. Chang and J.R. Hwu. 1996. Efficient One-Flask Synthesis of Water-Soluble [60]Fullerenols. **Tetrahedron** 52 (14): 4963-4972.

Cho and Caruso. 2005. Investigation of the Interactions between Ligand-Stabilized Gold Nanoparticles and Polyelectrolyte Multilayer Films. **Chem. Mater.** 17 (17): 4547-4553.

Cho, C. Kim, H. Moon, Y. Choi, S. Park, C.K. Lee and S. Han. 2008. Electronic Structure Tailoring and Selective Adsorption Mechanism of Metal-Coated Nanotubes. **Nano Lett.** 8 (1): 81-86.

Choi, H.C., M. Shim, S. Bangsaruntip and H. Dai. 2002. Spontaneous Reduction of Metal Ions on the Sidewalls of Carbon Nanotubes. **J. Am. Chem. Soc.** 124 (31): 9058-9059.

Choi, H.J., I.Y. Jeon, D.W. Chang, D. Yu, L. Dai, L.S. Tan and J.B. Baek. 2011. Preparation and Electrocatalytic Activity of Gold Nanoparticles Immobilized on the Surface of 4-Mercaptobenzoyl-Functionalized Multiwalled Carbon Nanotubes. **J. Phys. Chem. C** 115 (5): 1746-1751.

Cindrella, A.M. Kannan, J.F. Lin, K. Saminathan, Y. Ho, C.W. Lin and J. Wertz. 2009. Gas Diffusion Layer for Proton Exchange Membrane Fuel Cells-a Review. **J. Power Sources** 194 (1): 146-160.

Coleman, K.S., S.R. Bailey, S. Fogden and M.L.H. Green. 2003. Functionalization of Single-Walled Carbon Nanotubes Via the Bingel Reaction. **J. Am. Chem. Soc.** 125 (29): 8722-8723.

Coq, M. Mauvezin, G. Delahay and S. Kieger. 2000. Kinetics and Mechanism of the N_2O Reduction by NH_3 on a Fe-Zeolite-Beta Catalyst. **J. Catal.** 195 (2): 298-303.

Correa-Duarte, M.A., N. Sobal, L.M. Liz-Marzán and M. Giersig. 2004. Linear Assemblies of Silica-Coated Gold Nanoparticles Using Carbon Nanotubes as Templates. **Adv. Mater.** 16 (23-24): 2179-2184.

Correa-Duarte, M.A., J. Pérez-Juste, A. Sánchez-Iglesias, M. Giersig and L.M. Liz-Marzán. 2005. Aligning Au Nanorods by Using Carbon Nanotubes as Templates. **Angew. Chem. Int. Ed.** 44 (28): 4375-4378.

Costamagna and Srinivasan. 2001. Quantum Jumps in the Pemfc Science and Technology from the 1960s to the Year 2000: Part I. Fundamental Scientific Aspects. **J Power Sources** 102 (1-2): 242-252.

Dai, H. 2002. Carbon Nanotubes: Synthesis, Integration, and Properties. **Acc. Chem. Res.** 35 (12): 1035-1044.

Dai, A.G. Rinzler, P. Nikolaev, A. Thess, D.T. Colbert and R.E. Smalley. 1996. Single-Wall Nanotubes Produced by Metal-Catalyzed Disproportionation of Carbon Monoxide. **Chem. Phys. Lett.** 260 (3-4): 471-475.

Danger, B.R., D. Fan, J.P. Vivek and I.J. Burgess. 2012. Electrochemical Studies of Capping Agent Adsorption Provide Insight into the Formation of Anisotropic Gold Nanocrystals. **ACS Nano** 6 (12): 11018-11026.

Debbagh, M.N., A. Bueno-López, C.S.M.d. Lecea and J. Pérez-Ramírez. 2007. Kinetics of the N_2O + CO Reaction over Steam-Activated Fezsm-5. **Appl. Catal. A: Gen** 327 (1): 66-72.

Delabie, C. Vinckier, M. Flock and K. Pierloot. 2001. Evaluating the Activation Barriers for Transition Metal N_2O Reactions. **J. Phys. Chem. A** 105 (22): 5479-5485.

Delley, B. 1990. An All-Electron Numerical Method for Solving the Local Density Functional for Polyatomic Molecules. **J. Chem. Phys.** 92 (1): 508-517.

Delley, B. 2000. From Molecules to Solids with the Dmol 3 Approach. **J. Chem. Phys.** 113 (18): 7756-7764.

Delley, B. 2002. Hardness Conserving Semilocal Pseudopotentials. **Phys. Rev. B: Condens. Matter Mater. Phys.** 66 (15): 1551251-1551259.

Dicks, A.L. 2006. The Role of Carbon in Fuel Cells. **J. Power Sources** 156 (2): 128-141.

Dong, S.K., T. Lee and K.E. Geckeler. 2006. Hole-Doped Single-Walled Carbon Nanotubes: Ornamenting with Gold Nanoparticles in Water. **Angew. Chem. Int. Ed.** 45 (1): 104-107.

Dong, C.M. Lau, A. Lohani, S.G. Mhaisalkar, J. Kasim, Z. Shen, X. Ho, J.A. Rogers and L.J. Li. 2008. Electrical Detection of Femtomolar DNA Via Gold-Nanoparticle Enhancement in Carbon-Nanotube-Network Field-Effect Transistors. **Adv. Mater.** 20 (12): 2389-2393.

Dudin, P.V., P.R. Unwin and J.V. Macpherson. 2010. Electrochemical Nucleation and Growth of Gold Nanoparticles on Single-Walled Carbon Nanotubes: New Mechanistic Insights. **J. Phys. Chem. C** 114 (31): 13241-13248.

Durgun, S. Dag, V.M.K. Bagci, O. Gülseren, T. Yildirim and S. Ciraci. 2003. Systematic Study of Adsorption of Single Atoms on a Carbon Nanotube. **Phys. Rev. B: Condens. Matter Mater. Phys.** 67 (20): 2014011-2014014.

Ellis, A.V., K. Vijayamohanan, R. Goswami, N. Chakrapani, L.S. Ramanathan, P.M. Ajayan and G. Ramanath. 2003. Hydrophobic Anchoring of Monolayer-Protected Gold Nanoclusters to Carbon Nanotubes. **Nano Lett.** 3 (3): 279-282.

Endo, K. Takeuchi, K. Kobori, K. Takahashi, H.W. Kroto and A. Sarkar. 1995. Pyrolytic Carbon Nanotubes from Vapor-Grown Carbon Fibers. **Carbon** 33 (7): 873-881.

Fraga, M.A., E. Jordão, M.J. Mendes, M.M.A. Freitas, J.L. Faria and J.L. Figueiredo. 2002. Properties of Carbon-Supported Platinum Catalysts: Role of Carbon Surface Sites. **J. Catal.** 209 (2): 355-364.

Futerko, P.M. and A. Fontijn. 1991. Activation Barriers for Series of Exothermic Homologous Reactions. I. Metal Atom Reactions with N_2O. **J. Chem. Phys.** 95 (11): 8065-8072.

Gamez, D. Richard, P. Gallezot, F. Gloaguen, R. Faure and R. Durand. 1996. Oxygen Reduction on Well-Defined Platinum Nanoparticles inside Recast Ionomer. **Electrochim. Acta** 41 (2): 307-314.

Gasteiger, H.A., S.S. Kocha, B. Sompalli and F.T. Wagner. 2005. Activity Benchmarks and Requirements for Pt, Pt-Alloy, and Non-Pt Oxygen Reduction Catalysts for PEMFCs. **Appl. Catal. B: Environ.** 56 (1-2 SPEC. ISS.): 9-35.

Georgakilas, D. Gournis, V. Tzitzios, L. Pasquato, D.M. Guldi and M. Prato. 2007. Decorating Carbon Nanotubes with Metal or Semiconductor Nanoparticles. **J. Mater. Chem.** 17 (26): 2679-2694.

Ghosh, S.K. and T. Pal. 2007. Interparticle Coupling Effect on the Surface Plasmon Resonance of Gold Nanoparticles: From Theory to Applications. **Chem. Rev.** 107 (11): 4797-4862.

Gingery and Bühlmann. 2008. Formation of Gold Nanoparticles on Multiwalled Carbon Nanotubes by Thermal Evaporation. **Carbon** 46 (14): 1966-1972.

Gittins, D.I. and F. Caruso. 2001. Spontaneous Phase Transfer of Nanoparticulate Metals from Organic to Aqueous Media. **Angew. Chem. Int. Ed.** 40 (16): 3001-3004.

Gittins, D.I., A.S. Susha, B. Schoeler and F. Caruso. 2002. Dense Nanoparticulate Thin Films Via Gold Nanoparticle Self-Assembly. **Adv. Mater.** 14 (7): 508-512.

Gobbo, M.C. Biesinger and M.S. Workentin. 2013. Facile Synthesis of Gold Nanoparticle (Aunp)-Carbon Nanotube (CNT) Hybrids through an Interfacial Michael Addition Reaction. **Chem. Commun.** 49 (27): 2831-2833.

Gong, F. Du, Z. Xia, M. Durstock and L. Dai. 2009. Nitrogen-Doped Carbon Nanotube Arrays with High Electrocatalytic Activity for Oxygen Reduction. **Science** 323 (5915): 760-764.

Grabow, L.C., A.A. Gokhale, S.T. Evans, J.A. Dumesic and M. Mavrikakis. 2008. Mechanism of the Water Gas Shift Reaction on Pt: First Principles, Experiments, and Microkinetic Modeling. **J. Phys. Chem. C** 112 (12): 4608-4617.

Grot, W. 1985. Discovery and Development of Nafion Perfluorinated Membranes. **Chem. Ind. (London)** (19): 647-649.

Gruver, G.A. 1978. The Corrosion of Carbon Black in Phosphoric Acid. **J. Electrochem. Soc.** 125 (10): 1719-1720.

Gülseren, T. Yildirim and S. Ciraci. 2002. Systematic Ab Initio Study of Curvature Effects in Carbon Nanotubes. **Phys. Rev. B: Condens. Matter Mater. Phys.** 65 (15): 1534051-1534054.

Guo, P. Nikolaev, A. Thess, D.T. Colbert and R.E. Smalley. 1995. Catalytic Growth of Single-Walled Manotubes by Laser Vaporization. **Chem. Phys. Lett.** 243 (1-2): 49-54.

Guo, S. Guo, Y. Fang and S. Dong. 2010. Gold Nanoparticle/Carbon Nanotube Hybrids as an Enhanced Material for Sensitive Amperometric Determination of Tryptophan. **Electrochim. Acta** 55 (12): 3927-3931.

Hafner, J.H., M.J. Bronikowski, B.R. Azamian, P. Nikolaev, A.G. Rinzler, D.T. Colbert, K.A. Smith and R.E. Smalley. 1998. Catalytic Growth of Single-Wall Carbon Nanotubes from Metal Particles. **Chem. Phys. Lett.** 296 (1-2): 195-202.

Haile, S.M. 2003. Fuel Cell Materials and Components. **Acta Mater.** 51 (19): 5981-6000.

Hamada, S.I. Sawada and A. Oshiyama. 1992. New One-Dimensional Conductors: Graphitic Microtubules. **Phys. Rev. Lett.** 68 (10): 1579-1581.

Hatanaka, H. Nakanishi, S. Matsumoto and Y. Morimoto. 2006. PEFC Electrodes Based on Vertically Oriented Carbon Nanotubes, 277-284. *In*. ECS Transactions

Hernadi, A. Fonseca, J.B. Nagy, D. Bernaerts and A.A. Lucas. 1996. Fe-Catalyzed Carbon Nanotube Formation. **Carbon** 34 (10): 1249-1257.

Herrero, M.A., J. Guerra, V.S. Myers, M.V. Gómez, R.M. Crooks and M. Prato. 2010. Gold Dendrimer Encapsulated Nanoparticles as Labeling Agents for Multiwalled Carbon Nanotubes. **ACS Nano** 4 (2): 905-912.

Hirano, Y. Kazahaya, A. Nakamura, T. Miyao and S. Naito. 2007. Remarkable Effect of Addition of in and Pb on the Reduction of N_2O by CO over SiO_2 Supported Pd Catalysts. **Catal. Lett.** 117 (1-2): 73-78.

Hoar, T.P. and N.F. Mott. 1959. A Mechanism for the Formation of Porous Anodic Oxide Films on Aluminium. **J. Phys. Chem. Solids** 9 (2): 97-99.

Holton, O.T. and J.W. Stevenson. 2013. The Role of Platinum in Proton Exchange Membrane Fuel Cells. **Platinum Met. Rev.** 57 (4): 259-271.

Hu, J. Shi, S. Li, Y. Qin, Z.X. Guo, Y. Song and D. Zhu. 2005. Efficient Method to Functionalize Carbon Nanotubes with Thiol Groups and Fabricate Gold Nanocomposites. **Chem. Phys. Lett.** 401 (4-6): 352-356.

Hyeon, S. Han, Y.E. Sung, K.W. Park and Y.W. Kim. 2003. High-Performance Direct Methanol Fuel Cell Electrodes Using Solid-Phase-Synthesized Carbon Nanocoils. **Angew. Chem. Int. Ed.** 42 (36): 4352-4356.

Iijima, S. 1991. Helical Microtubules of Graphitic Carbon. **Nature** 354 (6348): 56-58.

Iijima, S. and T. Ichihashi. 1993. Single-Shell Carbon Nanotubes of 1-Nm Diameter. **Nature** 363 (6430): 603-605.

Ismaili, F. Lagugné-Labarthet and M.S. Workentin. 2011. Covalently Assembled Gold Nanoparticle-Carbon Nanotube Hybrids Via a Photoinitiated Carbene Addition Reaction. **Chem. Mater.** 23 (6): 1519-1525.

Iwamoto, J.I. Hirata, K. Matsukami and S. Kagawa. 1983. Catalytic Oxidation by Oxide Radical Ions. 1. One-Step Hydroxylation of Benzene to Phenol over Group 5 and 6 Oxides Supported on Silica Gel. **J. Phys. Chem.** 87 (6): 903-905.

Jacquet, P.A. 1935. Electrolytic Method for Obtaining Bright Copper Surfaces [14]. **Nature** 135 (3426): 1076.

Jaksic, J.M., N.M. Ristic, N.V. Krstajic and M.M. Jaksic. 1998. Electrocatalysis for Hydrogen Electrode Reactions in the Light of Fermi Dynamics and Structural Bonding Factors - I. Individual Electrocatalytic Properties of Transition Metals. **Int. J. Hydrogen Energy** 23 (12): 1121-1156.

Jenkin, M.E. and K.C. Clemitshaw. 2000. Ozone and Other Secondary Photochemical Pollutants: Chemical Processes Governing Their Formation in the Planetary Boundary Layer. **Atmos. Environ.** 34 (16): 2499-2527.

Jessensky, F. Müller and U. Gösele. 1998. Self-Organized Formation of Hexagonal Pore Arrays in Anodic Alumina. **Appl. Phys. Lett.** 72 (10): 1173-1175.

Jia, K.S. Pillai and W.M.H. Sachtler. 2004. One-Step Oxidation of Benzene to Phenol with Nitrous Oxide over Fe/Mfi Catalysts. **J. Catal.** 221 (1): 119-126.

Jiang, A. Eitan, L.S. Schadler, P.M. Ajayan, R.W. Siegel, N. Grobert, M. Mayne, M. Reyes-Reyes, H. Terrones and M. Terrones. 2003. Selective Attachment of Gold Nanoparticles to Nitrogen-Doped Carbon Nanotubes. **Nano Lett.** 3 (3): 275-277.

Jiang and Gao. 2003. Modified Carbon Nanotubes: An Effective Way to Selective Attachment of Gold Nanoparticles. **Carbon** 41 (15): 2923-2929.

Jiao, H. Zhang, L. Yu, X. Wang and R. Wang. 2012. Decorating Multi-Walled Carbon Nanotubes with Au Nanoparticles by Amphiphilic Ionic Liquid Self-Assembly. **Colloids Surf. A: Physicochem. Eng. Asp** 408 1-7.

Jin Seung, G. Geun Hoi, H. Kim, J. Kwang Seok, J. Bae and S. Jung Sang. 2001. Growth of Carbon Nanotubes on Anodic Aluminum Oxide Templates: Fabrication of a Tube-in-Tube and Linearly Joined Tube. **Chem. Mater.** 13 (7): 2387-2391.

Joo, S.H., S.J. Choi, I. Oh, J. Kwak, Z. Liu, O. Terasaki and R. Ryoo. 2001. Ordered Nanoporous Arrays of Carbon Supporting High Dispersions of Platinum Nanoparticles. **Nature** 412 (6843): 169-172.

José-Yacamán, M. Miki-Yoshida, L. Rendón and J.G. Santiesteban. 1993. Catalytic Growth of Carbon Microtubules with Fullerene Structure. **Appl. Phys. Lett.** 62 (6): 657-659.

Journet, W.K. Maser, P. Bernier, A. Loiseau, M. Lamy de la Chapelle, S. Lefrant, P. Deniard, R. Lee and J.E. Fischer. 1997. Large-Scale Production of Single-Walled Carbon Nanotubes by the Electric-Arc Technique. **Nature** 388 (6644): 756-758.

Jurczyk, K. and R.S. Drago. 1998. Low-Temperature Reduction of $(NO)_X$ with CO and N-Hexane Using Metal Oxides on Carbon. **Appl. Catal. A: Gen** 173 (2): 145-151.

Kang, Y.Y. Heung, J.H. Kim, J.W. Lee, R. Gollapudi, S. Subramaniam, S. Narasimhadevara, D. Hurd, G.R. Kirikera, V. Shanov, M.J. Schulz, D. Shi, J. Boerio, S. Mall and M. Ruggles-Wren. 2006. Introduction to Carbon Nanotube and Nanofiber Smart Materials. **Compos. Part B-Eng** 37 (6): 382-394.

Kapteijn, J. Rodriguez-Mirasol and J.A. Moulijn. 1996. Heterogeneous Catalytic Decomposition of Nitrous Oxide. **Appl. Catal. B: Environ.** 9 (1-4): 25-64.

Kasimir-Klemedtsson, Å., L. Klemedtsson, K. Berglund, P. Martikainen, J. Silvola and O. Oenema. 1997. Greenhouse Gas Emissions from Farmed Organic Soils: A Review. **Soil Use and Management** 13 (4 SUPPL.): 245-250.

Khalil, M.A.K. 2000. Special Issue: Atmospheric Nitrous Oxide. **Chemosphere - Global Change Science** 2 (3-4): 233.

Kim, B. and W.M. Sigmund. 2004. Functionalized Multiwall Carbon Nanotube/Gold Nanoparticle Composites. **Langmuir** 20 (19): 8239-8242.

Kim, Y.J. Kim, Y.A. Kim, T. Yanagisawa, K.C. Park, M. Endo and M.S. Dresselhaus. 2004. High Performance of Cup-Stacked-Type Carbon Nanotubes as a Pt-Ru Catalyst Support for Fuel Cell Applications. **J. Appl. Phys.** 96 (10): 5903-5905.

Kim, S.W. Lee, P.T. Hammond and Y. Shao-Horn. 2009. Electrostatic Layer-by-Layer Assembled Au Nanoparticle/MWNT Thin Films: Microstructure, Optical Property, and Electrocatalytic Activity for Methanol Oxidation. **Chem. Mater.** 21 (13): 2993-3001.

Kim, M.M. Rabbani, D. Kim, M. Ree, J.H. Yeum, C.H. Ko, Y. Kim, J.S. Bae and W. Oh. 2010. Structural and Electrochemical Properties of Gold-Deposited Carbon Nanotube Composites. **Curr. Appl. Phys.** 10 (2 SUPPL.): S201-S205.

Kim, S.H. Lee, W. Yi, J. Kim, J.W. Choi, Y. Park and J.I. Jin. 2003. Efficient Field Emission from Highly Aligned, Graphitic Nanotubes Embedded with Gold Nanoparticles. **Adv. Mater.** 15 (19): 1618-1622.

Kim, S.J., Y.J. Park, E.J. Ra, K.K. Kim, K.H. An, Y.H. Lee, J.Y. Choi, C.H. Park, S.K. Doo, M.H. Park and C.W. Yang. 2007. Defect-Induced Loading of Pt Nanoparticles on Carbon Nanotubes. **Appl. Phys. Lett.** 90 (2):

Kinoshita, K. 1990. Particle Size Effects for Oxygen Reduction on Highly Dispersed Platinum in Acid Electrolytes. **J. Electrochem. Soc.** 137 (3): 845-848.

Kirubakaran, S. Jain and R.K. Nema. 2009. A Review on Fuel Cell Technologies and Power Electronic Interface. **Renew.Sust.Energ.Rev.** 13 (9): 2430-2440.

Kögel, R. Mönnig, W. Schwieger, A. Tissler and T. Turek. 1999. Simultaneous Catalytic Removal of NO and N_2O Using Fe-Mfi. **J. Catal.** 182 (2): 470-478.

Kong, A.M. Cassell and H. Dai. 1998. Chemical Vapor Deposition of Methane for Single-Walled Carbon Nanotubes. **Chem. Phys. Lett.** 292 (4-6): 567-574.

Kong, N.R. Franklin, C. Zhou, M.G. Chapline, S. Peng, K. Cho and H. Dai. 2000. Nanotube Molecular Wires as Chemical Sensors. **Science** 287 (5453): 622-625.

Kongkanand, S. Kuwabata, G. Girishkumar and P. Kamat. 2006. Single-Wall Carbon Nanotubes Supported Platinum Nanoparticles with Improved Electrocatalytic Activity for Oxygen Reduction Reaction. **Langmuir** 22 (5): 2392-2396.

Kordesch, K.V. and G.R. Simader. 1995. Environmental Impact of Fuel Cell Technology. **Chem. Rev.** 95 (1): 191-207.

Krishna Kumar and Ramaprabhu. 2006. Nanostructured Pt Functionlized Multiwalled Carbon Nanotube Based Hydrogen Sensor. **J. Phys. Chem. B** 110 (23): 11291-11298.

Kroto, H.W., J.R. Heath, S.C.O. Brien, R.F. Curl and R.E. Smalley. 1985. C60: Buckminsterfullerene. **Nature** 318 (14): 162-163.

Kumar, N.A., A. Bund, B.G. Cho, K.T. Lim and Y.T. Jeong. 2009. Novel Amino-Acid-Based Polymer/Multi-Walled Carbon Nanotube Bio-Nanocomposites: Highly Water Dispersible Carbon Nanotubes Decorated with Gold Nanoparticles. **Nanotechnology** 20 (22):

Kyotani, T. 2006. Synthesis of Various Types of Nano Carbons Using the Template Technique. **Bull. Chem. Soc. Jpn.** 79 (9): 1322-1337.

Kyotani, L.F. Tsai and A. Tomita. 1995. Formation of Ultrafine Carbon Tubes by Using an Anodic Aluminum Oxide Film as a Template. **Chem. Mater.** 7 (8): 1427-1428.

Kyotani, L.F. Tsai and A. Tomita. 1996. Preparation of Ultrafine Carbon Tubes in Nanochannels of an Anodic Aluminum Oxide Film. **Chem. Mater.** 8 (8): 2109-2113.

Landolt, D. 1987. Fundamental Aspects of Electropolishing. **Electrochim. Acta** 32 (1): 1-11.

Le Gratiet, H. Remita, G. Picq and M.O. Delcourt. 1996. Co-Stabilized Supported Pt Catalysts for Fuel Cells: Radiolytic Synthesis. **J. Catal.** 164 (1): 36-43.

Lee, J. Kim and T. Hyeon. 2006. Recent Progress in the Synthesis of Porous Carbon Materials. **Adv. Mater.** 18 (16): 2073-2094.

Lee, J. Zhang, H. Wang and D.P. Wilkinson. 2006. Progress in the Synthesis of Carbon Nanotube- and Nanofiber-Supported Pt Electrocatalysts for Pem Fuel Cell Catalysis. **J. Appl. Electrochem.** 36 (5): 507-522.

Li, L. Zhang and R.M. Metzger. 1998. On the Growth of Highly Ordered Pores in Anodized Aluminum Oxide. **Chem. Mater.** 10 (9): 2470-2480.

Li, Z. Wang, C. Shan, J. Song, D. Han and L. Niu. 2009. Preparation of Gold Nanoparticles/Functionalized Multiwalled Carbon Nanotube Nanocomposites and Its Glucose Biosensing Application. **Biosens. Bioelectron.** 24 (6): 1765-1770.

Li, C. Papadopoulos and J. Xu. 1999. Growing Y-Junction Carbon Nanotubes. **Nature** 402 (6759): 253-254.

Li, Q. Xu, M. Zhou, W. Xia, X. Chen, M. Bron, W. Schuhmann and M. Muhler. 2010. Ethylenediamine-Anchored Gold Nanoparticles on Multi-Walled Carbon Nanotubes: Synthesis and Characterization. **Electrochem. Commun.** 12 (7): 939-943.

Li, X. Zhu, W. Zhang, G. Xie and W. Feng. 2012. Hydrogen Peroxide Biosensor Based on Gold Nanoparticles/Thionine/Gold Nanoparticles/Multi-Walled Carbon Nanotubes-Chitosans Composite Film-Modified Electrode. **Appl. Surf. Sci.** 258 (7): 2802-2807.

Li, X. Wang, Z. Chen, M. Waje and Y. Yan. 2005. Carbon Nanotube Film by Filtration as Cathode Catalyst Support for Proton-Exchange Membrane Fuel Cell. **Langmuir** 21 (21): 9386-9389.

Li, C. Liang, W. Zhou, J. Qiu, Z. Zhou, G. Sun and Q. Xin. 2003. Preparation and Characterization of Multiwalled Carbon Nanotube-Supported Platinum for Cathode Catalysts of Direct Methanol Fuel Cells. **J. Phys. Chem. B** 107 (26): 6292-6299.

Li and Sabir. 2005. Review of Bipolar Plates in Pem Fuel Cells: Flow-Field Designs. **Int. J. Hydrogen Energy** 30 (4): 359-371.

Liang, A.S. Susha and F. Caruso. 2002. Metallodielectric Opals of Layer-by-Layer Processed Coated Colloids. **Adv. Mater.** 14 (16): 1160-1164.

Liang, A. Susha and F. Caruso. 2003. Gold Nanoparticle-Based Core-Shell and Hollow Spheres and Ordered Assemblies Thereof. **Chem. Mater.** 15 (16): 3176-3183.

Lim, S.H., J. Wei and J. Lin. 2004. Electrochemical Genosensing Properties of Gold Nanoparticle-Carbon Nanotube Hybrid. **Chem. Phys. Lett.** 400 (4-6): 578-582.

Lin, C. He, L. Zhang and S. Zhang. 2009. Sensitive Amperometric Immunosensor for A-Fetoprotein Based on Carbon Nanotube/Gold Nanoparticle Doped Chitosan Film. **Anal. Biochem.** 384 (1): 130-135.

Litster and McLean. 2004. Pem Fuel Cell Electrodes. **J. Power Sources** 130 (1-2): 61-76.

Liu, A.G. Rinzler, H. Dai, J.H. Hafner, R. Kelley Bradley, P.J. Boul, A. Lu, T. Iverson, K. Shelimov, C.B. Huffman, F. Rodriguez-Macias, Y.S. Shon, T.R. Lee, D.T. Colbert and R.E. Smalley. 1998. Fullerene Pipes. **Science** 280 (5367): 1253-1256.

Liu, J. Chen, W. Zhang, Z. Ma, G.F. Swiegers, C.O. Too and G.G. Wallace. 2008. Nano-Pt Modified Aligned Carbon Nanotube Arrays Are Efficient, Robust, High Surface Area Electrocatalysts. **Chem. Mater.** 20 (8): 2603-2605.

Liu, X.Y. Ling, X. Su and J.Y. Lee. 2004. Carbon-Supported Pt and Ptru Nanoparticles as Catalysts for a Direct Methanol Fuel Cell. **J. Phys. Chem. B** 108 (24): 8234-8240.

Liu, X. Lin, J.Y. Lee, W. Zhang, M. Han and L.M. Gan. 2002. Preparation and Characterization of Platinum-Based Electrocatalysts on Multiwalled Carbon Nanotubes for Proton Exchange Membrane Fuel Cells. **Langmuir** 18 (10): 4054-4060.

Lu, S. Nagase, Y. Maeda, T. Wakahara, T. Nakahodo, T. Akasaka, D. Yu, Z. Gao, R. Han and H. Ye. 2005. Adsorption Configuration of Nh3 on Single-Wall Carbon Nanotubes. **Chem. Phys. Lett.** 405 (1-3): 90-92.

Lu, F. Tian and Q. Zhang. 2003. The [2+1] Cycloadditions of Dichlorocarbene, Silylene, Germylene, and Oxycarbonylnitrene onto the Sidewall of Armchair (5,5) Single-Wall Carbon Nanotube. **J. Phys. Chem. B** 107 (33): 8388-8391.

Lu, L. Zhang, X. Xu, N. Wang and Q. Zhang. 2002. Can the Sidewalls of Single-Wall Carbon Nanotubes Be Ozonized? **J. Phys. Chem. B** 106 (9): 2136-2139.

Lu, J. Li, J. Han, H.T. Ng, C. Binder, C. Partridge and M. Meyyappan. 2004. Room Temperature Methane Detection Using Palladium Loaded Single-Walled Carbon Nanotube Sensors. **Chem. Phys. Lett.** 391 (4-6): 344-348.

Ma, L. Zhang, Y. Pan, K. Zhang and Y. Zhang. 2008. A Novel Electrochemical DNA Biosensor Fabricated with Layer-by-Layer Covalent Attachment of Multiwalled Carbon Nanotubes and Gold Nanoparticles. **Electroanalysis** 20 (11): 1220-1226.

Ma, N.M. Rodriguez, M.A. Vannice and R.T.K. Baker. 2000. Nitrous Oxide Decomposition and Reduction over Copper Catalysts Supported on Various Types of Carbonaceous Materials. **Top. Catal.** 10 (1-2): 27-38.

Maiyalagan, B. Viswanathan and U.V. Varadaraju. 2005. Nitrogen Containing Carbon Nanotubes as Supports for Pt - Alternate Anodes for Fuel Cell Applications. **Electrochem. Commun.** 7 (9): 905-912.

Masuda, H. and K. Fukuda. 1995. Ordered Metal Nanohole Arrays Made by a Two-Step Replication of Honeycomb Structures of Anodic Alumina. **Science** 268 (5216): 1466-1468.

Matsumoto, T. Komatsu, K. Arai, T. Yamazaki, M. Kijima, H. Shimizu, Y. Takasawa and J. Nakamura. 2004a. Reduction of Pt Usage in Fuel Cell Electrocatalysts with Carbon Nanotube Electrodes. **Chem. Commun.** 10 (7): 840-841.

Matsumoto, T. Komatsu, H. Nakano, K. Arai, Y. Nagashima, E. Yoo, T. Yamazaki, M. Kijima, H. Shimizu, Y. Takasawa and J. Nakamura. 2004b. Efficient Usage of Highly Dispersed Pt on Carbon Nanotubes for Electrode Catalysts of Polymer Electrolyte Fuel Cells. **Catal. Today** 90 (3-4): 277-281.

McBreen, H. Olender, S. Srinivasan and K.V. Kordesch. 1981. Carbon Supports for Phosphoric Acid Fuel Cell Electrocatalysts: Alternative Materials and Methods of Evaluation. **J. Appl. Electrochem.** 11 (6): 787-796.

Mehta, V. and J.S. Cooper. 2003. Review and Analysis of Pem Fuel Cell Design and Manufacturing. **J. Power Sources** 114 (1): 32-53.

Mercuri, A. Sgamellotti, L. Valentini, I. Armentano and J.M. Kenny. 2005. Vacancy-Induced Chemisorption of NO_2 on Carbon Nanotubes: A Combined Theoretical and Experimental Study. **J. Phys. Chem. B** 109 (27): 13175-13179.

Monkhorst, H.J. and J.D. Pack. 1976. Special Points for Brillouin-Zone Integrations. **Phys. Rev. B** 13 (12): 5188-5192.

Mubeen, T. Zhang, B. Yoo, M.A. Deshusses and N.V. Myung. 2007. Palladium Nanoparticles Decorated Single-Walled Carbon Nanotube Hydrogen Sensor. **J. Phys. Chem. C** 111 (17): 6321-6327.

Nagle, L.C. and J.F. Rohan. 2008. Aligned Carbon Nanotube-Pt Composite Fuel Cell Catalyst by Template Electrodeposition. **J. Power Sources** 185 (1): 411-418.

Namuangruk, P. Khongpracha, Y. Tantirungrotechai and J. Limtrakul. 2007. Decomposition of Nitrous Oxide on Carbon Nanotubes. **J. Mol. Graphics Modell.** 26 (1): 179-186.

Niyogi, M.A. Hamon, H. Hu, B. Zhao, P. Bhowmik, R. Sen, M.E. Itkis and R.C. Haddon. 2002. Chemistry of Single-Walled Carbon Nanotubes. **Acc. Chem. Res.** 35 (12): 1105-1113.

Nobukawa, K. Sugawara, K. Okumura, K. Tomishige and K. Kunimori. 2007. Role of Active Oxygen Transients in Selective Catalytic Reduction of N_2O with CH_4 over Fe-Zeolite Catalysts. **Appl. Catal. B: Environ.** 70 (1-4): 342-352.

Nørskov, J.K., J. Rossmeisl, A. Logadottir, L. Lindqvist, J.R. Kitchin, T. Bligaard and H. Jónsson. 2004. Origin of the Overpotential for Oxygen Reduction at a Fuel-Cell Cathode. **J. Phys. Chem. B** 108 (46): 17886-17892.

Odom, T.W., J.L. Huang, P. Kim and C.M. Lieber. 1998. Atomic Structure and Electronic Properties of Single-Walled Carbon Nanotubes. **Nature** 391 (6662): 62-64.

Ohnishi, K. Asano, S. Iwamoto, K. Chikama and M. Inoue. 2007. Alkali-Doped CO_3O_4 Catalysts for Direct Decomposition of N_2O in the Presence of Oxygen. **Catal. Today** 120 (2): 145-150.

Ono, M. Saito, M. Ishiguro and H. Asoh. 2004. Controlling Factor of Self-Ordering of Anodic Porous Alumina. **J. Electrochem. Soc.** 151 (8): B473-A478.

Orikasa, N. Inokuma, S. Okubo, O. Kitakami and T. Kyotani. 2006. Template Synthesis of Water-Dispersible Carbon Nano "Test Tubes" without Any Post-Treatment. **Chem. Mater.** 18 (4): 1036-1040.

Orikasa, N. Inokuma, S. Ittisanronnachai, X.H. Wang, O. Kitakami and T. Kyotani. 2008. Template Synthesis of Water-Dispersible and Magnetically Responsive Carbon Nano Test Tubes. **Chem. Commun.** (19): 2215-2217.

Orita and Inada. 2005. Dft Investigation of Co Adsorption on Pt(211) and Pt(311) Surfaces from Low to High Coverage. **J. Phys. Chem. B** 109 (47): 22469-22475.

Ou, Y.Y. and M.H. Huang. 2006. High-Density Assembly of Gold Nanoparticles on Multiwalled Carbon Nanotubes Using 1-Pyrenemethylamine as Interlinker. **J. Phys. Chem. B** 110 (5): 2031-2036.

Pannopard, P. Khongpracha, M. Probst and J. Limtrakul. 2009. Gas Sensing Properties of Platinum Derivatives of Single-Walled Carbon Nanotubes: A Dft Analysis. **J. Mol. Graphics Modell.** 28 (1): 62-69.

Panov, G.I., A.K. Uriarte, M.A. Rodkin and V.I. Sobolev. 1998. Generation of Active Oxygen Species on Solid Surfaces. Opportunity for Novel Oxidation Technologies over Zeolites. **Catal. Today** 41 (4): 365-385.

Pantu, B. Boekfa, B. Sunpetch and J. Limtrakul. 2008. Nanocavity Effects on N_2O Decomposition on Different Types of Fe-Zeolites (Fe-Fer, Fe-Bea, Fe-ZSM-5 and Fe-FAU): A Combined Theoretical and Experimental Study. **Chem. Eng. Commun.** 195 (11): 1477-1485.

Park, K.W., Y.E. Sung, S. Han, Y. Yun and T. Hyeon. 2004. Origin of the Enhanced Catalytic Activity of Carbon Nanocoil-Supported Ptru Alloy Electrocatalysts. **J. Phys. Chem. B** 108 (3): 939-944.

Park, K.W., B.K. Kwon, J.H. Choi, I.S. Park, Y.M. Kim and Y.E. Sung. 2002. New RuO_2 and Carbon-RuO_2 Composite Diffusion Layer for Use in Direct Methanol Fuel Cells. **J. Power Sources** 109 (2): 439-445.

Parkhutik, V.P. and V.I. Shershulsky. 1992. Theoretical Modelling of Porous Oxide 1 Growth on Aluminium. **J. Phys. D: Appl. Phys.** 25 1258-1263.

Peighambardoust, S.J., S. Rowshanzamir and M. Amjadi. 2010. Review of the Proton Exchange Membranes for Fuel Cell Applications. **Int. J. Hydrogen Energy** 35 (17): 9349-9384.

Peng and Cho. 2003. Ab Initio Study of Doped Carbon Nanotube Sensors. **Nano Lett.** 3 (4): 513-517.

Peng, X. and S.S. Wong. 2009. Controlling Nanocrystal Density and Location on Carbon Nanotube Templates. **Chem. Mater.** 21 (4): 682-694.

Penza, R. Rossi, M. Alvisi, G. Cassano, M.A. Signore, E. Serra and R. Giorgi. 2008. Pt- and Pd-Nanoclusters Functionalized Carbon Nanotubes Networked Films for Sub-ppm Gas Sensors. **Sens. Actuator B-Chem** 135 (1): 289-297.

Penza, G. Cassano, R. Rossi, M. Alvisi, A. Rizzo, M.A. Signore, T. Dikonimos, E. Serra and R. Giorgi. 2007. Enhancement of Sensitivity in Gas

Chemiresistors Based on Carbon Nanotube Surface Functionalized with Noble Metal (Au, Pt) Nanoclusters. **Appl. Phys. Lett.** 90 (17):

Perdew, J.P. and Y. Wang. 1992. Accurate and Simple Analytic Representation of the Electron-Gas Correlation Energy. **Phys. Rev. B** 45 (23): 13244-13249.

Perry, M.L. and T.F. Fuller. 2002. A Historical Perspective of Fuel Cell Technology in the 20th Century. **J. Electrochem. Soc.** 149 (7): S59-S67.

Pillai, K.S., J. Jia and W.M.H. Sachtler. 2004. Effect of Steaming on One-Step Oxidation of Benzene to Phenol with Nitrous Oxide over Fe/MFI Catalysts. **Appl. Catal. A: Gen** 264 (2): 133-139.

Pirutko, L.V., V.S. Chernyavsky, A.K. Uriarte and G.I. Panov. 2002. Oxidation of Benzene to Phenol by Nitrous Oxide: Activity of Iron in Zeolite Matrices of Various Composition. **Appl. Catal. A: Gen** 227 (1-2): 143-157.

Popov, V.N. 2004. Carbon Nanotubes: Properties and Application. **Mater. Sci. Eng. R-Rep.** 43 (3): 61-102.

Qin, H. Wang, X. Wang, Z. Miao, L. Chen, W. Zhao, M. Shan and Q. Chen. 2010. Amperometric Biosensors Based on Gold Nanoparticles-Decorated Multiwalled Carbon Nanotubes-Poly(Diallyldimethylammonium Chloride) Biocomposite for the Determination of Choline. **Sens. Actuator B-Chem** 147 (2): 593-598.

Quinn, B.M., C. Dekker and S.G. Lemay. 2005. Electrodeposition of Noble Metal Nanoparticles on Carbon Nanotubes. **J. Am. Chem. Soc.** 127 (17): 6146-6147.

Rabbani, M.M., C.H. Ko, J.S. Bae, J.H. Yeum, I.S. Kim and W. Oh. 2009. Comparison of Some Gold/Carbon Nanotube Composites Prepared by Control of Electrostatic Interaction. **Colloids Surf. A: Physicochem. Eng. Asp.** 336 (1-3): 183-186.

Raghuveer, M.S., S. Agrawal, N. Bishop and G. Ramanath. 2006. Microwave-Assisted Single-Step Functionalization and in Situ Derivatization of Carbon Nanotubes with Gold Nanoparticles. **Chem. Mater.** 18 (6): 1390-1393.

Raistrick, I.D. 1989. Electrode Assembly for Use in a Solid Polymer Eleci'Rolyte Fuel Cell. **US Patent** 4876155

Raj, M.A., S.B. Revin and S.A. John. 2011. Selective Determination of 3,4-Dihydroxyphenylacetic Acid in the Presence of Ascorbic Acid Using 4-(Dimethylamino)Pyridine Capped Gold Nanoparticles Immobilized on Gold Electrode. **Colloids and Surfaces B: Biointerfaces** 87 (2): 353-360.

Rajesh, V. Karthik, S. Karthikeyan, K. Ravindranathan Thampi, J.M. Bonard and B. Viswanathan. 2002. Pt-WO_3 Supported on Carbon Nanotubes as Possible Anodes for Direct Methanol Fuel Cells. **Fuel** 81 (17): 2177-2190.

Rakhi, R.B., A.L.M. Reddy, M.M. Shaijumon, K. Sethupathi and S. Ramaprabhu. 2008. Electron Field Emitters Based on Multiwalled Carbon Nanotubes Decorated with Nanoscale Metal Clusters. **J. Nanopart. Res.** 10 (1): 179-189.

Ralph, T.R. and M.P. Hogarth. 2002. Catalysis for Low Temperature Fuel Cells. **Platinum Met. Rev.** 46 (1): 3-14.

Rance, G.A., D.H. Marsh, S.J. Bourne, T.J. Reade and A.N. Khlobystov. 2010. Van Der Waals Interactions between Nanotubes and Nanoparticles for Controlled Assembly of Composite Nanostructures. **ACS Nano** 4 (8): 4920-4928.

Rao, P.A. Simonov, E.R. Savinova, G.V. Plaksin, S.V. Cherepanova, G.N. Kryukova and U. Stimming. 2005. The Influence of Carbon Support Porosity on the

Activity of Ptru/Sibunit Anode Catalysts for Methanol Oxidation. **J Power Sources** 145 (2): 178-187.

Ravishankara, A.R., J.S. Daniel and R.W. Portmann. 2009. Nitrous Oxide (N_2O): The Dominant Ozone-Depleting Substance Emitted in the 21st Century. **Science** 326 (5949): 123-125.

Ritter, D. and J.C. Weisshaar. 1990. Kinetics of Neutral Transition-Metal Atoms in the Gas Phase: Oxidation of Sc(A^2d), Ti(A^3f), and V(A^4f) by NO, O_2, and N_2O. **J. Phys. Chem.** 94 (12): 4907-4913.

Ruiz-Martínez, J.M. Sánchez-Hervás and J. Otero-Ruiz. 2005. Effect of Operating Conditions on the Reduction of Nitrous Oxide by Propane over a Fe-Zeolite Monolith. **Appl. Catal. B: Environ.** 61 (3-4): 306-315.

Saito, M. Fujita, G. Dresselhaus and M.S. Dresselhaus. 1992. Electronic Structure of Chiral Graphene Tubules. **Appl. Phys. Lett.** 60 (18): 2204-2206.

Santucci, S. Picozzi, F. Di Gregorio, L. Lozzi, C. Cantalini, L. Valentini, J.M. Kenny and B. Delley. 2003. NO_2 and CO Gas Adsorption on Carbon Nanotubes: Experiment and Theory. **J. Chem. Phys.** 119 (20): 10904-10910.

Satishkumar, B.C., E.M. Vogl, A. Govindaraj and C.N.R. Rao. 1996. The Decoration of Carbon Nanotubes by Metal Nanoparticles. **J. Phys. D: Appl. Phys.** 29 (12): 3173-3176.

Sharma, S. and B.G. Pollet. 2012. Support Materials for Pemfc and Dmfc Electrocatalysts - a Review. **J. Power Sources** 208 96-119.

Shi, Z. Wang and H.L. Li. 2006. Selfassembly of Gold Nanoparticles onto the Surface of Multiwall Carbon Nanotubes Functionalized with Mercaptobenzene Moieties. **J. Nanopart. Res.** 8 (5): 743-747.

Shi, R. Yang and P.K. Yuet. 2009. Easy Decoration of Carbon Nanotubes with Well Dispersed Gold Nanoparticles and the Use of the Material as an Electrocatalyst. **Carbon** 47 (4): 1146-1151.

Singh, T. Premkumar, J.Y. Shin and K.E. Geckeler. 2010. Carbon Nanotube and Gold-Based Materials: A Symbiosis. **Chemistry - A European Journal** 16 (6): 1728-1743.

Slanina, X. Zhao, L.Y. Chiang and E. Osawa. 1999. Biologically Active Fullerene Derivatives: Computations of Structures, Energetics, and Vibrations of $C_{60}(OH)X$ and $C_{60}(NO_2)Y$. **Int. J. Quantum Chem** 74 (3): 343-349.

Srinivasan, D.J. Manko, H. Koch, M.A. Enayetullah and A.J. Appleby. 1990. Recent Advances in Solid Polymer Electrolyte Fuel Cell Technology with Low Platinum Loading Electrodes. **J Power Sources** 29 (3-4): 367-387.

Star, V. Joshi, S. Skarupo, D. Thomas and J.C.P. Gabriel. 2006. Gas Sensor Array Based on Metal-Decorated Carbon Nanotubes. **J. Phys. Chem. B** 110 (42): 21014-21020.

Steigerwalt, E.S., G.A. Deluga, D.E. Cliffel and C.M. Lukehart. 2001. A Pt-Ru/Graphitic Carbon Nanofiber Nanocomposite Exhibiting High Relative Performance as a Direct-Methanol Fuel Cell Anode Catalyst. **J. Phys. Chem. B** 105 (34): 8097-8101.

Stevens, D.A. and J.R. Dahn. 2005. Thermal Degradation of the Support in Carbon-Supported Platinum Electrocatalysts for Pem Fuel Cells. **Carbon** 43 (1): 179-188.

Stirling 1998. Oxygen Abstraction from N_2O with Ground-State Transition Metal Atoms: Density Functional Study on the Mechanism of the Reactions of Sc, Ti, and V + N_2O. **J. Phys. Chem. A** 102 (32): 6565-6570.

Stirling 2002. Oxygen-Transfer Reactions between 3d Transition Metals and N_2O and NO_2. **J. Am. Chem. Soc.** 124 (15): 4058-4067.

Stonehart, P. 1984. Carbon Substrates for Phosphoric Acid Fuel Cell Cathodes. **Carbon** 22 (4-5): 423-431.

Sugawara, T. Nobukawa, M. Yoshida, Y. Sato, K. Okumura, K. Tomishige and K. Kunimori. 2007. The Importance of Fe Loading on the N_2O Reduction with NH_3 over Fe-MFI: Effect of Acid Site Formation on Fe Species. **Appl. Catal. B: Environ.** 69 (3-4): 154-163.

Sun, H. Xia, E. Hensen, R. Van Santen and C. Li. 2006. Chemistry of N_2O Decomposition on Active Sites with Different Nature: Effect of High-Temperature Treatment of Fe/Zsm-5. **J. Catal.** 238 (1): 186-195.

Takasu, T. Kawaguchi, W. Sugimoto and Y. Murakami. 2003. Effects of the Surface Area of Carbon Support on the Characteristics of Highly-Dispersed Pt-Ru Particles as Catalysts for Methanol Oxidation. **Electrochim. Acta** 48 (25-26): 3861-3868.

Tang, J.H. Chen, Z.P. Huang, D.Z. Wang, Z.F. Ren, L.H. Nie, Y.F. Kuang and S.Z. Yao. 2004. High Dispersion and Electrocatalytic Properties of Platinum on Well-Aligned Carbon Nanotube Arrays. **Carbon** 42 (1): 191-197.

Tang, H.Y. Ng, J. Lin, A.T.S. Wee and D.H.C. Chua. 2010. Pt/Cnt-Based Electrodes with High Electrochemical Activity and Stability for Proton Exchange Membrane Fuel Cells. **J. Electrochem. Soc.** 157 (2): B245-B250.

Tasis, N. Tagmatarchis, A. Bianco and M. Prato. 2006. Chemistry of Carbon Nanotubes. **Chem. Rev.** 106 (3): 1105-1136.

Tauster, S.J., S.C. Fung, R.T.K. Baker and J.A. Horsley. 1981. Strong Interactions in Supported-Metal Catalysts. **Science** 211 (4487): 1121-1125.

Tello, G. Cárdenas, P. Häberle and R.A. Segura. 2008. The Synthesis of Hybrid Nanostructures of Gold Nanoparticles and Carbon Nanotubes and Their Transformation to Solid Carbon Nanorods. **Carbon** 46 (6): 884-889.

Thess, R. Lee, P. Nikolaev, H. Dai, P. Petit, J. Robert, C. Xu, Y.H. Lee, S.G. Kim, A.G. Rinzler, D.T. Colbert, G.E. Scuseria, D. Tománek, J.E. Fischer and R.E. Smalley. 1996. Crystalline Ropes of Metallic Carbon Nanotubes. **Science** 273 (5274): 483-487.

Thompson, S.D., L.R. Jordan and M. Forsyth. 2001. Platinum Electrodeposition for Polymer Electrolyte Membrane Fuel Cells. **Electrochim. Acta** 46 (10-11): 1657-1663.

Ticianelli, E.A., C.R. Derouin, A. Redondo and S. Srinivasan. 1988. Methods to Advance Technology of Proton Exchange Membrane Fuel Cells. **J. Electrochem. Soc.** 135 (9): 2209-2214.

Trogler, W.C. 1999. Physical Properties and Mechanisms of Formation of Nitrous Oxide. **Coord. Chem. Rev.** 187 (1): 303-327.

Tsunoyama, H. Sakurai and T. Tsukuda. 2006. Size Effect on the Catalysis of Gold Clusters Dispersed in Water for Aerobic Oxidation of Alcohol. **Chem. Phys. Lett.** 429 (4-6): 528-532.

Tsunoyama, N. Ichikuni and T. Tsukuda. 2008. Microfluidic Synthesis and Catalytic Application of Pvp-Stabilized, ~1 Nm Gold Clusters. **Langmuir** 24 (20): 11327-11330.

Tsunoyama, H. Sakurai, Y. Negishi and T. Tsukuda. 2005. Size-Specific Catalytic Activity of Polymer-Stabilized Gold Nanoclusters for Aerobic Alcohol Oxidation in Water. **J. Am. Chem. Soc.** 127 (26): 9374-9375.

Tsunoyama, H. Sakurai, N. Ichikuni, Y. Negishi and T. Tsukuda. 2004. Colloidal Gold Nanoparticles as Catalyst for Carbon-Carbon Bond Formation: Application to Aerobic Homocoupling of Phenylboronic Acid in Water. **Langmuir** 20 (26): 11293-11296.

Tsunoyama, P. Nickut, Y. Negishi, K. Al-Shamery, Y. Matsumoto and T. Tsukuda. 2007. Formation of Alkanethiolate-Protected Gold Clusters with Unprecedented Core Sizes in the Thiolation of Polymer-Stabilized Gold Clusters. **J. Phys. Chem. C** 111 (11): 4153-4158.

Tsunoyama, Y. Liu, T. Akita, N. Ichikuni, H. Sakurai, S. Xie and T. Tsukuda. 2011. Size-Controlled Synthesis of Gold Clusters as Efficient Catalysts for Aerobic Oxidation. **Catalysis Surveys from Asia** 15 (4): 230-239.

Uchida, Y. Fukuoka, Y. Sugawara, N. Eda and A. Ohta. 1996. Effects of Microstructure of Carbon Support in the Catalyst Layer on the Performance of Polymer-Electrolyte Fuel Cells. **J. Electrochem. Soc.** 143 (7): 2245-2252.

Uchida, Y. Aoyama, M. Tanabe, N. Yanagihara, N. Eda and A. Ohta. 1995. Influences of Both Carbon Supports and Heat-Treatment of Supported Catalyst on Electrochemical Oxidation of Methanol. **J. Electrochem. Soc.** 142 (8): 2572-2576.

Umeda, M. Kokubo, M. Mohamedi and I. Uchida. 2003. Porous-Microelectrode Study on Pt/C Catalysts for Methanol Electrooxidation. **Electrochim. Acta** 48 (10): 1367-1374.

Vairavapandian, P. Vichchulada and M.D. Lay. 2008. Preparation and Modification of Carbon Nanotubes: Review of Recent Advances and Applications in Catalysis and Sensing. **Anal. Chim. Acta** 626 (2): 119-129.

Valentini, F. Mercuri, I. Armentano, C. Cantalini, S. Picozzi, L. Lozzi, S. Santucci, A. Sgamellotti and J.M. Kenny. 2004. Role of Defects on the Gas Sensing Properties of Carbon Nanotubes Thin Films: Experiment and Theory. **Chem. Phys. Lett.** 387 (4-6): 356-361.

Wącław, K. Nowińska, W. Schwieger and A. Zielińska. 2004. N2o Decomposition over Iron Modified Zeolites Zsm-5. **Catal. Today** 90 (1-2): 21-25.

Wang, M. Waje, X. Wang, J.M. Tang, R.C. Haddon and Y. Yan. 2004. Proton Exchange Membrane Fuel Cells with Carbon Nanotube Based Electrodes. **Nano Lett.** 4 (2): 345-348.

Wang, G. Yin, Y. Shao, S. Zhang, Z. Wang and Y. Gao. 2007. Effect of Carbon Black Support Corrosion on the Durability of Pt/C Catalyst. **J Power Sources** 171 (2): 331-339.

Wang, D. Zhang, Y. Zhang and C. Liu. 2006. Boron-Doped Carbon Nanotubes Serving as a Novel Chemical Sensor for Formaldehyde. **J. Phys. Chem. B** 110 (37): 18267-18271.

Wang, D. Zhang, W. Sun, Z. Han and C. Liu. 2007. A Novel Aluminum-Doped Carbon Nanotubes Sensor for Carbon Monoxide. **J. Mol. Struct. THEOCHEM** 806 (1-3): 93-97.

Wang, X. Hu, X. Qu and S. Dong. 2006. Noncovalent Functionalization of Multiwalled Carbon Nanotubes: Application in Hybrid Nanostructures. **J. Phys. Chem. B** 110 (13): 6631-6636.

Wang, W. Li, Z. Chen, M. Waje and Y. Yan. 2006. Durability Investigation of Carbon Nanotube as Catalyst Support for Proton Exchange Membrane Fuel Cell. **J Power Sources** 158 (1): 154-159.

Wang, Y. and P.B. Balbuena. 2004. Roles of Proton and Electric Field in the Electroreduction of O_2 on Pt(111) Surfaces: Results of an Ab-Initio Molecular Dynamics Study. **J. Phys. Chem. B** 108 (14): 4376-4384.

Wang, K.S. Chen, J. Mishler, S.C. Cho and X.C. Adroher. 2011. A Review of Polymer Electrolyte Membrane Fuel Cells: Technology, Applications, and Needs on Fundamental Research. **Applied Energy** 88 (4): 981-1007.

Wang, M. Li, Y. Zhang, J. Yuan, Y. Shen, L. Niu and A. Ivaska. 2007. Thionine-Interlinked Multi-Walled Carbon Nanotube/Gold Nanoparticle Composites. **Carbon** 45 (10): 2111-2115.

Warakulwit, T. Nguyen, J. Majimel, M.H. Delville, V. Lapeyre, P. Garrigue, V. Ravaine, J. Limtrakul and A. Kuhn. 2008. Dissymmetric Carbon Nanotubes by Bipolar Electrochemistry. **Nano Lett.** 8 (2): 500-504.

Watanabe, S. Saegusa and P. Stonehart. 1988. Electro-Catalytic Activity on Supported Platinum Crystallites for Oxygen Reduction in Sulphuric Acid. **Chem. Lett.** 9 1487-1490.

Watanabe, H. Sei and P. Stonehart. 1989. The Influence of Platinum Crystallite Size on the Electroreduction of Oxygen. **J. Electroanal. Chem.** 261 (2 PART 2): 375-387.

Wee, J.H. 2007. Applications of Proton Exchange Membrane Fuel Cell Systems. **Renew.Sust.Energ.Rev.** 11 (8): 1720-1738.

Wee, J.H., K.Y. Lee and S.H. Kim. 2007. Fabrication Methods for Low-Pt-Loading Electrocatalysts in Proton Exchange Membrane Fuel Cell Systems. **J. Power Sources** 165 (2): 667-677.

Wildöer, J.W.G., L.C. Venema, A.G. Rinzler, R.E. Smalley and C. Dekker. 1998. Electronic Structure of Atomically Resolved Carbon Nanotubes. **Nature** 391 (6662): 59-62.

Wilson, M.S. and S. Goffesfeld. 1992. High Performance Catalyzed Membranes of Ultra-Low Pt Loadings for Polymer Electrolyte Fuel Cells. **J. Electrochem. Soc.** 139 (2): L28-L30.

Xiao, G.G. Wildgoose and R.G. Compton. 2008. Sensitive Electrochemical Detection of Arsenic (III) Using Gold Nanoparticle Modified Carbon Nanotubes Via Anodic Stripping Voltammetry. **Anal. Chim. Acta** 620 (1-2): 44-49.

Xing, Y. 2004. Synthesis and Electrochemical Characterization of Uniformly-Dispersed High Loading Pt Nanoparticles on Sonochemically-Treated Carbon Nanotubes. **J. Phys. Chem. B** 108 (50): 19255-19259.

Xiong, Q. Wang and H. Xia. 2004. Preparation of Polyaniline Nanotubes Array Based on Anodic Aluminum Oxide Template. **Mater. Res. Bull.** 39 (10): 1569-1580.

Xiong, F. Du, Y. Liu, A. Perez Jr, M. Supp, T.S. Ramakrishnan, L. Dai and L. Jiang. 2010. 3-D Carbon Nanotube Structures Used as High Performance Catalyst for Oxygen Reduction Reaction. **J. Am. Chem. Soc.** 132 (45): 15839-15841.

Xu, L. Zeng, S. Xing, G. Shi, Y. Xian and L. Jin. 2008. Microwave-Radiated Synthesis of Gold Nanoparticles/Carbon Nanotubes Composites and Its

Application to Voltammetric Detection of Trace Mercury(Ii). **Electrochem. Commun.** 10 (12): 1839-1843.

Xue, P. Chen, Q. Hong, J. Lin and T. Kuang Lee. 2001. Growth of Pd, Pt, Ag and Au Nanoparticles on Carbon Nanotubes. **J. Mater. Chem.** 11 (9): 2378-2381.

Yang, J.Y. Lee, T.C. Deivaraj and H.P. Too. 2003. An Improved Procedure for Preparing Smaller and Nearly Monodispersed Thiol-Stabilized Platinum Nanoparticles. **Langmuir** 19 (24): 10361-10365.

Ye, H. Liu, I. Schultz, W. Wu, D.G. Naugle and I. Lyuksyutov. 2008. Template-Based Fabrication of Nanowire-Nanotube Hybrid Arrays. **Nanotechnology** 19 (32):

Yoshida, T. Nobukawa, S.I. Ito, K. Tomishige and K. Kunimori. 2004. Structure Sensitivity of Ion-Exchanged Fe-MFI in the Catalytic Reduction of Nitrous Oxide by Methane under an Excess Oxygen Atmosphere. **J. Catal.** 223 (2): 454-464.

Yoshitake, Y. Shimakawa, S. Kuroshima, H. Kimura, T. Ichihashi, Y. Kubo, D. Kasuya, K. Takahashi, F. Kokai, M. Yudasaka and S. Iijima. 2002. Preparation of Fine Platinum Catalyst Supported on Single-Wall Carbon Nanohorns for Fuel Cell Application. **Physica B: Condensed Matter** 323 (1-4): 124-126.

Yu, Z. Liang, J. Cho and F. Caruso. 2003. Nanostructured Electrochemical Sensor Based on Dense Gold Nanoparticle Films. **Nano Lett.** 3 (9): 1203-1207.

Yu, X. Zhang, H. Zhang, D. Han and A.R. Knight. 2011. Preparation and Electrochemical Properties of Gold Nanoparticles Containing Carbon Nanotubes-Polyelectrolyte Multilayer Thin Films. **Electrochim. Acta** 56 (25): 9015-9019.

Yu, G.A. Rance and A.N. Khlobystov. 2009. Electrostatic Interactions for Directed Assembly of Nanostructured Materials: Composites of Titanium Dioxide Nanotubes with Gold Nanoparticles. **J. Mater. Chem.** 19 (47): 8928-8935.

Yu and Ye. 2007a. Recent Advances in Activity and Durability Enhancement of Pt/C Catalytic Cathode in PEMFC. Part I. Physico-Chemical and Electronic Interaction between Pt and Carbon Support, and Activity Enhancement of Pt/C Catalyst. **J. Power Sources** 172 (1): 133-144.

Yu and Ye. 2007b. Recent Advances in Activity and Durability Enhancement of Pt/C Catalytic Cathode in PEMFC. Part Ii: Degradation Mechanism and Durability Enhancement of Carbon Supported Platinum Catalyst. **J. Power Sources** 172 (1): 145-154.

Zhai, H. Zhang, D. Xing and Z.G. Shao. 2007. The Stability of Pt/C Catalyst in H_3PO_4/PBI PEMFC During High Temperature Life Test. **J. Power Sources** 164 (1): 126-133.

Zhang, R. Yuan, Y. Chai and X. Li. 2007. Investigation of the Electrochemical and Electrocatalytic Behavior of Positively Charged Gold Nanoparticle and L-Cysteine Film on an Au Electrode. **Anal. Chim. Acta** 596 (1): 99-105.

Zhang and Wang. 2007. One Step Synthesis of Multiwalled Carbon Nanotube/Gold Nanocomposites for Enhancing Electrochemical Response. **Chem. Mater.** 19 (5): 976-978.

Zhang, M. Hummelgård and H. Olin. 2009. Simple and Efficient Gold Nanoparticles Deposition on Carbon Nanotubes with Controllable Particle Sizes. **Materials Science and Engineering B: Solid-State Materials for Advanced Technology** 158 (1-3): 48-52.

Zhang, Q. Wang, L. Zhang, S. Yang, Z. Yang and B. Ding. 2008. The Growth of Uncoated Gold Nanoparticles on Multiwalled Carbon Nanotubes. **Colloids Surf. A: Physicochem. Eng. Asp.** 312 (2-3): 136-141.

Zhang, R.Y. and H. Olin. 2011. Gold-Carbon Nanotube Nanocomposites: Synthesis and Applications. **international Journal Biomedical Nanoscience and Nanotechnology** 2 (2): 112-135.

Zhang, P. Sherrell, A.I. Minett, J.M. Razal and J. Chen. 2010a. Carbon Nanotube Architectures as Catalyst Supports for Proton Exchange Membrane Fuel Cells. **Energy and Environmental Science** 3 (9): 1286-1293.

Zhang, J. Chen, A.I. Minett, G.F. Swiegers, C.O. Too and G.G. Wallace. 2010b. Novel Acnt Arrays Based Mea Structure-Nano-Pt Loaded ACNT/Nafion/ACNT for Fuel Cell Applications. **Chem. Commun.** 46 (26): 4824-4826.

Zhang, W.H., J.L. Shi, L.Z. Wang and D.S. Yan. 2000. Preparation and Characterization of ZnO Clusters inside Mesoporous Silica. **Chem. Mater.** 12 (5): 1408-1413.

Zhang, N.W. Franklin, R.J. Chen and H. Dai. 2000. Metal Coating on Suspended Carbon Nanotubes and Its Implication to Metal-Tube Interaction. **Chem. Phys. Lett.** 331 (1): 35-41.

Zhang, C. Suc, Z. Liu and J. Li. 2006. Carbon Nanotubes Functionalized by NO_2: Coexistence of Charge Transfer and Radical Transfer. **J. Phys. Chem. B** 110 (45): 22462-22470.

Zhou, J. Wu, A. Nie, R.C. Forrey, A. Tachibana and H. Cheng. 2007. On the Sequential Hydrogen Dissociative Chemisorption on Small Platinum Clusters:

A Density Functional Theory Study. **J. Phys. Chem. C** 111 (34): 12773-12778.

Zhou, S. Wang, W. Zhou, G. Wang, L. Jiang, W. Li, S. Song, J. Liu, G. Sun and Q. Xin. 2003. Novel Synthesis of Highly Active Pt/C Cathode Electrocatalyst for Direct Methanol Fuel Cell. **Chem. Commun.** 9 (3): 394-395.

Zhu, X. Lu, M. Li, Y. Shao and Z. Zhu. 2009. Nonenzymatic Glucose Voltammetric Sensor Based on Gold Nanoparticles/Carbon Nanotubes/Ionic Liquid Nanocomposite. **Talanta** 79 (5): 1446-1453.

Zhu, Z.H., S. Wang, G.Q. Lu and D.K. Zhang. 1999. The Role of Carbon Surface Chemistry in N_2O Conversion to N_2 over Ni Catalyst Supported on Activated Carbon. **Catal. Today** 53 (4): 669-681.

APPENDIX

Presentations and Publications

Publications

Panvika Pannopard, Chaiyan Boonyuen, Chompunuch Warakulwit, Yasuto Hoshikawa, Takashi Kyotani and Jumras Limtrakul. Size-Tailored Synthesis of Gold Nanoparticles and Their Facile Deposition on AAO-Templated Carbon Nanotubes via Electrostatic Self-Assembly: Application to H_2O_2 detection (to be submitted).

Panvika Pannopard, Pipat Khongpracha, Chompunuch Warakulwit, Supawadee Namuangruk, Michael Probst and Jumras Limtrakul 2012. Structures, Energetics and Reaction Mechanisms of Nitrous Oxide on Transition-Metal-Doped and -Undoped Single-Wall Carbon Nanotubes. **ChemPhyChem** 13: 583-587.

Risako Tsunoyama, Hironori Tsunoyama, Panvika Pannopard, Jumras Limtrakul and Tatsuya Tsukuda 2010. MALDI Mass Analysis of 11 kDa Gold Clusters Protected by Octadecanethiolate Ligands. **J. Phys Chem. C** 114: 16004–16009.

Panvika Pannopard, Pipat Kongpracha, Michael Probst and Jumras Limtrakul 2009. Gas Sensing Properties of Platinum Derivatives of Single-Walled Carbon Nanotubes: A DFT Analysis. **J. Mol. Graphics Model.** 28: 62–69.

Panvika Pannopard, Pipat Kongpracha, Michael Probst and Jumras Limtrakul 2008. Structure and Electronic Properties of "DNA-Gold-Nanotube" Systems: A Quantum Chemical Analysis. **J. Mol. Graphics Model.** 26: 1066–1075.

Presentations

Poster Presentation

Gas Sensing Properties of Platinum Derivatives of Single-Walled Carbon Nanotubes: A DFT analysis. 1st Chemistry Postgraduate Symposium (ChPGS), Department of Chemistry, Kasetsart University, Thailand (August 8, 2012).

MALDI Mass Analysis of 11 kDa Gold Clusters Protected by Octadecanethiolate Ligand. RGJ – Ph.D. Congress XIII (The Thailand Research Fund), Jomtien Palm Beach Resort, Chonburi, Thailand (April 6-8, 2012).

Enhancement of Gas Sensing Properties based on Platinum Derivatives of Single Walled Carbon Nanotubes: A DFT analysis. Pure and Applied Chemistry International Conference 2009 (PACCON 2009), Pitsanulok, Thailand (January 14-16, 2009).

Structure and Electronic Properties of "DNA-Gold-Nanotube" Systems: A Quantum Chemical Analysis. Nanotech 2007, Santa Clara, California, USA. (May 20-24, 2007).

Oral Presentation

Nitrous Oxide Decomposition on Transition Metal Doped and Undoped Carbon Nanotubes : A DFT study. 1st National Research Symposium on Petroleum, Petrochemicals, and Advanced Materials and 16th PPC Symposium on Petroleum, Petrochemicals, and Polymers, Montien Hotel, Bangkok, Thailand (April 22, 2010).

Decomposition of nitrous oxide on transition metal-doped carbon nanotubes. 239th ACS National Meeting & Exposition, San Francisco, California, USA (March 21-25, 2010).

Mass Spectrometric Determination of Molecular Formula of 11-kDa Au:Alkanethiolate Cluster Compounds. General Meeting and Mini Symposium of JENESYS Programme 2009, Institute for molecular Science, National Institute of Natural Sciences, Okazaki, Japan (July 31, 2009).

CURRICULUM VITAE

NAME	:	Miss Panvika Pannopard
BIRTH DATE	:	June 9, 1980
BIRTH PLACE	:	Saraburi, Thailand

EDUCATION :

YEAR	INSTITUTE	DEGREE/DIPLOMA
2007	Kasetsart University	M.Sc.(Chemistry), Major Physical Chemistry
2001	Thammasat University	B.Sc. (Chemistry) 2nd Class Honours

AWARDS :

Outstanding Poster Presentation in 1st Chemistry Postgraduate Symposium (ChPGS), Department of Chemistry, Kasetsart University (2012).

Outstanding Poster Presentation in RGJ – Ph.D. Congress XIII, the Thailand Research Fund (2012).

Honor and Outstanding on Her Thesis Award, Graduate School, Kasetsart University (2007).

Medal Award and Certificate of Academic Excellence, Professor Dr. Tab Nilanidhi Foundation (2001).